UNICA

UNIVERSITÀ
DEGLI STUDI
DI CAGLIARI

Ph.D. DEGREE IN

Physics

Cycle XXXV

TITLE OF THE Ph.D. THESIS

J/ψ production and polarization with the inclusion of transverse momentum effects

Scientific Disciplinary Sector(s)

FIS/02

Ph.D. Student:	Luca Maxia
Supervisor	Umberto D'Alesio
Co-Supervisor	Cristian Pisano

Final exam. Academic Year 2021/2022
Thesis defence: March 2023 Session

Contents

List of Publications

This thesis is based on:

U. D'Alesio, L. Maxia, F. Murgia, C. Pisano, and S. Rajesh. "Process dependence of the gluon Sivers function in $p^{\uparrow}p \to J/\psi + X$ within a TMD scheme in NRQCD". In: Phys. Rev. D 102.9 (2020), p. 094011. arXiv: 2007.03353 [hep-ph].

U. D'Alesio, L. Maxia, F. Murgia, C. Pisano, and S. Rajesh. "J/ψ polarization in semi-inclusive DIS at low and high transverse momentum". In: JHEP 03 (2022), p. 037. arXiv: 2110.07529 [hep-ph].

U. D'Alesio, L. Maxia, F. Murgia, C. Pisano, and S. Rajesh. "J/ψ polarization in large-P_T semi-inclusive deep-inelastic scattering at the EIC ". Submitted for publication. arXiv: 2301.11987 [hep-ph]

List of Abbreviations

BNL	**B**rookhaven **N**ational **L**aboratory
CEM	**C**olor **E**vaporation **M**odel
CF	**C**olor **F**actor
CGI-GPM or **CGI**	**C**olor **G**auge **I**nvariant - Generalized Parton Model
cm	**c**enter-of-**m**ass
CO	**C**olor **O**ctet
CS	**C**olor **S**inglet
CSM	**C**olor **S**inglet **M**odel
DY	**D**rell-**Y**an
EIC	**E**lectron-**I**on **C**ollider
FNAL	**F**ermi **N**ational **A**ccelarator **L**aboratory
FSI	**F**inal **S**tate **I**nteraction
GPM	**G**eneralized **P**arton **M**odel
GSF	**G**luon-**S**ivers **F**unction
iCEM	**i**mproved **C**olor **E**vaporation **M**odel
HERA	**H**adron-**E**lectron **R**ing **A**ccelerator
ISI	**I**nitial **S**tate **I**nteraction
LDME	**L**ong **D**istance **M**atrix **E**lement
LO	**L**eading **O**rder
NLO	**N**ext-to-**L**eading **O**rder
NRQCD	**N**on-**R**elativistic **QCD**
PDF	**P**arton **D**istribution **F**unction
RHIC	**R**elativistic **H**eavy **I**on **C**ollider
SIDIS	**S**emi-**I**nclusive **DIS**
SSA	**S**ingle-**S**pin **A**symmetry
TMD	**T**ransverse **M**omentum **D**ependent
TMD-PDF	**T**ransverse **M**omentum **D**ependent **P**arton **D**istribution **F**unction
TMDs	**T**ransverse **M**omentum **D**ependent Parton Distribution**s**
TMDShF	**TMD-Sh**ape **F**unction
w.r.t.	**w**ith **r**espect **t**o

Chapter 1

Introduction

1.1 J/ψ production

The J/ψ meson has drawn great interest among the experimental and theoretical communities since its simultaneous discovery in 1974, at the Brookhaven National Laboratory (BNL) [1] and the Standford Linear Accelerator Center (SLAC) [2]. As a consequence of its relatively light mass, it can be abundantly produced at all high-energy electron-proton and proton-proton colliders. Moreover, it is a bound state of a $c\bar{c}$ pair with the same total angular-momentum, parity and charge-conjugation quantum numbers of a photon ($J^{PC} = 1^{--}$). Hence, the J/ψ decays into electron-positron and muon-antimuon pairs with a significant branching ratio of about 6% for each channel [3], making its detection less experimentally challenging compared to other quarkonia. From a theoretical point of view, it is an excellent tool to probe both the perturbative and nonperturbative aspects of QCD, as well as their interplay. Since the charm mass m_c is much larger than the QCD scale parameter $\Lambda_{\rm QCD}$, J/ψ production involves the perturbative production of a $c\bar{c}$ pair and its subsequent, nonperturbative transition to the observed quarkonium state. Different frameworks provide different descriptions of the latter hadronization process; see Refs. [4, 5] for some reviews.

Among the various hadronization models, the present thesis will mainly focus on the effective field theory approach of Non-Relativitic QCD (NRQCD) [6, 7]. This framework takes into account the non-relativistic nature of the relative velocity v of the heavy quark-antiquark pair, and uses it to perform an expansion, in addition to the usual one with respect to (w.r.t.) the strong coupling constant α_s. As a consequence, the $c\bar{c}$ pair at short distance can be produced in any Fock state $n = {}^{2S+1}L_J^{(c)}$ with definite orbital angular momentum L, spin S, total angular momentum J and color configuration $c = 1, 8$. NRQCD therefore predicts the existence of intermediate color-singlet (CS) and color-octet (CO) states, which subsequently evolve into physical, CS quarkonia by the emission of soft gluons. This transition is encoded in proper long-distance matrix elements (LDMEs), that depend on the considered quarkonium and the Fock-state from which it is generated. In the specific case of J/ψ production, the leading-order contribution in the v expansion originates from the ${}^3S_1^{(1)}$ CS state, while the leading relativistic corrections to the order $\mathcal{O}(v^4)$ are given by the CO states ${}^1S_0^{(8)}$, ${}^3S_1^{(8)}$, and ${}^3P_J^{(8)}$ with $J = 0, 1, 2$.

For S-wave quarkonia like the J/ψ charmonium, the traditional Color Singlet Model (CSM) is recovered in the limit $v \to 0$. In the CSM, the $c\bar{c}$ pair is therefore produced at short distances directly with the quantum numbers of the observed S-wave quarkonium state. It is worth mentioning that this model cannot be considered as a complete theory, since at the next-to-leading order (NLO) P-wave quarkonia are affected by uncancelled infrared singularities, which are properly removed in

NRQCD. We would like to emphasize, however, that a purely CS approach is not a synonym of a poor description. Although the CSM predictions systematically undershot J/ψ and $\psi(2S)$ production data at $\sqrt{s} = 1.8$ TeV [8, 9], it has been recently shown that higher order corrections in α_s to the CSM can improve the agreement between experimental data and theory estimates. For example, in Refs. [10, 11], the effects of higher order contributions at the Relativistic Heavy Ion Collider (RHIC) at Brookhaven National Laboratory (BNL) are shown to play an important role, while in Ref. [12, 13] they discussed the same topic for HERA experiments (and potentially at the new Electron-Ion Collider). Furthermore, the values of the CO LDMEs extracted from different fits to data on J/ψ and Y yields [14–18] are not compatible with each other, even within large uncertainties [4, 5, 19], illustrating that the role of the CO contributions has still to be clarified.

For completeness, we mention also a third model with historical relevance, as it was one of the first developed, and is still used nowadays: the Color Evaporation Model (CEM) [20–23]. This approach considers the production of the unbound heavy quark-antiquark pair with an invariant mass m in a specific range. In the case of J/ψ, this region is limited by the production of the $c\bar{c}$ pair ($2m_c$) and the open production of the lightest D meson ($2M_D$). Despite this, even if it is intuitive and successful in the explanation of some J/ψ production data, the model still has some drawbacks. Firstly, predictions from CEM were poor compared to other models; in Ref. [24] CEM and NRQCD were both compared with J/ψ production data from FermiLab (FNAL), finding a better χ^2 agreement within the NRQCD approach. In addition, the CEM is based on too strong and limited assumptions that are not supported by data. Recently, an improved version of this model, called improved CEM (iCEM), has been developed [25]. In this case, they explicitly identify the soft gluons exchanged (with other color sources) and emitted (which eventually evolve in experimentally observable particles), addressing the latter problem.

It is then clear that the quarkonium hadronization mechanism has not yet been fully understood and is still a puzzling issue. In spite of that, it is extremely important to identify a "*golden*" model that can provide reliable predictions. Thus, we need to study observables with the potential to discern among different hadronization models and frameworks. In this sense, the study of J/ψ polarization can be extremely powerful. Indeed, since the angular parameters associated to this observable are defined as ratios of helicity matrix elements, model and theoretical uncertainties are naturally suppressed. Hence, such a study can represent an invaluable tool to shed light on the quarkonium hadronization process.

1.2 Theoretical description of the Semi-Inclusive DIS process

In principle, it is more robust to develop formal and phenomenological analyses considering processes for which QCD factorization holds, or where there are arguments supporting it. A remarkable process is J/ψ production in Semi-Inclusive DIS (SIDIS), namely $e\,p \to e'\,J/\psi + X$. When performing SIDIS-related studies, we are generally interested in the P_T distribution, where P_T is the J/ψ transverse momentum in the centre-of-mass (cm) frame of the photon-proton system. Since different scales are present in SIDIS, we can identify different regions that depend on the value of P_T w.r.t. such scales. In particular, we have a hard scale μ, which could be a combination of the large scales of the specific process, namely the J/ψ mass M_ψ and

the photon virtuality Q, as well as a soft scale, like the typical nonperturbative QCD scale $\Lambda_{\rm QCD}$ or the proton mass.

If $P_T \gg \Lambda_{\rm QCD}$, we identify a region where usual collinear factorization holds. Explicitly, in this region, we can separate the hard (perturbative) term from the nonperturbative quantities, which are described by collinear (*i.e.* integrated over transverse momentum) parton distribution functions (PDFs) and the usual LDMEs, if we assume the validity of NRQCD as well.

Considering instead $P_T \ll \mu$, we expect that a correct factorization should involve quantities that also include the transverse momentum dependence. In the specific case of quarkonium production, however, transverse momentum dependent (TMD) factorization is not formally proven. Nevertheless, it has been extensively studied when a light-hadron h is produced in the final state, namely in $e\,p \to e'\,h + X$; in this thesis we will refer to this process as the *standard* SIDIS. The standard SIDIS is one of the processes in which it is possible to define two well-separated scales and for which TMD factorization is proven [26]. Note that the replacement of the light hadron with a quarkonium in the final state does not modify the color flow, which determines the gauge-link structure of the TMD correlator (see Ref. [27]). Furthermore, this structure is not affected by the presence of the quarkonium mass or its spin. Thus, it is reasonable to assume that no factorization breaking effects are present in quarkonium production in SIDIS. Even if we expect TMD factorization to be a valid and correct description of this process at low P_T, the exact factorized form of the observables is still unknown.

A common assumption is to write SIDIS observables in terms of a hard perturbative term, combined with a TMD-PDF and the usual LDMEs. In particular, such observables are sensitive to the almost unknown gluon TMDs, which can be singled out by looking at different transverse momentum distributions and azimuthal asymmetries [27]. Within basically the same framework, other proposals have been put forward to use inclusive quarkonium production as a probe of gluon TMDs, both in lepton-proton [28–30] and in proton-proton collisions [31–35].

More recently, it has been shown [36, 37] that a generalization of the CO LDMEs, called TMD shape functions (TMDShFs), is required to obtain a proper TMD factorization for the above-mentioned processes. These new objects describe the transverse momentum smearing due to soft gluon interactions in the hadronization process; this is in contrast to the collinear picture, where the J/ψ momentum has the same direction as the $c\bar{c}$-pair. We can then try to understand the role of these new TMD quantities by comparing the TMD and collinear expressions in an overlapping region given by $\Lambda_{\rm QCD} \ll P_T \ll \mu$.

Note that from an experimental point of view, both the J/ψ polarization and the role of the TMDShFs can be explored by the future Electron-Ion Collider (EIC) [38–40]. Thus, our aim will be to provide polarization estimates in kinematic regimes that will be explored at this facility, including both high- and low-P_T regimes. In particular, the latter could be extremely useful to understand the gluon content of protons, together with a correct parameterization of the TMDShF.

1.3 Single-Spin Asymmetries in J/ψ hadroproduction

J/ψ production studies in SIDIS processes, as investigated at the EIC, will certainly be a great opportunity. At the same time, it is extremely interesting to explore other possibilities. Although it is well known that TMD factorization has been proven only for a limited class of processes, namely for standard SIDIS, Drell-Yan

($h_1\, h_2 \;\to\; l^+\, l^- + X$) and almost back-to-back hadron production in $e^+\, e^-$ annihilation processes, several hadron facilities provide a large amount of experimental information, relevant in this context. For instance, the PHENIX experiment at RHIC collected data for J/ψ production in proton-proton collisions, both for unpolarized beams and for single transversely polarized protons [41, 42], namely $p\, p \to J/\psi + X$ and $p\, p^\uparrow \to J/\psi + X$. The second process allows the study of a particular observable; when one of the initial protons is transversely polarized, we can look at the left-right asymmetry w.r.t. the direction of the proton polarization. This observable is the well-known transverse Single-Spin Asymmetry (SSA), also denoted as A_N. For inclusive production, independently of the final hadron species, this observable cannot be understood within a collinear scheme at leading twist, as shown in Ref. [43]. On the other hand, sizeable SSAs in inclusive pion production were observed at FNAL [44–47]. To overcome this difficulty, two theoretical approaches were formulated.

One, formally proven, is based on higher-twist parton-hadron correlation functions [48–51], and it is usually referred to as the twist-three formalism. Its formulation was developed by Qiu and Sterman [49, 52], and independently proposed also by Efremov and Teryaev, *e.g.* Ref. [48]. This formalism considers the interference between one active collinear parton with two collinear partons. The SSA is then given in terms of new twist-3 quark-gluon correlation functions, defined as the expectation values of three field operators between hadronic states, depending on two light-cone momentum fractions. Even if they do not have a direct partonic interpretation, these functions, convoluted with ordinary twist-2 distribution functions and perturbative calculable hard scattering parts, are able to produce sizeable asymmetries, and to describe SSA data. This success motivates several extensions and refinements [50, 51, 53–59]. For the latest updates and a recent global analysis of SSAs and azimuthal asymmetries within this formalism, see Ref. [60].

A second one, more phenomenological and with a direct partonic interpretation, is based on transverse momentum dependent parton distributions (shortly referred to as TMDs) and it is usually called Generalized Parton Model (GPM) [61–63]. This approach, easily formulated within the helicity formalism, see Ref. [64], was originally applied to SSAs for single-inclusive processes and still reveals very important features. Indeed, several interesting phenomenological analysis with the GPM have been carried out.

An astonishing result from BRAHMS, PHENIX and STAR Collaborations at RHIC, operating at cm energies $\sqrt{s} = 63$, 200 and 500 GeV, is that even at such large energies the SSAs for inclusive pion production persist and are still sizeable [65–69]. This caused an increasing interest in the TMD formalism, which was then developed on more formal grounds for the three processes mentioned above [26, 70–75] and adopted in phenomenological studies, *e.g.* Refs. [76–80]. An ambitious program still underway consists in including, within the GPM approach, different processes to perform a global analysis; see for example Refs. [77, 80, 81] for combined analyses of the Sivers effect in SIDIS and $p^\uparrow p$ collisions.

The study of SSAs, both in processes where TMD factorization is proven, *e.g.* standard SIDIS, and where it is assumed on phenomenological grounds, *e.g.* inclusive production in pp collisions, still drives phenomenological interest. In all cases, the main result achieved so far is getting information on the quark contribution. On the other hand, in order to have a more complete picture of the internal structure of hadrons, this knowledge alone is not sufficient. As already shown a long time ago by the European Muon Collaboration (EMC) experiment [82], the quark spin contributes less than 1/3 to the total proton spin, invalidating the simple quark model picture where the proton spin is given in terms of the valence quark spins. The

missing contributions can then be ascribed both to the gluon spin and (as nowadays believed) to the partons (quark and gluon) orbital angular momentum. This problem is indeed one of the open questions in hadron physics.

In order to access directly the gluon contribution, it is almost necessary, or at least worth attempting, to go beyond the standard processes for which TMD factorization is proven[1], since these are mostly dominated by quark initial states. Indeed, the aforementioned studies at RHIC, focusing on $p\,p \to J/\psi + X$ and $p\,p^{\uparrow} \to J/\psi + X$ processes, represent potential tools for extracting valuable information on gluon distributions. In particular, the study of SSAs in J/ψ production is crucial since these asymmetries may give access to an important, still poorly known, gluon TMD distribution, namely the Sivers function [83, 84]. Unfortunately, such phenomenological study is very demanding, and the provided A_N data are still too few and not precise enough to draw any significant conclusions. On the other hand, upcoming experiments are planned and can eventually provide sufficient number of data points to perform more robust phenomenological analyses.

For these reasons, we will provide SSA estimates in different frameworks to understand their potential role in constraining the gluon Sivers function. More precisely, our estimates will be obtained, from the perspective of a coherent and more complete analysis, by adopting the GPM phenomenological approach, but considering also the inclusion of initial- and final-state interactions (ISIs and FSIs). This formal extension, with a close connection to the twist-three formalism, is referred to as the Color-Gauge Invariant GPM [85]. This analysis will help us in deepening our understanding on color TMD effects in the production and polarization of J/ψ mesons in hadronic collisions.

1.4 Outline

This thesis is organized as follows:

- In Chapter 2 we present the formal and model independent derivation of the cross section for polarized J/ψ production in SIDIS, expressed in terms of helicity structure functions. We then discuss how to evaluate these quantities within the NQRCD and the CSM approaches in two domains, namely the high- and low-transverse momentum regions. Moreover, estimates up to order α_s^2 in the two mentioned regimes are provided for the EIC kinematics, allowing for a comparison of NRQCD and CSM predictions.

- In Chapter 3 we consider the overlapping region between the TMD and collinear frameworks in SIDIS to determine the perturbative tail of the TMDShFs. Both unpolarized and polarized J/ψ production are discussed.

- In Chapter 4 we study the SSA observables in pp collision when in the final state a J/ψ is produced. We introduce the key points of the phenomenological GPM approach needed for the calculation of SSAs. We then show how to include ISIs and FSIs according to the CGI-GPM. All estimates are evaluated within both the GPM and CGI-GPM, while for the quarkonium formation mechanism the CSM and NRQCD have been adopted. Results are shown for different kinematics available at PHENIX, LHC fixed target, NICA SPD and SpinQuest.

[1] Namely, the three processes: SIDIS, DY and e^+e^- annihilation.

- Conclusions are drawn in Chapter 5, where also some perspectives for the future are presented.

Finally, a number of useful relations and results are collected in the appendices.

Chapter 2

J/ψ polarization in SIDIS

In this chapter we study the polarization of J/ψ mesons produced in SIDIS as a potential tool to deepen our knowledge of the quarkonium formation mechanism, as well as to probe the gluon content of the proton. The study of this process at finite values of the exchanged photon virtuality Q^2 has several theoretical and experimental advantages as compared to photoproduction. More specifically, as Q^2 increases, theoretical uncertainties decrease and resolved photon contributions are expected to be negligible. Background from diffractive J/ψ production is also supposed to decrease with Q^2 faster than the SIDIS cross section. From the experimental point of view, the distinct signature of the scattered electron makes the process particularly easy to detect. Clearly, cross sections are smaller than those relative to photoproduction; however, considering the achievable high luminosities, this study should be feasible at the EIC.

The present chapter is organized as follows. In Sec. 2.1 we first consider the theoretical description of SIDIS based on collinear factorization, and we derive the cross section for unpolarized J/ψ production in terms of Lorentz-invariant structure functions. We then move to the analysis of J/ψ polarization in Sec. 2.2, where we introduce the helicity structure functions (Sec. 2.2.2). The J/ψ polarization parameters are calculated within the NRQCD framework in the collinear regime in Sec. 2.2.3, while in Sec. 2.2.4 we discuss the typical frames adopted to measure the J/ψ angular decay distributions. In particular, considering two of them, in Sec 2.3 we present numerical estimates of the polarization parameter for the EIC kinematics. Finally, in Sec. 2.4 we discuss the formal derivation of the polarization parameters in the TMD approach.

2.1 SIDIS cross section

Before moving our focus to the study of the J/ψ polarization states, it is useful to examine some formal aspects of the SIDIS process for unpolarized J/ψ production. We consider a kinematic region where the photon virtuality Q is equal or greater than the J/ψ mass M_ψ, namely $Q \geq M_\psi$. More explicitly, we look at the reaction (see Fig. 2.1)

$$e\,(l_e) + p\,(P) \to e'\,(l_{e'}) + J/\psi\,(P_\psi) + X\,(P_X), \tag{2.1}$$

with X corresponding to a system of undetected hadrons, and where in the parenthesis we provide the momenta of the corresponding particles. The process is mediated by a virtual photon with momentum q, where

$$q = l_e - l_{e'}, \tag{2.2}$$

with $Q^2 \equiv -q^2 > 0$.

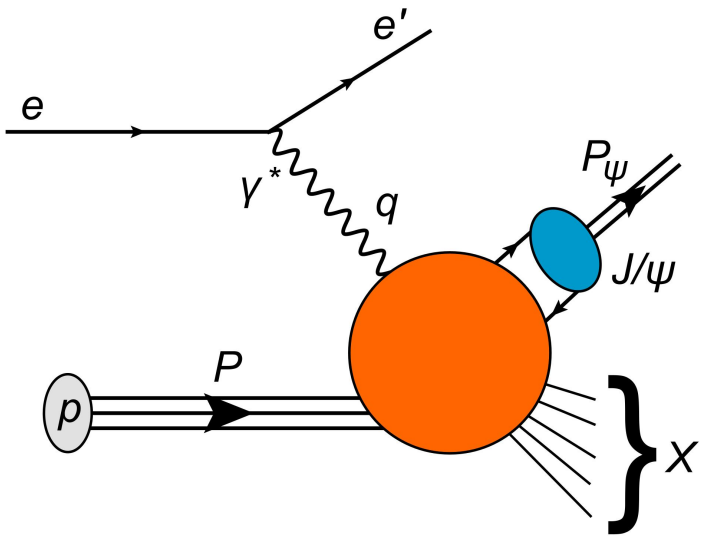

FIGURE 2.1: This figure depicts the J/ψ unpolarized production in semi-inclusive DIS. The orange circle corresponds to the hard term of the process, perturbative calculable. Instead, the blue bubble describes the bound and hadronization of the $c\bar{c}$ pair into the J/ψ.

The SIDIS cross section in its most differential form reads

$$\mathrm{d}\sigma = \frac{1}{2S}\,\frac{\mathrm{d}^3 P_X}{(2\pi)^3 2P_X^0}\,\frac{\mathrm{d}^3 l_{e'}}{(2\pi)^3 2E_{e'}}\,\frac{\mathrm{d}^3 P_\psi}{(2\pi)^3 2E_\psi}\,|\mathcal{M}|^2\,(2\pi)^4\delta^{(4)}\left(q+P-P_\psi-P_X\right). \quad (2.3)$$

The denominator $2S$ is the flux factor, where $S = (l_e + P)^2 \approx 2\,l_e \cdot P$. Instead, the amplitude squared $|\mathcal{M}|^2$ corresponds to the perturbative part of the process, namely it is related to the orange circle in Fig. 2.1. Even if we need a model to produce estimates for the J/ψ yield and polarization (see Sec. 2.2.3), results in the following discussion are completely model independent.

When studying SIDIS processes, it is convenient to introduce the following Lorentz-invariant variables

$$x_B = \frac{Q^2}{2P\cdot q}, \quad y = \frac{P\cdot q}{P\cdot l_e}, \quad z = \frac{P\cdot P_\psi}{P\cdot q}, \quad (2.4)$$

which fulfill the bounds $0 \leq x_B, y, z \leq 1$.

Finally, we note that in this section and in the following, the mass of the leptons, *light* quarks and antiquarks will be ignored. We will neglect the proton mass m_p as well, unless otherwise stated.

2.1.1 Kinematics

In a reference frame where the virtual photon and the proton have no transverse momentum, we can choose two light-like four-vectors κ_+ and κ_-, with $\kappa_+ \cdot \kappa_- = 1$, and perform a Sudakov decomposition of the four-momenta of the particles involved in

the process,

$$
\begin{aligned}
P^\mu &= \kappa_-^\mu, \\
q^\mu &= \frac{Q^2}{2x_B}\kappa_+^\mu - x_B\kappa_-^\mu, \\
P_\psi^\mu &= \hat{z}\frac{Q^2}{2x_B}\,\kappa_+^\mu + \frac{M_T^2}{\hat{z}\,Q^2}x_B\kappa_-^\mu + P_\perp^\mu, \\
l_e^\mu &= \frac{1}{y}\left[\frac{Q^2}{2\,x_B}\kappa_+^\mu + (1-y)\,x_B\,\kappa_-^\mu + Q\sqrt{1-y}\,\hat{l}_\perp^\mu\right],
\end{aligned}
\tag{2.5}
$$

with $\hat{l}_\perp^2 = -1$. We note that, within a more specific choice of the reference frame, where the proton and the photon move along the $\hat{Z}$-axis and the azimuthal angles of the leptons $\phi_e = \phi_{e'} = 0$, l_e can still have a non-zero component in the transverse direction, along the $\hat{X}$-axis.

A different decomposition will be employed to study J/ψ polarization, since one needs to move to the quarkonium rest frame, where the J/ψ transverse momentum has to be zero.

Before going on with the study of the SIDIS cross section, it is convenient to rewrite the phase space in Eq. (2.3) in terms of the typical Lorentz-invariant quantities, x_B, y and z. In particular, in terms of the lepton energies E_e, $E_{e'}$ and the scattering angle $\theta_{e'}$ defined in the proton rest-frame, we have

$$
x_B = \frac{Q^2}{2\,m_p\,(E_e - E_{e'})}, \quad y = 1 - \frac{E_{e'}}{E_e},
$$

$$
Q^2 = 2\,E_e\,E_{e'}\,(1-\cos\theta_{e'}), \quad S = 2\,m_p\,E_e. \tag{2.6}
$$

From these expressions, we can write the Jacobian of the transformation from $(x_B,\, y)$ to $(E_{e'},\, \cos\theta_{e'})$

$$
J = \begin{vmatrix} \frac{\mathrm{d}x_B}{\mathrm{d}E_{e'}} & \frac{\mathrm{d}x_B}{\mathrm{d}\cos\theta_{e'}} \\ \frac{\mathrm{d}y}{\mathrm{d}E_{e'}} & \frac{\mathrm{d}y}{\mathrm{d}\cos\theta_{e'}} \end{vmatrix} = \begin{vmatrix} \frac{\mathrm{d}x_B}{\mathrm{d}E_{e'}} & -\frac{E_{e'}}{m_p y} \\ -\frac{1}{E_e} & 0 \end{vmatrix} = \frac{2E_{e'}}{yS}. \tag{2.7}
$$

Hence, one obtains

$$
\begin{aligned}
\frac{\mathrm{d}^3 l_{e'}}{(2\pi)^3 2E_{e'}} &= \frac{E_{e'}\mathrm{d}E_{e'}\,\mathrm{d}\cos\theta_{e'}\,\mathrm{d}\varphi_{e'}}{2(2\pi)^3} \\
&= \frac{y\,S}{4(2\pi)^3}\,\mathrm{d}x_B\,\mathrm{d}y\,\mathrm{d}\varphi_{e'} = \frac{y\,S}{4(2\pi)^2}\,\mathrm{d}x_B\,\mathrm{d}y,
\end{aligned}
\tag{2.8}
$$

where in the last step we have integrated over the azimuthal angle $\varphi_{e'}$ of the final electron in the proton rest frame.

Finally, the phase space for the J/ψ meson can be expressed as

$$
\mathrm{d}^4 P_\psi \equiv \frac{\mathrm{d}^3 P_\psi}{2E_\psi} = \frac{P_\perp}{2\,z}\,\mathrm{d}z\,\mathrm{d}P_\perp\,\mathrm{d}\phi_\psi. \tag{2.9}
$$

2.1.2 Lorentz-invariant structure functions

In this section we present a model independent parameterization of the differential cross section in terms of Lorentz-invariant structure functions. First of all, we separate the amplitude squared in Eq. (2.3) in the product of two tensors, one leptonic

and the other one hadronic,

$$|\mathcal{M}|^2 = \frac{L^{\mu\nu}\, H_{\mu\nu}}{Q^4}. \tag{2.10}$$

The (unintegrated) hadronic tensor $H_{\mu\nu}$ is defined as the product of current matrix elements

$$H_{\mu\nu} = \langle P|J_\mu(0)|P_X; P_\psi\rangle \, \langle P_X; P_\psi|J_\nu(0)|P\rangle \, . \tag{2.11}$$

Moreover, we define $W_{\mu\nu}$ as its integral over the phase space of the undetected system

$$W_{\mu\nu} = \int \frac{\mathrm{d}^3 P_X}{(2\pi)^3 2P_X^0}\, \delta^{(4)}(q + P - P_\psi - P_X) H_{\mu\nu}. \tag{2.12}$$

Hence, from Eq. (2.3) the following differential cross section can be obtained

$$\frac{\mathrm{d}\sigma}{\mathrm{d}x_B\, \mathrm{d}y\, \mathrm{d}^4 P_\psi} = \frac{1}{16\pi}\frac{y}{Q^4} L^{\mu\nu} W_{\mu\nu}, \tag{2.13}$$

where the integration over the azimuthal angle of the scattered lepton e' has been performed.

The hadronic tensor $W_{\mu\nu}$ depends on the momenta q^μ, P^μ and P_ψ^μ, namely $W^{\mu\nu} \equiv W^{\mu\nu}(q, P, P_\psi)$. Furthermore, it has to fulfill the properties of hermeticity, parity and gauge invariance.

Hermeticity:
From its definition we have that

$$W_{\mu\nu}(q, P, P_\psi) = W^*_{\nu\mu}(q, P, P_\psi), \tag{2.14}$$

which implies that the symmetric and antisymmetric parts are respectively real and imaginary. Since we sum over the lepton spins, the lepton tensor is symmetric in the indices (μ, ν) and only the symmetric part of the hadronic tensor contributes to the cross section.

Parity:
If we define a vector and its parity transformed version respectively as $v^\mu = (v^0, \boldsymbol{v})$ and $\bar{v} \equiv v_\mu = (v^0, -\boldsymbol{v})$, parity invariance of the electromagnetic and strong interactions implies

$$W_{\mu\nu}(q, P, P_\psi) = W_{\mu\nu}(\bar{q}, \bar{P}, \bar{P}_\psi). \tag{2.15}$$

Gauge Invariance:
It is a consequence of the conservation of the hadronic current $J_\mu(0)$ and corresponds to the Ward Identity

$$q^\mu W_{\mu\nu}(q, P, P_\psi) = q^\nu W_{\mu\nu}(q, P, P_\psi) = 0. \tag{2.16}$$

Therefore the hadronic tensor has to be defined in a space orthogonal to q^μ.

Since $W^{\mu\nu}$ fulfills the Ward Identity, it is convenient to introduce the projections of the four-momenta onto the space orthogonal to q, and use them to write the hadron tensor. To perform this operation, we introduce the projector

$$\hat{\eta}^{\mu\nu} = \eta^{\mu\nu} + \frac{q^\mu q^\nu}{Q^2}, \tag{2.17}$$

with $\eta^{\mu\nu}$ being the Minkowski metric with signature $(+,-,-,-)$. The tensor $\hat{\eta}^{\mu\nu}$ fulfills the relations $q^\mu \hat{\eta}_{\mu\nu} = q^\nu \hat{\eta}_{\mu\nu} = 0$. Hence, we construct the following vectors orthogonal to q,

$$\begin{aligned}\hat{P}^\mu &= \hat{\eta}^{\mu\nu}\frac{P_\nu}{m_p} = \frac{1}{m_p}\left(P^\mu + \frac{P\cdot q}{Q^2}q^\mu\right),\\ \hat{P}^\mu_\psi &= \hat{\eta}^{\mu\nu}\frac{P_{\psi\nu}}{M_\psi} = \frac{1}{M_\psi}\left(P^\mu_\psi + \frac{P_\psi\cdot q}{Q^2}q^\mu\right).\end{aligned} \tag{2.18}$$

The hadronic tensor is then decomposed in terms of four independent structure functions

$$W^{\mu\nu}(q,P,P_\psi) = -W_1\hat{\eta}^{\mu\nu} + W_2\hat{P}^\mu\hat{P}^\nu - \frac{1}{2}W_3\left(\hat{P}^\mu\hat{P}^\nu_\psi + \hat{P}^\nu\hat{P}^\mu_\psi\right) + W_4\hat{P}^\mu_\psi\hat{P}^\nu_\psi, \tag{2.19}$$

which are the only non-vanishing ones after applying the hermeticity and parity conditions. The structure functions W_i are functions of the available Lorentz invariant quantities.

On the other hand, the lepton tensor is related to the emission of the virtual photon from the incoming electron and its symmetric part reads

$$\begin{aligned}L^{\mu\nu} &= e^2\left[-\eta^{\mu\nu}Q^2 + 2(l_e^\mu l_{e'}^\nu + l_e^\nu l_{e'}^\mu)\right]\\ &= e^2\frac{Q^2}{y^2}\Big[-\left(1+(1-y)^2\right)\eta_\perp^{\mu\nu} + 4(1-y)\epsilon_\parallel^\mu\epsilon_\parallel^\nu\\ &\quad + 4(1-y)\left(\hat{l}_T^\mu\hat{l}_T^\nu + \frac{1}{2}\eta_\perp^{\mu\nu}\right) + 2(2-y)\sqrt{1-y}\left(\epsilon_\parallel^\mu\hat{l}_T^\nu + \epsilon_\parallel^\nu\hat{l}_T^\mu\right)\Big],\end{aligned} \tag{2.20}$$

where the average over the electron spin is taken into account, and we keep the dependence on the azimuthal angle of the scattered electron. In the previous equation, $\eta_\perp^{\mu\nu}$ is a tensor transverse w.r.t. the momenta P and q, defined as

$$\eta_\perp^{\mu\nu} = \eta^{\mu\nu} - \frac{1}{P\cdot q}\left(P^\mu q^\nu + P^\nu q^\mu\right) - \frac{Q^2}{(P\cdot q)^2}P^\mu P^\nu, \tag{2.21}$$

while $\epsilon_\parallel$ is the longitudinal polarization vector

$$\epsilon_\parallel^\mu(q) = \frac{1}{Q}\left(q^\mu + \frac{Q^2}{P\cdot q}P^\mu\right). \tag{2.22}$$

Upon integration over the azimuthal angle of the scattered electron, the two terms in the last row of Eq. (2.20) do not contribute to the amplitude squared. The lepton tensor reduces then to the simpler form

$$L^{\mu\nu} = e^2\frac{Q^2}{y^2}\left[-\left(1+(1-y)^2\right)\eta_\perp^{\mu\nu} + 4(1-y)\epsilon_\parallel^\mu\epsilon_\parallel^\nu\right], \tag{2.23}$$

as shown in Ref. [86] in the framework of dimensional regularization. The latter expression for the lepton tensor is used also by Kniehl and Zwirner in Ref. [87]. In this form, one can identify the first term as the emission of transversely polarized photons, while the second corresponds to longitudinally polarized photons. In the photoproduction limit, $Q \to 0$, the second contribution, being proportional to Q,

vanishes (see as example Appendix. B.2.3).

In the following, since in Eq. (2.13) the integration over $\phi_{e'}$ has already been performed, we consider the lepton tensor given in Eq. (2.23). Furthermore, due to the gauge invariance of the hadron tensor, the terms in Eq. (2.13) proportional to q^μ can be dropped, too.

After contracting the lepton and hadron tensors, the SIDIS differential cross section is parameterized as

$$\frac{\mathrm{d}\sigma}{\mathrm{d}x_B\,\mathrm{d}y\,\mathrm{d}z\,\mathrm{d}P_\perp^2} = \frac{2\pi}{z^2}\frac{\alpha}{y\,Q^2}\Big[\,(1+(1-y)^2)\,F_{UU,\perp} + (1-y)F_{UU,\parallel}\Big], \tag{2.24}$$

where the contributions from the transversely and longitudinally polarized photons are manifestly separated. We introduced the structure functions $F_{UU,\mathcal{P}}$, where $\mathcal{P} = \perp,\ \parallel$ is the virtual photon polarization. The structure functions can be projected out of the hadron tensor as follows

$$\begin{aligned} F_{UU,\perp} &= -\frac{z}{16}\eta_\perp^{\mu\nu}\,W_{\mu\nu}, \\ F_{UU,\parallel} &= \frac{z}{4}\,\epsilon_\parallel^\mu \epsilon_\parallel^\nu\,W_{\mu\nu}, \end{aligned} \tag{2.25}$$

or after imposing gauge invariance

$$\begin{aligned} F_{UU,\perp} &= -\frac{z}{16}\left(W_\mu^\mu - \frac{Q^2}{(P\cdot q)^2}P^\mu P^\nu W_{\mu\nu}\right), \\ F_{UU,\parallel} &= \frac{z}{4}\,\frac{Q^2}{(P\cdot q)^2}P^\mu P^\nu W_{\mu\nu} = 4\,F_{UU,\perp} + z\,W_\mu^\mu. \end{aligned} \tag{2.26}$$

2.2 Formal aspects of quarkonium polarization in SIDIS

In the previous section we have discussed the production of unpolarized J/ψ mesons in SIDIS. Here, we explicitly explain how to formally take into account its polarization. This can be accessed experimentally by looking at the angular distributions of the J/ψ decay products, mostly $e^+\,e^-$ or $\mu^+\,\mu^-$ pairs with a branching ratio of about 6% for each channel [3]. For this reason, next to the SIDIS process we also study the subsequent decay of the J/ψ meson into a lepton-antilepton pair,

$$J/\psi\,(P_\psi) \to \ell^+(l^+) + \ell^-(l^-). \tag{2.27}$$

2.2.1 Kinematics

In Eq. (2.3), the phase space for the J/ψ meson has to be replaced by the one for the final leptons. Hence, the differential cross section now reads

$$\begin{aligned} \mathrm{d}\sigma^{J/\psi\to\ell^+\ell^-} \propto\ & \frac{1}{2S}|\mathcal{M}|^2\,(2\pi)^4\delta^{(4)}\left(q+P-l^+-l^--P_X\right) \\ & \times \frac{\mathrm{d}^3P_X}{(2\pi)^3 2P_X^0}\,\frac{\mathrm{d}^3l_{e'}}{(2\pi)^3 2E_{e'}}\,\frac{\mathrm{d}^3l^+}{(2\pi)^3 2E^+}\,\frac{\mathrm{d}^3l^-}{(2\pi)^3 2E^-}, \end{aligned} \tag{2.28}$$

where we omitted the branching ratio $B_{\ell\ell}$, while we explicitly indicated that we are looking at the J/ψ leptonic decay channel.

In the J/ψ rest frame, ℓ^+ and ℓ^- are produced back to back, therefore their energies are the same ($E^+ = E^-$). Moreover, by imposing momentum conservation in

the decay process we find

$$\begin{aligned}\frac{\mathrm{d}^3 l^+}{(2\pi)^3 2E^+}\frac{\mathrm{d}^3 l^-}{(2\pi)^3 2E^-} &= \frac{\mathrm{d}^3 l^+}{(2\pi)^3 2E^+}\frac{\mathrm{d}^3 l^-}{(2\pi)^3 2E^-}\left[\mathrm{d}^4 P_\psi\, \delta^{(4)}(l^+ + l^- - P_\psi)\right] \\ &= \frac{\mathrm{d}^3 l^+}{(2\pi)^3 2E^+}\frac{\mathrm{d}^4 P_\psi}{(2\pi)^3 2E^-}\,\delta(E^+ + E^- - M_\psi^2) \\ &= \frac{E^+}{E^-}\frac{\mathrm{d}E^+\mathrm{d}\Omega}{2(2\pi)^3}\frac{\mathrm{d}^4 P_\psi}{2(2\pi)^3}\delta(E^+ + E^- - M_\psi^2) \\ &= \frac{\mathrm{d}E^+\mathrm{d}\Omega}{2(2\pi)^3}\frac{\mathrm{d}^4 P_\psi}{2(2\pi)^3}\,\delta(2E^+ - M_\psi^2) \\ &= \frac{1}{16\pi^2}\frac{\mathrm{d}^4 P_\psi}{(2\pi)^3}\frac{\mathrm{d}\Omega}{4\pi}. \end{aligned} \tag{2.29}$$

The solid angle Ω refers to the lepton ℓ^+, and it depends on the choice of the frame, more specifically on the $\hat{Z}$-axis. For more details, see Sec. 2.2.4.

Using the phase elements in Eqs. (2.8) and (2.29), together with the definition of hadronic tensor in Eq. (2.12), the SIDIS differential cross section with the inclusion of the J/ψ decay can be written as

$$\frac{\mathrm{d}\sigma^{J/\psi\to\ell^+\ell^-}}{\mathrm{d}x_B\,\mathrm{d}y\,\mathrm{d}^4 P_\psi\,\mathrm{d}\Omega} \propto \frac{y}{Q^4} L^{\mu\nu} W_{\mu\nu}. \tag{2.30}$$

In order to study its polarization, we choose a reference frame where the J/ψ meson is at rest or it moves with no transverse momentum. In this case, in terms of two light-like vectors n_+^μ and n_-^μ, with $n_+ \cdot n_- = 1$, the Sudakov decomposition of the particle momenta is

$$\begin{aligned} P^\mu &= \frac{1}{\sqrt{2}}\frac{z\,Q^2}{x_B\,M_\psi} n_-^\mu, \\ q^\mu &= \frac{1}{\sqrt{2}}\left(\frac{M_\psi}{z} n_+^\mu - z\frac{Q^2 + q_T^2}{M_\psi} n_-^\mu\right) + q_T^\mu, \\ P_\psi^\mu &= \frac{M_\psi}{\sqrt{2}}\left(n_+^\mu + n_-^\mu\right), \end{aligned} \tag{2.31}$$

where $q_T^2 = -\boldsymbol{q}_T^2$. The relation between the photon transverse momentum in this frame and the J/ψ transverse momentum in the frame defined in Eq. (2.5) reads

$$|\boldsymbol{q}_T| = \frac{|\boldsymbol{P}_\perp|}{\hat{z}}. \tag{2.32}$$

The momentum of the initial lepton now takes the form

$$\begin{aligned} l_e^\mu = \frac{1}{\sqrt{2}}\frac{M_\psi}{y}&\left[\left(1 - y - 2\sqrt{1-y}\frac{q_T}{Q}\cos\phi_{e'} - \frac{q_T^2}{Q^2}\right)\frac{z\,Q^2}{M_\psi^2} n_+^\mu + \frac{1}{z} n_-^\mu\right] \\ &+ \frac{Q}{y}\left(\frac{q_T^\mu}{Q} + \sqrt{1-y}\,\hat{l}_T^\mu\right), \end{aligned} \tag{2.33}$$

with $\hat{l}_T^2 = -1$ and $\hat{l}_T \cdot q_T = q_T \cos\phi_{e'}$. As a consequence, the lepton tensor can be written as

$$L^{\mu\nu} = L^{(0)\mu\nu} + L^{(1)\mu\nu}, \tag{2.34}$$

where $L^{(0)\mu\nu}$ is the same of Eq. (2.20) (with the replacement $l_\perp \to l_T$) and

$$\begin{aligned} L^{(1)\mu\nu} = -e^2\frac{Q^2}{y^2}\Bigg[&\frac{4(1-y)}{p_a\cdot q}\left(\frac{q_T^2}{p_a\cdot q}\cos^2\phi_{e'}\, p_a^\mu p_a^\nu + q_T\cos\phi_{e'}\left(p_a^\mu \hat{l}_T^\nu + p_a^\nu l_T^\mu\right)\right) \\ &+ 2(2-y)\sqrt{1-y}\frac{q_T}{Q}\cos\phi_{e'}\left(\epsilon_\parallel^\mu\epsilon_\parallel^\nu + \frac{Q^2}{(p_a\cdot q)^2}p_a^\mu p_a^\nu - \frac{q^\mu q^\nu}{Q^2}\right) \\ &+ \frac{y^2}{p_a\cdot q}\left(q_T^2\frac{p_a^\mu p_a^\nu}{p_a\cdot q} - p_a^\mu q_T^\nu - p_a^\nu q_T^\mu\right)\Bigg]. \end{aligned} \tag{2.35}$$

Upon integration over the electron azimuthal angle, $L^{(1)\mu\nu}$ vanishes, and the lepton tensor reduces to the expression in Eq. (2.23). The differential cross section can therefore be written as

$$\frac{\mathrm{d}\sigma^{J/\psi\to\ell^+\ell^-}}{\mathrm{d}x_B\,\mathrm{d}y\,\mathrm{d}^4P_\psi\,\mathrm{d}\Omega} \propto \frac{\alpha}{y\,Q^2}\left[\left(1+(1-y)^2\right)\mathcal{W}^\perp + (1-y)\mathcal{W}^\parallel\right]. \tag{2.36}$$

The structure functions $\mathcal{W}^\perp$ and $\mathcal{W}^\parallel$ in the above equation are, respectively, the analogous of $F_{UU,\perp}$ and $F_{UU,\parallel}$ as defined in Eq. (2.26). The only difference is that $\mathcal{W}^\perp$ and $\mathcal{W}^\parallel$ describe the decay process $J/\psi \to \ell^+\,\ell^-$ in addition to J/ψ production.

2.2.2 Helicity structure functions

The structure functions $\mathcal{W}^\mathcal{P}$ introduced in Eq. (2.36) do not depend on the spin state of the J/ψ meson. Information on both photon and J/ψ polarizations is encoded in the frame-dependent helicity structure functions, which are defined as

$$\mathcal{W}^\mathcal{P}_{\lambda\lambda'} = \mathcal{W}^\mathcal{P}_{\alpha\beta}\,\epsilon^\alpha_\lambda(P_\psi)\,\epsilon^{*\beta}_{\lambda'}(P_\psi), \tag{2.37}$$

where, as before, $\mathcal{P} = \perp, \parallel$ refers to the photon polarization, while $\epsilon^\alpha_\lambda(P_\psi)$ are the J/ψ polarization vectors. The structure functions $\mathcal{W}^\mathcal{P}$ are then recovered by summing over the J/ψ helicities

$$\mathcal{W}^\mathcal{P} = \sum_{\lambda,\lambda'}\mathcal{W}^\mathcal{P}_{\alpha\beta}\,\epsilon^\alpha_\lambda(P_\psi)\,\epsilon^{*\beta}_{\lambda'}(P_\psi)\,\delta_{\lambda\lambda'} = \sum_{\lambda,\lambda'}\mathcal{W}^\mathcal{P}_{\lambda\lambda'}\,\delta_{\lambda\lambda'}. \tag{2.38}$$

The constraints due to parity conservation and hermeticity imposed by QCD on the hadronic tensor imply the following relations

$$\mathcal{W}^\mathcal{P}_{\lambda\lambda'} = \mathcal{W}^{*\mathcal{P}}_{\lambda\lambda'}, \qquad \mathcal{W}^\mathcal{P}_{\lambda\lambda'} = (-1)^{\lambda+\lambda'}\mathcal{W}^\mathcal{P}_{-\lambda-\lambda'}. \tag{2.39}$$

The polarization vectors can be defined w.r.t. a covariant set of coordinate axes $(T^\mu, X^\mu, Y^\mu, Z^\mu)$, normalized in such a way that $T^2 = 1$ and $X^2 = Y^2 = Z^2 = -1$. The axes in turn can be expressed in terms of the particle momenta q^μ, P^μ and P^μ_ψ so that X^μ, Y^μ, Z^μ become three-vectors in the quarkonium rest frame. The choice is not unique and depends, in particular, on how the $\hat{Z}$-axis direction is chosen. More details on the most used reference frames and their connections can be found in Sec. 2.2.4.

Once the coordinate set is chosen, the J/ψ polarization vectors are given by

$$\epsilon_0^\mu(P_\psi) = Z^\mu = (0,0,0,1), \quad \epsilon_{\pm1}^\mu(P_\psi) = \frac{1}{\sqrt{2}}\left(\mp X^\mu - iY^\mu\right) = \frac{1}{\sqrt{2}}(0,\mp1,-i,0), \tag{2.40}$$

and obey the completeness and orthogonality relations

$$\begin{aligned}\sum_{\lambda=-1,0,1} \epsilon^{*\alpha}_\lambda(P_\psi)\,\epsilon^\beta_\lambda(P_\psi) &= -\eta^{\alpha\beta} + T^\alpha T^\beta = -\eta^{\alpha\beta} + \frac{P_\psi^\alpha P_\psi^\beta}{M^2},\\ \epsilon^{*\alpha}_\lambda(P_\psi)\,\epsilon^\alpha_{\lambda'}(P_\psi) &= -\delta_{\lambda\lambda'}.\end{aligned} \tag{2.41}$$

Using the definition of the polarization vectors in Eq. (2.40), the tensor $\mathcal{W}^{\mathcal{P}}_{\alpha\beta}$ in Eq. (2.37) can be explicitly decomposed in terms of different helicity structure functions

$$\begin{aligned}\mathcal{W}^{\mathcal{P}}_{\alpha\beta} &= \mathcal{W}^{\mathcal{P}}_{00}\,Z_\alpha Z_\beta + \frac{\mathcal{W}^{\mathcal{P}}_{11}+\mathcal{W}^{\mathcal{P}}_{-1-1}}{2}\left(X_\alpha X_\beta + Y_\alpha Y_\beta\right) + \frac{\mathcal{W}^{\mathcal{P}}_{1-1}+\mathcal{W}^{\mathcal{P}}_{-11}}{2}\left(-X_\alpha X_\beta + Y_\alpha Y_\beta\right)\\ &\quad + \frac{\mathcal{W}^{\mathcal{P}}_{10}-\mathcal{W}^{\mathcal{P}}_{-10}}{\sqrt{2}}X_\alpha Z_\beta + \frac{\mathcal{W}^{\mathcal{P}}_{01}-\mathcal{W}^{\mathcal{P}}_{0-1}}{\sqrt{2}}Z_\alpha X_\beta - i\frac{\mathcal{W}^{\mathcal{P}}_{11}-\mathcal{W}^{\mathcal{P}}_{-1-1}}{2}\left(X_\alpha Y_\beta - Y_\alpha X_\beta\right)\\ &\quad - i\frac{\mathcal{W}^{\mathcal{P}}_{1-1}-\mathcal{W}^{\mathcal{P}}_{-11}}{2}\left(X_\alpha Y_\beta + Y_\alpha X_\beta\right) - i\frac{\mathcal{W}^{\mathcal{P}}_{10}+\mathcal{W}^{\mathcal{P}}_{-10}}{\sqrt{2}}Y_\alpha Z_\beta + i\frac{\mathcal{W}^{\mathcal{P}}_{01}+\mathcal{W}^{\mathcal{P}}_{0-1}}{\sqrt{2}}Z_\alpha Y_\beta\\ &= \mathcal{W}^{\mathcal{P}}_{00}\,Z_\alpha Z_\beta + \mathcal{W}^{\mathcal{P}}_{11}\left(X_\alpha X_\beta + Y_\alpha Y_\beta\right) + \mathcal{W}^{\mathcal{P}}_{1-1}\left(-X_\alpha X_\beta + Y_\alpha Y_\beta\right)\\ &\quad + \sqrt{2}\,\mathcal{W}^{\mathcal{P}}_{10}\,X_\alpha Z_\beta + \sqrt{2}\,\mathcal{W}^{\mathcal{P}}_{01}\,Z_\alpha X_\beta.\end{aligned} \tag{2.42}$$

Notice that, due to the parity constraint in Eq. (2.39), only the real terms survive. Using the completeness relation, one can rewrite the $Y_\alpha Y_\beta$ tensor in terms of the other directions and the tensor $\eta_{\alpha\beta}$. Hence, we obtain

$$\begin{aligned}\mathcal{W}^{\mathcal{P}}_{\alpha\beta} &= -\left(\mathcal{W}^{\mathcal{P}}_T + \mathcal{W}^{\mathcal{P}}_{\Delta\Delta}\right)\left(\eta_{\alpha\beta} - T_\alpha T_\beta\right) + \left(\mathcal{W}^{\mathcal{P}}_L - \mathcal{W}^{\mathcal{P}}_T - \mathcal{W}^{\mathcal{P}}_{\Delta\Delta}\right)Z_\alpha Z_\beta\\ &\quad - \mathcal{W}^{\mathcal{P}}_\Delta\left(X_\alpha Z_\beta + Z_\alpha X_\beta\right) - 2\,\mathcal{W}^{\mathcal{P}}_{\Delta\Delta}\,X_\alpha X_\beta,\end{aligned} \tag{2.43}$$

where the eight independent helicity structure functions have been introduced

$$\begin{aligned}\mathcal{W}^{\mathcal{P}}_T &\equiv \mathcal{W}^{\mathcal{P}}_{11} = \mathcal{W}^{\mathcal{P}}_{-1-1},\\ \mathcal{W}^{\mathcal{P}}_L &\equiv \mathcal{W}^{\mathcal{P}}_{00},\\ \mathcal{W}^{\mathcal{P}}_\Delta &\equiv \frac{1}{\sqrt{2}}\left(\mathcal{W}^{\mathcal{P}}_{10} + \mathcal{W}^{\mathcal{P}}_{01}\right) = \sqrt{2}\,\mathrm{Re}\left[\mathcal{W}^{\mathcal{P}}_{10}\right],\\ \mathcal{W}^{\mathcal{P}}_{\Delta\Delta} &\equiv \mathcal{W}^{\mathcal{P}}_{1-1} = \mathcal{W}^{\mathcal{P}}_{-11}.\end{aligned} \tag{2.44}$$

In the previous equation the subscripts T, L, Δ, $\Delta\Delta$ refer to the J/ψ polarization. More specifically, $\mathcal{W}^{\mathcal{P}}_T$ and $\mathcal{W}^{\mathcal{P}}_L$ denote the structure functions for transversely and longitudinally polarized J/ψ meson, respectively. Moreover, $\mathcal{W}^{\mathcal{P}}_\Delta$ are the single-helicity flip structure functions and $\mathcal{W}^{\mathcal{P}}_{\Delta\Delta}$ the double-helicity flip ones.

A further simplification occurs if one takes into account that the coupling between the J/ψ meson and the decaying leptons is electromagnetic, so helicity must be conserved in the process. In the quarkonium rest frame, the leptons are produced

back to back along a direction l^+, identified by the three-component unit vector [1]

$$\hat{\boldsymbol{l}}^+ = (\sin\theta\,\cos\phi,\ \sin\theta\,\sin\phi,\ \cos\theta). \tag{2.45}$$

The component along $\hat{\boldsymbol{l}}^+$ of the total angular momentum of the dilepton system, and therefore of the J/ψ meson, can be equal to $+1$ or -1, but not *zero*. If one chooses a specific set of the J/ψ polarization vector $\epsilon_\sigma(P_\psi)$, where σ is the quarkonium helicity along the direction l^+, the sum over helicities in Eq. (2.38) is limited to the values $\sigma = \pm 1$,

$$\mathcal{W}^{\mathcal{P}} = \mathcal{W}^{\mathcal{P}}_{\alpha\beta} \sum_{\sigma=\pm1} \epsilon^{\alpha}_{\sigma}(P_\psi)\,\epsilon^{*\beta}_{\sigma}(P_\psi) = -\mathcal{W}^{\mathcal{P}}_{\alpha\beta}\,\eta_{l\perp}^{\alpha\beta}, \tag{2.46}$$

where we have introduced the transverse projector $\eta_{l\perp}$ w.r.t. the directions of the four-vectors P_ψ and $\hat{\boldsymbol{l}}^+$,

$$\eta_{l\perp}^{\alpha\beta} = \eta^{\alpha\beta} - \frac{l^{+\alpha}P_\psi^\beta + l^{+\beta}P_\psi^\alpha}{l^+\cdot P_\psi} + \frac{M^2}{(l^+\cdot P_\psi)^2} l^{+\alpha}l^{+\beta}. \tag{2.47}$$

By contracting the tensor above with the parameterization for $\mathcal{W}^{\mathcal{P}}_{\alpha\beta}$ in Eq. (2.43), one obtains

$$\mathcal{W}^{\mathcal{P}} = \mathcal{W}^{\mathcal{P}}_T(1+\cos^2\theta) + \mathcal{W}^{\mathcal{P}}_L(1-\cos^2\theta) + \mathcal{W}^{\mathcal{P}}_\Delta\,\sin 2\theta\,\cos\phi + \mathcal{W}^{\mathcal{P}}_{\Delta\Delta}\sin^2\theta\,\cos 2\phi. \tag{2.48}$$

This provides a common parameterization of the differential cross section

$$\frac{\mathrm{d}\sigma^{J/\psi\to\ell^+\ell^-}}{\mathrm{d}x_B\,\mathrm{d}y\,\mathrm{d}^4P_\psi\,\mathrm{d}\Omega} = \frac{B_{\ell\ell}}{4}\frac{\alpha}{yQ^2}\frac{3}{8\pi}\Big[\mathcal{W}_T(1+\cos^2\theta) + \mathcal{W}_L(1-\cos^2\theta) + \mathcal{W}_\Delta\,\sin 2\theta\,\cos\phi + \mathcal{W}_{\Delta\Delta}\sin^2\theta\,\cos 2\phi\Big], \tag{2.49}$$

where

$$\mathcal{W}_\Lambda = \big(1+(1-y)^2\big)\,\mathcal{W}^\perp_\Lambda + (1-y)\mathcal{W}^\parallel_\Lambda \tag{2.50}$$

and $\Lambda = T,\ L,\ \Delta,\ \Delta\Delta$. The above expression, Eq. (2.49), is written such that the integration over the solid angle correctly reproduces the (semi-)inclusive J/ψ production, namely

$$\frac{\mathrm{d}\sigma^{J/\psi\to\ell^+\ell^-}}{\mathrm{d}x_B\,\mathrm{d}y\,\mathrm{d}^4P_\psi} = B_{\ell\ell}\,\frac{\mathrm{d}\sigma}{\mathrm{d}x_B\,\mathrm{d}y\,\mathrm{d}^4P_\psi}, \tag{2.51}$$

where in the right-hand side we have the (total) differential cross section for J/ψ production in SIDIS.

We remark that this angular structure of the cross section is typical for the decays of spin-1 particles: it has been already derived, for instance, for J/ψ photoproduction in Ref. [88] and for the Drell-Yan processes in Refs. [89, 90].

2.2.3 J/ψ polarization in the NRQCD approach

The helicity structure functions $\mathcal{W}^{\mathcal{P}}_\Lambda$ introduced in Eq. (2.48) can be calculated explicitly once a model describing quarkonium hadronization is chosen. In the following we consider the high transverse momentum region ($q_T \gg \Lambda_{\mathrm{QCD}}$) and adopt the NRQCD theoretical framework, assuming the validity of collinear factorization.

[1] The angles are defined with respect to a specific frame; more details in Sec. 2.2.4.

Indeed, we can describe the J/ψ yield via the partonic subprocess

$$\gamma^*(q) + a(p_a) \to c\bar{c}(P_\psi) + a(p'_a), \tag{2.52}$$

which is the lowest perturbative order in the strong coupling constant α_s, corresponding to the order $\alpha\alpha_s^2$ diagrams in Appendix B.2. In the previous equation a can be either a gluon or a quark/antiquark, with

$$p_a \approx \xi P, \quad 0 \leq \xi \leq 1. \tag{2.53}$$

One needs to determine the partonic structure functions $w^{\mathcal{P}(a)}$ for each of the underlying hard scattering subprocesses in Eq. (2.52). If we denote the scattering amplitudes for the process $\gamma^* a \to J/\psi + X$ as $\mathcal{M}_{\mu\alpha}(\gamma^* a \to J/\psi X)$, the partonic helicity structure functions are given by

$$w^{\mathcal{P}(a)}_{\lambda\lambda'} = \sum_{\lambda_a} \frac{1}{2} \epsilon^{\mu\nu}_{\mathcal{P}} \, \mathcal{M}_{\mu\alpha}(\gamma^* a \to J/\psi X) \, \mathcal{M}^*_{\nu\beta}(\gamma^* a \to J/\psi X) \, \epsilon^{\alpha}_{\lambda}(P_\psi) \, \epsilon^{\beta}_{\lambda'}(P_\psi). \tag{2.54}$$

The sum runs over the two possible helicity states of the initial parton a, *i.e.* a quark, an antiquark, or a gluon. Moreover, the tensor $\epsilon_{\mathcal{P}}$, with $\mathcal{P} = \perp, \parallel$, is given by $\epsilon^{\mu\nu}_{\perp} = -\eta^{\mu\nu}_{\perp}$ in case of the photon transverse polarization, and $\epsilon^{\mu\nu}_{\parallel} = \epsilon^{\mu}_{\parallel} \epsilon^{\nu}_{\parallel}$ for the longitudinal one. We note that $\epsilon_{\mathcal{P}}$ has been used to parameterize the lepton tensor in Eq. (2.23). The partonic helicity structure functions in Eq. (2.54) can be written in terms of the Mandelstam variables $\hat{s}$, $\hat{t}$ and $\hat{u}$, defined as

$$\begin{aligned} \hat{s} &= (p_a + q)^2 = -Q^2 + 2\, q \cdot p_a, \\ \hat{t} &= (q - P_\psi)^2 = M_\psi^2 - Q^2 - 2\, q \cdot P_\psi, \\ \hat{u} &= (p_a - P_\psi)^2 = M_\psi^2 - 2\, p_a \cdot P_\psi. \end{aligned} \tag{2.55}$$

By introducing the partonic Bjorken-x ($\hat{x}$) and the partonic J/ψ energy fraction ($\hat{z}$),[2]

$$\begin{aligned} \hat{x} &= \frac{Q^2}{2 p_a \cdot q} = \frac{x_B}{\xi}, \\ \hat{z} &= \frac{p_a \cdot P_\psi}{p_a \cdot q} = z, \end{aligned} \tag{2.56}$$

we have that the Mandelstam variables assume the following explicit fomulae

$$\begin{aligned} \hat{s} &= \frac{1 - \hat{x}}{\hat{x}} Q^2, \\ \hat{t} &= -(1 - \hat{z}) \left(Q^2 + \frac{M_\psi^2}{\hat{z}} \right) + \hat{z}\, q_T^2, \\ \hat{u} &= M_\psi^2 - \frac{\hat{z}}{\hat{x}} Q^2. \end{aligned} \tag{2.57}$$

Notice that $\hat{s}$, which is the cm energy squared of the partonic process, must be at least equal to the J/ψ mass, in order to produce the particle, implying that

$$\hat{s} \geq M_\psi^2. \tag{2.58}$$

[2]Note that the last equation relates them to the corresponding hadronic variables in Eq. (2.4).

The equality $\hat{s} = M_\psi^2$ in Eq. (2.58) holds when the J/ψ meson is produced at rest, from which we find that the maximal value of the partonic Bjorken-x is

$$\hat{x}_{\max} = \frac{Q^2}{M_\psi^2 + Q^2}. \tag{2.59}$$

Analogous kinematic constraints can also be found for the other Mandelstam variables (see Appendix C for more details).

Once the short-distance coefficients are perturbative evaluated, we can employ the NRQCD factorization to obtain theoretical estimates for the helicity structure functions. In particular, according to NRQCD, the J/ψ polarization state λ can be reached from the $c\bar{c}$-pairs produced in various orbital and spin angular momentum states. We take into account the CS ${}^3S_1^{(1)}$ state, as well those CO states that are relatively suppressed at most by a factor v^4 in the velocity parameter v with respect to the CS one, namely ${}^1S_0^{(8)}$, ${}^3S_1^{(8)}$ and ${}^3P_J^{(8)}$, with $J = 0,\ 1,\ 2$.

When studying polarization, a simplification occurs due to charge and parity conjugation, which forbids the presence of interference effects among states with different orbital angular momentum L and spin S. Thus, the partonic helicity structure functions can be decomposed as (see also Refs. [88, 91–93])

$$w_{\lambda\lambda'}^{\mathcal{P}\,(a)} = w_{\lambda\lambda'}^{\mathcal{P}\,(a)}\left[{}^3S_1^{(1)}\right] + w_{\lambda\lambda'}^{\mathcal{P}\,(a)}\left[{}^1S_0^{(8)}\right] + w_{\lambda\lambda'}^{\mathcal{P}\,(a)}\left[{}^3S_1^{(8)}\right] + w_{\lambda\lambda'}^{\mathcal{P}\,(a)}\left[\{L=1,S=1\}^{(8)}\right]. \tag{2.60}$$

The ${}^1S_0^{(8)}$ state is rotational invariant (since $S = L = 0$), leading to a random orientation of the J/ψ spin. As a consequence, this state contributes evenly to all helicity states with $\lambda' = \lambda$; hence, its contribution corresponds precisely to $1/3$ of the unpolarized cross section. Moving to the ${}^3S_1^{(1,8)}$ states, for both color configurations the $c\bar{c}$ pair has non-zero spin. Since the S_z quantum number does not vary in the nonperturbative evolution into the physical J/ψ meson, we have that $S_z = \lambda$. Finally, for the last term in Eq. (2.60) it is necessary to take into account the interference among states with different total angular momentum J, because they have the same values of spin and orbital angular momentum ($S = L = 1$). Notice that, while the S_z value is fixed by the J/ψ helicity as in the ${}^3S_1$ case, L_Z is free and therefore one should sum over all its possible values,

$$\begin{aligned} w_{\lambda\lambda'}^{\mathcal{P}\,(a)}\left[\{L=1,S=1\}^{(8)}\right] &\propto \sum_{L_z,\,\lambda_a} \frac{1}{2}\epsilon_{\mathcal{P}}^{\mu\nu}\,\mathcal{M}_{\mu\alpha}\left(\gamma^* a \to c\bar{c}\left[(1,L_z;1,\lambda)\right]\ a\right) \\ &\quad \times \mathcal{M}^*_{\nu\beta}\left(\gamma^* a \to c\bar{c}\left[(1,L_z;1,\lambda')\right]\ a\right)\ \epsilon_\lambda^\alpha(P_\psi)\,\epsilon_{\lambda'}^\beta(P_\psi) \\ &\neq \sum_{J=0,1,2} w_{\lambda\lambda'}^{\mathcal{P}\,(a)}[{}^3P_J^{(8)}], \end{aligned} \tag{2.61}$$

where the notation $(L, L_z; S, S_z)$ is used for the quantum numbers of the $c\bar{c}$ pair. In the last equation we point out that this procedure is different from taking the sum over all the intermediate states with total angular momentum J, as is done for the calculation of the unpolarized cross section. The latter is recovered by performing a trace over the helicity indices of $w_{\lambda\lambda'}^{\mathcal{P}\,(a)}$.

By further exploiting the symmetries of NRQCD it can be shown that the perturbative and nonperturbative contributions to the partonic structure functions $w_{\lambda\lambda'}^{\mathcal{P}\,(a)}$ factorize. The former are given by some short distance coefficients $K_{\alpha\beta}^{\mathcal{P}\,(a)}$ written in terms of the Mandelstam variables in Eq. (2.55), while the latter are encoded in the

LDMEs. Therefore, the partonic structure functions can be written as [88])

$$w^{\mathcal{P}\,(a)}_{\lambda\lambda'} = \sum_n w^{\mathcal{P}\,(a)}_{\lambda\lambda'}[n] \equiv \sum_n K^{\mathcal{P}\,(a)}_{\alpha\beta} \epsilon^{\alpha}_{\lambda}(P_\psi)\, \epsilon^{\beta}_{\lambda'}(P_\psi)\, \langle \mathcal{O}[n] \rangle\,, \tag{2.62}$$

where the sum runs over the Fock states $n = {}^1S_0^{(8)}, {}^3S_1^{(1)}, {}^3S_1^{(8)}, {}^3P_0^{(8)}$, with the P-wave contribution corresponding to the last term in Eq. (2.60).

Once the partonic structure functions are calculated, the hadronic ones are determined through a convolution,

$$(2\pi)^3 \mathcal{W}^{\mathcal{P}}_{\lambda\lambda'} = \sum_a \int_{x_B}^{\hat{x}_{\max}} \frac{\mathrm{d}\hat{x}}{\hat{x}} \int_z^1 \mathrm{d}\hat{z}\, f_1^a\left(\frac{x_B}{\hat{x}}, \mu^2\right)\, w^{\mathcal{P}\,(a)}_{\lambda\lambda'}\, \delta\left(\hat{s} + \hat{t} + \hat{u} - M_\psi^2 + Q^2\right) \delta(\hat{z} - z), \tag{2.63}$$

where the upper limit of the integration over $\hat{x}$, $\hat{x}_{\max}$, is given in Eq. (2.59). In deriving the above formula, momentum conservation has been used to integrate over the phase-space of the final parton, leading to a Dirac-delta function expressed in terms of the Mandelstam variables,

$$\begin{aligned} \int \frac{\mathrm{d}^3 p'_a}{2E_{a'}}\, \delta^{(4)}(q + p_a - P_\psi - p'_a) &= \int \mathrm{d}^4 p'_a\, \delta({p'_a}^2)\, \delta^{(4)}(q + p_a - P_\psi - p'_a) \\ &= \delta\Big((q + p_a - P_\psi)^2\Big) = \delta(\hat{s} + \hat{t} + \hat{u} - M_\psi^2 + Q^2). \end{aligned} \tag{2.64}$$

The explicit results for the $w^{\mathcal{P}\,(a)}_{\Lambda}$ in the Gottfried-Jackson frame are presented in Appendix B.2.3. Once the hadronic helicity structure functions $W^{\mathcal{P}}_{\lambda\lambda'}$ are calculated through Eq. (2.63), the $\mathcal{W}^{\mathcal{P}}_{\Lambda}$, with $\Lambda = L, T, \Delta, \Delta\Delta$, can be obtained by means of equations similar to Eqs. (2.44).

2.2.4 Reference frames

As already mentioned, the quarkonium rest frame is not unique. Several frames can be identified, depending on the choice of $\hat{Z}$-axis, while the $\hat{X}$ and $\hat{Y}$ axes are fixed by convention, see Ref. [88]. In all the frames, T^μ is taken to be

$$T^\mu = \frac{P^\mu_\psi}{M_\psi}, \tag{2.65}$$

while

$$Y^\mu = \epsilon^{\mu\nu\rho\sigma} X_\nu Z_\rho T_\sigma, \tag{2.66}$$

where $\epsilon^{0123} = +1$. Z^μ and X^μ can be easily expressed as linear combinations of the auxiliary four-vectors

$$\begin{aligned} \widetilde{q}^\mu &= q^\mu - \frac{q \cdot P_\psi}{M_\psi^2} P^\mu_\psi, \\ \widetilde{P}^\mu &= P^\mu - \frac{P \cdot P_\psi}{M_\psi^2} P^\mu_\psi, \end{aligned} \tag{2.67}$$

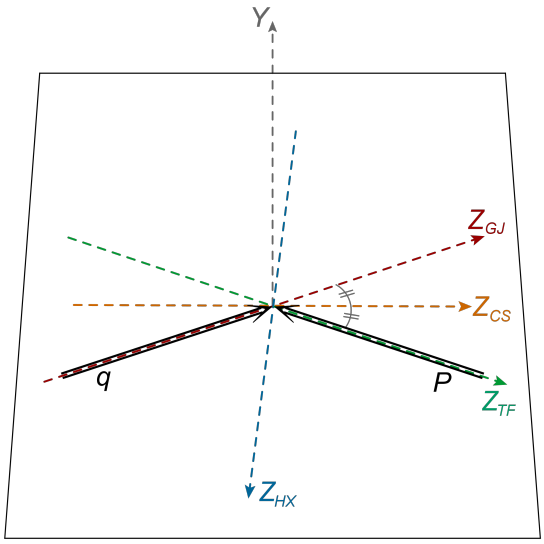

FIGURE 2.2: Different choices of the Z direction corresponding to four typical frames in which the J/ψ is at rest: *Gottfried-Jackson* (GJ), *Collins-Soper* (CS), *Target* (TF) and *Helicity* (HX).

because $\tilde{q} \cdot T = \tilde{P} \cdot T = 0$. One starts by writing

$$Z^\mu = A_z\, \tilde{q}^\mu + B_z\, \tilde{P}^\mu,$$
$$X^\mu = A_x\, \tilde{q}^\mu + B_x\, \tilde{P}^\mu. \tag{2.68}$$

The normalization conditions $Z^2 = -1$ and $X^2 = -1$ can be used to fix, for example, the coefficients A_z and A_x, respectively. B_x is determined by the orthogonality relation $X \cdot Z = 0$. The overall sign ambiguity for A_x and B_x is solved by requiring that the three-vector $\boldsymbol{Y}$ points in the direction of $\boldsymbol{q} \times (-\boldsymbol{P})$ in the J/ψ rest frame. The choice of B_z specifies the four commonly used reference frames illustrated in Fig. 2.2 and described in the following.

Despite being model independent, we introduce the explicit forms of Z^μ and X^μ in the four reference frames after the adoption of the parton model. Indeed, we found more convenient to write them in terms of the modified Mandelstam variables

$$s = \hat{s} + Q^2, \quad t = \hat{t}, \quad u = \hat{u} + Q^2, \tag{2.69}$$

where $\hat{s}$, $\hat{t}$, $\hat{u}$ are defined in Eq. (2.55) and $s + t + u = M_\psi^2 + Q^2$. Moreover, in the following we assume collinear factorization, hence the parton momentum p_a^μ is related to its parent hadron momentum P, via Eq. (2.53), namely $p_a = \xi P$.

We remark that similar frames can also be identified in the study of the virtual photon in Drell-Yan processes, Ref. [89].

Gottfried-Jackson frame (GJ). It is also known as u-channel, and it is defined by selecting $\hat{Z}$ in the same direction of the photon three-momentum, $\boldsymbol{Z} = \boldsymbol{q}/|\boldsymbol{q}|$, from

which one finds

$$
\begin{aligned}
Z^\mu_{\rm GJ} &= \frac{1}{M_\psi\, N_{\rm GJ}}\Big[2M_\psi^2\, q^\mu - (s+u-2\,Q^2)P^\mu_\psi\Big],\\
X^\mu_{\rm GJ} &= -\frac{1}{N_{\rm GJ}\sqrt{t(Q^2t+s\,u)t}}\Bigg[\Big(s\,(M_\psi^2+Q^2)+t\,(2Q^2-u)\Big)\,q^\mu\\
&\quad + \big(4\,Q^2t+(s+u)^2\big)\,p_a^\mu - \Big(2\,Q^2t+s\,(s+u)\Big)P^\mu_\psi\Bigg],
\end{aligned}
\tag{2.70}
$$

with

$$
N_{\rm GJ} = \sqrt{4\,Q^2t+(s+u)^2}. \tag{2.71}
$$

Helicity frame (HX). It is also known as recoil frame, and in this case the $\hat{Z}$-axis is chosen to be along the direction of the J/ψ three-momentum in the hadronic cm frame, corresponding to $\boldsymbol{Z} = -(\boldsymbol{P}+\boldsymbol{q})/|\boldsymbol{P}+\boldsymbol{q}|$, and

$$
\begin{aligned}
Z^\mu_{\rm HX} &= -\frac{1}{M_\psi\, N_{\rm HX}}\Big[2M_\psi^2\,(\xi\,q^\mu+p_a^\mu) - \big(\xi(s+u-2\,Q^2)+(s+t)\big)\,P^\mu_\psi\Big],\\
X^\mu_{\rm HX} &= \frac{1}{N_{\rm HX}\sqrt{t(Q^2t+s\,u)t}}\Bigg\{\Big[\xi\,\Big(s\,(M_\psi^2+Q^2)+t\,(2Q^2-u)\Big)-(s+t)^2\Big]q^\mu\\
&\quad + \Big[\xi\,\big(4\,Q^2t+(s+u)^2\big) - \Big(s\,(M_\psi^2+Q^2)+t\,(2\,Q^2-u)\Big)\Big]p_a^\mu\\
&\quad + \Big[s\,(s+t) - \xi\,\big(2\,Q^2t+s\,(s+u)\big)\Big]P^\mu_\psi\Bigg\},
\end{aligned}
\tag{2.72}
$$

with

$$
N_{\rm HX} = \sqrt{\xi^2\,[4\,Q^2t+(s+u)^2] - 2\,\xi\,\Big[s\,(M_\psi^2+Q^2)+t\,(2\,Q^2-u)\Big]+(s+t)^2}. \tag{2.73}
$$

Target frame (TF). It is defined by choosing $\hat{Z}$ in a such a way that it points in the opposite direction of the proton momentum, *i.e.* $\boldsymbol{Z} = -\boldsymbol{P}/|\boldsymbol{P}|$. Explicitly, we have

$$
\begin{aligned}
Z^\mu_{\rm TF} &= \frac{1}{M_\psi N_{\rm TF}}\Big[-2\,M_\psi^2\,p_a^\mu + (s+t)P^\mu_\psi\Big],\\
X^\mu_{\rm TF} &= -\frac{1}{N_{\rm TF}\sqrt{t(Q^2t+s\,u)t}}\\
&\quad\times\Big[(s+t)^2q^\mu + \Big(s\,(M_\psi^2+Q^2)+t\,(2\,Q^2-u)\Big)\,p_a^\mu - s(s+t)P^\mu_\psi\Big],
\end{aligned}
\tag{2.74}
$$

with

$$
N_{\rm TF} = (s+t). \tag{2.75}
$$

Collins-Soper frame (CS). It is defined choosing $\hat{Z}$ as the bisect of the two beams, *i.e.* $\boldsymbol{Z} = \boldsymbol{q}/|\boldsymbol{q}| - \boldsymbol{P}/|\boldsymbol{P}|$, so

$$\begin{aligned} Z^\mu_{\rm CS} &= \frac{1}{N_{\rm CS}}\Big[(s+t)q^\mu - (s+u-2\,Q^2)p_a^\mu\Big], \\ X^\mu_{\rm CS} &= -\frac{1}{M_\psi\, N_{\rm CS}\sqrt{t(Q^2 t + s\,u)t}} \\ &\quad\times\Big[M_\psi^2\, s\,(s+t)\,q^\mu + M_\psi^2\left(s(s+u)+2\,Q^2 t\right)p_a^\mu - (s+t)\left(s(M_\psi^2-t)+Q^2 t\right)P_\psi^\mu\Big], \end{aligned} \tag{2.76}$$

with

$$N_{\rm CS} = \sqrt{(s+t)\left[s\,(M_\psi^2 - t) + Q^2 t\right]}. \tag{2.77}$$

Relations among different frames

Since all frames share the same $\hat{X}$-$\hat{Z}$ plane, a proper rotation around the $\hat{Y}$-axis connects a starting frame F to a final frame F', namely

$$\begin{pmatrix} X \\ Z \end{pmatrix}_{F'} = \begin{pmatrix} \cos\psi_{F\to F'} & -\sin\psi_{F\to F'} \\ \sin\psi_{F\to F'} & \cos\psi_{F\to F'} \end{pmatrix}\begin{pmatrix} X \\ Z \end{pmatrix}_{F}. \tag{2.78}$$

It is convenient to show the rotational angles from one specific frame to all the others, since the other relations can be derived by a proper product of matrices. Considering the *Gottfried-Jackson* as the starting frame, we have that:

- from GJ to HX:

$$\begin{aligned} \cos\psi_{GJ\to HX} &= \frac{s\,(M_\psi^2+Q^2) + t\,(2\,Q^2-u) - \xi\left(4\,Q^2 t + (s+u)^2\right)}{N_{HX}\,N_{GJ}}, \\ \sin\psi_{GJ\to HX} &= \frac{2\,M_\psi^2\,\sqrt{t(Q^2 t + s\,u)}}{N_{HX}\,N_{GJ}}; \end{aligned} \tag{2.79}$$

- from GJ to CS:

$$\begin{aligned} \cos\psi_{GJ\to CS} &= \frac{M_\psi\left(s\,(s+u)+2\,Q^2 t\right)}{N_{CS}\,N_{GJ}}, \\ \sin\psi_{GJ\to CS} &= \frac{(s+u-2\,Q^2)\,\sqrt{t(Q^2 t + s\,u)}}{N_{CS}\,N_{GJ}}; \end{aligned} \tag{2.80}$$

- from GJ to TF:

$$\begin{aligned} \cos\psi_{GJ\to TF} &= \frac{s\,(M_\psi^2+Q^2) + t\,(2\,Q^2-u)}{N_{TF}\,N_{GJ}}, \\ \sin\psi_{GJ\to TF} &= \frac{2\,M_\psi\,\sqrt{t(Q^2 t + s\,u)}}{N_{TF}\,N_{GJ}}. \end{aligned} \tag{2.81}$$

By noticing that in Eq. (2.44) the helicity structure functions are defined in terms of the J/ψ polarization vectors, which in turn are given as linear combination of the four vectors X^μ, Y^μ, Z^μ in Eq. (2.40), one can easily evaluate the rotation matrix for

$\mathcal{W}_\Lambda$

$$\begin{pmatrix} \mathcal{W}_T \\ \mathcal{W}_L \\ \mathcal{W}_\Delta \\ \mathcal{W}_{\Delta\Delta} \end{pmatrix}_{F'} = \begin{pmatrix} 1-\frac{1}{2}\sin^2\psi & \frac{1}{2}\sin^2\psi & \frac{1}{2}\sin 2\psi & \frac{1}{2}\sin^2\psi \\ \sin^2\psi & \cos^2\psi & -\sin 2\psi & -\sin^2\psi \\ -\frac{1}{2}\sin^2\psi & \frac{1}{2}\sin 2\psi & \cos 2\psi & \frac{1}{2}\sin 2\psi \\ \frac{1}{2}\sin^2\psi & -\frac{1}{2}\sin^2\psi & -\frac{1}{2}\sin 2\psi & 1-\frac{1}{2}\sin^2\psi \end{pmatrix} \begin{pmatrix} \mathcal{W}_T \\ \mathcal{W}_L \\ \mathcal{W}_\Delta \\ \mathcal{W}_{\Delta\Delta} \end{pmatrix}_{F} . \tag{2.82}$$

In the previous, the explicit subscript remarking that the rotation is from F to F' has been omitted to simplify the notation.

2.3 Phenomenological predictions for the EIC

In this section, based on Ref. [94], we present a detailed phenomenological analysis of J/ψ polarization at Electron-Ion Collider kinematics.

J/ψ polarization has been widely studied both in pp, *e.g.* at LHC by the ALICE Collaboration [95] and ep collisions, *e.g.* at HERA, which provided data for both photoproduction [96] and SIDIS [13]. In Ref. [87] the latter case was addressed from a theoretical point of view, showing that the kinematic coverage and the precision reached by the experiment were not optimal to discern between the CSM and NRQCD approaches. J/ψ polarization measured at HERA was also discussed in Ref. [97], leading to similar conclusions.

The situation could certainly improve in the upcoming future with the advent of the EIC. It is indeed expected that the luminosity reached by this facility is much higher compared to HERA, even if no final decision has yet been made regarding the detector. In this section, we will then remark the importance of the study of J/ψ polarization, highlighting which frames and kinematic regions could be more effective in this respect.

To collect more statistics, it is almost mandatory to evaluate both the unpolarized cross section and the polarization parameters in a wide enough region of the phase space. The angular distribution is given, at fixed kinematics, by

$$\begin{aligned} \frac{1}{N}\frac{\mathrm{d}N}{\mathrm{d}x_B\,\mathrm{d}y\,\mathrm{d}^4P_\psi\,\mathrm{d}\Omega} = \frac{3}{8\pi}\frac{1}{2\mathcal{W}_T+\mathcal{W}_L}\Big[&\mathcal{W}_T\left(1+\cos^2\theta\right)+\mathcal{W}_L\left(1+\cos^2\theta\right) \\ &+\mathcal{W}_\Delta\sin 2\theta\,\cos\phi+\mathcal{W}_{\Delta\Delta}\sin^2\theta\,\cos 2\phi\Big], \end{aligned} \tag{2.83}$$

or equivalently

$$\frac{1}{N}\frac{\mathrm{d}N}{\mathrm{d}x_B\,\mathrm{d}y\,\mathrm{d}^4P_\psi\,\mathrm{d}\Omega} = \frac{3}{4\pi}\frac{1}{\lambda+3}\Big[1+\lambda\cos^2\theta+\mu\sin 2\theta\,\cos\phi+\frac{\nu}{2}\sin^2\theta\,\cos 2\phi\Big], \tag{2.84}$$

with

$$\lambda=\frac{\mathcal{W}_T-\mathcal{W}_L}{\mathcal{W}_T+\mathcal{W}_L},\quad \mu=\frac{\mathcal{W}_\Delta}{\mathcal{W}_T+\mathcal{W}_L},\quad \nu=\frac{2\mathcal{W}_{\Delta\Delta}}{\mathcal{W}_T+\mathcal{W}_L}. \tag{2.85}$$

The parameterization in Eq. (2.84) is the standard one adopted in experimental analysis.

These parameters can be related to the quantities $\mathrm{d}\sigma_{\lambda\lambda'} \equiv \frac{\mathrm{d}\sigma_{\lambda\lambda'}}{\mathrm{d}x_B \mathrm{d}y \mathrm{d}^4 P_\psi}$ (ultimately related to the J/ψ helicity density matrix $\rho_{\lambda\lambda'}$). In particular, we have

$$\begin{aligned} \mathrm{d}\sigma_{1,1} = \mathrm{d}\sigma_{-1,-1} &\propto \frac{\alpha}{y\,Q^2}\,\mathcal{W}_T, \\ \mathrm{d}\sigma_{0,0} &\propto \frac{\alpha}{y\,Q^2}\,\mathcal{W}_L, \\ \sqrt{2}\,\mathrm{Re}\left[\mathrm{d}\sigma_{1,0}\right] &\propto \frac{\alpha}{y\,Q^2}\,\mathcal{W}_\Delta, \\ \mathrm{d}\sigma_{1,-1} &\propto \frac{\alpha}{y\,Q^2}\,2\,\mathcal{W}_{\Delta\Delta}, \end{aligned} \tag{2.86}$$

from which

$$\lambda = \frac{\mathrm{d}\sigma_{1,1} - \mathrm{d}\sigma_{0,0}}{\mathrm{d}\sigma_{1,1} + \mathrm{d}\sigma_{0,0}}, \quad \mu = \frac{\sqrt{2}\,\mathrm{Re}\left[\mathrm{d}\sigma_{1,0}\right]}{\mathrm{d}\sigma_{1,1} + \mathrm{d}\sigma_{0,0}}, \quad \nu = \frac{\mathrm{d}\sigma_{1,-1}}{\mathrm{d}\sigma_{1,1} + \mathrm{d}\sigma_{0,0}}. \tag{2.87}$$

To obtain the event distribution over a region of the phase space $\mathrm{d}PS$, it is needed to integrate separately each $\mathrm{d}\sigma_{\lambda\lambda'}$. We define $\langle \mathrm{d}\sigma_{\lambda,\lambda'} \rangle$ as the integrated $\mathrm{d}\sigma_{\lambda,\lambda'}$ in a region Γ of the phase space, namely

$$\langle \mathrm{d}\sigma_{\lambda,\lambda'} \rangle = \int_\Gamma \frac{\mathrm{d}\sigma_{\lambda\lambda'}}{\mathrm{d}x_B\,\mathrm{d}y\,\mathrm{d}^4 P_\psi}\,\mathrm{d}PS. \tag{2.88}$$

From these we can compute the “integrated" polarization parameters as

$$\langle\lambda\rangle = \frac{\langle \mathrm{d}\sigma_{1,1}\rangle - \langle \mathrm{d}\sigma_{0,0}\rangle}{\langle \mathrm{d}\sigma_{1,1}\rangle + \langle \mathrm{d}\sigma_{0,0}\rangle}, \quad \langle\mu\rangle = \frac{\sqrt{2}\,\mathrm{Re}\left[\langle \mathrm{d}\sigma_{1,0}\rangle\right]}{\langle \mathrm{d}\sigma_{1,1}\rangle + \langle \mathrm{d}\sigma_{0,0}\rangle}, \quad \langle\nu\rangle = \frac{\langle \mathrm{d}\sigma_{1,-1}\rangle}{\langle \mathrm{d}\sigma_{1,1}\rangle + \langle \mathrm{d}\sigma_{0,0}\rangle}. \tag{2.89}$$

These quantities parameterize the integrated yield in the same way as Eq. (2.84). More explicitly, by integration over the phase space $\mathrm{d}PS \equiv \mathrm{d}x_B\,\mathrm{d}y\,\mathrm{d}^4 P_\psi$, we have

$$\frac{1}{N}\frac{\mathrm{d}N}{\mathrm{d}\Omega} = \frac{3}{4\pi}\frac{1}{\langle\lambda\rangle + 3}\Big[1 + \langle\lambda\rangle\cos^2\theta + \langle\mu\rangle\sin 2\theta\,\cos\phi + \frac{\langle\nu\rangle}{2}\sin^2\theta\,\cos 2\phi\Big]. \tag{2.90}$$

For simplicity, we will drop henceforth the bracket notation.

In next sections we will provide predictions for the angular parameters λ, ν and μ, evaluated at fixed z, the J/ψ energy fraction, and $P_\perp$, its transverse momentum component.[3] We will also show how to properly combine them to get rotational invariant quantities, extremely important from both the theoretical and experimental points of view. Our estimates will be presented in a frame where the virtual photon and the proton are (anti-)collinear. Even if variables are usually labelled by the superscript * within this frame choice, corresponding to a so-called z frame [98], in the following we will not adopt the same convention. Moreover, we mention that in Ref. [98] the azimuthal dependence of the lepton tensor has been widely studied. It has been found that, this dependence cannot be dropped from the tensor even upon its integration, if observables are studied in frames such as the laboratory one. Indeed, the Jacobian of the transformation from a variable in a z frame and the laboratory one can depend on the azimuthal angle itself, providing residual contribution

[3] We recall that $P_\perp$ is the J/ψ transverse momentum in a frame where the proton and the photon are (anti)collinear.

from it. Thus, considering the lepton defined in Eq. (2.23) in such cases leads to incorrect results. This has also been numerically demonstrated in Ref. [99], where a comparison with the expression in the laboratory frame provided by Ref. [87] has been carried out. Since our estimates of the angular parameters are only given in the aforementioned z frame, they will not be afflicted by the same issue. However, it is important to stress that they are leading-order predictions. In Ref. [100] the authors evaluated the J/ψ angular parameters λ and ν at next-to-leading order (NLO) in photoproduction adopting both CSM and NRQCD, finding a significant deviation from the corresponding leading-order estimates. Nevertheless, we expect that this is less relevant in the large Q^2 region.

Hence, it is extremely important to carry on studies on the angular parameters, which can be used in combination with unpolarized data to shed light on the quarkonium hadronization mechanism. In particular, in Ref. [101] it has been shown that the study of unpolarized J/ψ production at the EIC, and especially $\cos 2\phi_\psi$ modulation measurements, could be extremely vital to test the ${}^1S_0^{(8)}$ dominance picture, which is predicted in various phenomenological extractions (see also Appendix A.3). In addition, by studying the small transverse momentum region where the TMD factorization is applicable, in Ref. [102] it has been proposed to compare unpolarized J/ψ production data with open-heavy quark ones to isolate the LDME dependence. This is motivated by the fact that the ratio of the two differential cross sections is independent of the TMDs, at least at the leading order. Nevertheless, these proposals mostly focus on the LDME related to the ${}^1S_0^{(8)}$ wave and/or on the ratio between $\langle O_8^\psi[{}^1S_0]\rangle$ and $\langle O_8^\psi[{}^3P_0]\rangle$. At variance, the study of the J/ψ polarization states is less dependent on $\langle O_8^\psi[{}^1S_0]\rangle$, since this state is purely unpolarized and leads to a random polarization of the J/ψ. Hence, the polarization parameter numerators are independent of $\langle O_8^\psi[{}^1S_0]\rangle$, giving a complementary description to the aforementioned, fully unpolarized analyses proposed.

Before focusing on the angular parameters, we will present estimates for the unpolarized cross section at the EIC kinematics. In the present study, for the unpolarized parton distributions, we will adopt the CTEQ6L1 set [103]. Moreover, for each case considered we will provide predictions both within the CSM and the NRQCD approach, employing the following three different LDME sets: the BK11 [104] set, extracted including also photoproduction data at low transverse momentum; the C12 [15] set, obtained including polarization data in pp collisions; the G13 [105] set, to be compared with the C12 set. More details can be found in Appendix A.3.

It is worth noticing that the use of different LDME sets, fundamental in the quarkonium formation mechanism, allows to understand their impact also on its polarization.

2.3.1 Unpolarized cross sections

In this section we present leading-order estimates for unpolarized cross sections, both as functions of z and P_T, adopting different frameworks. A more extensive study on the unpolarized cross section at the EIC was done in Ref. [12], even if limited to the CSM and providing only differential cross sections as functions of the J/ψ transverse momentum.

It is worth recalling that our main focus is on the angular/polarization parameters (evaluated at LO), discussed in the next sections. Hence, it is useful to look at the unpolarized cross sections at the same level of accuracy.

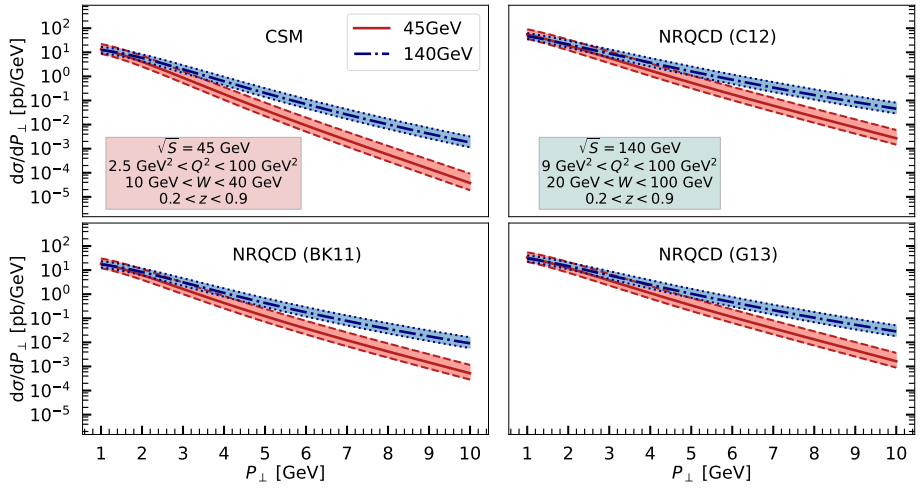

FIGURE 2.3: Unpolarized differential cross section for the SIDIS process $e\,p \to e'\,J/\psi + X$ at EIC kinematics as a function of $P_\perp$, at two cm energies and for different approaches and LDME sets. The integration ranges are given in the boxes, red (on the left) for $\sqrt{S} = 45$ GeV and blue (on the right) for $\sqrt{S} = 140$ GeV. The uncertainty bands are computed by varying the factorization scale in the range $\mu_0/2 < \mu_F < 2\mu_0$, with $\mu_0 = \sqrt{M_\psi^2 + Q^2}$.

One of the opportunities offered by the EIC is the study of ep scattering processes at high luminosity and at different energies. In particular, we will consider two cm energies, corresponding to two extreme values potentially explored by the facility, namely $\sqrt{S} = 45$ GeV and $\sqrt{S} = 140$ GeV.

In Fig. 2.3 we show our predictions for the unpolarized cross section vs. $P_\perp$ at two cm energies and for different approaches, while in Fig. 2.4 we show its z dependence. The uncertainties bands are obtained by letting the factorization scale μ_F vary in the range $\mu_0/2 < \mu_F < 2\mu_0$, around the central value $\mu_0 = \sqrt{M_\psi^2 + Q^2}$. Moreover, in both cases we integrate over Q and W; the former is the photon virtuality while the latter is the cm energy of the photon-proton system. We will adopt different integration ranges for the two energies. For $\sqrt{S} = 140$ GeV, we perform the integration in the intervals 3 GeV $< Q <$ 10 GeV and 20 GeV $< W <$ 100 GeV. The Q range covers most of the high contributing virtuality region while, at the same time, avoids the very small Q values, where photoproduction could play a role and interfere; W integration covers instead almost half of its available region. For the lower cm energy, $\sqrt{S} = 45$ GeV, we reduce the lower bound of the Q integration to improve the statistics, taking 1.6 GeV $< Q <$ 10 GeV. Consistently, the W integration range must be changed, to respect the physical kinematical limits; we then choose 10 GeV $< W <$ 40 GeV, covering almost its whole available region.

The $P_\perp$ spectrum for $P_\perp > 1$ GeV, Fig. 2.3, is evaluated integrating the energy fraction in the region $0.2 < z < 0.9$. Notice that, in the low-$P_\perp$ region, the TMD factorization is supposed to be the correct description of the process. This means that we are pushing our predictions down to $P_\perp$ values that could belong to the overlapping region between the two frameworks (collinear and TMD), giving a hint on what we could expect from the TMD sector. Similarly, in the study of the differential cross section w.r.t. z, Fig. 2.4, we keep considering only $P_\perp > 1$ GeV.

From Fig. 2.3 we see that the differential cross sections drop as $P_\perp$ increases. In particular, the curves relative to the lower energy (red lines) drop faster compared to

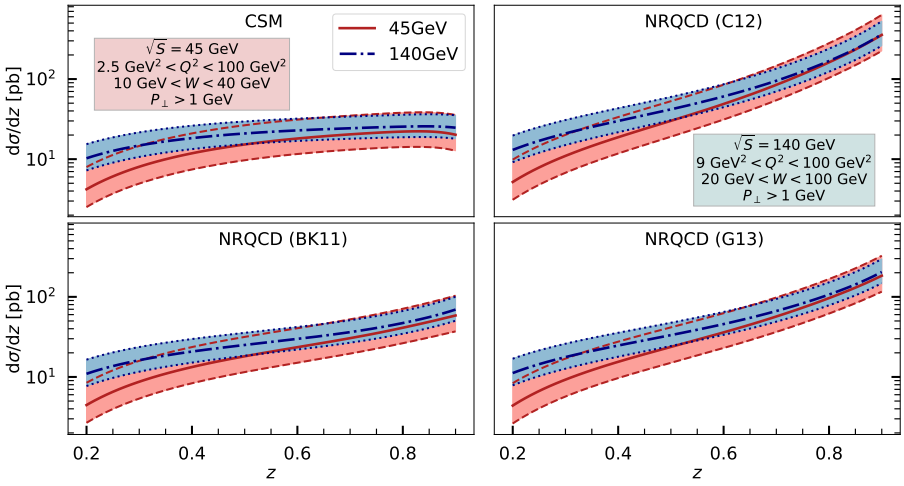

FIGURE 2.4: Same as in Fig. 2.3 but as a function of z.

the corresponding ones evaluated at higher energy (blue lines); at small $P_\perp$ the size in the two cases is similar due to the different Q integration range. Moreover, the presence of CO waves increases the magnitude of NRQCD predictions compared to the CSM ones, at both energies.

It is worth noticing that the main contribution, within the NRQCD framework, comes from the ${}^1S_0^{(8)}$ wave, followed by the CS one (P-wave) at low (high) $P_\perp$. The $P_\perp$ values where the P-waves contribution becomes greater than the CS one differ depending on the LDME set, but it is systematically lower at $\sqrt{S} = 45$ GeV. The ${}^3S_1^{(8)}$ wave gives in all cases a subleading contribution.

Regarding the role of partons, at $\sqrt{S} = 140$ GeV we found that the ${}^1S_0^{(8)}$ and ${}^3P_J^{(8)}$ waves are dominated by gluons, at least in the region shown in the plot; at $P_\perp > 10$ GeV valence quarks become dominant, due to a less suppressed $P_\perp$ distribution. At $\sqrt{S} = 45$ GeV, the quark channel dominates over gluons at lower $P_\perp$, with both ${}^1S_0^{(8)}$ and ${}^3P_J^{(8)}$ waves being dominated by quark channels at $P_\perp \gtrsim 5.5$ GeV, independently of the LDME set considered.

In Fig. 2.4 we observe the (well known) discrepancy between CSM and NRQCD predictions [87, 106, 107], with the latter presenting a divergent behavior at high z. This is related to the singularities of the ${}^1S_0^{(8)}$ and ${}^3P_J^{(8)}$ waves when $\hat{t} \to 0$, that can potentially spoil the NRQCD factorization. More precisely, the full wave/parton decomposition in NRQCD shows that the main CO contribution is the gluon ${}^1S_0^{(8)}$ wave, followed by the gluon ${}^3P_J^{(8)}$ and the quark ${}^1S_0^{(8)}$ waves. These are relevant at high z, while NRQCD predictions at $z \lesssim 0.5$ are mostly dominated by the CS-wave at both energies.

In Refs. [108, 109], the authors tried to deal with this problem by introducing a new set of objects, called shape functions. These allow to extend the convergence of NRQCD in photoproduction up to $1 - z \sim v^2$. Analogous quantities can be expected to play a role also in the electroproduction case. Moreover, a TMD version of them, the TMD shape functions, were subsequently introduced in Refs. [36, 110] for pp processes, to provide the correct TMD factorized expression. Finally, their perturbative tails in SIDIS processes were firstly derived in Refs. [111, 112]. We will revisit this last derivation in Chapter 3.

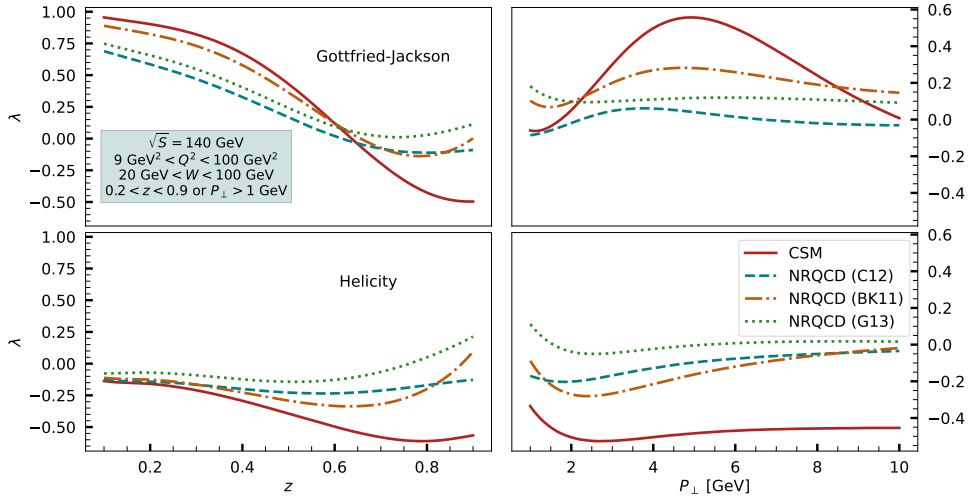

FIGURE 2.5: LO estimates for λ at $\sqrt{S} = 140$ GeV as a function of z (left panels) and as a function of $P_\perp$ (right panels) for different models and LDME sets. Two reference frames are considered: the *Gottfried-Jackson* (upper panels) and the *Helicity* (lower panels) frames. Integration ranges are given in the blue legend box in the right panel.

While it is certainly important to address these issues, they will not be included in the following discussion. Indeed, while smearing effects can play a significant role in quarkonium production, we expect that their importance is markedly reduced when considering the angular parameters [88], being ratios of cross sections. We will anyway point out whenever they may affect our predictions.

2.3.2 The angular parameter λ

We now move to the angular parameters, starting with λ. This quantity is remarkable, being the most experimentally investigated and with great potential from the phenomenological point of view.

As done for the unpolarized cross section, we consider two cm energies, namely $\sqrt{S} = 140$ GeV (Fig. 2.5) and $\sqrt{S} = 45$ GeV (Fig. 2.6). Moreover, we focus our attention on two frames: the *Gottfried-Jackson* (GJ) and the *Helicity* (HX) ones; the proper definition of these frames is given in Sec. 2.2.4. As will become clearer shortly, the *Gottfried-Jackson* frame is a remarkable choice, since the predictions relative to this frame are more sizeable compared to others, while at the same time they present interesting features. As a complementary frame, we have found that the *Helicity* one is more suitable. On the other hand, the *Collins-Soper* frame provides predictions in general less sizeable (even close to zero) compared to the GJ ones, while the *Target* frame predictions are almost overlapping with the HX ones. For these reasons, in the following, we will not explicitly show the last two frames mentioned.

In the next figures we present our results as follows: in the upper panels we show the predictions in the GJ frame, while in the lower panels we present the corresponding ones in the HX frame; left panels refer to the energy fraction z dependence, while right panels to the $P_\perp$ dependence. We consider the same integration regions used for the unpolarized cross section, as also given in the legend boxes in the figures.

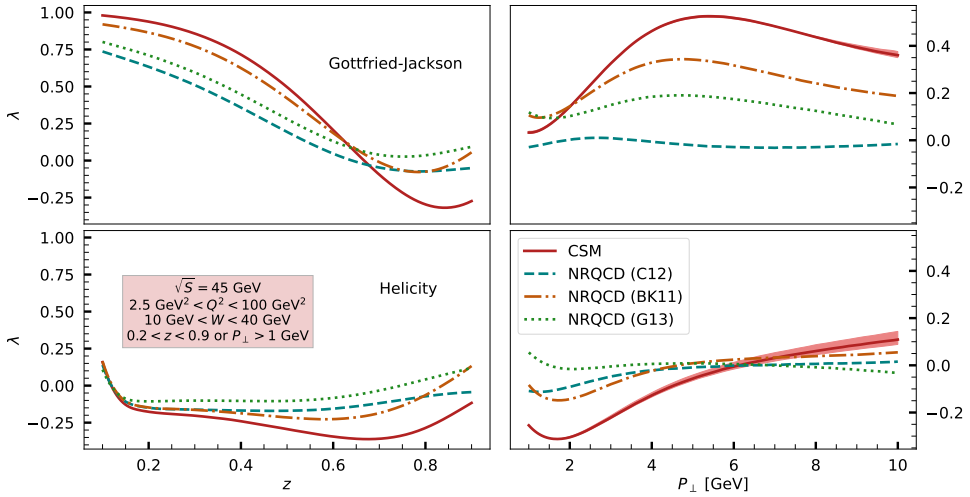

FIGURE 2.6: Same results as in Fig. 2.5 but at lower energy, $\sqrt{S} = 45$ GeV. The corresponding integration regions are given in the red legend box on the left. The error bands for the CSM predictions as a function of $P_\perp$ correspond to the scale variation error, which is sizeable only in this case.

Notice that the band relative to the factorization scale variation is not present, except for some CSM predictions at $\sqrt{S} = 45$ GeV. Indeed, it has been found that this variation is not sizeable enough to be appreciated.

As one can see, left panels of Fig. 2.5 ($\sqrt{S} = 140$ GeV), the magnitude of the λ distribution with respect to z is relatively high. The separation among different frameworks is however relatively small, being all curves very close to each other for $z < 0.6$. High precise data would be required to disentangle them, which might not even be possible at the EIC. The situation is slightly different in the high-z region ($z > 0.6$). Especially in the GJ frame, the separation between the CSM and different NRQCD predictions is relatively significant. Notice that this is the same region where shape functions are expected to start playing a role in the unpolarized case; data at these z values could be then used to understand if they are also required when analyzing the J/ψ polarization.

On the other hand, from the right panels of Fig. 2.5 we can see what we could expect from a $P_\perp$ analysis. Indeed, the $P_\perp$ distribution is a more powerful tool to discern among different frameworks. In particular, precise enough data may be able to discriminate among the predicted shapes of the estimates within the CSM and NRQCD in the GJ frame, or their size in the HX one. Notice that these studies could be performed at $P_\perp$ values significantly far away from the TMD region, avoiding any possible interference from the TMD sector.

Moving to the lower cm energy $\sqrt{S} = 45$ GeV, we present the corresponding results in Fig. 2.6. We see that the distributions w.r.t. z (left panels) do not vary significantly for $z < 0.6$, while at higher values ($z > 0.6$) the estimates are reduced. In addition, we observe in the HX frame a rapid variation of all curves at $z \sim 0.1$. We remark that this is caused by an energy dependent factor, see Eq. (2.79); the same variation should be observed in Fig. 2.5 but, happening at a lower z value, it is outside the range shown.

CSM estimates as functions of $P_\perp$ (right panels) present a more visible variation w.r.t. those in the higher energy case. From the other side, NRQCD results are more

stable in the two energies analysed. In particular, this is evident when considering the λ distributions (w.r.t. $P_\perp$) in HX frame, where the CSM prediction presents a sign change at medium/high $P_\perp$ (Fig. 2.6). Moreover, considering the GJ frame, the CSM prediction at medium/high $P_\perp$ is stable around the value $\lambda \approx 0.4$, without dropping to 0 as in Fig. 2.5. These differences are mostly caused by the lower bound used in the Q^2 integration at $\sqrt{S} = 45$ GeV. Namely, while within NRQCD the impact of small virtualities (1.6 GeV $\lesssim Q \lesssim$ 3 GeV) is not relevant, within the CSM two competitive behaviors appear, causing the difference of the curves in the two figures. In principle, a very similar result can be observed at the higher cm energy, performing a proper binning of Q^2.

We conclude the discussion on the λ parameter with the parton and/or wave decomposition.

From the z analysis, the so close predictions in different frameworks can be traced back to the fact that the numerators are dominated, at both energies, by the (gluon) CS wave, over most of the z values. The subdominant contribution comes from the gluon CO P-wave,[4] which is also the cause of the separation among the results at $z > 0.6$.

In contrast, the same analysis in $P_\perp$ shows that the numerator gets a significant contribution from both the gluon and the quark sectors. In particular, at $\sqrt{S} =$ 140 GeV we find that the (gluon) CS contribution is the most relevant. Nevertheless, at high $P_\perp$ the full (quark+gluon) ${}^3P_J^{(8)}$ wave contribution to the numerator of λ is bigger compared to the CSM term. In addition, for $P_\perp \to 1$ GeV we find that the size of the gluon P-wave is comparable to the CS one. Since the predictions at high z are obtained by an integration over $P_\perp$, mostly dominated by low-$P_\perp$ values, different ${}^3P_J^{(8)}$ LDMEs drive the discrepancies observed at $z > 0.6$ for different frameworks.

Moving to the lower cm energy, $\sqrt{S} = 45$ GeV, it is worth separating the discussion between the two frames. In the GJ frame we find similar conclusions as in the higher cm energies, but where the role of quarks is magnified, making it the leading term of the numerator at high $P_\perp$. In the HX case, the contributions to the numerator of λ from CSM and P-waves are highly suppressed at high $P_\perp$, so the differences in NRQCD are fully driven by the ${}^3S_1^{(8)}$ quark wave.

2.3.3 The angular parameter ν

From the previous discussion, it is clear that the study of a single angular parameter is not exhaustive, especially if limited to a single frame.

For this reason, we now focus on the parameter ν. Indeed, this parameter is very intriguing by itself. As shown in the last section of this chapter (Sec. 2.4), ν is directly related to the linearly polarized gluon TMD distribution within an unpolarized proton, $h_1^{\perp g}$, with great theoretical and phenomenological relevance. Moreover, it is possible to combine λ and ν to construct rotational invariant quantities, as discussed in Sec. 2.3.5. We will then present our LO predictions for ν at the same cm energies and with the same integration range choices, namely $\sqrt{S} = 140$ GeV (Fig. 2.7) and $\sqrt{S} = 45$ GeV (Fig. 2.8).

We start the discussion from the distributions w.r.t. z at these two energies, left panels of Figs. 2.7 and 2.8. As it has been previously found for λ, predictions within the two hadronization models considered are very close (even overlapping) to each other. Once again, although the parameter is sizeable, as in the *Helicity* frame, future data will be hardly able to discriminate among different frameworks.

[4] Remember that ${}^1S_0$ wave cannot contribute to the numerator.

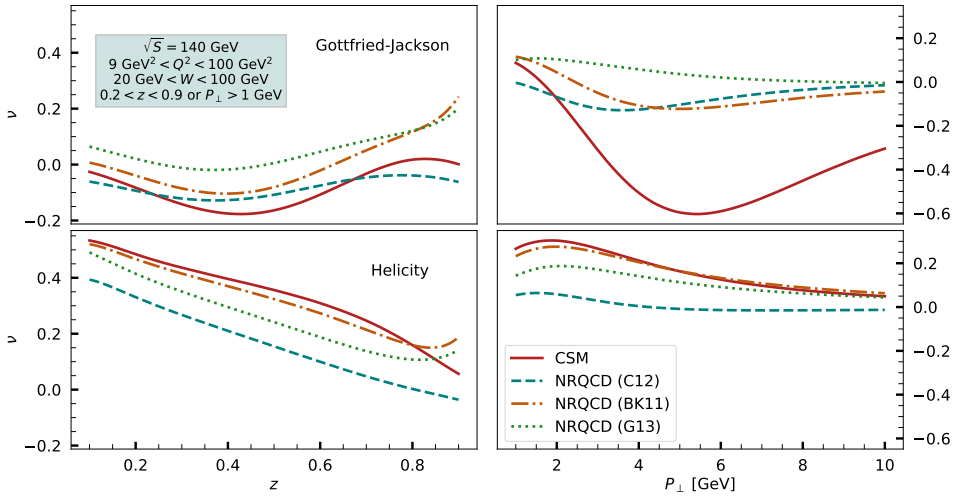

FIGURE 2.7: LO estimates for ν at $\sqrt{S} = 140$ GeV. Panelling order is the same as in Fig. 2.5, with integration ranges given in the blue legend box on the left.

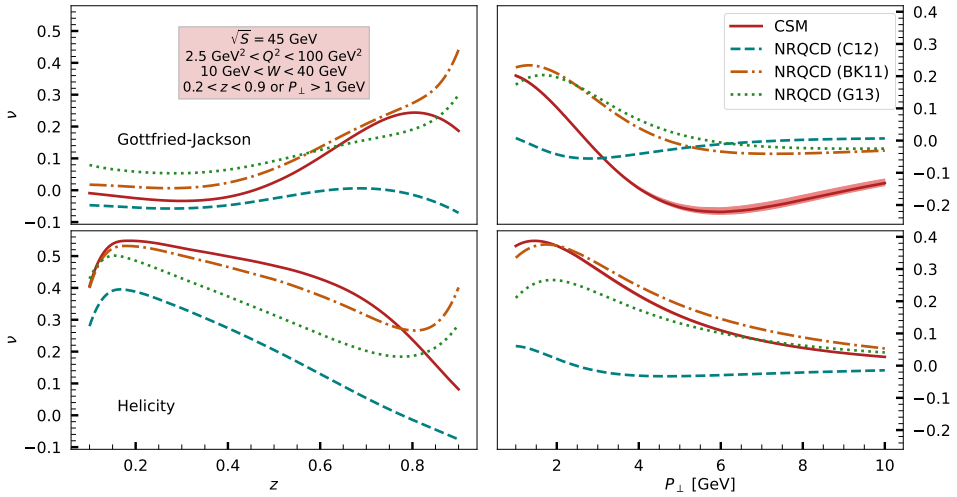

FIGURE 2.8: Same results as in Fig. 2.7 but at $\sqrt{S} = 45$ GeV, with integration ranges given in the red legend box on the left. Error bands, where visible, derive from factorization scale variation.

The situation is more promising when considering the $P_\perp$ dependence, at least within the *Gottfried-Jackson* frame, where there is a significant separation between CSM and NRQCD estimates and where we can still observe the different dependence on the energy/Q-binning, left panels of Figs. 2.7 and 2.8. On the contrary, the *Helicity* frame does not offer the same possibility. Therefore, if limited to the HX frame and within the collinear region, the ν parameter is not able to provide any valuable information by itself.

We remark, however, that the high-z/low-$P_\perp$ regions are quite interesting, due to their connection to the TMD framework, with the potential access to the $h_1^{\perp g}$ gluon TMD. Moreover, in the same region it is possible to study residual effects

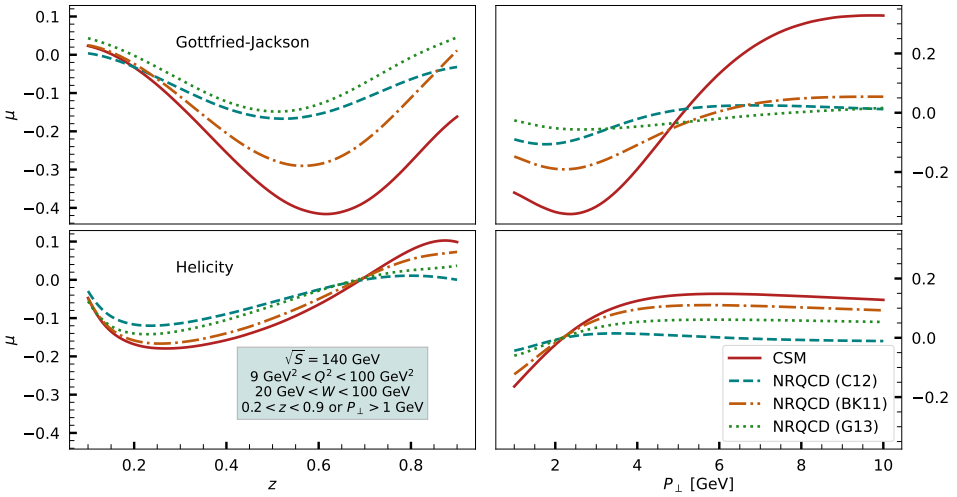

FIGURE 2.9: Estimates for the parameter μ at $\sqrt{S} = 140$ GeV. Panelling order is the same as in Fig. 2.5. Integration ranges are given in the blue legend box.

from (TMD) shape functions, which could depend on quarkonium polarization. In particular, this issue could be better studied at the lower cm energy (or with a proper binning over small-Q values) which, as shown in Fig. 2.8, provides larger sizes. Nevertheless, as discussed in the next Chapter, to properly study the perturbative tails of the polarization dependent shape functions one needs a complete description at the order $\alpha^2\alpha_s^3$ within NRQCD factorization, which is still missing.

Let us now discuss the parton/wave decomposition of the numerator of ν, which is directly related to the helicity structure function $\mathcal{W}_{\Delta\Delta}$.

First of all, we can say that its z dependence is dominated by the CS wave at $\sqrt{S} = 140$ GeV, except for $z \to 0.9$, where the CS contribution is negligible compared to the CO P-wave one. Regarding the $\mathcal{W}_{\Delta\Delta}$ decomposition w.r.t. $P_\perp$ at $\sqrt{S} = 140$ GeV, we find that the contribution of the CS term is significant in the whole spectrum of $P_\perp$, together with the gluon P-wave. At variance with the λ parameter case, quark contributions become relevant already at small-$P_\perp$ values.

An analogous decomposition is also found for the lower cm energy, with the CO P-wave (for both quarks and gluons) being enhanced, because of the lower photon virtualities explored at $\sqrt{S} = 45$ GeV.

2.3.4 The angular parameter μ

We conclude the angular parameter section providing μ estimates in the two selected frames, *Gottfried-Jackson* and *Helicity*, as a function of z and $P_\perp$ at $\sqrt{S} = 140$ GeV, Fig. 2.9, and $\sqrt{S} = 45$ GeV, Fig. 2.10.

We found that the *Gottfried-Jackson* frame is overall the best choice to discern between the CSM and NRQCD approach. This conclusion is driven by the clear separation among NRQCD and CSM predictions for $z \gtrsim 0.5$ and $P_\perp \gtrsim 5$ GeV at $\sqrt{S} = 140$ GeV (Fig. 2.5). On the contrary, estimates in the *Helicity* frame are closer to each other, and it is not foreseeable to come to any conclusion from it.

Even at $\sqrt{S} = 45$ GeV (Fig. 2.10), the *Gottfried-Jackson* has more interesting features. Indeed, we see that CSM μ estimates vary significantly for $z \gtrsim 0.5$ and $P_\perp \gtrsim 5$ GeV, compared to what happens at $\sqrt{S} = 140$ GeV. We remark that the

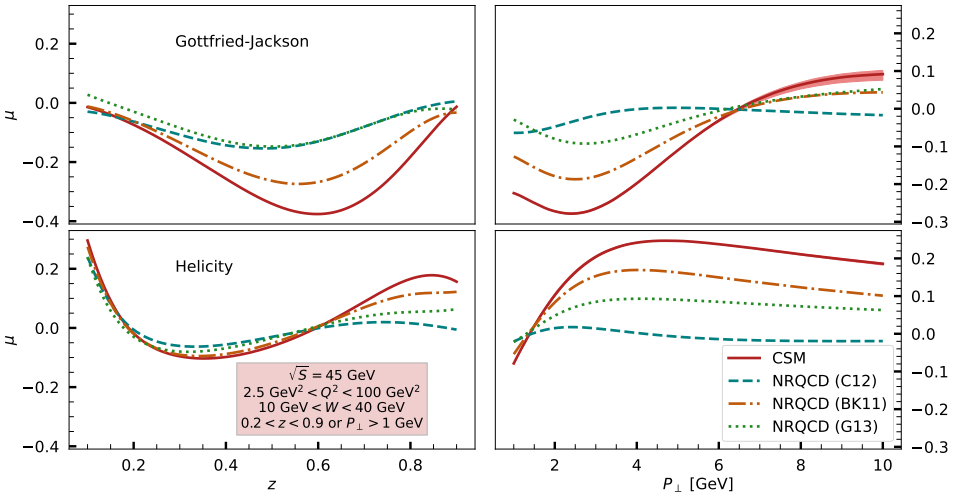

FIGURE 2.10: Estimates for the parameter μ distribution predictions at $\sqrt{S} = 45$ GeV. Panelling order is the same as in Fig. 2.5. Integration ranges are given in the red legend box.

same variation can be observed in the higher cm energy case ($\sqrt{S} = 140$ GeV) via a proper binning in Q. Differently, estimates within the *Helicity* frame at lower energies (lower panels of Fig. 2.10) present a significant energy/Q-binning dependence only for predictions w.r.t. $P_\perp$. In particular, at this (lower) energy the CSM estimate reaches values up to ~ 0.20, while the corresponding one at $\sqrt{S} = 140$ GeV does not exceed ~ 0.13.

Again, we conclude the μ section discussing the wave/parton decomposition of its numerator, directly related to the helicity function $\mathcal{W}_\Delta$. At the higher energy ($\sqrt{S} = 140$ GeV) the main CO contribution comes from the P-wave term, more specifically the gluon P-wave. Thus, the P-wave LDMEs are those that drive the differences in the NRQCD estimates w.r.t. z (left panels of Fig. 2.9). Moreover, for $P_\perp \lesssim 3$ GeV and in the *Gottfried-Jackson* frame, the gluon P-wave provides a significant contribution to the NRQCD predictions (see upper-right panel of Fig. 2.9). In addition, at high $P_\perp$ and especially when considering the *Helicity* frame we have that the quark P-wave channel is relevant, too. Moving to the decomposition at the lower energy ($\sqrt{S} = 45$ GeV), the role of quarks is enhanced. This is particularly true for the $P_\perp$ dependence, since for $P_\perp \gtrsim 6$ GeV NRQCD predictions are mostly driven by the quark P-wave. Furthermore, even the ${}^3S_1^{(8)}$ quark wave is non-negligible in the same high-$P_\perp$ region.

2.3.5 Rotational invariant quantities

As clear from their definition and from the previous discussion, the polarization parameters (λ, μ and ν) are frame-dependent quantities. Nevertheless, as explained in Sec. 2.2.4, the difference among the most used frames is computable, since it corresponds to a rotation around the (common) $\hat{Y}$-axis. In particular, two frame F and F' can be connected via a rotation of an angle ψ, and the rotational matrix that relates

the angular parameters in these two frames is given by[5]

$$\begin{pmatrix}\lambda\\ \mu\\ \nu\end{pmatrix}_{F'} = \frac{1}{1+\rho}\begin{pmatrix}1-\frac{3}{2}\sin^2\psi & \frac{3}{2}\sin 2\psi & \frac{3}{4}\sin^2\psi\\ -\frac{1}{2}\sin 2\psi & \cos 2\psi & \frac{1}{4}\sin 2\psi\\ \sin^2\psi & -\sin 2\psi & 1-\frac{1}{2}\sin^2\psi\end{pmatrix}\begin{pmatrix}\lambda\\ \mu\\ \nu\end{pmatrix}_{F}, \tag{2.91}$$

with

$$\rho = \frac{\sin^2\psi}{2}\left(\lambda_F - \frac{\nu_F}{2}\right) - \sin 2\psi\,\frac{\mu_F}{2}. \tag{2.92}$$

Notice that the quantity ρ depends on the kinematics, since the rotation angle itself depends on the Mandelstam variables (see Eqs. (2.79) - (2.81)).

From Eq. (2.91), it is possible to define auxiliary quantities that are frame independent by construction. They can be considered as complementary and powerful tools to study the J/ψ polarization, both from the experimental and phenomenological points of view. A first group of rotational invariant quantities has been proposed in Ref. [113], defined in terms of λ and ν. Indeed, by using the following relations

$$3+\lambda_{F'} = \frac{1}{1+\rho}(3+\lambda_F), \qquad 1-\frac{\nu_{F'}}{2} = \frac{1}{1+\rho}\left(1-\frac{\nu_F}{2}\right), \tag{2.93}$$

we define a class of invariant quantities

$$\mathcal{F}_{\{c_i\}} = \frac{c_0(3+\lambda)+c_1(1-\nu/2)}{c_2(3+\lambda)+c_3(1-\nu/2)}, \tag{2.94}$$

where c_i are suitable free constants.

Among all possible, independent combinations, here we mention two of them that received special attention [114–118]

$$\mathcal{F} \equiv \mathcal{F}_{(1,-2,1,0)} = \frac{1+\lambda+\nu}{3+\lambda} = \frac{1}{2}\,\frac{2\,\mathrm{d}\sigma_{1,1}+\mathrm{d}\sigma_{1,-1}}{2\,\mathrm{d}\sigma_{1,1}+\mathrm{d}\sigma_{0,0}}, \tag{2.95}$$

and

$$\tilde{\lambda} \equiv \mathcal{F}_{(1,-3,0,1)} = \frac{2\lambda+3\nu}{2-\nu} = \frac{2\,\mathrm{d}\sigma_{1,1}-2\,\mathrm{d}\sigma_{0,0}+3\,\mathrm{d}\sigma_{1,-1}}{2\,\mathrm{d}\sigma_{1,1}+2\,\mathrm{d}\sigma_{0,0}-\mathrm{d}\sigma_{1,-1}}, \tag{2.96}$$

where in the last equalities we used Eq. (2.87) to write them in terms of helicity differential cross sections.

Notice that similar invariants can be also defined in Drell-Yan. If the Lam-Tung relation holds ($1-\lambda = 2\nu$), they acquire constant values [89], namely $\mathcal{F}_{\mathrm{DY}} = 1/2$ and $\tilde{\lambda}_{\mathrm{DY}} = +1$. This was also pointed out in Refs. [115, 118]. Nevertheless, the constant behavior of these quantities arise from dynamics, and in the case of Drell-Yan is a direct consequence of rotational invariance and helicity conservation [119]. Therefore, when moving to J/ψ polarization in SIDIS, the different coupling may cause the breaking of thee Lam-Tung relation.

This can be observed in Fig. 2.11, where our LO predictions for the invariant quantity $\mathcal{F}$ within the collinear framework are presented, as a function of z (left panels) and $P_\perp$ (righ panels). Upper panels refer to $\sqrt{S} = 140$ GeV and lower ones to $\sqrt{S} = 45$ GeV. We adopt again the CSM and NRQCD (with different LDME sets), and we consider the same integration ranges, as done before.

It is clear that in none of the kinematics explored $\mathcal{F}$ is constant, and it can deviate significantly from the expected $1/2$ value, as dictated by the Lam-Tung relation.

[5] Here μ_F stands for the μ parameter related to the frame F.

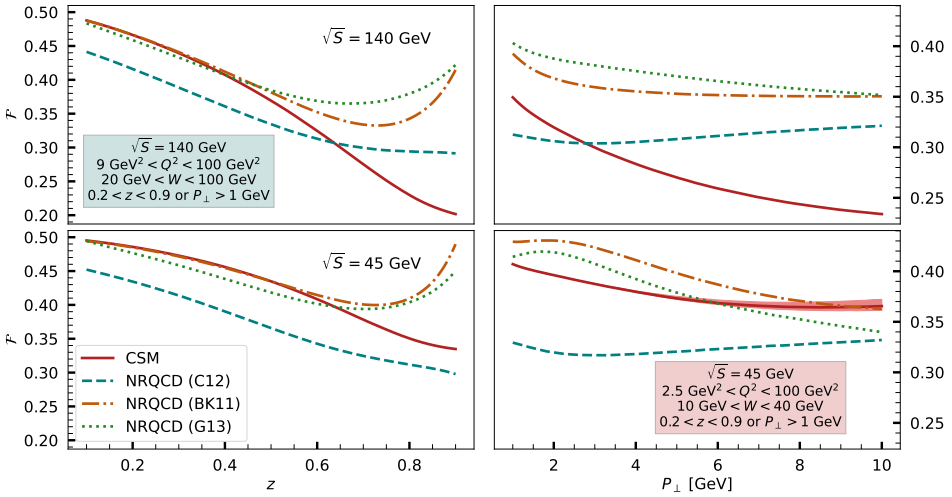

FIGURE 2.11: LO estimates for the invariant $\mathcal{F}$, Eq. (2.95), as a function of z (left panels) and $P_\perp$ (right panels) at two cm energies $\sqrt{S} = 140$ GeV (upper panels) and $\sqrt{S} = 45$ GeV (lower panels), for different approaches and LDME sets. Kinematic ranges are given in the legend boxes.

Its value seems to depend on both z and $P_\perp$ variables; notice that in principle its behavior could appear constant for a certain combination of LDMEs, but this would still be limited to a specific kinematic region. Another interesting aspect is that, while the denominator of $\mathcal{F}$ is proportional to the unpolarized cross section, its numerator is controlled by the relative size of the λ and ν parameters.

Apart from the previous family, it is possible to identify other rotational invariant quantities, that involve all polarization parameters. To obtain them, one can exploit another relation derived from Eq. (2.91)

$$(\lambda_{F'} - \nu_{F'}/2)^2 + 4\mu_{F'}^2 = \frac{(\lambda_F - \nu_F/2)^2 + 4\mu_F^2}{(1+\rho)^2}, \tag{2.97}$$

from which one can construct invariant quantities involving the polarization parameters squared, as first pointed in Ref. [120]. For example, we mention

$$\tilde{\lambda}' = \frac{(\lambda - \nu/2)^2 + 4\mu^2}{(3+\lambda)^2}, \tag{2.98}$$

as defined in Ref. [118].

While we are not aware of measurements on rotational invariant quantities for J/ψ production in SIDIS, they have been explored in pp and heavy-ion processes, *e.g.* in Refs. [95, 121]. In these studies, data are provided only for the first class of invariants (Eq. (2.94)), confirming their expected invariance, but with poor significance. Due to their nature, providing data relative to the second type of invariants, as Eq. (2.98), could be an extremely difficult task.

Nevertheless, all the above invariant quantities have both theoretical and experimental interest. First of all, they represent an important tool to learn on the J/ψ polarization mechanism. Secondly, their expected equality in different frames is an important check of experimental acceptances. In conclusion, even if not easy to be accessed, we believe that their study could be extremely important for the upcoming

EIC.

2.4 TMD framework

In this section we study J/ψ polarization in SIDIS in a frame where the J/ψ meson has no transverse momentum and the transverse momentum of the exchanged virtual photon q_T is small, $q_T^2 \ll Q^2$. In this kinematic regime, TMD factorization is expected to hold.

At leading order the quarkonium state is produced via the partonic process (diagram of order $\alpha\alpha_s$ in Appendix B.2)

$$\gamma^*(q) + g(p_a) \to c\bar{c}(P_\psi), \tag{2.99}$$

where the parton has now a non-negligible transverse component

$$p_a^\mu = \frac{1}{\sqrt{2}} \frac{\hat{z}\, Q^2}{\hat{x}\, M_\psi^2} n_-^\mu + p_{a_T}^\mu, \tag{2.100}$$

with $p_{a_T}^2 = -\boldsymbol{p}_{a_T}^2$. All the other particle momenta are as in Eq. (2.31). We recall that $\hat{z}$ and $\hat{x}$ are, respectively, the partonic version of the J/ψ energy fraction z and of the Bjorken-x (x_B), see Eq. (2.56). Furthermore, n_- and n_+ are the two light-cone directions, defined in a frame where the proton and the J/ψ have no transverse components.

For the time being, smearing effects are neglected in the final state. Being model independent, the angular structure of the cross section is the same as in the collinear framework,

$$\begin{aligned}\frac{\mathrm{d}\sigma^{J/\psi\to\ell^+\ell^-}}{\mathrm{d}x_B\,\mathrm{d}y\,\mathrm{d}^4P_\psi\,\mathrm{d}\Omega} = \frac{B_{\ell\ell}}{4}\frac{\alpha}{yQ^2}\frac{3}{8\pi}\Big[&\widetilde{\mathcal{W}}_T(1+\cos^2\theta) + \widetilde{\mathcal{W}}_L(1-\cos^2\theta) \\ &+ \widetilde{\mathcal{W}}_\Delta \sin 2\theta\, \cos\phi + \widetilde{\mathcal{W}}_{\Delta\Delta} \sin^2\theta\, \cos 2\phi\Big],\end{aligned} \tag{2.101}$$

where $\widetilde{\mathcal{W}}_\Lambda$ are the structure functions in Eq. (2.49), but evaluated in the TMD approach.

Momentum conservation in the process in Eq. (2.99) allows us to write

$$\begin{aligned}\delta^{(4)}(q + p_a - P_\psi) &= \delta\left(\frac{M_\psi}{\sqrt{2}\,\hat{z}} - \frac{M_\psi}{\sqrt{2}}\right)\,\delta\left(\frac{\hat{z}\,Q^2}{\sqrt{2}\,\hat{x}\,M_\psi} - \hat{z}\frac{Q^2+q_T^2}{\sqrt{2}M_\psi} - \frac{M_\psi}{\sqrt{2}}\right)\,\delta^{(2)}(\boldsymbol{p}_{a_T} + \boldsymbol{q}_T) \\ &\approx \frac{2}{M_\psi^2 + Q^2}\,\delta\left(1 - \frac{\hat{x}}{\hat{x}_{\max}}\right)\,\delta(1-\hat{z})\,\delta^{(2)}(\boldsymbol{p}_{a_T} + \boldsymbol{q}_T)\,,\end{aligned} \tag{2.102}$$

where the delta has been expanded in the different light-cone directions and, in the last step, we have impose the condition $q_T \ll Q^2$. It is clear from the above equation that in the TMD regime both $\hat{z}$ and $\hat{x}' = \hat{x}/\hat{x}_{\max}$ are fixed and equal to 1. Furthermore, the partonic Mandelstam variables read

$$\hat{s} = M_\psi^2, \quad \hat{t} \approx -\boldsymbol{q}_T^2, \quad \hat{u} = -Q^2, \tag{2.103}$$

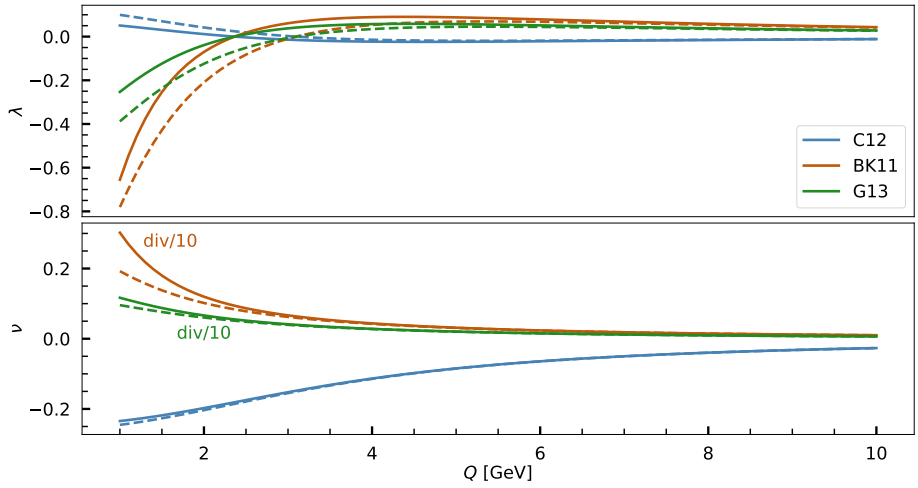

FIGURE 2.12: Estimates of the J/ψ polarization parameters λ and ν in SIDIS as a function of Q and for different LDME sets. The solid (dashed) lines correspond to $y = 0$ ($y = 1$). Estimates for ν are obtained saturating the positivity bound of $h_1^{\perp g}$. The BK11 and G13 curves for the parameter ν are divided by 10.

as a consequence of the following scalar products

$$P_\psi^2 = (q + p_a)^2 = M_\psi^2, \quad q \cdot p_a = P_\psi \cdot p_a = \frac{M_\psi^2 + Q^2}{2}, \quad P_\psi \cdot q = \frac{M_\psi^2 - Q^2}{2}. \tag{2.104}$$

The gluon content of the proton is encoded in a correlation function, which, at leading twist and for an unpolarized spin-1/2 hadron is given by [122–124]

$$\Gamma_U^{\mu\nu}(\xi, p_T^2) = \frac{1}{2\xi}\left[-g_T^{\mu\nu} f_1(\xi, p_T^2) + \frac{1}{m_p^2}\left(p_T^\mu p_T^\nu + \frac{\eta_\perp^{\mu\nu}}{2} p_T^2\right) h_1^\perp(\xi, p_T^2)\right], \tag{2.105}$$

where we have omitted any dependence on the gauge links. The factor $1/2$ is due to the average over the spin. Moreover, m_p is the proton mass, ξ is the light-cone momentum fraction of the proton carried by the gluon, while p_T is its transverse momentum with respect to the proton one. In the above expression, $f_1(\xi, p_T^2)$ is the TMD unpolarized gluon distribution, while $h_1^\perp(\xi, p_T^2)$ is the distribution of linearly polarized gluons in an unpolarized proton.

Similarly to Eq. (2.63), the hadronic helicity structure functions can be written in terms of the partonic ones as follows

$$\begin{aligned}\widetilde{\mathcal{W}}_\Lambda^{\mathcal{P}} &= \int \mathrm{d}\xi \int \mathrm{d}\hat{z} \int \mathrm{d}^2 p_{aT}\, \Gamma_U^{\mu\nu}(\xi, p_T^2)\, \widetilde{w}_{\Lambda\,\mu\nu}^{\mathcal{P}}\, \delta^{(4)}(q + p_a - P_\psi)\delta(\hat{z} - z) \\ &= \left[\widetilde{w}_\Lambda^{\mathcal{P}\,(f)}\, f_1^g(x_B/\hat{x}_{\max}, q_T^2; \mu^2) - \frac{q_T^2}{2m^2}\widetilde{w}_\Lambda^{\mathcal{P}\,(h)}\, h_1^{\perp g}(x_B/\hat{x}_{\max}, q_T^2; \mu^2)\right]\delta(1 - z).\end{aligned} \tag{2.106}$$

Very interestingly, for a specific value of the J/ψ helicity and photon polarization, respectively Λ and $\mathcal{P}$, there is never a contribution from both $\widetilde{w}_\Lambda^{\mathcal{P}\,(f)}$ and $\widetilde{w}_\Lambda^{\mathcal{P}\,(h)}$. Hence, the superscript corresponding to the specific TMD distribution function can

be dropped in the explicit expressions of the partonic structure functions listed below,

$$\widetilde{w}_L^{\perp\,(f)} \equiv \widetilde{w}_L^{\perp} = 2\,(4\pi)^2 \frac{\alpha\alpha_s e_c^2}{M_\psi \left(M_\psi^2 + Q^2\right)} \left[\frac{1}{3}\,\langle \mathcal{O}_8(^1S_0)\rangle + \frac{4}{M_\psi^2}\,\langle \mathcal{O}_8(^3P_0)\rangle\right],$$

$$\widetilde{w}_T^{\perp\,(f)} \equiv \widetilde{w}_T^{\perp} = 2\,(4\pi)^2 \frac{\alpha\alpha_s e_c^2}{M_\psi \left(M_\psi^2 + Q^2\right)} \left[\frac{1}{3}\,\langle \mathcal{O}_8(^1S_0)\rangle + \frac{4}{M_\psi^2}\,\frac{3M_\psi^4 + Q^4}{(M_\psi^2 + Q^2)^2}\,\langle \mathcal{O}_8(^3P_0)\rangle\right],$$

$$\widetilde{w}_{\Delta\Delta}^{\perp\,(h)} \equiv \widetilde{w}_{\Delta\Delta}^{\perp} = -16\,(4\pi)^2 \frac{\alpha\alpha_s e_c^2}{M_\psi \left(M_\psi^2 + Q^2\right)^2}\,\langle \mathcal{O}_8(^3P_0)\rangle\,,$$

$$\widetilde{w}_L^{\parallel\,(f)} \equiv \widetilde{w}_L^{\parallel} = 128\,(4\pi)^2 \frac{\alpha\alpha_s e_c^2\,Q^2}{M_\psi \left(M_\psi^2 + Q^2\right)^3}\,\langle \mathcal{O}_8(^3P_0)\rangle\,. \tag{2.107}$$

While most of the helicity structure functions are directly connected to the unpolarized TMD distribution f_1^g, we have found that the double-helicity flip structure function $\widetilde{\mathcal{W}}_{\Delta\Delta}$ in the small q_T-region could probe the linearly polarized gluon distribution $h_1^{\perp\,g}$, as well as the P-wave LDME. It is important to stress that the results in Eq. (2.107), valid at leading twist and in the small-q_T region, are the same in all the four frames mentioned in Sec. 2.2.4.

We point out that in the above study within the TMD approach at order α_s, we include those CO contributions that are relatively suppressed by a factor of v^4 w.r.t. the CS ones. Nevertheless, higher order corrections in α_s but with an enhanced v scaling, possibly with a different q_T^2 behavior, can be relevant and need to be investigated in future studies.

From Eq. (2.107), we can now obtain an estimate of the polarization parameters in the TMD region. To this aim, we saturate the positivity bound for the (unknown) distribution $h_1^{\perp\,g}$,

$$\frac{p_T^2}{2\,m_p^2}\left|h_1^{\perp\,g}(\xi, p_T^2)\right| \leq f_1^g(\xi, p_T^2). \tag{2.108}$$

The results are shown in Fig. 2.12, at fixed values of the inelasticity y and as a function of the virtuality Q. The parameter λ is shown in the upper panel, while ν is presented in the lower one. The CO contribution is calculated using the same LDME sets considered in Sec. 2.3. We clearly see that the results depend significantly on the choice of the LDMEs, at least for the lower values of Q. This is particularly true for ν: note that its results relative to BK11 and G13 sets are divided by 10. Data in this kinematic region may therefore be extremely important to improve our knowledge of the CO LDMEs. On the other hand, these results do not show a significant dependence on the inelasticity variable y, as can be seen from the two curves presented for each set: solid line for $y = 0$ and dashed line for $y = 1$.

While for the λ parameter we do not expect a significant dependence on the unpolarized gluon TMD f_1^g, since it is present both in the numerator and denominator, the situation can be very different for ν. More specifically, the correct parameterization of $h_1^{\perp\,g}(\xi, p_T^2)$, together with f_1^g, can cause a deviation with respect to our result. In this sense, data at low transverse momentum are valuable to test phenomenological models used to describe such distributions.

Finally, we observe again that in the study presented in this section we did not include any smearing effect in the final state. Such effects are encoded in the so-called

TMD shape functions. In the next chapter we will analyse the matching between the collinear and TMD results for the SIDIS cross section. In this way, we will be able to determine the perturbative tail of the TMD shape functions for the J/ψ meson in this process.

Chapter 3

Matching high- and low-transverse momentum in electron-proton scattering

In this chapter we discuss the matching procedure between two different factorization schemes, both of which are applicable to the theoretical description of J/ψ production in SIDIS, in two complementary kinematical regions. These are the so-called collinear and TMD factorization schemes. Their regions of validity are defined according to the value of the transverse momentum of the exchanged virtual photon q_T, in a frame where the J/ψ has no transverse momentum. More explicitly, in the high-q_T region, $q_T \gg \Lambda_{\rm QCD}$, collinear factorization holds. In the low-q_T region, $q_T \ll \mu$, where μ is a hard scale of the process, we expect TMD factorization to be valid, in analogy to light-hadron production in standard SIDIS [27] for which TMD factorization has been rigorously proven [26]. Moreover, an intermediate region can be identified, where $\Lambda_{\rm QCD} \ll q_T \ll \mu$. Here both descriptions are applicable and results obtained within the two formalisms have to match if they describe the same underlying mechanism. Such a feature has been proven for several observables for which TMD factorization at the twist-two level has been rigorously established, like the unpolarized cross sections for light hadron production in SIDIS [125], integrated over the azimuthal angles of the final particles and differential in q_T, as well as for Drell-Yan dilepton production, $p\,p \to l\,l' + X$ [126, 127].

While in the collinear description, adopting NRQCD [6], J/ψ production is described in terms of PDFs and the common LDMEs, in Refs. [36, 37] it was found that TMD factorization requires the convolution of TMD-PDFs with a generalization of the LDMEs, the TMD shape functions (TMDShFs). These new objects describe transverse momentum smearing due to soft gluon interactions in the hadronization processes. This is at variance with the collinear picture, where the J/ψ momentum has the same direction as the original $c\bar{c}$ pair.

In this chapter we show how the perturbative tail of the TMDShFs can be determined by looking at the SIDIS process. We start from the relation between the TMDShFs and the collinear LDMEs based on the Operator Product Expansion [36],

$$\Delta[n] = \sum_i \left(\frac{\alpha_s}{\pi}\right)^{(i)} C^{(i)}[n]\,\langle \mathcal{O}[n]\rangle \ , \tag{3.1}$$

where $C^{(i)}[n]$ are perturbative calculable coefficients. The non-trivial, leading order coefficients can be obtained by requiring that the observables calculated in the TMD approach at the order $\alpha^2\alpha_s$ correctly match, at high transverse momentum, with the corresponding collinear factorization results at order $\alpha^2\alpha_s^2$.

The chapter is organized as follows. Along the lines of Ref. [111], in Sec. 3.1 we discuss the matching for the production of unpolarized J/ψ in SIDIS. More precisely, in Sec. 3.1.1 we discuss the *naive* Dirac-delta expansion needed to obtain the small-q_T limit of the collinear expression of the structure functions, while in Sec. 3.1.2 we analyse the pole structure of the cross section. Whilst in Ref. [111] these poles were supposed to be negligible, they provide instead a significant contribution and are therefore included in the present derivation. Thus, in Sec. 3.1.3 we present the low-q_T limit of the structure functions evaluated within the collinear factorization approach. Finally, in Sec. 3.1.4 we present the high-q_T limit of the same quantities evaluated within the TMD factorization scheme, and we compare them in order to derive the TMDShF perturbative tail. Lastly, in Sec. 3.2 we briefly discuss the same matching procedure applied to polarized J/ψ production in SIDIS, which has been derived first in Ref. [112].

3.1 Matching procedure for unpolarized J/ψ production in SIDIS

We start our discussion focusing on unpolarized J/ψ production. In this section we will follow the derivation presented in Ref. [111]. Notice that, at variance from what discussed in Sec. 2.1, the dependence on the J/ψ azimuthal angle is kept explicitly. This implies that extra structure functions are present compared to those in Eq. (2.24). In particular, in the high-q_T region we have

$$\frac{\mathrm{d}\sigma}{\mathrm{d}x_B\,\mathrm{d}y\,\mathrm{d}z\,\mathrm{d}\boldsymbol{q}_T^2\,\mathrm{d}\phi_\psi} = \frac{\alpha}{y\,Q^2}\Big[\Big(1+(1-y)^2\Big)F_{UU,\perp} + (1-y)\,F_{UU,\parallel} + (2-y)\,\sqrt{1-y}\,\cos\phi_\psi\,F_{UU}^{\cos\phi_\psi} + (1-y)\,\cos 2\phi_\psi\,F_{UU}^{\cos 2\phi_\psi}\Big], \tag{3.2}$$

where the first two structure functions have been also introduced in Eq. (2.24). We note that the same notation as the one adopted for light-hadron production [125, 128] has been used. Namely, the subscripts UU always refer to initial particle polarizations, while in $F_{UU,\mathcal{P}}$, with $\mathcal{P} = \perp, \parallel$, the last subscript denotes the photon polarization. The superscripts in $F_{UU}^{\cos\phi_\psi}$ and $F_{UU}^{\cos 2\phi_\psi}$ refer to the relative modulations accompanying them in the differential cross section. The full expressions of the structure functions in the collinear regime are available in the literature, *e.g.* Ref. [125]. For completeness, in Appendix B.2 we present the unpolarized partonic structure functions related to $F_{UU,\mathcal{P}}$. In this section, we focus on the small-q_T limit of these expressions, as presented in Sec. 3.1.3. Before carrying out that, we have to elaborate on some relevant elements in this derivation, namely the Dirac-delta expansion (Sec. 3.1.1) and the pole analysis (Sec. 3.1.2).

The small-q_T limit of Eq. (3.2) has to match with the cross section calculated in the TMD factorization approach, which reads

$$\frac{\mathrm{d}\sigma}{\mathrm{d}x_B\,\mathrm{d}y\,\mathrm{d}z\,\mathrm{d}\boldsymbol{q}_T^2\,\mathrm{d}\phi_\psi} = \frac{\alpha}{y\,Q^2}\Big[\Big(1+(1-y)^2\Big)\mathcal{F}_{UU,\perp} + (1-y)\,\mathcal{F}_{UU,\parallel} + (1-y)\,\cos 2\phi_\psi\,\mathcal{F}_{UU}^{\cos 2\phi_\psi}\Big], \tag{3.3}$$

where the structure functions denoted with calligraphic $\mathcal{F}$ are the ones obtained in the TMD framework. Their leading-order expressions will be explicitly given in Sec. 3.1.4, together with their matching onto the corresponding collinear ones.

3.1.1 Dirac-delta expansion in the high transverse momentum expression

Following the same procedure as the one adopted for the helicity structure functions $\mathcal{W}^{\mathcal{P}}$ in Eq. (2.63), it is possible to write the structure functions F in terms of partonic quantities. Indeed, the differential cross section in Eq. (3.2) can be recast as

$$\begin{aligned}\frac{\mathrm{d}\sigma}{\mathrm{d}y\,\mathrm{d}x_B\,\mathrm{d}z\,\mathrm{d}\boldsymbol{q}_T^2\,\mathrm{d}\phi_\psi} &= \frac{1}{4\,(4\pi)^4} y\,z \sum_a \sum_n \int_{x_B}^{\hat{x}_{\max}} \frac{\mathrm{d}\hat{x}}{\hat{x}} \int_z^1 \mathrm{d}\hat{z}\, f_1^a\left(\frac{x_B}{\hat{x}}, \mu^2\right) \\ &\quad \times \frac{L^{\mu\nu}\mathcal{M}_{\mu\nu}^{(a)}[n]}{Q^2}\,\delta\left(\hat{s}+\hat{t}+\hat{u}-M_h^2+Q^2\right)\delta(\hat{z}-z) \\ &= \frac{1}{4\,(4\pi)^4} y\,z \sum_a \sum_n \int_{x_B}^{\hat{x}_{\max}} \frac{\mathrm{d}\hat{x}}{\hat{x}} \int_z^1 \frac{\mathrm{d}\hat{z}}{\hat{z}}\, f_1^a\left(\frac{x_B}{\hat{x}}, \mu^2\right) \\ &\quad \times \frac{L^{\mu\nu}\mathcal{M}_{\mu\nu}^{(a)}[n]}{Q^6}\,\delta\left(\frac{(1-\hat{x})(1-\hat{z})}{\hat{x}\,\hat{z}} - \frac{1-\hat{z}}{\hat{z}^2}\frac{M_\psi^2}{Q^2} + \frac{q_T^2}{Q^2}\right)\delta(\hat{z}-z),\end{aligned} \tag{3.4}$$

where $\mathcal{M}_{\mu\nu}^{(a)}[n]$ is the amplitude squared for the process $\gamma^* a \to c\bar{c}[n] + a$ (built from the operators presented in Appendix B.2), and the lepton tensor is given in Eq. (2.20). In the second equation we have used the explicit form for the Mandelstam variables, see Eq. (2.57), to rewrite the delta function in terms of the integration variables.

As done in Ref. [111], and based on previous works, *e.g.* Ref. [125], here we re-derive the Dirac-delta expansion at small q_T; this allows us to get the structure functions in the same limit.

We consider the Dirac-delta function in the last line of Eq. (3.4), and apply it to two continuous test functions

$$I = \int_0^1 \mathrm{d}\hat{z} \int_0^{\hat{x}_{\max}} \mathrm{d}\hat{x}\, g(\hat{z})\, f(\hat{x})\, \delta\left(\frac{(1-\hat{x})(1-\hat{z})}{\hat{x}\,\hat{z}} - \frac{1-\hat{z}}{\hat{z}^2}\frac{M_\psi^2}{Q^2} + \frac{q_T^2}{Q^2}\right), \tag{3.5}$$

where g and f incorporate the $\hat{z}$ and the $\hat{x}$ dependences, respectively. The continuity of the functions will have important consequences in the final result.

We start noticing that the integration over $\hat{x}$ in Eq. (3.5) is limited by the upper value $\hat{x}_{\max} = Q^2/(M_\psi^2 + Q^2)$, as defined in Eq. (2.59). It is then convenient to introduce a new variable $\hat{x}'$, defined as

$$\hat{x}' = \frac{\hat{x}}{\hat{x}_{\max}} = \frac{M_\psi^2 + Q^2}{2\,p_a \cdot q}, \tag{3.6}$$

so that $0 \le \hat{x}' \le 1$. In the previous equation p_a and q are the initial parton and photon momenta.

After this change of variable in Eq. (3.5), we have

$$I = \hat{x}_{\max} \int_0^1 \mathrm{d}\hat{z} \int_0^1 \mathrm{d}\hat{x}'\,\hat{z}\, g(\hat{z})\, f(\hat{x}')\, \delta\left((1-\hat{x}')(1-\hat{z}) - \frac{1-\hat{z}}{\hat{z}}(\hat{x}'-\hat{z})\frac{M_\psi^2}{Q^2} + \hat{x}'\,\hat{z}\,\frac{q_T^2}{Q^2}\right), \tag{3.7}$$

and the integration over $\hat{x}'$ can be performed using the Dirac-delta function, setting its value at

$$\hat{x}'_0(\hat{z}) = \frac{1}{\hat{x}_{\max}} \frac{(1-\hat{z})\,\hat{z}\,Q^2}{(1-\hat{z})\left(\hat{z}Q^2 + M_\psi^2\right) - \hat{z}^2 q_T^2}. \tag{3.8}$$

Then, only the integral over $\hat{z}$ is left

$$I = \hat{x}_{\max} \int_0^1 \mathrm{d}\hat{z} \left[(1-\hat{z}) + \frac{1-\hat{z}}{\hat{z}}\frac{M_\psi^2}{Q^2} - \hat{z}\frac{q_T^2}{Q^2}\right]^{-1} \left(1 + \frac{M_\psi^2}{\hat{z}\,Q^2}\right) \tilde{g}(\hat{z})\,\tilde{f}(\hat{x}'_0), \tag{3.9}$$

where we have introduced

$$\begin{aligned} \tilde{g}(\hat{z}) &= \hat{z}\left(1 + \frac{M_\psi^2}{\hat{z}\,Q^2}\right)^{-1} g(\hat{z}), \\ \tilde{f}(\hat{x}') &= \hat{x}'\, f(\hat{x}'). \end{aligned} \tag{3.10}$$

To deal with it, we separate I into three integrals

$$I = \hat{x}_{\max}\Big(I_1 + I_2 + I_3\Big), \tag{3.11}$$

via the relation

$$\tilde{g}(\hat{z})\,\tilde{f}(\hat{x}') = \tilde{g}(1)\,\tilde{f}(1) + \Big[\tilde{g}(\hat{z}) - \tilde{g}(1)\Big]\,\tilde{f}(1) + \tilde{g}(\hat{z})\,\Big[\tilde{f}(\hat{x}') - \tilde{f}(1)\Big]. \tag{3.12}$$

From this we get

$$\begin{aligned} I_1 &= \int_0^1 \mathrm{d}\hat{z} \left[(1-\hat{z}) + \frac{1-\hat{z}}{\hat{z}}\frac{M_\psi^2}{Q^2} - \hat{z}\frac{q_T^2}{Q^2}\right]^{-1} \left(1 + \frac{M_\psi^2}{\hat{z}\,Q^2}\right) \tilde{g}(1)\,\tilde{f}(1), \\ I_2 &= \int_0^1 \mathrm{d}\hat{z} \left[(1-\hat{z}) + \frac{1-\hat{z}}{\hat{z}}\frac{M_\psi^2}{Q^2} - \hat{z}\frac{q_T^2}{Q^2}\right]^{-1} \left(1 + \frac{M_\psi^2}{\hat{z}\,Q^2}\right) \Big[\tilde{g}(\hat{z}) - \tilde{g}(1)\Big]\,\tilde{f}(1), \\ I_3 &= \int_0^1 \mathrm{d}\hat{z} \left[(1-\hat{z}) + \frac{1-\hat{z}}{\hat{z}}\frac{M_\psi^2}{Q^2} - \hat{z}\frac{q_T^2}{Q^2}\right]^{-1} \left(1 + \frac{M_\psi^2}{\hat{z}\,Q^2}\right) \tilde{g}(\hat{z})\,\Big[\tilde{f}(\hat{x}'_0) - \tilde{f}(1)\Big]. \end{aligned} \tag{3.13}$$

The first integral can be performed exactly, and then we can extract the leading term in the small-q_T expansion

$$
\begin{aligned}
I_1 &= \tilde{g}(1)\,\tilde{f}(1)\,\int_0^1 \mathrm{d}\hat{z}\,\frac{\hat{z}\,Q^2+M_\psi^2}{(1-\hat{z})\left(\hat{z}\,Q^2+M_\psi^2\right)-\hat{z}^2\,q_T^2} \\
&= \tilde{g}(1)\,\tilde{f}(1)\left\{\ln\frac{M_\psi^2+Q^2}{\boldsymbol{q}_T^2}-\hat{x}_{\max}\frac{\boldsymbol{q}_T^2}{M_\psi^2+Q^2}\left[\left(1+2\frac{M_\psi^2}{Q^2}\right)\ln\frac{M_\psi^2+Q^2}{\boldsymbol{q}_T^2}\right.\right. \\
&\quad \left.\left.-\frac{M_\psi^2}{Q^2}\left(1+\frac{M_\psi^2}{Q^2}\,\ln\frac{M_\psi^2+Q^2}{M_\psi^2}\right)\right]\right\}+\mathcal{O}\left(\frac{\boldsymbol{q}_T^4}{\left(M_\psi^2+Q^2\right)^2}\right) \\
&\approx \tilde{g}(1)\,\tilde{f}(1)\,\ln\frac{M_\psi^2+Q^2}{\boldsymbol{q}_T^2} \\
&= \int_0^1 \mathrm{d}\hat{z}\int_0^{\hat{x}_{\max}}\mathrm{d}\hat{x}\,g(\hat{z})\,f(\hat{x})\,\ln\frac{M_\psi^2+Q^2}{\boldsymbol{q}_T^2}\,\delta(1-\hat{x}/\hat{x}_{\max})\,\delta(1-\hat{z})\,. \qquad (3.14)
\end{aligned}
$$

The second integral can be directly evaluated by taking the limit $q_T \to 0$ in the denominator

$$
\begin{aligned}
I_2 &= \tilde{f}(1)\,\int_0^1 \mathrm{d}\hat{z}\,\frac{\left(\hat{z}\,Q^2+M_\psi^2\right)\left[\tilde{g}(\hat{z})-\tilde{g}(1)\right]}{(1-\hat{z})\left(\hat{z}\,Q^2+M_\psi^2\right)-\hat{z}^2\,q_T^2} \\
&\approx \tilde{f}(1)\,\int_0^1 \mathrm{d}\hat{z}\,\frac{\tilde{g}(\hat{z})-\tilde{g}(1)}{(1-\hat{z})} = \tilde{f}(1)\,\int_0^1 \mathrm{d}\hat{z}\,\frac{\tilde{g}(\hat{z})}{(1-\hat{z})_+} \\
&= \hat{x}_{\max}^{-1}\int_0^1 \mathrm{d}\hat{z}\int_0^{\hat{x}_{\max}}\mathrm{d}\hat{x}\,g(\hat{z})\,f(\hat{x})\,\frac{\hat{z}}{(1-\hat{z})_+}\left(1+\frac{M_\psi^2}{\hat{z}\,Q^2}\right)^{-1}\delta(1-\hat{x}/\hat{x}_{\max})\,, \qquad (3.15)
\end{aligned}
$$

where we have introduced the "+"-distribution, defined in such a way that the integral of a sufficiently smooth function G is given by

$$
\int_a^1 \frac{G(y)}{(1-y)_+} = \int_a^1 \frac{G(y)-G(1)}{(1-y)} + G(1)\ln(1-a). \qquad (3.16)
$$

Finally, we focus on the third integral, which requires more care. We start noticing that by inverting the relation in Eq. (3.8), it is possible to properly express the

integration variable. Since Eq. (3.8) is quadratic in $\hat{z}$, we have two solutions

$$\begin{aligned}
\hat{z}_+ &= \frac{1}{2}\frac{(1+\hat{x}')\left(M_\psi^2+Q^2\right)+\sqrt{(1-\hat{x}')^2\left(M_\psi^2+Q^2\right)^2+2\,\hat{x}'^2\,M_\psi^2\,q_T^2}}{M_\psi^2+(1-\hat{x}')\,Q^2-\hat{x}'\,q_T^2} \\
&= 1+\frac{q_T^2}{M_\psi^2+Q^2}\frac{\hat{x}'}{1-\hat{x}'}+\mathcal{O}\left(\frac{\boldsymbol{q}_T^4}{\left(M_\psi^2+Q^2\right)^2}\right), \\
\hat{z}_- &= \frac{1}{2}\frac{(1+\hat{x}')\left(M_\psi^2+Q^2\right)-\sqrt{(1-\hat{x}')^2\left(M_\psi^2+Q^2\right)^2+2\,\hat{x}'^2\,M_\psi^2\,q_T^2}}{M_\psi^2+(1-\hat{x}')\,Q^2-\hat{x}'\,q_T^2} \\
&= \frac{\hat{x}'\,M_\psi^2}{M_\psi^2+(1-\hat{x}')\,Q^2}+\frac{q_T^2}{M_\psi^2+Q^2}\left(\frac{\hat{x}'\,M_\psi^2}{M_\psi^2+(1-\hat{x}')\,Q^2}\right)^2\frac{\hat{x}'}{1-\hat{x}'} \\
&\quad+\mathcal{O}\left(\frac{\boldsymbol{q}_T^4}{\left(M_\psi^2+Q^2\right)^2}\right).
\end{aligned} \tag{3.17}$$

By looking at the q_T expansion, we realize that the second solution is not physically acceptable. Indeed, from momentum conservation (see the Dirac-delta function in Eq. (3.7)), at $q_T=0$ it is mandatory that $\hat{z}=1$ independently of $\hat{x}'$, whereas $\hat{z}_-\to 1$ if and only if $\hat{x}'\to 1$. Furthermore, we notice that in the massless limit, the $\hat{z}_+$ solution is the only one surviving.

Therefore, by taking $\hat{z}\equiv\hat{z}_+$ and neglecting terms of order $\boldsymbol{q}_T^4/\left(M_\psi^2+Q^2\right)^2$, we have

$$\mathrm{d}\hat{z}=\frac{q_T^2}{M_\psi^2+Q^2}\frac{1}{(1-\hat{x}')^2}\mathrm{d}\hat{x}'+\mathcal{O}\left(\frac{\boldsymbol{q}_T^4}{\left(M_\psi^2+Q^2\right)^2}\right) \tag{3.18}$$

and

$$\frac{\hat{z}^2\,Q^2}{(1-\hat{z})\left(\hat{z}\,Q^2+M_\psi^2\right)-\hat{z}^2\,q_T^2}=-\frac{Q^2}{q_T^2}\,(1-\hat{x}')+\mathcal{O}\left(q_T^0\right). \tag{3.19}$$

Introducing these relations in the third integral, and taking the limit $g(\hat{z})\to g(1)$, valid when $q_T\to 0$, we get

$$\begin{aligned}
I_3 &= \int_0^1 \mathrm{d}\hat{z}\,\tilde{g}(\hat{z})\,\frac{\left(\hat{z}\,Q^2+M_\psi^2\right)\left[\tilde{f}(\hat{x}'_0)-\tilde{f}(1)\right]}{(1-\hat{z})\left(\hat{z}\,Q^2+M_\psi^2\right)-\hat{z}^2\,q_T^2} \\
&= \int_0^1 \mathrm{d}\hat{z}\,g(\hat{z})\,\frac{\hat{z}^2\,Q^2}{(1-\hat{z})\left(\hat{z}\,Q^2+M_\psi^2\right)-\hat{z}^2\,q_T^2}\left[\tilde{f}(\hat{x}'_0)-\tilde{f}(1)\right] \\
&\approx \hat{x}_{\max}\,g(1)\int_0^1 \mathrm{d}\hat{x}'\,\frac{\tilde{f}(\hat{x}')-\tilde{f}(1)}{(1-\hat{x}')}=g(1)\int_0^1 \mathrm{d}\hat{x}'\,\hat{x}_{\max}\frac{\hat{x}'}{(1-\hat{x}')_+}f(\hat{x}') \\
&= \int_0^1 \mathrm{d}\hat{z}\int_0^{\hat{x}_{\max}}\mathrm{d}\hat{x}\,g(1)\,f(\hat{x})\,\frac{\hat{x}/\hat{x}_{\max}}{(1-\hat{x}/\hat{x}_{\max})_+}\,\delta(1-\hat{z}),
\end{aligned} \tag{3.20}$$

where we have used once again the "+"-distribution (see Eq. (3.16)) for the $\hat{x}'$ variable.

Finally, the sum of the three integrals in the $q_T^2 \ll \mu^2$ region reads

$$
\begin{aligned}
I \approx \hat{x}_{\max} \int_0^1 \mathrm{d}\hat{z} \int_0^{\hat{x}_{\max}} \mathrm{d}\hat{x}\, g(\hat{z})\, f(\hat{x}) \\
\times \left[\ln \frac{M_\psi^2 + Q^2}{q_T^2}\, \delta\big(1 - \hat{x}/\hat{x}_{\max}\big)\, \delta(1-\hat{z}) + \frac{\hat{x}/\hat{x}_{\max}}{(1-\hat{x}/\hat{x}_{\max})_+} \delta(1-\hat{z}) \right. \\
\left. + \frac{M_\psi^2 + Q^2}{M_\psi^2/\hat{z} + Q^2} \frac{\hat{z}}{(1-\hat{z})_+} \delta\big(1 - \hat{x}/\hat{x}_{\max}\big) \right],
\end{aligned}
\tag{3.21}
$$

from which the Dirac-delta expansion is

$$
\begin{aligned}
\delta\left(\frac{(1-\hat{x})(1-\hat{z})}{\hat{x}\,\hat{z}} - \frac{1-\hat{z}}{\hat{z}^2} \frac{M_\psi^2}{Q^2} + \frac{q_T^2}{Q^2} \right) \to \\
\to \hat{x}_{\max} \left[\ln \frac{M_\psi^2 + Q^2}{q_T^2}\, \delta(1-\hat{x}')\, \delta(1-\hat{z}) + \frac{\hat{x}'}{(1-\hat{x}')_+} \delta(1-\hat{z}) \right. \\
\left. + \frac{M_\psi^2 + Q^2}{M_\psi^2/\hat{z} + Q^2} \frac{\hat{z}}{(1-\hat{z})_+} \delta(1-\hat{x}') \right].
\end{aligned}
\tag{3.22}
$$

Note that in the limit $M_\psi \to 0$, for which $\hat{x}_{\max} \to 1$ and $\hat{x}' \to \hat{x}$, our expansion coincides with the known relation found in standard SIDIS, see *e.g.* Ref. [129].

Before plugging Eq. (3.22) into Eq. (3.4), it is necessary to separate the continuous part of the structure functions from poles, that can lead to indeterminate forms in the double limit $\hat{x}', \hat{z} \to 1$. Indeed, if a discontinuity is present, the above derivation is not valid and the treatment of those terms needs a different approach.

3.1.2 Pole structure of the squared amplitudes

In this section we analyze the poles appearing in some structure functions. These poles must still be included in our discussion, since they provide a non-negligible contribution to the divergent behaviour at small q_T. In particular, we have found that their role is relevant only for the structure functions $F_{UU,\perp}$ and $F_{UU,\parallel}$. More precisely, they appear in the three gluonic-initiated channels. In the following we discuss how to deal with them.

By defining the projectors $\epsilon_{\mathcal{P}}^{\mu\nu}$ (with $\mathcal{P} = \perp, \parallel$)

$$
\epsilon_\perp^{\mu\nu} = -\eta_\perp^{\mu\nu}, \quad \epsilon_\parallel^{\mu\nu} = 4\, \epsilon_\parallel^\mu \epsilon_\parallel^\nu,
\tag{3.23}
$$

also appearing in Eq. (2.54), we identify the contractions of these projectors with the hadron tensor $\mathcal{M}_{\mu\nu}$ as

$$
\left| \mathcal{M}_{\mathcal{P}}^{(a)}[n] \right|^2 = \frac{1}{2} \epsilon_{\mathcal{P}}^{\mu\nu}\, \mathcal{M}_{\mu\nu}^{(a)}[n].
\tag{3.24}
$$

Among them, the following amplitudes squared, $\left| \mathcal{M}_\perp^{(g)}[{}^1S_0^{(8)}] \right|^2$, $\left| \mathcal{M}_\perp^{(g)}[{}^3P_0^{(8)}] \right|^2$ and $\left| \mathcal{M}_\parallel^{(g)}[{}^3P_0^{(8)}] \right|^2$, manifest a problematic behavior. Even if poles can appear also in other gluon channels, their overall q_T divergence is less severe compared to the ones

mentioned above. For this reason, they can be safely neglected in the small-q_T expansion. Lastly, quark channels are free from singularities and will not be further addressed in this context.

For simplicity, we will use the general notation $\left|\mathcal{M}_{\mathcal{P}}^{(g)}[n]\right|^2$, keeping in mind that we only refer to the above three amplitudes squared. After applying the relation

$$\frac{1}{1-\hat{z}} = \frac{1}{\boldsymbol{q}_T^2}\frac{(1-\hat{x}')\,\hat{z}\,Q^2 + (\hat{z}-\hat{x}')\,M_\psi^2}{\hat{x}'\,\hat{z}^2}, \tag{3.25}$$

obtained from the Dirac-delta function in Eq. (3.7), the amplitudes squared can be decomposed into three terms

$$\left|\mathcal{M}_{\mathcal{P}}^{(g)}[n]\right|^2(\hat{x}',\hat{z}) = M_0^{[n],\mathcal{P}}(\hat{x}',\hat{z}) + \left(\frac{1-\hat{z}}{1-\hat{x}'}\right)M_1^{[n],\mathcal{P}}(\hat{z}) + \left(\frac{1-\hat{z}}{1-\hat{x}'}\right)^2 M_2^{[n],\mathcal{P}}(\hat{z}). \tag{3.26}$$

The first term, $M_0^{[n],\mathcal{P}}(\hat{x}',\hat{z})$, is continuous in the double limit, and we can directly use the Dirac-delta expansion in Eq. (3.22). On the other hand, the last two terms are those containing a pole. Since $M_1^{[n],\mathcal{P}}(\hat{z})$ and $M_2^{[n],\mathcal{P}}(\hat{z})$ are continuous, it is then legit to approximate these quantities as

$$M_1^{[n],\mathcal{P}}(1) = -2\,\frac{M_\psi^2}{M_\psi^2+Q^2}\,M_0^{[n],\mathcal{P}}(1,1), \tag{3.27}$$

and

$$M_2^{[n],\mathcal{P}}(1) = \left(\frac{M_\psi^2}{M_\psi^2+Q^2}\right)^2 M_0^{[n],\mathcal{P}}(1,1). \tag{3.28}$$

Therefore, we can directly evaluate the integrals $I_{\rm sp}$ and $I_{\rm dp}$, corresponding respectively to the single and double poles. The former reads

$$\begin{aligned} I_{\rm sp} &= \int_0^1 \mathrm{d}\hat{z}\int_0^1 \mathrm{d}\hat{x}'\,\frac{1-\hat{z}}{1-\hat{x}'}\,\delta\left(\hat{z}\,(1-\hat{x}')\,(1-\hat{z}) - (1-\hat{z})\,(\hat{x}'-\hat{z})\,\frac{M_\psi^2}{Q^2} + \hat{x}'\,\hat{z}^2\,\frac{q_T^2}{Q^2}\right) \\ &= \int_0^1 \mathrm{d}\hat{z}\int_0^1 \mathrm{d}\hat{x}'\,\frac{1-\hat{z}}{M_\psi^2\,(1-\hat{z})^2 + \hat{z}^2\,\boldsymbol{q}_T^2} \\ &= \frac{1}{2}\frac{Q^2}{M_\psi^2}\,\log\frac{M_\psi^2}{\boldsymbol{q}_T^2} + \mathcal{O}\left(\frac{|\boldsymbol{q}_T|}{M_\psi^2}\right), \end{aligned} \tag{3.29}$$

while the second one

$$\begin{aligned} I_{\rm dp} &= \int_0^1 \mathrm{d}\hat{z}\int_0^1 \mathrm{d}\hat{x}'\,\left(\frac{1-\hat{z}}{1-\hat{x}'}\right)^2\,\delta\left(\hat{z}\,(1-\hat{x}')\,(1-\hat{z}) - (1-\hat{z})\,(\hat{x}'-\hat{z})\,\frac{M_\psi^2}{Q^2} + \hat{x}'\,\hat{z}^2\,\frac{q_T^2}{Q^2}\right) \\ &\approx \left(M_\psi^2+Q^2\right)\int_0^1 \mathrm{d}\hat{z}\int_0^1 \mathrm{d}\hat{x}'\,\frac{(1-\hat{z})^3}{\left[M_\psi^2\,(1-\hat{z})^2 + \hat{z}^2\,\boldsymbol{q}_T^2\right]^2} \\ &= -\frac{1}{2}\frac{\left(M_\psi^2+Q^2\right)Q^2}{M_\psi^4}\left(1+\log\frac{M_\psi^2}{\boldsymbol{q}_T^2}\right) + \mathcal{O}\left(\frac{|\boldsymbol{q}_T|}{M_\psi^2}\right). \end{aligned} \tag{3.30}$$

Due to the proportionality of $M_1^{[n],\mathcal{P}}(1)$ and $M_2^{[n],\mathcal{P}}(1)$ to $M_0^{[n],\mathcal{P}}(1,1)$ (see Eqs. (3.27) and (3.28)), $I_{\rm sp}$ and $I_{\rm dp}$ can be effectively added to the double delta coefficient in Eq. (3.22), leading to

$$\left|\mathcal{M}_{\mathcal{P}}^{(g)}[n]\right|^2(\hat{x}',\hat{z})\,\delta\left(\frac{(1-\hat{x})(1-\hat{z})}{\hat{x}\,\hat{z}}-\frac{1-\hat{z}}{\hat{z}^2}\frac{M_\psi^2}{Q^2}+\frac{q_T^2}{Q^2}\right)\to M_0^{[n],\mathcal{P}}(\hat{x}',\hat{z})\,\delta_{\rm eff}^{[n],\mathcal{P}}\,, \tag{3.31}$$

with an effective delta expansion given by

$$\begin{aligned}\delta_{\rm eff}^{[n],\mathcal{P}}=\hat{x}_{\rm max}\Bigg[&\frac{1}{2}\left(\log\frac{M_\psi^2+Q^2}{\boldsymbol{q}_T^2}-1+\log\frac{M_\psi^2+Q^2}{M_\psi^2}\right)\delta(1-\hat{x}')\,\delta(1-\hat{z})\\&+\frac{\hat{x}'}{(1-\hat{x}')_+}\delta(1-\hat{z})+\frac{M_\psi^2+Q^2}{M_\psi^2/\hat{z}+Q^2}\frac{\hat{z}}{(1-\hat{z})_+}\delta(1-\hat{x}')\Bigg]\,.\end{aligned} \tag{3.32}$$

3.1.3 From high to intermediate transverse momentum

By using the Dirac-delta expansion for the continuous terms (Eq. (3.22)), and the above pole analysis, we can obtain the small-q_T limit of the structure functions in Eq. (3.2)

$$\begin{aligned}F_{UU,\perp}&=\sigma_{UU,\perp}\left[L\left(\frac{\mu^2}{\boldsymbol{q}_T^2}\right)f_1^g(x,\mu^2)+\left(P_{gg}\otimes f_1^g+P_{gi}\otimes f_1^i\right)(x,\mu^2)\right]+\mathcal{O}\left(\frac{|\boldsymbol{q}_T|}{\mu}\right),\\F_{UU,\parallel}&=\sigma_{UU,\parallel}\left[L\left(\frac{\mu^2}{\boldsymbol{q}_T^2}\right)f_1^g(x,\mu^2)+\left(P_{gg}\otimes f_1^g+P_{gi}\otimes f_1^i\right)(x,\mu^2)\right]+\mathcal{O}\left(\frac{|\boldsymbol{q}_T|}{\mu}\right),\\F_{UU}^{\cos\phi_\psi}&=\mathcal{O}\left(\frac{|\boldsymbol{q}_T|}{\mu}\right),\\F_{UU}^{\cos 2\phi_\psi}&=\sigma_{UU}^{\cos 2\phi_\psi}\left(\delta P_{gg}\otimes f_1^g+\delta P_{gi}\otimes f_1^i\right)(x,\mu^2)+\mathcal{O}\left(\frac{|\boldsymbol{q}_T|}{\mu}\right).\end{aligned} \tag{3.33}$$

The results presented in Eq. (3.33) are valid up to $\mathcal{O}\left(\frac{|\boldsymbol{q}_T|}{\mu}\right)$, but also up to corrections of the order $\mathcal{O}\left(\frac{\Lambda_{\rm QCD}}{|\boldsymbol{q}_T|}\right)$.

In the above expressions the momentum fraction x is fixed by

$$x\equiv\frac{x_B}{\hat{x}_{\rm max}}\,, \tag{3.34}$$

and the function $L(\mu^2/\boldsymbol{q}_T^2)$ is defined as

$$L\left(\frac{\mu^2}{\boldsymbol{q}_T^2}\right)=C_A\left(\log\frac{\mu^2}{\boldsymbol{q}_T^2}-1+\log\frac{(M_\psi^2+Q^2)^2}{\mu^2\,M_\psi^2}\right)-\frac{11\,C_A-4\,n_f\,T_R}{6}, \tag{3.35}$$

where $T_R = 1/2$, $C_A = N_c$, $N_c = 3$ (number of colors) and n_f is the number of active flavors. Moreover, the leading-order unpolarized splitting functions are given by

$$P_{gg}(\hat{x}) = 2\,C_A \left[\frac{\hat{x}}{(1-\hat{x})_+} + \frac{1-\hat{x}}{\hat{x}\left(1-\hat{x}\right)} + \hat{x} \right] + \delta\left(1-\hat{x}\right) \frac{11\,C_A - 4\,n_f\,T_R}{6},$$
$$P_{gi}(\hat{x}) = C_F \frac{1+\left(1-\hat{x}\right)^2}{\hat{x}}, \tag{3.36}$$

with $C_F = 4/3$, while the splitting functions for an unpolarized parton into a linearly polarized gluon read (see also Refs. [130, 131])

$$\delta P_{gg}(\hat{x}) = C_A \frac{1-\hat{x}}{\hat{x}},$$
$$\delta P_{gi}(\hat{x}) = C_F \frac{1-\hat{x}}{\hat{x}}. \tag{3.37}$$

Furthermore, the symbol "$\otimes$" denotes the convolution between the splitting function P and the collinear gluon PDF f_1^g in the light-cone momentum fraction

$$\left(P \otimes f_1^g\right)(x,\mu^2) = \int_x^1 \frac{\mathrm{d}\hat{x}}{\hat{x}}\, P(\hat{x})\, f_1^g\left(x/\hat{x},\mu^2\right). \tag{3.38}$$

Finally, the partonic cross sections for the $2 \to 1$ process, namely $\gamma^* g \to c\bar{c}[n]$, are given by

$$\sigma_{UU,\perp} = \frac{e_c^2\,\alpha\,\alpha_s^2}{M_\psi\left(M_\psi^2+Q^2\right)\boldsymbol{q}_T^2} \times \left[\langle \mathcal{O}_8^\psi[^1S_0]\rangle + 4\,\frac{7\,M_\psi^4 + 2\,M_\psi^2\,Q^2 + 3\,Q^4}{M_\psi^2\left(M_\psi^2+Q^2\right)^2}\,\langle \mathcal{O}_8^\psi[^3P_0]\rangle \right] \delta(1-z),$$
$$\sigma_{UU,\parallel} = \frac{e_c^2\,\alpha\,\alpha_s^2}{M_\psi\left(M_\psi^2+Q^2\right)\boldsymbol{q}_T^2} \left[64\,\frac{Q^2}{\left(M_\psi^2+Q^2\right)^2}\,\langle \mathcal{O}_8^\psi[^3P_0]\rangle \right] \delta(1-z),$$
$$\sigma_{UU}^{\cos 2\phi_\psi} = \frac{e_c^2\,\alpha\,\alpha_s^2}{M_\psi\left(M_\psi^2+Q^2\right)\boldsymbol{q}_T^2} \times \left[-4\,\langle \mathcal{O}_8^\psi[^1S_0]\rangle + 16\,\frac{3\,M_\psi^2 - Q^2}{M_\psi^2\left(M_\psi^2+Q^2\right)}\,\langle \mathcal{O}_8^\psi[^3P_0]\rangle \right] \delta(1-z), \tag{3.39}$$

where e_c is the fractional charm charge in units of the proton one.

Notice that, up to this order, the structure function $F_{UU}^{\cos\phi_\psi}$ is suppressed compared to the others and will not be considered in the following.

Our study, at order $\alpha^2\alpha_s^2$, includes both the CS wave and the subleading CO contributions, even if suppressed up to a factor v^4, with the dominant ones at small-q_T being the ${}^1S_0^{(8)}$ and the ${}^3P_J^{(8)}$ terms. On the other hand, we cannot exclude *a priori* that higher-order corrections in α_s might contribute in this limit, since an enhanced scaling in v and a potentially different $\boldsymbol{q}_T$ behaviour could make them relevant in

the $q_T \ll \mu$ region. Nevertheless, the q_T behaviour found here is similar to the analogous case of light-hadron production in SIDIS, Ref. [125]. In this case, extra terms appear due to the presence of a fragmentation function, not present in quarkonium production within the NRQCD approach. Moreover, their underlying partonic process is $\gamma^* q \to q$, and the corresponding logarithmic term is given by $C_F\left(2\ln Q^2/q_T^2 - 3\right)$, with C_F replacing C_A, as expected for a quark initiated process.

Notice that the logarithmic divergence in Eq. (3.35) is half compared to what appears in standard SIDIS processes ($e\,p \to e'\,h + X$). This is in agreement with other results, *e.g.* Ref. [132]. Similarly in Ref. [133] they found that in $p\,p \to J/\psi + X$ process, there are no logarithmic divergences associated to the J/ψ meson in the small transverse momentum region. In our case, the single pole causes the reduction of the number of logarithmic divergences, see Eq. (3.29). On the other hand, from the double pole (Eq. (3.30)) we have a constant term, partially found also in Ref. [133]. Its exact meaning is still under investigation and will be addressed in a future work [134].

Finally, we mention that in Ref. [135], the authors evaluated the Sudakov factor for open heavy-quark/antiquark production in electron-proton collisions. We have checked that the logarithmic divergences in Eq. (3.35) are in agreement with the results in Ref. [135], when one considers the limit in which the heavy quark pair forms a bound state.

3.1.4 From low to intermediate transverse momentum

At low transverse momentum, where TMD factorization applies, the differential cross section is given by Eq. (3.3). The $\mathcal{F}$ are the structure functions evaluated in the TMD regime, and they are explicitly given by

$$\begin{aligned}
\mathcal{F}_{UU,\perp} &= 2\pi^2 \frac{e_c^2\,\alpha\,\alpha_s}{M_\psi\left(M_\psi^2+Q^2\right)}\delta(1-z) \\
&\quad\times\left[\mathcal{C}\left[f_1^g\,\Delta^{[^1S_0^{(8)}]}\right] + 4\,\frac{7\,M_\psi^4 + 2\,M_\psi^2\,Q^2 + 3\,Q^4}{M_\psi^2\left(M_\psi^2+Q^2\right)^2}\,\mathcal{C}\left[f_1^g\,\Delta^{[^3P_0^{(8)}]}\right]\right], \\
\mathcal{F}_{UU,\parallel} &= 2\pi^2 \frac{e_c^2\,\alpha\,\alpha_s}{M_\psi\left(M_\psi^2+Q^2\right)}\left[64\frac{Q^2}{\left(M_\psi^2+Q^2\right)^2}\,\mathcal{C}\left[f_1^g\,\Delta^{[^3P_0^{(8)}]}\right]\right]\delta(1-z),
\end{aligned}$$

$$\begin{aligned}
\mathcal{F}_{UU}^{\cos 2\phi_\psi} &= 2\pi^2 \frac{e_c^2\,\alpha\,\alpha_s}{M_\psi\left(M_\psi^2+Q^2\right)}\delta(1-z) \\
&\quad\times\left[-4\,\mathcal{C}\left[w\,h_1^{\perp,g}\,\Delta_h^{[^1S_0^{(8)}]}\right] + 16\,\frac{3\,M_\psi^2 - Q^2}{M_\psi^2\left(M_\psi^2+Q^2\right)}\,\mathcal{C}\left[w\,h_1^{\perp,g}\,\Delta_h^{[^3P_0^{(8)}]}\right]\right].
\end{aligned} \tag{3.40}$$

$\Delta^{[n]}$ are the TMDShFs and their convolutions with the TMD-PDFs are defined as

$$\begin{aligned}\mathcal{C}\left[f_1^g\,\Delta^{[n]}\right] &= \int \mathrm{d}^2\boldsymbol{p}_T \int \mathrm{d}^2\boldsymbol{k}_T \delta^{(2)}(\boldsymbol{q}_T-\boldsymbol{p}_T-\boldsymbol{k}_T)\, f_1^g(x,p_T^2;\mu^2)\,\Delta^{[n]}(k_T^2;\mu^2),\\ \mathcal{C}\left[w\,h_1^{\perp,g}\,\Delta_h^{[n]}\right] &= \int \mathrm{d}^2\boldsymbol{p}_T \int \mathrm{d}^2\boldsymbol{k}_T \delta^{(2)}(\boldsymbol{q}_T-\boldsymbol{p}_T-\boldsymbol{k}_T)\, w\,h_1^{\perp,g}(x,p_T^2;\mu^2)\,\Delta_h^{[n]}(k_T^2;\mu^2).\end{aligned} \tag{3.41}$$

with

$$w(\boldsymbol{p}_T,\boldsymbol{q}_T) = \frac{1}{m_p^2 q_T^2}\left[2\,(\boldsymbol{p}_T\cdot\boldsymbol{q}_T)^2 - \boldsymbol{p}_T^2\,\boldsymbol{q}_T^2\right], \tag{3.42}$$

as shown in Ref. [111]. Notice that the above convolutions depend on x, q_T^2 and μ^2. Moreover, as a consequence of ultraviolet and rapidity divergences, TMDs should depend on two scales, here both set equal to μ. In Eq. (3.41), we suppose a different shape function contributing to the structure function $\mathcal{F}_{UU}^{\cos 2\phi_\psi}$.

The evaluation of the above convolutions in the $\boldsymbol{q}_T \gg \Lambda_{\mathrm{QCD}}$ limit is more easily performed in the parameter (or b_T) space. We will mostly focus on the first convolution of Eq. (3.41), since at this order it is the only one allowing for the extraction of the TMDShF tail.

The Fourier transform of the unpolarized TMD distribution f_1^g is defined as

$$\begin{aligned}\hat{f}_1^g(x,b_T^2;\mu^2) &= \frac{1}{2\pi}\int \mathrm{d}^2\boldsymbol{p}_T\, \mathrm{e}^{i\,\boldsymbol{b}_T\cdot\boldsymbol{p}_T}\, f_1^g(x,p_T^2;\mu^2)\\ &= \int_0^\infty \mathrm{d}p_T\, p_T J_0(b_T\,p_T)\, f_1^g(x,p_T^2;\mu^2),\end{aligned} \tag{3.43}$$

while the Fourier transform of the TMDShF is given by

$$\hat{\Delta}^{[n]}(b_T^2;\mu^2) = \frac{1}{2\pi}\int \mathrm{d}^2\boldsymbol{k}_T\, \mathrm{e}^{i\,\boldsymbol{b}_T\cdot\boldsymbol{k}_T}\,\Delta^{[n]}(k_T^2;\mu^2). \tag{3.44}$$

From these, the first convolution in Eq. (3.41) in b_T-space takes the following form

$$\mathcal{C}\left[f_1^g\,\Delta^{[n]}\right](x,q_T^2;\mu^2) = \int \mathrm{d}^2\boldsymbol{b}_T\, \hat{f}_1^g(x,b_T^2;\mu^2)\,\hat{\Delta}^{[n]}(b_T^2;\mu^2). \tag{3.45}$$

The perturbative expansion of the unpolarized TMD distribution for $b_T \ll 1/\Lambda_{\mathrm{QCD}}$ is well known, *e.g.* Ref. [26], and reads

$$\hat{f}_1^g(x,b_T^2;\mu^2) = \frac{1}{2\pi}\sum_{a=q,\bar{q},g}\left(C_{g/a}\otimes f_1^a\right)(x;\mu_b^2)\,\mathrm{e}^{-\frac{1}{2}S_A(b_T^2;\mu^2)}. \tag{3.46}$$

The function f_1^a is the collinear parton distribution for a specific (anti)quark flavor or gluon, while the $C_{g/a}$'s are the (perturbative) matching coefficients between the TMD and the collinear PDFs. They can be expanded in series of α_s as follows

$$C_{g/a}(x;\mu_b) = \delta_{ga}\,\delta(1-x) + \sum_{k=1}^{\infty} C_{g/a}^{(k)}\left(\frac{\alpha_s(\mu_b)}{\pi}\right)^k, \tag{3.47}$$

where the scale $\mu_b = 2\mathrm{e}^{-\gamma_E}/b_T$ reduces the number of large logarithms in the expansion [136]. For those processes in which TMD factorization is valid, as SIDIS, the soft gluon radiation to all orders is included into an exponential Sudakov factor. In particular, its perturbative part S_A resums large logarithms of the type $\log(b_T\,\mu)$,

and at leading order is given by

$$S_A(b_T^2;\mu^2) = \frac{C_A}{\pi}\int_{\mu_b^2}^{\mu^2}\frac{\mathrm{d}\zeta^2}{\zeta^2}\alpha_s(\zeta)\left(\log\frac{\mu^2}{\zeta^2} - \frac{11-2\,n_f/C_A}{6}\right)$$
$$= \frac{\alpha_s}{2\,\pi}C_A\left(\log^2\frac{\mu^2}{\mu_b^2} - \frac{11-2\,n_f/C_A}{3}\log\frac{\mu^2}{\mu_b^2}\right). \tag{3.48}$$

Notice that the running of α_s is not considered in the last line, since its effect would enter at the next order.

Therefore, in the $b_T \ll \Lambda_{\rm QCD}$ region, the LO Fourier transform of the unpolarized TMD is given by

$$\hat{f}_1(x,b_T^2;\mu^2) = \frac{1}{2\pi}\Bigg\{f_1^g(x;\mu^2) - \frac{\alpha_s}{2\pi}\left(P_{gg}\otimes f_1^g + P_{gi}\otimes f_1^i\right)(x,\mu^2)\,\log\frac{\mu^2}{\mu_b^2}$$
$$- \frac{\alpha_s}{2\pi}\left(\frac{C_A}{2}\log^2\frac{\mu^2}{\mu_b^2} - \frac{11\,C_A-2\,n_f}{6}\log\frac{\mu^2}{\mu_b^2}\right)f_1^g(x;\mu^2)$$
$$+ \frac{\alpha_s}{\pi}\sum_a\left(C_{g/a}^{(1)}\otimes f_1^a\right)(x;\mu_b^2)\Bigg\}. \tag{3.49}$$

Note that the LO DGLAP equations (already applied previously), allows to evolve the collinear PDF, f_1^g, from the scale μ down to the other scale $\mu_b < \mu$ and introduce the same unpolarized splitting functions given in Eq. (3.36).

Plugging Eq. (3.49) into the convolution (3.45) and considering only terms up to the order α_s, we get

$$\mathcal{C}\left[f_1^g\,\Delta^{[n]}\right](x,q_T^2;\mu^2) = \frac{1}{(2\pi)}\int \mathrm{d}^2\boldsymbol{b}_T\,\mathrm{e}^{-i\,\boldsymbol{b}_T\cdot\boldsymbol{q}_T}\,\hat{\Delta}^{[n]}(b_T^2;\mu^2)$$
$$\times\Bigg\{f_1^g(x;\mu^2) - \frac{\alpha_s}{2\pi}\left(P_{gg}\otimes f_1^g + P_{gi}\otimes f_1^i\right)(x,\mu^2)\,\log\frac{\mu^2}{\mu_b^2}$$
$$- \frac{\alpha_s}{2\pi}\left(\frac{C_A}{2}\log^2\frac{\mu^2}{\mu_b^2} - \frac{11\,C_A-2\,n_f}{6}\log\frac{\mu^2}{\mu_b^2}\right)f_1^g(x;\mu^2)\Bigg\}, \tag{3.50}$$

where we have neglected the last term in Eq. (3.49) since it is subdominant for $b_T \ll \Lambda_{\rm QCD}$. Using the results

$$\int \mathrm{d}^2\boldsymbol{b}_T\,\mathrm{e}^{-i\,\boldsymbol{b}_T\cdot\boldsymbol{q}_T}\,\log^2\frac{\mu^2}{\mu_b^2} = -\frac{8\pi}{\boldsymbol{q}_T^2}\,\log\frac{\mu^2}{\boldsymbol{q}_T^2}, \quad \int \mathrm{d}^2\boldsymbol{b}_T\,\mathrm{e}^{-i\,\boldsymbol{b}_T\cdot\boldsymbol{q}_T}\,\log\frac{\mu^2}{\mu_b^2} = -\frac{4\pi}{\boldsymbol{q}_T^2}, \tag{3.51}$$

we can transform back to the momentum space, and compare the TMD structure functions with the corresponding collinear ones in the $\Lambda_{\rm QCD}^2 \leq \boldsymbol{q}_T^2 \leq \mu^2$ region. In particular, comparing the term that includes the splitting functions, we derive that, as expected, at leading order (α_s^0) the shape function corresponds to the LDME without any smearing effect. On the other hand, from the mismatch with the logarithmic

function L, we get the α_s-order correction. Finally, the perturbative tail of the TMDShF up to order α_s is

$$\hat{\Delta}^{[n]}(b_T^2;\mu^2) = \frac{1}{2\pi}\langle \mathcal{O}[n]\rangle \left[1 + \frac{\alpha_s}{2\pi} C_A \left(1 + \log \frac{\mu^2 M_\psi^2}{\left(M_\psi^2 + Q^2\right)^2}\right) \log \frac{\mu^2}{\mu_b^2}\right]. \tag{3.52}$$

In momentum space, the above equation reads

$$\Delta^{[n]}(k_T^2;\mu^2) = \langle \mathcal{O}[n]\rangle \left[\delta(\boldsymbol{k}_T^2) - \frac{\alpha_s}{2\pi^2\,\boldsymbol{k}_T^2} C_A \left(1 + \log \frac{\mu^2 M_\psi^2}{\left(M_\psi^2 + Q^2\right)^2}\right)\right]. \tag{3.53}$$

Moving to the second convolution of Eq. (3.41), involving the linearly polarized TMD distribution, it is possible to verify that $\mathcal{F}_{UU}^{\cos 2\phi_\psi}$ matches with the corresponding collinear quantity $F_{UU}^{\cos 2\phi_\psi}$ in the intermediate region, without the necessity to include any smearing effect. Notice that, differently from f_1^g, $h_1^{\perp,g}$ disappears in the collinear limit, so the equivalent expression of Eq. (3.47) for $h_1^{\perp,g}$ starts already at order α_s . Indeed, the dominant term of the $h_1^{\perp,g}$ perturbative tail follows a DGLAP-like equation [130]

$$\frac{q_T^2}{2m_p^2} h_1^{\perp,g}(x,q_T^2;\mu^2) = \frac{\alpha_s}{\pi^2}\frac{1}{q_T^2}\sigma_{UU}^{\cos 2\phi_\psi}\left(\delta P_{gg}\otimes f_1^g + \delta P_{gi}\otimes f_1^i\right)(x,\mu^2). \tag{3.54}$$

Ultimately, the equivalence $\mathcal{F}_{UU}^{\cos 2\phi_\psi} = F_{UU}^{\cos 2\phi_\psi}$ precludes the possibility to extract any new information on the TMDShF $\Delta_h^{[n]}$. This would require a complete calculation at $\alpha^2\alpha_s^3$ within the NRQCD approach, still lacking at the moment.

3.2 TMD shape functions for J/ψ polarization in SIDIS

In this section we discuss the corresponding derivation of the TMDShFs in the study of J/ψ polarization.

Notice that the kinematics involved when explicitly including the J/ψ decay and the angular distribution of its decay products are the same as for the unpolarized case. Consequently, the expansion of the Dirac-delta function in Eq. (3.22) applies. Moreover, in the gluon induced CO channel, the pole structure described in Sec. 3.1.2 appears, leading to the effective Dirac-delta function in Eq. (3.32).

In the end, the behavior of the collinear helicity structure functions in the small-q_T limit is very similar to what discussed in the previous section, namely

$$\begin{aligned}
\mathcal{W}_L^{\perp} &= \frac{\alpha_s}{2\pi^2 \boldsymbol{q}_T^2}\widetilde{w}_L^{\perp}\left[L\left(\frac{\mu^2}{\boldsymbol{q}_T^2}\right) f_1^g(x,\mu^2) + \left(P_{gg}\otimes f_1^g + P_{gi}\otimes f_1^i\right)(x,\mu^2)\right] + \mathcal{O}\left(\frac{|\boldsymbol{q}_T|}{\mu}\right), \\
\mathcal{W}_T^{\perp} &= \frac{\alpha_s}{2\pi^2 \boldsymbol{q}_T^2}\widetilde{w}_T^{\perp}\left[L\left(\frac{\mu^2}{\boldsymbol{q}_T^2}\right) f_1^g(x,\mu^2) + \left(P_{gg}\otimes f_1^g + P_{gi}\otimes f_1^i\right)(x,\mu^2)\right] + \mathcal{O}\left(\frac{|\boldsymbol{q}_T|}{\mu}\right), \\
\mathcal{W}_{\Delta\Delta}^{\perp} &= \frac{\alpha_s}{\pi^2 \boldsymbol{q}_T^2}\widetilde{w}_{\Delta\Delta}^{\perp}\left(\delta P_{gg}\otimes f_1^g + \delta P_{gi}\otimes f_1^i\right)(x,\mu^2) + \mathcal{O}\left(\frac{|\boldsymbol{q}_T|}{\mu}\right), \\
\mathcal{W}_L^{\parallel} &= \frac{\alpha_s}{2\pi^2 \boldsymbol{q}_T^2}\widetilde{w}_L^{\parallel}\left[L\left(\frac{\mu^2}{\boldsymbol{q}_T^2}\right) f_1^g(x,\mu^2) + \left(P_{gg}\otimes f_1^g + P_{gi}\otimes f_1^i\right)(x,\mu^2)\right] + \mathcal{O}\left(\frac{|\boldsymbol{q}_T|}{\mu}\right),
\end{aligned} \tag{3.55}$$

where $\widetilde{w}_\Lambda^{\mathcal{P}}$ are the same quantities appearing in Eq. (2.107) and the light-cone momentum fraction is fixed at $x = x_B/\hat{x}_{\max}$. Furthermore, the logarithmic function $L(\mu^2/\boldsymbol{q}_T^2)$ is defined as in Eq. (3.35), while P_{ab} and δP_{ab} are the splitting functions in Eqs. (3.36) and (3.37).

Similarly, the TMD evolved results can be derived from the expressions in Sec. 2.4, substituting the naive TMD-PDFs with their convolutions with the TMDShFs. Explicitly, the leading-twist helicity structure functions at small transverse momentum are given by

$$\begin{aligned}
\widetilde{W}_L^{\perp} &= 2\,(4\pi)^2 \frac{\alpha\alpha_s e_c^2}{M_\psi\left(M_\psi^2+Q^2\right)}\left(\frac{1}{3}\mathcal{C}\left[f_1^g\,\Delta_L^{[^1S_0^{(8)}]}\right] + \frac{4}{M_\psi^2}\mathcal{C}\left[f_1^g\,\Delta_L^{[^3P_0^{(8)}]}\right]\right), \\
\widetilde{W}_T^{\perp} &= 2\,(4\pi)^2 \frac{\alpha\alpha_s e_c^2}{M_\psi\left(M_\psi^2+Q^2\right)}\left(\frac{1}{3}\mathcal{C}\left[f_1^g\,\Delta_T^{[^1S_0^{(8)}]}\right] + \frac{4}{M_\psi^2}\frac{3M_\psi^4+Q^4}{(M_\psi^2+Q^2)^2}\mathcal{C}\left[f_1^g\,\Delta_T^{[^3P_0^{(8)}]}\right]\right), \\
\widetilde{W}_{\Delta\Delta}^{\perp} &= -16\,(4\pi)^2 \frac{\alpha\alpha_s e_c^2}{M_\psi\left(M_\psi^2+Q^2\right)^2}\mathcal{C}\left[w\,h_1^{\perp,g}\,\Delta_{\Delta\Delta}^{[^3P_0^{(8)}]}\right], \\
\widetilde{W}_L^{\parallel} &= 128\,(4\pi)^2 \frac{\alpha\alpha_s e_c^2\,Q^2}{M_\psi\left(M_\psi^2+Q^2\right)^3}\mathcal{C}\left[f_1^g\,\Delta_L^{[^3P_0^{(8)}]}\right],
\end{aligned} \tag{3.56}$$

with the convolution defined as in Eq. (3.41). In addition, we have included an extra subscript that relates the TMDShF to the J/ψ polarization state. By comparing Eqs. (3.55) and (3.56) in the intermediate region, we can then obtain the perturbative tail of the TMDShF. As shown in Ref. [112], we find that $\Delta_T^{[n]}$ and $\Delta_L^{[n]}$ are independent of the J/ψ polarization state and they actually coincide with the unpolarized case, namely $\Delta_T^{[n]} = \Delta_L^{[n]} \equiv \Delta^{[n]}$, with the latter defined in Eq. (3.53). Once again, since the perturbative expansion of $h_1^{\perp,g}$ starts at α_s, it is not possible to determine the $\Delta_{\Delta\Delta}^{[n]}$ tail at this order.

The inclusion of smearing effects may have important consequences on the study of both the unpolarized and polarized sectors. Indeed, the structure functions defined in Eq. (3.56) substitute those in Eq. (2.106), since the latter involve the partonic process in Eq. (2.107). Thus, the effect from the TMDShF may be observed in figures like Fig. 2.12. Indeed, while up to order α_s the perturbative tails of the TMDShFs seem to be independent of J/ψ polarization, it may not be true in general. In this

case, a deviation in the λ behaviour (upper panel of Fig. 2.12) can be a hint of nonperturbative effects from the TMDShF. The analysis of the ν parameter (lower panel of Fig. 2.12) can be even more effective. Since TMDShFs for different J/ψ polarization states appear in its numerator and denominator, their (potentially) different nonperturbative behaviours could be less suppressed, resulting in a sizeable effect. On the other hand, we have to remark that ν depends also on other quantities, that are poorly known and can be a further source of uncertainties. We are referring to the linearly polarized gluon distribution $h_1^{\perp,g}$ and the LDME parameters, whose expected universality is still an open issue from the phenomenological point of view. Further studies on these aspects are certainly worth and necessary.

Once again, data in the region of validity of the TMD approach, potentially covered by the planned EIC, are highly valuable to deeply understand the TMD factorization in quarkonium production.

Chapter 4

Single-spin asymmetries within the Generalized Parton Model and its Color-Gauge Invariant extension

At variance with previous chapters, here we discuss the (more) inclusive J/ψ production in proton-proton collisions.

In particular, we are interested in studying the Single-Spin Asymmetry observable; this quantity can be measured if one of the initial protons is transversely polarized, namely via the process $p\,p^{\uparrow} \to J/\psi + X$. Due to the lack of a formal TMD factorization proof for pp collisions, a phenomenological approach, called Generalized Parton Model [61–63], was proposed, being quite successful in describing SSA data for light-meson production.

So far, phenomenological studies within the GPM have been focused on quark distributions [76, 77, 80, 81]. Nevertheless, our interest is to explore the gluon content of nucleons, too. This information is accessible considering processes that involve quarkonia, as shown in Refs. [30, 137–139]. In particular, one can potentially access the gluon Sivers function (GSF) from SSA for quarkonium production in inclusive processes. The PHENIX Collaboration provided data points for this observable in Ref. [42], but unfortunately they are not enough to perform a fit. Nevertheless, one can try to extract some constraints on the GSF by comparing this data set with SSA estimates, computed by maximizing TMD effects.

In this chapter, we will continue to adopt the NRQCD approach and compare its predictions with the CSM, to deeply understand the role of CO contributions. Moreover, we will use both the GPM and its Color-Gauge Invariant (CGI) extension. The latter, proposed in Ref. [85] and further developed in Refs. [137, 138, 140], assumes TMD factorization as in the GPM, but with the inclusion of initial- and final-state interactions. Although other formalisms can produce sizeable asymmetries, in this thesis we keep adopting the aforementioned phenomenological approaches, since we are interested in providing a coherent description in terms of TMDs.

This chapter is structured as follows. First in Sec. 4.1 we present some key features of the GPM and its application to SSAs. In Sec. 4.2 we introduce the formal steps to properly include initial- and final-state interactions, leading to the formulation of the CGI-GPM approach; in this context different cases will be considered, including quarkonium production in proton-proton collisions. Finally, in Sec. 4.3 we adopt these two approaches to provide numerical estimates of Single-Spin Asymmetries, comparing them to PHENIX data and giving useful predictions for upcoming experiments.

4.1 GPM: a phenomenological approach

In this section we present the phenomenological approach known as the Generalized Parton Model, adopting the helicity formalism. A more exhaustive treatment of the model can be found in Ref. [63], while in Ref. [141] some more recent phenomenological applications to pp processes are discussed.

In the GPM approach, we assume that a cross section can be written in a factorized form in terms of unintegrated TMD parton and fragmentation functions convoluted with elementary hard parts. The direct inclusion of spin and transverse momentum effects into these functions follows the spirit of the parton model itself, maintaining a simple interpretation in terms of partons. In the GPM, differently from the TMD factorization approach, the transverse momentum of partons are kept also in the hard parts, reproducing some kinematic higher-twist effects. Moreover, within this approach, it is possible to include partonic channels beyond the leading ones, as will be done in the following for $p\,p \to J/\psi + X$.

In Sec. 4.1.1 we present some key points of this model adopting the helicity formalism with the inclusion of TMD effects and show how helicity distributions so defined are directly related to ordinary TMDs. In particular, we will limit to the one of interest in our study, namely the Sivers distribution. In Sec. 4.1.2 we discuss SSAs and how they can be evaluated within the GPM formalism.

4.1.1 Helicity Formalism

The helicity formalism allows the evaluation of scattering amplitudes and cross sections via the decomposition into helicity states. This method, developed in the collinear framework, can be easily extended to the TMD formalism. In the following we focus explicitly on its use in inclusive quarkonium production.

The cross section for the process $p\,p \to J/\psi + X$, where the initial protons are in a momentum-spin configuration equal to P_A, S_A and P_B, S_B, within the GPM is schematically given by

$$E_Q \frac{\mathrm{d}\sigma}{\mathrm{d}^3 P_Q} = \sum_{\{\lambda\}} \int \frac{\mathrm{d}\xi_a\,\mathrm{d}\xi_b}{16\,\pi^2 \hat{s}}\,\mathrm{d}^2\boldsymbol{p}_{\perp a}\,\mathrm{d}^2\boldsymbol{p}_{\perp b} \times \rho^{a/p_{S_A}}_{\lambda_a,\lambda'_a} f_{a/p_{S_A}}(\xi_a, \boldsymbol{p}_{\perp a})\,\rho^{b/p_{S_B}}_{\lambda_b,\lambda'_b} f_{b/p_{S_B}}(\xi_b, \boldsymbol{p}_{\perp b})\,\mathrm{d}\hat{\sigma}_{\{\lambda\}}. \tag{4.1}$$

The explicit sum over $\{\lambda\}$ corresponds to a sum over all helicity configurations, while $\mathrm{d}\hat{\sigma}_{\{\lambda\}}$ is a shorthand notation for the helicity partonic cross section (more precisely a product of helicity scattering amplitudes)

$$\mathrm{d}\hat{\sigma}_{\{\lambda\}} = \mathcal{M}_{\{\lambda\}}\mathcal{M}^*_{\{\lambda'\}}\,\delta(\hat{s} + \hat{t} + \hat{u} - M_\psi^2), \tag{4.2}$$

where M_ψ is the J/ψ mass, which is the only massive particle in the process. For simplicity, in Eq. (4.1) we omitted the sum over partons. Since we are specifically interested in quarkonium production, the hard part must include also the quarkonium formation process. In the next section we will consider J/ψ production either within the Color Singlet Model (CSM) or the Non-relativistic QCD (NRQCD) approach. For the same reason, a helicity fragmentation function does not appear in Eq. (4.1), as happens in the master formula for light-meson production [63].

The main element in Eq. (4.1) is the helicity density matrix $\rho^{a/A_{S_A}}_{\lambda_a,\lambda'_a}$, describing the polarization state of a parton a in its rest-frame, defined as its *helicity-frame* [142]. In

particular, the quantity $\rho^{a/A_{S_A}}_{\lambda_a,\lambda'_a} f_{a/A_{S_A}}(\xi_a, \boldsymbol{p}_{\perp a})$ includes all information relative to the polarization of the parton a inside a polarized parent hadron A (in this case a proton) with spin-polarization S_A.

It is nevertheless more convenient to express the helicity density matrix in terms of measurable quantities. We then introduce the soft, nonperturbative, helicity amplitudes $\mathcal{F}_{\lambda_a,\lambda_X;\lambda_A}$ for the process $A \to a + X$, and their products $F^{\lambda_a,\lambda'_a}_{\lambda_A,\lambda'_A}$

$$\begin{aligned}\rho^{a/A_{S_A}}_{\lambda_a,\lambda'_a} f_{a/A_{S_A}}(\xi_a, \boldsymbol{p}_{\perp a}) &= \sum_{\lambda_A,\lambda'_A} \rho^{A_{S_A}}_{\lambda_A,\lambda'_A} \sum\!\!\!\!\!\!\int_{X,\lambda_X} \mathcal{F}_{\lambda_a,\lambda_X;\lambda_A}\, \mathcal{F}^*_{\lambda'_a,\lambda_X;\lambda'_A} \\ &= \sum_{\lambda_A,\lambda'_A} \rho^{A_{S_A}}_{\lambda_A,\lambda'_A} F^{\lambda_a,\lambda'_a}_{\lambda_A,\lambda'_A}(\xi_a, \boldsymbol{p}_{\perp a}),\end{aligned} \tag{4.3}$$

where in the first line $\sum\!\!\!\!\!\!\int_{X,\lambda_X}$ stands for the spin sum and the phase space integration with respect to the undetected system produced by A remnants.

These distributions depend on the light-cone momentum fraction ξ_a and its transverse momentum $\boldsymbol{p}_{\perp a}$, where the azimuthal dependence can be factorized as

$$F^{\lambda_a,\lambda'_a}_{\lambda_A,\lambda'_A}(\xi_a, \boldsymbol{p}_{\perp a}) = F^{\lambda_a,\lambda'_a}_{\lambda_A,\lambda'_A}(\xi_a, |\boldsymbol{p}_{\perp a}|)\, \mathrm{e}^{i(\lambda_A - \lambda'_A)\phi_a}. \tag{4.4}$$

Moreover, they fulfill the parity transformation property

$$F^{-\lambda_a,-\lambda'_a}_{-\lambda_A,-\lambda'_A}(\xi_a, |\boldsymbol{p}_{\perp a}|) = \mathrm{e}^{i\pi((\lambda_A-\lambda'_A)+(\lambda_a-\lambda'_a))}\, F^{\lambda_a,\lambda'_a}_{\lambda_A,\lambda'_A}(\xi_a, |\boldsymbol{p}_{\perp a}|), \tag{4.5}$$

analogous to the corresponding helicity distributions in the fragmentation sector [143]. These conditions reduce the number of independent complex quantities to six distributions, $F^{\lambda_a,\lambda'_a}_{\lambda_A,\lambda'_A}$, namely

$$F^{++}_{++}, \quad F^{++}_{--}, \quad F^{+-}_{+-}, \quad F^{-+}_{+-}, \quad F^{++}_{+-}, \quad F^{+-}_{++}, \tag{4.6}$$

where the $\pm$ superscripts correspond to $\pm 1/2$ for (anti)quarks and to ± 1 for gluons, while the subscripts are $\pm 1/2$ for a spin-1/2 hadron. In particular, the first two, F^{++}_{++} and F^{++}_{--}, are moduli squared, while F^{+-}_{+-} and F^{-+}_{+-} are purely imaginary (real) for gluons (quarks).

The helicity density matrix for a spin-1/2 hadron, in the left-hand side of Eq. (4.3), can be decomposed as

$$\rho^{A_{S_A}}_{\lambda_A,\lambda'_A} = \frac{1}{2}\begin{pmatrix} 1 + S_{AL} & S_{AT}\, \mathrm{e}^{-i\phi_{S_A}} \\ S_{AT}\, \mathrm{e}^{i\phi_{S_A}} & 1 - S_{AL} \end{pmatrix}, \tag{4.7}$$

where S_{AT} and S_{AL} are the transverse and longitudinal components of the polarization three-vector $\boldsymbol{S}_A$, while ϕ_{S_A} is its azimuthal angle,

$$\boldsymbol{S}_A = (S_{AT}\cos\phi_{S_A},\, S_{AT}\sin\phi_{S_A}, S_{AL})\,. \tag{4.8}$$

The same matrix form is found, in terms of the corresponding partonic polarization components S_{aL} and S_{aT}, for quarks and antiquarks

$$\rho^{a/A_{S_A}}_{\lambda_a,\lambda'_a} = \frac{1}{2}\begin{pmatrix} 1 + S_{aL} & S_{aT}\, \mathrm{e}^{-i\phi_{S_a}} \\ S_{aT}\, \mathrm{e}^{i\phi_{S_a}} & 1 - S_{aL} \end{pmatrix}_{A_{S_A}}, \tag{4.9}$$

while a similar one is also valid for gluons, where the role of longitudinal and transverse polarizations are substituted by circular $S^g_{\rm circ}$ and linear $S^g_{\rm lin}$ ones, respectively,

$$\rho^{g/A_{S_A}}_{\lambda_g,\lambda'_g} = \frac{1}{2}\begin{pmatrix} 1+S^g_{\rm circ} & -S^g_{\rm lin}\, e^{-i\phi_{S_a}} \\ -S^g_{\rm lin}\, e^{i\phi_{S_a}} & 1-S^g_{\rm circ}\end{pmatrix}_{A_{S_A}}. \tag{4.10}$$

It is worth noticing that all polarization directions are defined in their proper helicity frames.

Combining the matrix form in Eq. (4.7) with the corresponding one of the parton in Eq. (4.3), one can connect the distributions $F^{\lambda_a,\lambda'_a}_{\lambda_A,\lambda'_A}$ to the more common TMDs. For our discussion, we explicitly mention the relation with the fully unpolarized TMD f_1 (unpolarized parton distribution inside an unpolarized spin-1/2 hadron) and the Sivers distribution function $\Delta^N f_{a/p^\uparrow}$ (unpolarized parton distribution inside a transversely polarized spin-1/2 hadron)

$$\begin{aligned} f_1(\xi_a,|\boldsymbol{p}_{\perp a}|) &= F^{++}_{++}(\xi_a,|\boldsymbol{p}_{\perp a}|) + F^{++}_{--}(\xi_a,|\boldsymbol{p}_{\perp a}|), \\ \Delta^N f_{q/p^\uparrow}(\xi_a,|\boldsymbol{p}_{\perp a}|) &= -2\,\mathrm{Im}\left[F^{+-}_{++}(\xi_a,|\boldsymbol{p}_{\perp a}|)\right]. \end{aligned} \tag{4.11}$$

In the above expressions we have used the Torino-Cagliari notation, related to the Amsterdam one as [144]

$$\Delta^N f_{a/p^\uparrow} = \left(-2\frac{|\boldsymbol{p}_{\perp a}|}{m_p}\right) f_{1T}^{\perp a}, \tag{4.12}$$

where m_p is the proton mass.

4.1.2 SSAs for quarkonium production within the GPM approach

For inclusive particle production in proton-proton collisions, with a proton transversely polarized w.r.t. the production plane, the SSA is defined as

$$A_N = \frac{d\sigma^\uparrow - d\sigma^\downarrow}{d\sigma^\uparrow + d\sigma^\downarrow} = \frac{d\Delta\sigma}{2\,d\sigma}, \tag{4.13}$$

where the arrows $\uparrow$ and $\downarrow$ refer to the two possible polarization directions, while $d\sigma$ is the unpolarized differential cross section.

According to Eq. (4.1), to compute the differential cross sections entering Eq. (4.13), we have to consider the following kernel

$$K(S_A,S_B) = \sum_{\{\lambda\}} \rho^{a/p_{S_A}}_{\lambda_a,\lambda'_a} f_{a/p_{S_A}}\, \rho^{b/p_{S_B}}_{\lambda_b,\lambda'_b} f_{b/p_{S_B}}\, \mathcal{M}_{\{\lambda\}}\mathcal{M}^*_{\{\lambda'\}}. \tag{4.14}$$

If we take the proton A transversely polarized and the proton B unpolarized, the numerator in Eq. (4.13) is related to the difference $[K(\uparrow,0) - K(\downarrow,0)]$, while the denominator is related to the sum $[K(\uparrow,0) + K(\downarrow,0)]$. Helicity conservation and parity reduce the number of independent helicity amplitude $\mathcal{M}_{\{\lambda\}}$. In particular, for a subprocess of the type $a\,b \to c\,d$, we have only three independent amplitudes, corresponding to $\mathcal{M}_{++;++}$, $\mathcal{M}_{-+;-+}$ and $\mathcal{M}_{-+;+-}$, see *e.g.* Ref. [64].

Formally, by summing over the parton helicity, the SSA for the process $p\,p^\uparrow \to J/\psi + X$, could receive contributions from different TMD effects. Among them, the main contribution comes from the Sivers distribution, $\Delta^N f_{a/p^\uparrow}$, combined with the

unpolarized TMD, f_1, and the unpolarized partonic cross sections. Another potential source involves the transversity (in the polarized proton) and the Boer-Mulders (in the unpolarized proton) distributions, coupled to a double-spin partonic asymmetry; however, by integration over the partonic variables, this turns to be strongly suppressed, as explicitly checked for inclusive light meson production.[1] Since we are considering quarkonium production within the CSM or the NRQCD approach, the channel driven by the Collins fragmentation function [145] is absent.

Taking into account these arguments, the numerator of the asymmetry within the GPM is given by

$$\begin{aligned} \mathrm{d}\Delta\sigma^{2\to 2} = & \frac{1}{2(2\pi)^2}\frac{1}{2s}\int \frac{\mathrm{d}\xi_a}{\xi_a}\frac{\mathrm{d}\xi_b}{\xi_b}\mathrm{d}^2\boldsymbol{p}_{\perp a}\mathrm{d}^2\boldsymbol{p}_{\perp b} \\ & \times \Delta^N f_{a/p^\uparrow}(\xi_a, |\boldsymbol{p}_{\perp a}|)\, f_1^b(\xi_b, |\boldsymbol{p}_{\perp b}|)\, \cos\phi_a\, \mathrm{d}\hat{\sigma}, \end{aligned} \tag{4.15}$$

while the denominator involves only unpolarized TMD distributions

$$\mathrm{d}\sigma^{2\to 2} = \frac{1}{2(2\pi)^2}\frac{1}{2s}\int \frac{\mathrm{d}\xi_a}{\xi_a}\frac{\mathrm{d}\xi_b}{\xi_b}\mathrm{d}^2\boldsymbol{p}_{\perp a}\mathrm{d}^2\boldsymbol{p}_{\perp b}\, f_1^a(\xi_a, |\boldsymbol{p}_{\perp a}|)\, f_1^b(\xi_b, |\boldsymbol{p}_{\perp b}|)\, \mathrm{d}\hat{\sigma}. \tag{4.16}$$

In Sec. 4.3.3 we will present numerical estimates based on the previous formulae.

4.2 The Color Gauge Invariant - Generalized Parton Model

Despite several phenomenological achievements, the Generalized Parton Model has some intrinsic assumptions. Among them, here we recall that the Sivers function, $\Delta^N f_{a/p^\uparrow}$, in the GPM is universal by definition, being the same in any process. On the other hand, when one derives the TMD factorization in SIDIS and DY processes, the formal definition of the Sivers distribution manifests a process dependence.

In Refs. [146, 147] it has been shown how the interaction between the struck parton (a quark/antiquark or a gluon) and the proton remnants plays a significant role in the evaluation of SSAs. This effect can be described via a gauge link, whom explicit form depends on the process. As a consequence, the Sivers function itself becomes process dependent. In particular, a sign change is expected for the Sivers function when moving from SIDIS to DY processes.

This property is usually called *modified universality*, and it has been widely discussed, *e.g.* in the seminal articles [148, 149], but is still lacking an experimental confirmation.

In order to include a potential process dependence also in inclusive processes, following the same approach adopted in SIDIS and DY, a modified version of the GPM, named Color Gauge Invariant Generalized Parton Model (CGI-GPM or CGI for short), has been developed [85, 137, 138, 140]. The CGI approach, while keeping the fundamental features of the GPM, includes also initial- and final-state interactions (ISIs and FSIs), making the Sivers function process dependent. This process dependence can be absorbed into a redefinition of the hard parts: in this case, the modified hard parts show a close connection with the corresponding ones appearing in the twist-3 formalism.

In this section we present how ISIs and FSIs can be properly included in different processes, starting from DY and SIDIS ones. These two processes, indeed, allow

[1] Since for quarkonium production we have a subset of the same partonic subprocesses, we expect the same kind of suppression.

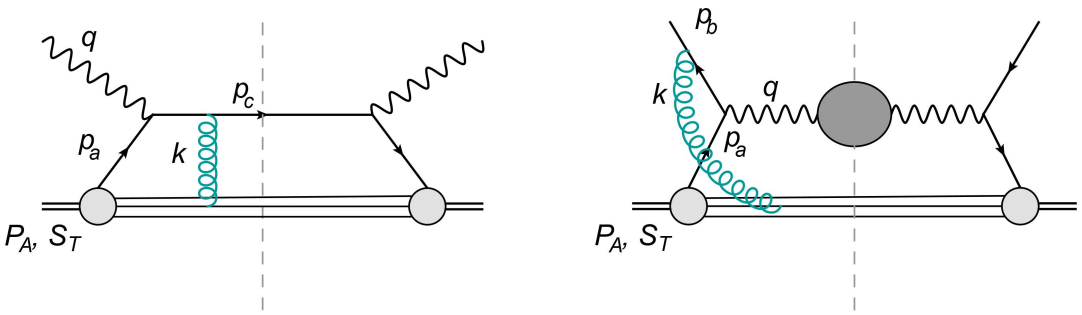

FIGURE 4.1: Representative diagrams in the CGI approach for SIDIS (on the left) and DY (on the right) processes in one-gluon-exchange approximation. The colored gluon, connecting the proton remnants to one of the partons, describes the FSI or ISI.

us to rederive the expected sign change of the quark Sivers function, as well as to understand how to include the process dependence in the hard parts.

As a second step, we consider the $q\,g \to q\,\gamma$ subprocess, relevant for accessing the gluon Sivers function in pp collisions. In this case, we will also discuss the role of FSIs from the (unobserved) quark in the final state.

Finally, we focus explicitly on the $p^\uparrow p \to J/\psi + X$ process, computing the ISIs involving a hard gluon and showing how FSIs behave in quarkonium production. To describe the hadronization mechanism we will adopt two approaches: the Color-Singlet Model and the Non-relativistic QCD framework. Notice that we will only recall some of their main properties, relevant in our discussion. More details on the CSM can be found in the seminal works [150, 151], while for the NRQCD approach we refer the reader to Ref. [6]. Some useful relations are collected in Appendix A, too.

Before entering into the main aspects of this derivation, it is worth spending few words on the notation. For the hard parts, we will use here and in the following the symbol $\mathcal{H}$, which corresponds to a partonic amplitude squared. This notation is much closer to the one commonly found in the literature, but different to the one adopted in Appendix B. Moreover, in the following derivation we will continue employing the Cagliari-Torino notation for the Sivers function. This choice is different from what usually adopted in the literature, where the Amsterdam notation is preferred. The two notations can be easily connected, see Eq. (4.12).

4.2.1 Initial- and Final-state interactions

In this section we discuss how one can compute initial- and final-state interactions for the process under consideration, referring the reader to Refs. [85, 137] for further details.

Quark Sivers function

We start considering the computation of ISIs and FSIs for two standard processes, namely SIDIS and DY. The leading order (LO) approximation is shown in Fig. 4.1, corresponding to a single-gluon exchange. The gluon line connects, along one of the light-cone directions, the proton remnants and a parton, which is either coming from the other hadron or produced in the final state. The former corresponds to a ISI, while the latter to a FSI.

In order to study the role of the extra gluon, we adopt the eikonal approximation, in which the exchanged gluon is longitudinally polarized. In particular, by using

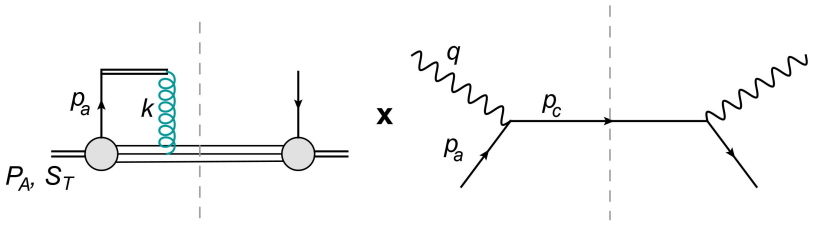

FIGURE 4.2: Visual factorization between the hard SIDIS amplitude and the TMD-PDF within its gauge-invariant definition at leading order.

the light-cone components, the gluon field is dominated by A^+. The extra gluon modifies how the particle (antiparticle) spinor $u(p)$ ($v(p)$) is connected to the rest of the diagram. More explicitly, the spinors, in the two cases, undergo the following replacement

$$\begin{aligned}
\text{SIDIS (FSI)}: \quad \bar{u}(p_c) &\to \bar{u}(p_c)\,(-ig\gamma^- t^a)\,i\frac{\not{p}_c - \not{k}}{(p_c-k)^2+i\epsilon} \\
&\approx \bar{u}(p_c)\left[gt^a\frac{\gamma^-\not{p}_c}{-2p_c^- k^+ + i\epsilon}\right] \\
&\approx \bar{u}(p_c)\left[gt^a\frac{2p_c^- - \not{p}_c\gamma^-}{-2p_c^- k^+ + i\epsilon}\right] \\
&\approx \bar{u}(p_c)\left[\frac{g}{-k^+ + i\epsilon}t^a\right], \qquad (4.17) \\
\text{DY (ISI)}: \quad \bar{v}(p_b) &\to \bar{v}(p_b)\,(-ig\gamma^- t^a)\,(-i)\frac{\not{p}_b + \not{k}}{(p_b+k)^2+i\epsilon} \\
&\approx \bar{v}(p_c)\left[-\frac{g}{k^+ + i\epsilon}t^a\right]. \qquad (4.18)
\end{aligned}$$

In the eikonal approximation, in the interaction vertex only the γ^- matrix appears. Moreover, since we are interested in the propagator pole, given by $k^+ = 0$, we can neglect this term in the numerator and impose the on-shell condition ($p_b^2 \wedge p_c^2 \wedge k^2 = 0$) whenever possible. Finally, via the massless Dirac equations $\bar{u}(p_c)\not{p}_c = 0$ and $\bar{v}(p_b)\not{p}_b = 0$, we obtain the squared brackets in the last lines of Eqs. (4.17) and (4.18). Notice that, since the eikonal gluon comes from a quark/antiquark, the Gell-Mann matrix T^a is in the fundamental representation t^a, with a being the (eikonal) gluon color index. The transformation rules obtained in Eqs. (4.17) and (4.18) can be seen as the first order expansion of the gauge-invariant definition of a TMD-PDF. The first non-trivial order for SIDIS is shown in Fig. 4.2.

To get the proper factorized expression, one should further expand Eqs. (4.17) and (4.18) in the *principal value* $\mathcal{P}$ and the imaginary part

$$\frac{1}{k^+ \pm i\epsilon} = \mathcal{P}\frac{1}{k^+} \mp i\pi\delta(k^+). \qquad (4.19)$$

Since this factor is contracted with the Born amplitude, only the second term survives. In the end, the particle and antiparticle spinors transform in the following way

$$\begin{aligned}
\text{SIDIS (FSI)}: \quad \bar{u}(p_c) &\to (-i\pi g)\,t^a\,\bar{u}(p_c)\,\delta(k^+), \\
\text{DY (ISI)}: \quad \bar{v}(p_b) &\to (+i\pi g)\,t^a\,\bar{v}(p_c)\,\delta(k^+). \qquad (4.20)
\end{aligned}$$

The different sign in the imaginary part between Eqs. (4.17) and (4.18) is directly related to a sign change between the Sivers function entering in SIDIS and DY processes. It is possible to prove that this relation holds at all orders, using parity and time reversal arguments, and that the two (T-odd) functions involve gauge links pointing in opposite directions, Ref. [152].

The presence of an extra T^a matrix (given by t^a in the fundamental representation) also modifies how the color flows through the diagram. When the eikonal gluon interacts with the proton remnants, this color must be neutralized. This operation is achieved by a proper projection.

Following the method developed in Refs. [49, 50, 52, 153], the color projector can be defined as

$$\mathcal{C}^a_{ij} = \mathcal{N}_{\mathcal{C}}\, t^a_{ij}, \tag{4.21}$$

where its normalization is

$$\mathcal{N}_{\mathcal{C}} = \mathrm{Tr}\left[t^a t^a\right]^{-1} = \frac{2}{N_c^2 - 1}. \tag{4.22}$$

If denote by C_U the unpolarized color factor, obtained without any extra eikonal gluon, we can introduce C_I and C_F for the color factors obtained when ISIs and FSIs are present, respectively. The appearance of the modified color factor C_I and/or C_F leads to the process dependence of the asymmetry.

This dependence can be ultimately absorbed in the definition of the Sivers function, leading to its modified universality property. At variance with this choice, within the CGI approach we can show that this dependence can also be absorbed into the hard parts. In the first case we have a different Sivers function for each process, *e.g.* $\Delta^N f^{\mathrm{SIDIS}}_{a/A^\uparrow}$ and $\Delta^N f^{\mathrm{DY}}_{a/A^\uparrow}$, with a simple relation between them, at least within the one-gluon-exchange approximation. In the second case we can introduce a process-dependent version of the hard scattering part, keeping the Sivers formally universal, as it is usually adopted in the GPM. In the following we describe how to relate these two choices.

Let us consider the unpolarized hard part of DY, namely $|\mathcal{M}^U_{\mathrm{DY}}|^2 \equiv \mathcal{H}^U_{\mathrm{DY}}$. We know that this is given by the corresponding partonic reduced hard term, h_{DY}, which does not include the color factor, multiplied by the unpolarized color factor C_U. The partonic hard part in DY is the same as the leptonic inhomogeneous scattering $l^+l^- \to l'^+l'^-$ (*e.g.* $e^+e^- \to \mu^+\mu^-$), with the inclusion of an average over colors. This implies

$$h_{\mathrm{DY}} = \frac{e_q^2\,(4\pi\alpha)^2}{3\,\hat{s}}, \quad C_U = \frac{1}{N_c}. \tag{4.23}$$

When ISIs are included, the color factor modifies in

$$C_I^{\mathrm{DY}} = -\mathcal{C}^a_{ij}\, t^a_{ji} \times C_U = -C_U. \tag{4.24}$$

The minus sign can be absorbed into a process-dependent Sivers function, leading to

$$\Delta^N f^{\mathrm{DY}}_{a/A^\uparrow} = \frac{C_I^{\mathrm{DY}}}{C_U}\Delta^N f_{a/A^\uparrow} = -\Delta^N f^{\mathrm{SIDIS}}_{a/A^\uparrow}, \tag{4.25}$$

where we have defined the general Sivers function in one-gluon approximation as $\Delta^N f_{a/A^\uparrow} \equiv \Delta^N f^{\mathrm{SIDIS}}_{a/A^\uparrow}$. Alternatively, we can introduce the process-dependent hard part $\mathcal{H}^{\mathrm{Inc}}$. For DY, where only ISIs are present, we can use a more complete notation

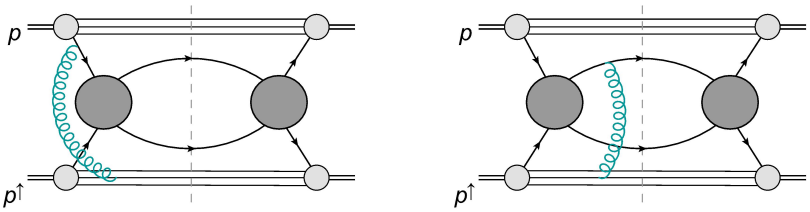

FIGURE 4.3: $q\,q' \to q\,q'$ process within the CGI-GPM approach: ISIs *and* FSIs at work.

$\mathcal{H}_{\rm DY}^{\rm Inc-I}$. This new hard part is related to $h_{\rm DY}$ via

$$\mathcal{H}_{\rm DY}^{\rm Inc-I} = \frac{C_I^{\rm DY}}{C_U}\mathcal{H}_{\rm DY}^{U} = C_I^{\rm DY} h_{\rm DY}. \tag{4.26}$$

In this case the Sivers function keeps its general and universal form, equal to the one defined for SIDIS processes.

If we extend this approach beyond the above processes, whose partonic subprocesses are both characterized by the exchange of a color-singlet mediator (a photon), we find a much more complex situation. For example, for the inclusive-hadron production in pp collisions, one has to consider the $qq' \to qq'$ subprocess. In this case, both C_I and C_F appear, as shown in Fig. 4.3. The Sivers function of this process can be still related to the SIDIS one as follows

$$\Delta^N f_{a/A^\uparrow}^{qq'\to qq'} = \frac{C_I + C_F}{C_U}\Delta^N f_{a/A^\uparrow}^{\rm SIDIS}, \tag{4.27}$$

or alternatively one can introduce the process-dependent cross section, that includes both ISIs and FSIs,

$$\mathcal{H}_{qq'\to qq'}^{\rm Inc} = \mathcal{H}_{qq'\to qq'}^{\rm Inc-I} + H_{qq'\to qq'}^{\rm Inc-F} = (C_I + C_F)\, h_{qq'\to qq'}. \tag{4.28}$$

For SSAs in J/ψ production, where different subprocesses enter, this simple relation is not valid for the entire hard part, even if a suitable modification can still be found.

Gluon Sivers function

We discuss here the extension of the CGI approach for subprocesses where gluons are involved. We start considering the partonic subprocess $g\,q \to \gamma\,q$, for which the CGI relevant diagrams are shown in Fig. 4.4. The first one, ⓐ, describes the initial-state interaction, while the last two, ⓑ and ⓒ, are the final-state interactions involving the unobserved parton. We will show that these last two contributions cancel out. This simplifies the whole approach, since this happens whenever an undetected parton is involved.

For each case, the spinors are replaced according to

$$\begin{aligned}
&\text{ⓐ}: \quad u(p_b) \to (-i\pi g)\, t^e\, \bar{u}(p_c)\, \delta(k^+),\\
&\text{ⓑ}: \quad \bar{u}(p_c) \to (+i\pi g)\, t^e\, \bar{u}(p_c)\, \delta(k^+),\\
&\text{ⓒ}: \quad u(p_c) \to (-i\pi g)\, t^e\, u(p_c)\, \delta(k^+).
\end{aligned} \tag{4.29}$$

The extra color carried by the exchanged gluon has to be neutralized by a proper color projector. Since the parton coming from the polarized proton is a gluon, within the one-gluon-exchange approximation there are two different ways to perform the

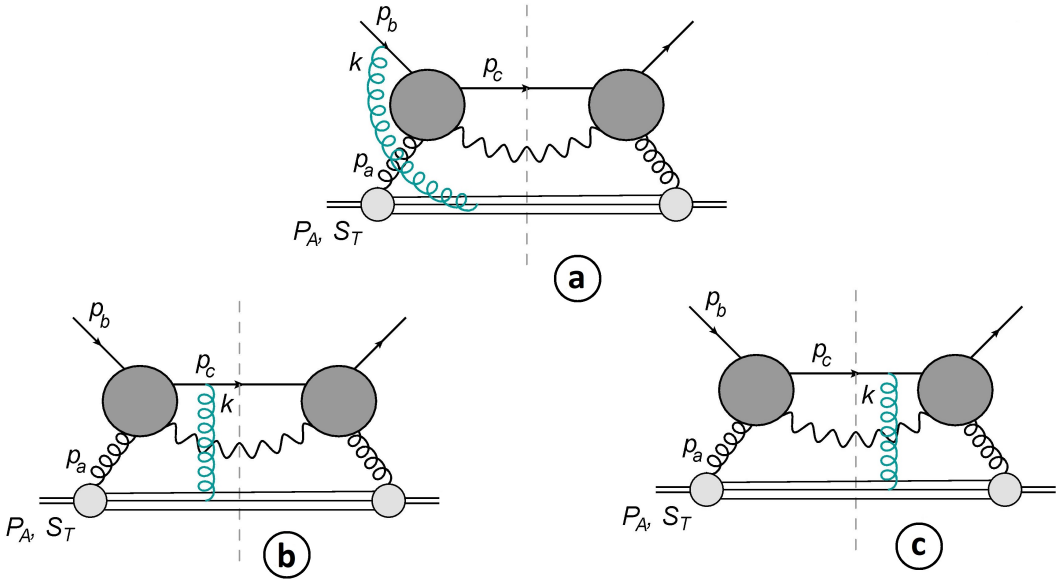

FIGURE 4.4: Diagrams relative to the subprocess $g\,q \to \gamma\,q$ within the CGI-GPM approach. They play a role in the study of the gluon Sivers function.

color neutralization. One projector, $\mathcal{T}^e_{aa'}$, is antisymmetric, while the second one, $\mathcal{D}^e_{aa'}$, is symmetric. Their explicit definitions are

$$\mathcal{T}^e{}_{aa'} = \mathcal{N}_{\mathcal{T}}\,(T^e)_{aa'} = -i\mathcal{N}_{\mathcal{T}}\,f_{eaa'}, \tag{4.30}$$

$$\mathcal{D}^e{}_{aa'} = \mathcal{N}_{\mathcal{D}}\,(D^e)_{aa'} = \mathcal{N}_{\mathcal{D}}\,d_{eaa'}, \tag{4.31}$$

where $f_{eaa'}$ ($d_{eaa'}$) is the antisymmetric (symmetric) structure constant of $SU(3)$, while the normalizations are given by

$$\mathcal{N}_{\mathcal{T}} = \mathrm{Tr}\,[T^e T^e]^{-1} = \frac{1}{N_c(N_c^2-1)}, \tag{4.32}$$

$$\mathcal{N}_{\mathcal{D}} = \mathrm{Tr}\,[D^e D^e]^{-1} = \frac{N_c}{(N_c^2-4)(N_c^2-1)}. \tag{4.33}$$

We first consider the diagram (a), where in the gray bubble we take only the tree-level diagram[2] of the process $g\,q \to \gamma\,q$. In this case, two different averaged color factors can be identified, depending on the color projector choice, namely

$$C_I^{(f)} = \frac{1}{N_c}\mathcal{T}^e{}_{ij}\,t^e_{ji}\,t^{a'}_{im}t^a_{mj} = \frac{-if_{eaa'}}{N_c^2(N_c^2-1)}\,\mathrm{Tr}\left[t^e t^{a'} t^a\right] = -\frac{1}{4N_c}, \tag{4.34}$$

$$C_I^{(d)} = \frac{1}{N_c}\mathcal{D}^e{}_{ij}\,t^e_{ji}\,t^{a'}_{im}t^a_{mj} = \frac{d_{eaa'}}{(N_c^2-4)(N_c^2-1)}\,\mathrm{Tr}\left[t^e t^{a'} t^a\right] = \frac{1}{4N_c}. \tag{4.35}$$

These two color factors are independent and cannot be associated to a unique gluon Sivers function. This implies that, even in one-gluon-exchange approximation, two different gluon Sivers functions arise. These are defined as the f-type GSF ($\Delta^N f^{(f)}_{a/A^\uparrow}$) and the d-type one ($\Delta^N f^{(d)}_{a/A^\uparrow}$). Once again, the process dependence can be moved to

[2] This allows us to obtain exact results, without loss of generality.

the hard part, by defining

$$\mathcal{H}^{\text{Inc }(f/d)}_{qg\to\gamma q} = C^{(f/d)}_{\text{Inc}}\, h_{qg\to\gamma q}, \tag{4.36}$$

where, in principle, the label "Inc" include both initial- and final-state interactions.

Moving to the undetected parton contributions, we have to study the two diagrams (b) and (c) in Fig. 4.4. Once again, we take into account only the tree level in the grey bubble to provide an explicit example. We start noticing that while in the (b) diagram the parton is strictly on-shell, in (c) this is not mandatory, and the parton can be slightly off-shell; this is possible only because the final parton is unobserved. Elaborating in more detail Eq. (4.29), we have

$$\begin{aligned}
&\text{(b)}: \quad \bar{u}(p_c)\,(-ig\gamma^- t^e)\,i\frac{\not{p}_c - \not{k}}{(p_c-k)^2+i\epsilon}\,\delta(p_c^2) \to (-i\pi g)\,t^e\,\bar{u}(p_c)\,\delta(k^+)\delta(p_c^2),\\
&\text{(c)}: \quad (-ig\gamma^- t^e)\,i\frac{\not{p}_c}{(p_c)^2-i\epsilon}\,u(p_c-k)\,\delta\left((p_c-k)^2\right) \to (+i\pi g)\,t^e\,u(p_c)\,\delta(k^+)\delta(p_c^2).
\end{aligned} \tag{4.37}$$

Since in both cases the remaining parts of the scattering amplitudes are the same, the opposite pole contributions add up directly, leading to a cancellation. As previously mentioned, this happens whenever an unobserved parton is involved.

Quarkonium formation and FSIs

In this section we explicitly discuss the FSIs in the context of SSAs for quarkonium production. The $pp^\uparrow \to J/\psi + X$ process involves three classes of partonic subprocesses at order α_s^3: $g\,g \to J/\psi\,g$, $g\,q(\bar{q}) \to J/\psi\,q(\bar{q})$ and $q\,\bar{q} \to J/\psi\,g$. Their representative diagrams are shown in Fig. 4.5. From diagrams (b) and (c), we see that ISIs are given by the extra eikonal gluon attached to the initial quark/antiquark. This does not provide any new information compared to what discussed in the previous sections. On the other hand, in diagram (a) ISIs will involve the attachment of the eikonal gluon to the hard one.

Let us consider it in more detail, as depicted in Fig. 4.6. Focusing on ISIs (left diagram) we can introduce the polarization vector transformation rule, while FSIs (right diagram) allow us to describe how the eikonal gluon insertion works when a heavy-quark-antiquark bound state is involved.

Via the eikonal approximation, the extra gluon field has a dominant component $A^\rho \approx A^+$, with momentum[3] $k \approx k^+$. Moreover, its presence dictates a replacement rule which, in this example, is applied to the hard gluon polarization vector $\epsilon^\nu(p_b)$

$$\epsilon^\nu(p_b) \to \epsilon^\nu(p_b)\,A^\rho(k)\,(-g\,f_{bkb'})\,C_{\nu\rho\rho'}\left(-i\frac{\eta^{\rho'\nu'}}{(k+p_b)^2+i\epsilon}\right), \tag{4.38}$$

with

$$\begin{aligned}
C_{\nu\rho\rho'} &= \eta_{\nu\rho}(p_b-k)_{\rho'} + \eta_{\rho\rho'}(2\,k+p_b)_\nu - \eta_{\rho'\nu}(2\,p_b+k)_\rho\\
&\approx \eta_{\nu\rho}(p_b)_{\rho'} + \eta_{\rho\rho'}(p_b)_\nu - \eta_{\rho'\nu}(2\,p_b)_\rho\\
&= -2\,\eta_{\rho'\nu}\,p_{b_\rho}.
\end{aligned} \tag{4.39}$$

[3]Do not confuse the momentum k with the color index k corresponding to the eikonal gluon.

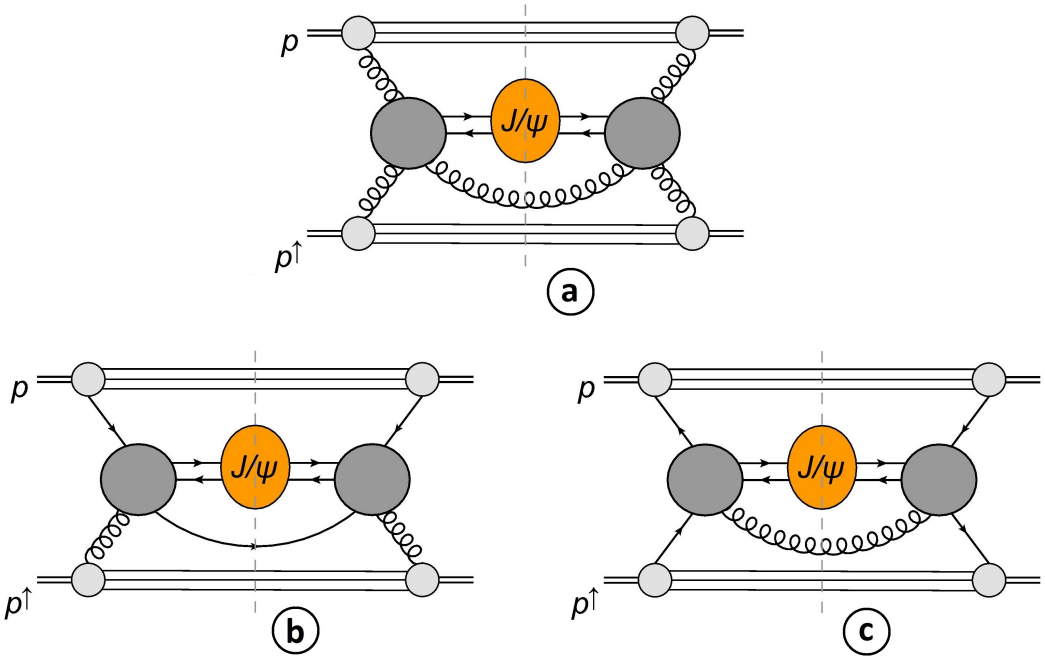

FIGURE 4.5: Representative $2 \to 2$ diagrams for the unpolarized process $p\,p \to J/\psi\, X$.

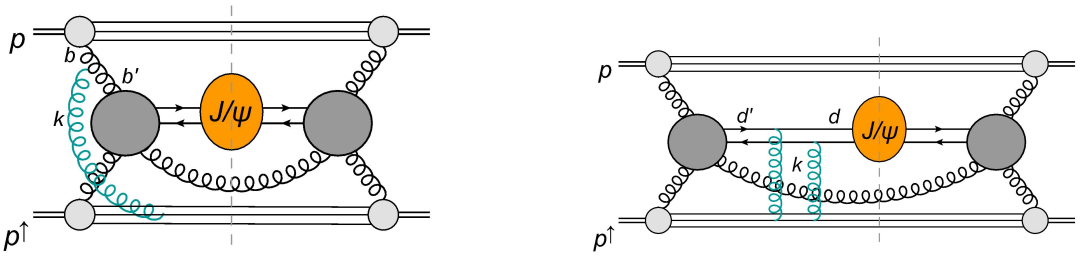

FIGURE 4.6: Diagrams corresponding to the insertion of ISIs (left diagram) and FSIs (right diagram) in the partonic process $g\,g \to J/\psi\, g$, Fig. 4.5 diagram (a). ISIs connect the polarized proton remnants to the hard gluon coming from the unpolarized proton, implying also a modification of the polarization vector. FSIs are obtained by combining the heavy quark and antiquark contributions; this depends on the hadronization model.

In the second line we have neglected k compared to p_b, while in the third line we have used the polarization vector gauge condition ($\epsilon^-(p_b) = 0$) and its orthogonality condition ($\epsilon(p_b) \cdot p_{b_\nu} = 0$). Applying the final (approximated) form of $C_{\nu\rho\rho'}$ to Eq. (4.38), the substitution becomes

$$\begin{aligned}
\epsilon^{\nu}(p_b)\, A^{\rho}(k)\, (-g\, f_{bkb'})\, C_{\nu\rho\rho'} \left(-i \frac{\eta^{\rho'\nu'}}{(k+p_b)^2 + i\epsilon}\right) \approx \\
&\approx \epsilon^{\nu'}(p_b)\, A^{+}(k)\, (ig f_{bkb'}) \frac{2p_{b_}}{2k^{+}p_{b_} + i\epsilon} \\
&\approx \epsilon^{\nu'}(p_b)\, (-ig\, f_{bkb'})\, \frac{A^{+}(k)}{k^{+} + i\epsilon} \\
&\approx \epsilon^{\nu'}(p_b)\, (-i\pi g)\, (-i f_{bkb'})\, \left(A^{+}(k)\delta(k^{+})\right). \qquad (4.40)
\end{aligned}$$

In the last step, we have decomposed the propagator in its principal value and the imaginary part, keeping only the latter. We notice that, since the index ν' is actually

contracted with the rest of the diagram, one can restore the original index ν. In this way, the following substitution rule for the polarization vector can be used

$$\epsilon^{\nu}(p_b) \to \epsilon^{\nu}(p_b)\,(-i\pi g)\,(-if_{bkb'})\,\left(A^{+}(k)\delta(k^{+})\right). \tag{4.41}$$

Moving to the FSIs, we have the most interesting case, given by the presence of the two heavy quarks bounded together.[4] These FSIs, within the one-gluon-exchange approximation, are shown in Fig. 4.6 (right diagram).

The form of FSIs for quarkonium production depends on the color nature of the quark-antiquark pair, *i.e.* if it is in a CS or a CO state. In the first case, the contributions coming from the quark and the antiquark are opposite in sign, leading to a cancellation. To demonstrate it, we explicitly impose the projection of the quark-antiquark pair into a CS state.

The color structure $C_{ij;mn}$ of one of the diagrams in Fig. 4.5 can be decomposed, in general, into two terms, $C^{\mathcal{Q}}_{ij}$ and C^{q}_{mn}, as

$$C_{ij;mn} = C^{\mathcal{Q}}_{ij}\, C^{q}_{mn}. \tag{4.42}$$

The first factor is identified by the color flow that follows the fermionic line that includes the heavy quark-antiquark pair. The second one follows the fermionic line identified by other quarks/antiquarks; notice that if this fermionic line is missing, then C^{q}_{mn} is just the identity matrix (*i.e.* it can be removed from the previous equation).

In the case of a CS state, the color projector is given in Eq. (A.6) (first equation) of Appendix A. From that, the unpolarized hard part $\mathcal{H}^{U}$ involves directly the trace of the quarkonium color structure $C^{\mathcal{Q}}$, namely $\mathrm{Tr}[C^{\mathcal{Q}}]$. With the inclusion of the extra eikonal gluon, an extra matrix $\mathcal{T}^{e}$ in its fundamental representation needs to be added. Following the fermion line backwards, the extra $\mathcal{T}^{e}$ term will be either in front of or after the quarkonium color structure $C^{\mathcal{Q}}$, if the gluon is attached to the heavy quark or antiquark, respectively. Due to the different sign in the imaginary contribution of the pole, the two terms enter with opposite signs (see also Eq. (4.20)). In the end, we have the following replacement rule

$$\frac{\mathrm{Tr}[C^{\mathcal{Q}}]}{\sqrt{N_c}} \to \left(t^{e}_{ik}C^{\mathcal{Q}}_{kj} - C^{\mathcal{Q}}_{ik}t^{e}_{kj}\right)\frac{\delta_{ji}}{\sqrt{N_c}} = \frac{\mathrm{Tr}[t^{e}C^{\mathcal{Q}}] - \mathrm{Tr}[C^{\mathcal{Q}}t^{e}]}{\sqrt{N_c}} = 0, \tag{4.43}$$

where, in the last step, we used the cyclic property of a trace.

When the pair is produced in a CO state, it behaves like a gluon. This implies that the sum of the two contributions leads to a similar substitution rule found for a hard gluon polarization vector. In this case the CO projector, given in Eq. (A.6) (second equation) of Appendix A, brings another matrix t^{d}, which plays a role in the trace of the hard part color structure, namely $\mathrm{Tr}[C^{\mathcal{Q}}t^{d}]$. Moreover, its presence prevents the cancellation between the contributions coming from the quark and the antiquark after the insertion of the eikonal gluon. Indeed, the FSIs for the CO case

[4] We remind that the other unobserved parton never contributes to the SSA in the CGI approach.

can be managed as follows

$$\begin{aligned}\sqrt{2}\mathrm{Tr}[C^{\mathcal{Q}}t^d] \to \sqrt{2}\left(t^e_{ik}C^{\mathcal{Q}}_{kj} - C^{\mathcal{Q}}_{ik}t^e_{kj}\right)t^d_{ji} &= \sqrt{2}\left(\mathrm{Tr}[t^e C^{\mathcal{Q}} t^d] - \mathrm{Tr}[C^{\mathcal{Q}} t^e t^d]\right)\\ &= \sqrt{2}\left(\mathrm{Tr}[C^{\mathcal{Q}} t^d t^e] - \mathrm{Tr}[C^{\mathcal{Q}} t^e t^d]\right)\\ &= \sqrt{2}\,(if_{ded'})\,\mathrm{Tr}[C^{\mathcal{Q}} t^{d'}]. \end{aligned} \tag{4.44}$$

Again, the cyclic property of the trace has been used. Furthermore, to reduce the number of traces, the anti-commutator fundamental property of the Gell-Mann matrices has been used, Eq. (A.33) of Appendix A. The sum of the two FSI contributions has the net effect of introducing an extra antisymmetric structure constant, $f_{ded'}$. As already anticipated, this is the same effect found when the eikonal gluon is attached to another, hard, gluon.

From these examples it is now clear that, when studying SSAs within the CGI-GPM framework, the gluonic-like nature of the quarkonium state has a real impact on the final result.

4.3 SSAs in $p^\uparrow p \to J/\psi + X$ within the CGI-GPM approach

The main goal of this section is to provide the formal tools to evaluate Single-Spin Asymmetries within the CGI-GPM framework for inclusive J/ψ production in pp collisions. As previously mentioned, for inclusive processes like $pp \to h + X$ or $pp \to \mathcal{Q} + X$ a formal proof of factorization in terms of TMDs does not exist. On the other hand, for their relevance, phenomenological TMD approaches, like the GPM and its CGI extension, are worth to be exploited.

In order to describe the SSAs for quarkonium production, it is necessary to combine these approaches (GPM or CGI) with a model, describing the hadronization formation. In this context, both the CSM and the NRQCD approaches will be adopted.

It is well known that quarkonium production is in general dominated by gluon channels; for this reason, within a TMD scheme, SSA measurements can provide information on the still poorly known gluon Sivers function.

To unveil the role of the gluonic content in a proton, it is then important to study as many processes as possible. While here we focus on J/ψ production in pp collisions, other processes, like $e\,p^\uparrow \to e'\,J/\psi + X$ have received considerable attention. This can be deeply explored with the advent of the Electron-Ion Collider. In Ref. [139], for instance, estimates for the Sivers SSA potentially accessible at the EIC ($\sqrt{s} = 140$ GeV) are presented, paying special attention to the role of ISIs and FSIs. Moreover, considering the real photon emission limit, it is possible to study the Sivers effect in inelastic J/ψ photoproduction. Estimates for SSAs, limiting to the GPM approach, in $\gamma\, g \to J/\psi + X$ are given in Ref. [30] for EIC (at $\sqrt{s} = 45$ and 100 GeV) and COMPASS (at $\sqrt{s} = 17.2$ GeV).

Unfortunately, at the moment the available data are not enough to perform a fit, and extract precious information on the GSF. For this reason, in this section (following Ref. [154]) we will show only "*maximized*" asymmetry estimates; their exact meaning will be explained in Sec. 4.3.2, where explicit parameterization choices will be discussed.

In details, the next sections are organized as follows. In Sec. 4.3.1 we apply the CGI-GPM approach to the case of quarkonium formation, gathering all color factors for each subprocess as well as the resulting process-dependent hard parts. Then, in Sec. 4.3.2, we describe the typical parameterization choice adopted in these studies.

Finally, in Sec. 4.3.3 and Sec. 4.3.4 we show numerical estimates compared against PHENIX data [41, 42], as well as predictions for future experiments.

4.3.1 CGI hard part in pp collisions

We start discussing the formal novelties of the $p^\uparrow p \to J/\psi + X$ SSA within the CGI-GPM approach, compared to the standard GPM. The latter can be found, for instance, in Ref. [155] and references therein.

All leading diagrams (both $2 \to 1$ and $2 \to 2$ partonic channels) and the corresponding unpolarized hard parts for the process $pp \to J/\psi + X$ are given in Appendix B.1.[5]

These quantities enter the denominator of the SSA, and they are always evaluated within the GPM approach, even when we adopt the CGI-GPM. The same diagrams are also involved in the numerator of the asymmetry evaluated both within GPM and CGI-GPM. On the other hand, in the former the same amplitudes $\mathcal{H}^U$ as those for the unpolarized cross section are used, while in the latter they are replaced by $\mathcal{H}^{\text{Inc}}$, including ISIs and FSIs. This replacement is carried out, as widely discussed in the previous section, by introducing new color factors related to initial- and final-state interactions, C_I and C_F respectively. Due to the high complexity of the process itself, the direct relation in Eq. (4.28) does not hold in this case. Indeed, it is not possible, in general, to identify a common color factor for all the relevant non-zero sub-diagram products. This is particularly evident for some Fock-states, *e.g.* ${}^3S_1^{(8)}$ CO state, whose corresponding color factors are given in Tab. 4.4. Nevertheless, it is still possible to apply the relation in Eq. (4.28) to a specific subset diagram product $I \times J$

$$\mathcal{H}^{I\times J,\,\text{Inc}} = \frac{C_I^{I\times J} + C_F^{I\times J}}{C_U^{I\times J}} \mathcal{H}^{I\times J,\,U} = \frac{C^{I\times J,\,\text{Inc}}}{C_U^{I\times J}} \mathcal{H}^{I\times J,\,U}, \tag{4.45}$$

where I and J correspond to two of the possible diagrams.

In the following, for different J/ψ states, we collect the analogous color factor tables shown in Appendix B.1.3 for the initial- and final-state interactions, as well as their sum C^{Inc}. Moreover, we provide the relative process-dependent hard parts, that enter the CGI-GPM numerator of the asymmetry.

Starting from the $2 \to 1$ process, the J/ψ particle can be produced only via a CO state, as shown in Appendix B.2 (unpolarized production). Thus, the A_N numerator receives contribution only from the CO sector, too. Moreover, when adopting the CGI framework, the insertion of ISIs and FSIs has an important consequence in the final result. In particular, in the gluon channel, the contributions from both f- and d-type GSFs turn out to be zero. The latter is true due to the projection in the symmetric color space, which is null by itself. The former, instead, is true due to the cancellation of the non-zero contributions coming from ISI and FSI. This result, presented also in Tab. 4.1, is in agreement with Ref. [28].

Hence, within the CGI approach, only the quark-antiquark annihilation channel produces a non-zero result, with a sign change if the parton coming from the polarized proton is a quark or a antiquark, as shown in Tab. 4.2. Finally, at order α_s^2, the amplitudes squared in the CGI framework are given by

$$\mathcal{H}^{\text{Inc}\ (f/d)}_{gg\to{}^1S_0^{(8)}} = \mathcal{H}^{\text{Inc}\ (f/d)}_{gg\to{}^3S_1^{(1,8)}} = \mathcal{H}^{\text{Inc}\ (f/d)}_{gg\to{}^3P_J^{(8)}} = 0 \tag{4.46}$$

[5] Notice that in this appendix we use a slightly different notation for the amplitude squared, namely $|\mathcal{M}|^2$, instead of $\mathcal{H}$.

State	Part. process	$C_I^{(f)}$	$C_I^{(d)}$	$C_F^{(f)}$	$C_F^{(d)}$	$C^{\text{Inc }(f)}$	$C^{\text{Inc }(d)}$
${}^1S_0^{(8)}$ & ${}^3P_J^{(8)}$	$gg \to \mathcal{Q}$	$-\frac{N^2-4}{4N(N^2-1)}$	0	$\frac{N^2-4}{4N(N^2-1)}$	0	0	0

TABLE 4.1: Color factors within the CGI framework for the $gg \to J/\psi[{}^1S_0^{(8)}]$ and $gg \to J/\psi[{}^3P_J^{(8)}]$ channels.

State	Part. process	C_I	C_F	C^{Inc}
${}^3S_1^{(8)}$	$q\bar{q} \to \mathcal{Q}$	$\pm\frac{1}{4N^2}$	$\pm\frac{1}{4}$	$\pm\frac{N^2+1}{4N^2}$

TABLE 4.2: Color factors within the CGI framework for the $q\bar{q} \to J/\psi[{}^3S_1^{(8)}]$ channel; upper (lower) sign is for quark (antiquark) parton in the polarized proton.

for gluon-gluon interaction, and

$$\mathcal{H}^{\text{Inc }(f)}_{q\bar{q}\to{}^1S_0^{(8)}} = \mathcal{H}^{\text{Inc }(f)}_{q\bar{q}\to{}^3P_J^{(8)}} = 0, \tag{4.47}$$

$$\mathcal{H}^{\text{Inc }(f)}_{q\bar{q}\to{}^3S_1^{(8)}} = \pm\frac{5(4\pi\alpha_s)^2}{108M_\psi} \tag{4.48}$$

for quark-antiquark annihilation, where the upper (lower) sign refers to a quark (antiquark) parton picked up from the polarized proton.

Like in the unpolarized case, the next order contribution ($2 \to 2$ subprocesses) leads to a more complex picture. The production of the CS state in the hard process is possible only via gg interaction and, since the $c\bar{c}$ pair is in a singlet state, only ISIs are possible. The relatively low number of active diagrams and the sole presence of initial-state interactions make the relation between the results in CGI and GPM approaches relatively simple

$$\mathcal{H}^{CSM,\text{ Inc }(f)} = -\frac{1}{2}\mathcal{H}^{CSM,\,U}, \tag{4.49}$$

which gives

$$\begin{aligned}\mathcal{H}^{\text{Inc }(f)}_{gg\to{}^3S_1^{(1)}g} &= -\frac{5(4\pi\alpha_s)^3 M_\psi}{162\,(\hat{s}+\hat{t})^2(\hat{s}+\hat{u})^2(\hat{t}+\hat{u})^2} \\ &\quad\times\left[\hat{s}^2\left(\hat{t}\,\hat{u}+\hat{t}^2+\hat{u}^2\right)+\hat{s}\,\hat{t}\,\hat{u}\,\left(\hat{t}+\hat{u}\right)+\hat{t}^2\hat{u}^2\right], \\ \mathcal{H}^{\text{Inc }(d)}_{gg\to{}^3S_1^{(1)}g} &= 0,\end{aligned} \tag{4.50}$$

with the latter (d-type contribution) being 0 due to color projection. This result is in agreement with Ref. [137].

Considering the CO state, the relation shown in Eq. (4.45) holds, and single products among different diagrams need to be considered. As also found in the previous case, the gluon-gluon interaction does not allow the presence of a d-type GSF since the projection in the symmetric color space is zero. This statement holds for all dominant CO waves, namely ${}^1S_0^{(8)}$ and ${}^3P_J^{(8)}$, Tab. 4.3, and ${}^3S_1^{(8)}$, Tab. 4.4.

For the ${}^1S_0^{(8)}$ and ${}^3P_J^{(8)}$ waves, only a subset of diagrams contributes, due to the

$gg \to \mathcal{Q}[(^1S_0^{(8)}\ \&\ ^3P_J^{(8)})]\, g$	$C_I^{(f)}$	$C_I^{(d)}$	$C_F^{(f)}$	$C_F^{(d)}$	$C^{\text{Inc }(f)}$	$C^{\text{Inc }(d)}$
$\text{Ⓐ}_1 \times \text{Ⓐ}_1$	$-\frac{N^2-4}{8(N^2-1)}$	0	$\frac{N^2-4}{8(N^2-1)}$	0	0	0
$\text{Ⓐ}_2 \times \text{Ⓐ}_2$	0	0	$\frac{N^2-4}{8(N^2-1)}$	0	$\frac{N^2-4}{8(N^2-1)}$	0
$\text{Ⓐ}_3 \times \text{Ⓐ}_3$	$-\frac{N^2-4}{8(N^2-1)}$	0	0	0	$-\frac{N^2-4}{8(N^2-1)}$	0
$\text{Ⓐ}_1 \times \text{Ⓑ}_1$	$-\frac{N^2-4}{8(N^2-1)}$	0	$\frac{N^2-4}{8(N^2-1)}$	0	0	0
$\text{Ⓐ}_1 \times \text{Ⓑ}_2$	$\frac{N^2-4}{8(N^2-1)}$	0	$-\frac{N^2-4}{8(N^2-1)}$	0	0	0
$\text{Ⓐ}_2 \times \text{Ⓑ}_2$	0	0	$\frac{N^2-4}{8(N^2-1)}$	0	$\frac{N^2-4}{8(N^2-1)}$	0
$\text{Ⓐ}_2 \times \text{Ⓑ}_3$	0	0	$\frac{N^2-4}{8(N^2-1)}$	0	$\frac{N^2-4}{8(N^2-1)}$	0
$\text{Ⓐ}_3 \times \text{Ⓑ}_1$	$\frac{N^2-4}{8(N^2-1)}$	0	$\frac{N^2-4}{8(N^2-1)}$	0	$\frac{N^2-4}{8(N^2-1)}$	0
$\text{Ⓐ}_3 \times \text{Ⓑ}_3$	$-\frac{N^2-4}{8(N^2-1)}$	0	0	0	$-\frac{N^2-4}{8(N^2-1)}$	0
$\text{Ⓑ}_1 \times \text{Ⓑ}_1$	$-\frac{N^2-4}{4(N^2-1)}$	0	$\frac{N^2-4}{8(N^2-1)}$	0	$-\frac{N^2-4}{8(N^2-1)}$	0
$\text{Ⓑ}_2 \times \text{Ⓑ}_2$	$-\frac{N^2-4}{8(N^2-1)}$	0	$\frac{N^2-4}{4(N^2-1)}$	0	$\frac{N^2-4}{8(N^2-1)}$	0
$\text{Ⓑ}_3 \times \text{Ⓑ}_3$	$-\frac{N^2-4}{8(N^2-1)}$	0	$\frac{N^2-4}{8(N^2-1)}$	0	0	0
$\text{Ⓑ}_1 \times \text{Ⓑ}_2$	$\frac{N^2-4}{8(N^2-1)}$	0	$-\frac{N^2-4}{8(N^2-1)}$	0	0	0
$\text{Ⓑ}_1 \times \text{Ⓑ}_3$	$\frac{N^2-4}{8(N^2-1)}$	0	0	0	$\frac{N^2-4}{8(N^2-1)}$	0
$\text{Ⓑ}_2 \times \text{Ⓑ}_3$	0	0	$\frac{N^2-4}{8(N^2-1)}$	0	$\frac{N^2-4}{8(N^2-1)}$	0

TABLE 4.3: Non-zero color factors within the CGI framework for the $gg \to J/\psi[^1S_0^{(8)}]\, g$ and $gg \to J/\psi[^3P_J^{(8)}]\, g$ channels; diagram letters follow the notation used in Appendix B.

Fock-state projector. The products among the surviving diagrams are gathered in Tab. 4.3, leading to

$$\mathcal{H}^{\text{Inc }(f)}_{gg\to{}^1S_0^{(8)}g} = \frac{(4\pi\alpha_s)^3}{64\hat{s}\hat{t}(\hat{s}+\hat{t})^2(\hat{s}+\hat{u})^2(\hat{t}+\hat{u})^2 M_\psi}\Bigg\{5(\hat{s}-\hat{t})\left(\hat{s}\left(2\,\hat{t}+\hat{u}\right)+\hat{t}\hat{u}\right) \times\left[\hat{s}^4+2\,\hat{s}^3\left(\hat{t}+\hat{u}\right)+3\,\hat{s}^2\left(\hat{t}+\hat{u}\right)^2+2\,\hat{s}\left(\hat{t}+\hat{u}\right)^3+\left(\hat{t}\,\hat{u}+\hat{t}^2+\hat{u}^2\right)^2\right]\Bigg\} \tag{4.51}$$

and

$$\mathcal{H}^{\text{Inc }(f)}_{gg\to{}^3P_J^{(8)}g} = \frac{(4\pi\alpha_s)^3}{16\hat{s}\hat{t}(\hat{s}+\hat{t})^3(\hat{s}+\hat{u})^3(\hat{t}+\hat{u})^3M_\psi^3}(\hat{s}-\hat{t})\Bigg\{5(\hat{s}-\hat{t})$$
$$\times\Big[7\hat{s}^7\left(2\hat{t}+\hat{u}\right)\left(\hat{t}+\hat{u}\right)+\hat{s}^6\left(44\hat{t}^3+106\hat{t}^2\hat{u}+91\hat{t}\hat{u}^2+21\hat{u}^3\right)$$
$$+\hat{s}^5\left(68\hat{t}^4+212\hat{t}^3\hat{u}+268\hat{t}^2\hat{u}^2+175\hat{t}\hat{u}^3+35\hat{u}^4\right)$$
$$+\hat{s}^4\left(68\hat{t}^5+254\hat{t}^4\hat{u}+426\hat{t}^3\hat{u}^2+398\hat{t}^2\hat{u}^3+213\hat{t}\hat{u}^4+35\hat{u}^5\right)$$
$$+\hat{s}^3\left(44\hat{t}^6+212\hat{t}^5\hat{u}+426\hat{t}^4\hat{u}^2+528\hat{t}^3\hat{u}^3+394\hat{t}^2\hat{u}^4+165\hat{t}\hat{u}^5+21\hat{u}^6\right)$$
$$+\hat{s}^2\left(14\hat{t}^7+106\hat{t}^6\hat{u}+268\hat{t}^5\hat{u}^2+398\hat{t}^4\hat{u}^3+394\hat{t}^3\hat{u}^4+236\hat{t}^2\hat{u}^5+75\hat{t}\hat{u}^6+7\hat{u}^7\right)$$
$$+\hat{s}\hat{t}\hat{u}\left(21\hat{t}^6+91\hat{t}^5\hat{u}+175\hat{t}^4\hat{u}^2+213\hat{t}^3\hat{u}^3+165\hat{t}^2\hat{u}^4+75\hat{t}\hat{u}^5+14\hat{u}^6\right)$$
$$+7\hat{t}^2\hat{u}^2\left(\hat{t}+\hat{u}\right)\left(\hat{t}\hat{u}+\hat{t}^2+\hat{u}^2\right)^2\Big]\Bigg\}. \tag{4.52}$$

Differently from the other two cases, all diagrams contribute to the production of the ${}^3S_1^{(8)}$ CO state. Despite this, another simplification arises, since some color factors coming from different diagrams are equal to each other. Explicitly, we have the following correspondences: $(\text{Ⓒ}_1, \text{Ⓓ}_1) \Leftrightarrow \text{Ⓑ}_1$, $(\text{Ⓒ}_2, \text{Ⓓ}_2) \Leftrightarrow \text{Ⓑ}_2$ and $(\text{Ⓒ}_3, \text{Ⓓ}_3) \Leftrightarrow \text{Ⓑ}_3$, where the letters follow the notation used in Appendix B.1. For this reason, in Tab. 4.4 only independent products are considered. From these color factors, the process-dependent hard part is

$$\mathcal{H}^{\text{Inc }(f)}_{gg\to{}^3S_1^{(8)}g} = -\frac{(4\pi\alpha_s)^3}{96(\hat{s}+\hat{t})^2(\hat{s}+\hat{u})^2(\hat{t}+\hat{u})^2M_\psi^3}$$
$$\times\Big[17\hat{s}^3\left(\hat{t}\hat{u}+\hat{t}^2+\hat{u}^2\right)+\hat{s}^2\left(54\hat{t}^2\hat{u}+66\hat{t}\hat{u}^2+17\hat{t}^3+26\hat{u}^3\right)$$
$$+\hat{s}\,\hat{t}\,\hat{u}\left(17\hat{t}^2+66\hat{t}\hat{u}+38\hat{u}^2\right)+\hat{t}^2\hat{u}^2\left(17\hat{t}+26\hat{u}\right)\Big]. \tag{4.53}$$

As already mentioned, the d-type GSF is not accessible via gg interaction, namely

$$\mathcal{H}^{\text{Inc }(d)}_{gg\to{}^1S_0^{(8)}g} = \mathcal{H}^{\text{Inc }(d)}_{gg\to{}^3S_1^{(1/8)}g} = \mathcal{H}^{\text{Inc }(d)}_{gg\to{}^3P_J^{(8)}g} = 0. \tag{4.54}$$

In principle, it is possible to access the d-type GSF through the $g\,q(\bar{q})$ channel, as shown in Tab. 4.5. Nevertheless, as will be shown in Sec. 4.3.3, this channel provides a relatively small contribution and, in general, the d-type GSF effect is suppressed compared to the f-type one. Depending on the specific product and state, it is possible to identify a sign change in the color factors when switching from a quark to an antiquark; in such a case both values are indicated in the table (upper and lower signs, respectively). The same logic is adopted in the following amplitudes squared. Moreover, in the production of a ${}^3S_1^{(8)}$ state, the color factors related to the diagrams Ⓐ and Ⓒ are found to be the same, where the letters follow the notation used in Appendix B.1. In Tab. 4.5 only the first case is explicitly given. From these results,

$gg \to \mathcal{Q}[^3S_1^{(8)}]\, g$	$C_I^{(f)}$	$C_I^{(d)}$	$C_F^{(f)}$	$C_F^{(d)}$	$C^{\text{Inc }(f)}$	$C^{\text{Inc }(d)}$
$\text{Ⓐ}_1 \times \text{Ⓐ}_1$	$-\frac{N^2+4}{8N^2(N^2-1)}$	0	$\frac{N^2+4}{8N^2(N^2-1)}$	0	0	0
$\text{Ⓐ}_1 \times \text{Ⓐ}_2$	$\frac{N^2-2}{4N^2(N^2-1)}$	0	$\frac{1}{2N^2(N^2-1)}$	0	$\frac{1}{4(N^2-1)}$	0
$\text{Ⓐ}_1 \times \text{Ⓐ}_3$	$-\frac{1}{2N^2(N^2-1)}$	0	$-\frac{N^2-2}{4N^2(N^2-1)}$	0	$-\frac{1}{4(N^2-1)}$	0
$\text{Ⓐ}_2 \times \text{Ⓐ}_2$	$\frac{1}{2N^2}$	0	$\frac{N^2+4}{8N^2(N^2-1)}$	0	$\frac{N^2+4}{8(N^2-1)}$	0
$\text{Ⓐ}_2 \times \text{Ⓐ}_3$	$\frac{N^2-2}{4N^2(N^2-1)}$	0	$-\frac{N^2-2}{8N^2(N^2-1)}$	0	0	0
$\text{Ⓐ}_3 \times \text{Ⓐ}_3$	$-\frac{N^2+4}{8N^2(N^2-1)}$	0	$-\frac{1}{2N^2}$	0	$-\frac{N^2+4}{8(N^2-1)}$	0
$\text{Ⓐ}_1 \times \text{Ⓑ}_1$	$\frac{N^2}{8(N^2-1)}$	0	$-\frac{N^2+2}{8(N^2-1)}$	0	$-\frac{1}{4(N^2-1)}$	0
$\text{Ⓐ}_1 \times \text{Ⓑ}_2$	$\frac{N^2+2}{8(N^2-1)}$	0	$-\frac{N^2}{8(N^2-1)}$	0	$\frac{1}{4(N^2-1)}$	0
$\text{Ⓐ}_2 \times \text{Ⓑ}_2$	$\frac{1}{4(N^2-1)}$	0	$\frac{N^2}{8(N^2-1)}$	0	$\frac{N^2+2}{8(N^2-1)}$	0
$\text{Ⓐ}_2 \times \text{Ⓑ}_3$	$-\frac{1}{4(N^2-1)}$	0	$-\frac{N^2+2}{8(N^2-1)}$	0	$-\frac{N^2+4}{8(N^2-1)}$	0
$\text{Ⓐ}_3 \times \text{Ⓑ}_1$	$-\frac{N^2}{8(N^2-1)}$	0	$-\frac{1}{4(N^2-1)}$	0	$-\frac{N^2+2}{8(N^2-1)}$	0
$\text{Ⓐ}_3 \times \text{Ⓑ}_3$	$-\frac{N^2+2}{8(N^2-1)}$	0	$-\frac{1}{4(N^2-1)}$	0	$-\frac{N^2+4}{8(N^2-1)}$	0
$\text{Ⓑ}_1 \times \text{Ⓑ}_1$	$-\frac{N^2}{4(N^2-1)}$	0	$\frac{N^2}{8(N^2-1)}$	0	$-\frac{N^2}{8(N^2-1)}$	0
$\text{Ⓑ}_1 \times \text{Ⓑ}_2$	$-\frac{N^2}{8(N^2-1)}$	0	$\frac{N^2}{8(N^2-1)}$	0	0	0
$\text{Ⓑ}_1 \times \text{Ⓑ}_3$	$-\frac{N^2}{8(N^2-1)}$	0	0	0	$-\frac{N^2}{8(N^2-1)}$	0
$\text{Ⓑ}_2 \times \text{Ⓑ}_2$	$-\frac{N^2}{8(N^2-1)}$	0	$\frac{N^2}{4(N^2-1)}$	0	$\frac{N^2}{8(N^2-1)}$	0
$\text{Ⓑ}_2 \times \text{Ⓑ}_3$	0	0	$-\frac{N^2}{8(N^2-1)}$	0	$-\frac{N^2}{8(N^2-1)}$	0
$\text{Ⓑ}_3 \times \text{Ⓑ}_3$	$-\frac{N^2}{8(N^2-1)}$	0	$\frac{N^2}{8(N^2-1)}$	0	0	0

TABLE 4.4: Non-zero color factors within the CGI framework for the $gg \to J/\psi[^3S_1^{(8)}]\, g$ channel; diagram letters follow the notation used in Appendix B.

$gq(\bar{q}) \to \mathcal{Q}[n]\, q(\bar{q})$	$C_I^{(f)}$	$C_I^{(d)}$	$C_F^{(f)}$	$C_F^{(d)}$	$C^{\text{Inc }(f)}$	$C^{\text{Inc }(d)}$
$\text{Ⓐ} \times \text{Ⓐ}$	$-\frac{N^2-4}{16N^2}$	$\pm\frac{N^2-12}{16N^2}$	$\frac{N^2-4}{8N^2}$	0	$\frac{N^2-4}{16N^2}$	$\pm\frac{N^2-12}{16N^2}$
$\text{Ⓐ} \times \text{Ⓐ}$	$-\frac{1}{16}$	$\pm\frac{1}{16}$	$\frac{1}{8}$	0	$\frac{1}{16}$	$\pm\frac{1}{16}$
$\text{Ⓐ} \times \text{Ⓑ}$	$\mp\frac{1}{16}$	$\frac{1}{16}$	$\pm\frac{1}{16}$	$\frac{1}{16}$	0	$\frac{1}{8}$
$\text{Ⓐ} \times \text{Ⓓ}$	0	0	$\mp\frac{1}{16}$	$\frac{1}{16}$	$\mp\frac{1}{16}$	$\frac{1}{16}$
$\text{Ⓑ} \times \text{Ⓑ}$	$-\frac{N^2-1}{16N^2}$	$\pm\frac{N^2-1}{16N^2}$	$\frac{1}{16}$	$\pm\frac{1}{16}$	$\frac{1}{16N^2}$	$\pm\frac{2N^2-1}{16N^2}$
$\text{Ⓑ} \times \text{Ⓓ}$	$\frac{1}{16N^2}$	$\mp\frac{1}{16N^2}$	0	0	$\frac{1}{16N^2}$	$\mp\frac{1}{16N^2}$
$\text{Ⓓ} \times \text{Ⓓ}$	$\frac{1}{16N^2}$	$\mp\frac{1}{16N^2}$	$\frac{1}{16}$	$\mp\frac{1}{16}$	$\frac{N^2+1}{16N^2}$	$\mp\frac{N^2+1}{16N^2}$

TABLE 4.5: Non-zero color factors within the CGI framework for the $g\,q(\bar{q}) \to J/\psi[^1S_0^{(8)}]\, q(\bar{q})$ and $g\,q(\bar{q}) \to J/\psi[^3P_J^{(8)}]\, q(\bar{q})$ (first row) and $gq(\bar{q}) \to J/\psi[^3S_1^{(8)}]\, q(\bar{q})$ (following rows) channels; the meaning of diagram letters can be found in Appendix B. Upper (lower) sign refers to quark (antiquark) parton in the polarized proton.

the hard parts for producing a $^1S_0^{(8)}$ state are given by

$$\mathcal{H}^{\text{Inc }(f)}_{g\,q(\bar{q})\to{}^1S_0^{(8)}q(\bar{q})} = -\frac{5(4\pi\alpha_s)^3}{288M_\psi}\frac{\hat{s}^2+\hat{u}^2}{\hat{t}(\hat{s}+\hat{u})^2}, \tag{4.55}$$

$$\mathcal{H}^{\text{Inc }(d)}_{g\,q(\bar{q})\to{}^1S_0^{(8)}q(\bar{q})} = \mp\frac{3}{5}\mathcal{H}^{\text{Inc }(f)}_{gq(\bar{q})\to{}^1S_0^{(8)}q(\bar{q})}, \tag{4.56}$$

while for ${}^3S_1^{(8)}$ are

$$\mathcal{H}^{\text{Inc }(f)}_{g\,q(\bar{q})\to{}^3S_1^{(8)}q(\bar{q})} = -\frac{5(4\pi\alpha_s)^3}{432M_\psi^3}\frac{(10\hat{s}^2+2\hat{s}\hat{u}+\hat{u}^2)(\hat{s}^2+2\hat{s}\hat{t}+2\hat{t}(\hat{t}+\hat{u})+\hat{u}^2)}{\hat{s}\hat{u}(\hat{s}+\hat{u})^4}, \tag{4.57}$$

$$\mathcal{H}^{\text{Inc }(d)}_{g\,q(\bar{q})\to{}^3S_1^{(8)}q(\bar{q})} = \pm\frac{5(4\pi\alpha_s)^3}{432M_\psi^3}\frac{\left(10\hat{s}^2+2\hat{s}\hat{u}-17\hat{u}^2\right)\left[\hat{s}^2+2\hat{s}\hat{t}+2\hat{t}\left(\hat{t}+\hat{u}\right)+\hat{u}^2\right]}{\hat{s}\hat{u}(\hat{s}+\hat{u})^4}, \tag{4.58}$$

and finally for ${}^3P_J^{(8)}$

$$\mathcal{H}^{\text{Inc }(f)}_{g\,q(\bar{q})\to{}^3P_J^{(8)}q(\bar{q})} = -\frac{5(4\pi\alpha_s)^3}{72M_\psi^3}\frac{(\hat{s}+\hat{u})\left(7\hat{s}^2+8\hat{t}^2+7\hat{u}^2\right)+4\hat{t}\left(3\hat{s}^2+4\hat{s}\hat{u}+3\hat{u}^2\right)}{\hat{t}(\hat{s}+\hat{u})^3}, \tag{4.59}$$

$$\mathcal{H}^{\text{Inc }(d)}_{g\,q(\bar{q})\to{}^3P_J^{(8)}q(\bar{q})} = \mp\frac{3}{5}\mathcal{H}^{\text{Inc }(f)}_{gq(\bar{q})\to{}^3P_J^{(8)}q(\bar{q})}. \tag{4.60}$$

Notice that, while for ${}^1S_0^{(8)}$ and ${}^3P_J^{(8)}$ states, the f- and d-type hard parts are directly related, as expected from the first row of Tab. 4.5, for ${}^3S_1^{(8)}$ the results have a slightly different dependence on the Mandelstam variables.

$q(\bar{q})g\to\mathcal{Q}[n]\,q(\bar{q})$	C_I	C_F	C^{Inc}
Ⓐ × Ⓐ	$\mp\frac{N^2-4}{8(N^2-1)}$	$\pm\frac{N^2}{8(N^2-1)}$	0
Ⓐ × Ⓐ	$\mp\frac{N^2}{8(N^2-1)}$	$\pm\frac{N^2}{8(N^2-1)}$	0
Ⓐ × Ⓑ	$-\frac{N^2}{8(N^2-1)}$	0	$-\frac{N^2}{8(N^2-1)}$
Ⓐ × Ⓓ	0	$-\frac{N^2}{8(N^2-1)}$	$-\frac{N^2}{8(N^2-1)}$
Ⓑ × Ⓑ	$\mp\frac{1}{8}$	$\mp\frac{1}{8(N^2-1)}$	$\mp\frac{N^2}{8(N^2-1)}$
Ⓑ × Ⓓ	$\pm\frac{1}{8(N^2-1)}$	$\mp\frac{1}{8(N^2-1)}$	0
Ⓓ × Ⓓ	$\pm\frac{1}{8(N^2-1)}$	$\pm\frac{1}{8}$	$\pm\frac{N^2}{8(N^2-1)}$

TABLE 4.6: Non-zero color factors within the CGI framework for the $q(\bar{q})g\to J/\psi[{}^1S_0^{(8)}]\,q(\bar{q})$ and $q(\bar{q})g\to J/\psi[{}^3P_J^{(8)}]\,q(\bar{q})$ (first row) and $q(\bar{q})g\to J/\psi[{}^3S_1^{(8)}]\,q(\bar{q})$ (following rows) channels; the meaning of diagram letters can be found in Appendix B. Upper (lower) sign is for a quark (antiquark) parton coming from the polarized proton.

Moving to the quark sector, the same initial states $g\,q(\bar{q})$ have to be considered, where now the quark (or the antiquark) belongs to the polarized proton. This modifies the color flow and, consequently, the color factor values for this channel, as shown in Tab. 4.6. Once again, the upper/lower sign refers to the quark/antiquark case. From this, one obtains

$$\mathcal{H}^{\text{Inc}}_{q(\bar{q})g\to{}^1S_0^{(8)}q(\bar{q})} = \mathcal{H}^{\text{Inc}}_{q(\bar{q})g\to{}^3P_J^{(8)}q(\bar{q})} = 0, \tag{4.61}$$

while

$$\mathcal{H}^{\text{Inc}}_{q(\bar{q})g\to{}^3S_1^{(8)}q(\bar{q})} = \mp\frac{3(4\pi\alpha_s)^3}{64M_\psi^3}\frac{\left(\hat{s}-\hat{t}\right)\left(\hat{s}^2+2\hat{t}^2+2M_\psi\hat{u}\right)}{\hat{s}\hat{t}(\hat{s}+\hat{t})}, \tag{4.62}$$

with the same sign convention.

$q\bar{q} \to \mathcal{Q}[n]\, g$	C_I	C_F	C^{Inc}
Ⓐ × Ⓐ	$\pm\frac{N^2-4}{4N^3}$	$\pm\frac{N^2-4}{8N}$	$\pm\frac{(N^2-4)(N^2+2)}{8N^3}$
Ⓐ × Ⓐ	$\pm\frac{1}{4N}$	$\pm\frac{N}{8}$	$\pm\frac{N^2+2}{8N}$
Ⓐ × Ⓒ	$-\frac{1}{8N}$	$-\frac{N}{8}$	$-\frac{N^2+1}{8N}$
Ⓐ × Ⓓ	$\frac{1}{8N}$	0	$\frac{1}{8N}$
Ⓒ × Ⓒ	$\mp\frac{1}{8N^3}$	$\pm\frac{N^2-1}{8N}$	$\pm\frac{N^4-N^2-1}{8N^3}$
Ⓒ × Ⓓ	$\mp\frac{N^2+1}{8N^3}$	$\mp\frac{1}{8N}$	$\mp\frac{2N^2+1}{8N^3}$
Ⓓ × Ⓓ	$\mp\frac{1}{8N^3}$	$\mp\frac{1}{8N}$	$\mp\frac{N^2+1}{8N^3}$

TABLE 4.7: Non-zero color factors within the CGI framework for the $q\bar{q} \to J/\psi[^1S_0^{(8)}]\, g$ and $q\bar{q} \to J/\psi[^3P_J^{(8)}]\, g$ (first row) and $q\bar{q} \to J/\psi[^3S_1^{(8)}]\, g$ (following rows) channels; the meaning of diagram letters can be found in Appendix B. Upper (lower) sign is for a quark (antiquark) parton coming from the polarized proton.

Finally, we have to consider the $q\bar{q}$ case. From the polarized proton, one can pick up either a quark or an antiquark. The corresponding color factors are shown in Tab. 4.7, with the upper sign referring to the former case, while the lower sign to the latter. Similarly to the previous subprocess, in the $^3S_1^{(8)}$ wave two diagrams (Ⓑ and Ⓐ) are found to possess the same color factor, so only the latter is shown explicitly in Tab. 4.7. From this, the following process-dependent hard parts are found

$$\mathcal{H}^{\text{Inc}}_{q\bar{q}\to{}^1S_0^{(8)}g} = \pm\frac{55(4\pi\alpha_s)^3}{432M_\psi}\frac{\hat{t}^2+\hat{u}^2}{\hat{s}\,(\hat{t}+\hat{u})^2}, \tag{4.63}$$

$$\mathcal{H}^{\text{Inc}}_{q\bar{q}\to{}^3S_1^{(8)}g} = \mp\frac{(4\pi\alpha_s)^3}{648M_\psi^3}\frac{\left(10\hat{t}^2+38\hat{t}\hat{u}-71\hat{u}^2\right)\left(2\hat{s}M_\psi+\hat{t}^2+\hat{u}^2\right)}{\hat{t}\,\hat{u}\,(\hat{t}+\hat{u})^2}, \tag{4.64}$$

$$\mathcal{H}^{\text{Inc}}_{q\bar{q}\to{}^3P_J^{(8)}g} = \pm\frac{55(4\pi\alpha_s)^3}{108M_\psi^3}\frac{\left(3\hat{s}^2+7M_\psi^4\right)\left(\hat{t}^2+\hat{u}^2\right)-2\,M_\psi^2\hat{s}\left(\hat{t}^2-8\hat{t}\hat{u}+\hat{u}^2\right)}{\hat{s}\,(\hat{t}+\hat{u})^4}, \tag{4.65}$$

where the same logic for the sign order has been adopted.

4.3.2 Parameterization choices

In this section we discuss the parameterizations adopted to perform a phenomenological analysis of SSAs. The SSA is defined in Eq. (4.13) of Sec. 4.1.2, where, as already discussed, the numerator of the asymmetry is strongly dominated by the Sivers contribution.

When including TMD effects, one has to properly parameterize the non-perturbative parts entering the process. A common TMD parameterization, adopted for instance in Refs. [138, 156], expresses the TMD-PDFs in terms of collinear PDFs. The TMD-PDF dependences on the light-cone momentum fraction ξ and the transverse momentum $p_\perp$ are factorized, with the latter described via a Gaussian (or Gaussian-like) ansatz. In particular, the unpolarized TMD $f_{a/p}(\xi_a, p_{\perp a})$ for a parton (a) inside

a proton (p), with light-cone momentum fraction ξ_a and intrinsic transverse momentum $\boldsymbol{p}_{\perp a}$ ($p_{\perp a} = |\boldsymbol{p}_{\perp a}|$), is parameterized as

$$f_{a/p}(\xi_a, p_{\perp a}) = \frac{\mathrm{e}^{-p_{\perp a}^2/\langle p_{\perp a}^2\rangle}}{\pi \langle p_{\perp a}^2\rangle} f_{a/p}(\xi_a), \tag{4.66}$$

where $\langle p_{\perp a}^2\rangle$ is the average transverse momentum squared of the specific parton a, that, a priori, could depend on its flavor. For quarks and antiquarks, we adopt the results obtained in Ref. [157], leading to a common average $\langle p_{\perp q}^2\rangle = 0.25\ \mathrm{GeV}^2$. For gluons, we use a different value, $\langle p_{\perp g}^2\rangle = 1\ \mathrm{GeV}^2$, which has been found to provide a good description of the unpolarized cross section data for J/ψ production in pp collisions [137, 155].

A similar parameterization is adopted for the Sivers function,

$$\Delta^N f_{a/p^\uparrow}(\xi_a, p_{\perp a}) = 2\,\mathcal{N}_a(\xi_a)\, h(p_{\perp a}) \frac{\mathrm{e}^{-p_{\perp a}^2/\langle p_{\perp a}^2\rangle}}{\pi \langle p_{\perp a}^2\rangle} f_{a/p}(\xi_a). \tag{4.67}$$

In Eq. (4.67) we have introduced $\mathcal{N}_a(\xi_a)$ and $h(p_{\perp a})$, which are two normalization functions for the collinear and transverse parts of the Sivers function. They must be consciously chosen, so that the Sivers function fulfills its positivity bound constraint

$$\left|\Delta^N f_{a/p^\uparrow}(\xi_a, p_{\perp a})\right| \leq 2\, f_{a/p}(\xi_a, p_{\perp a}). \tag{4.68}$$

A reasonable, but at the same time simple, choice for the normalization functions is given by

$$\mathcal{N}_a(\xi_a) = N_a\, \xi_a^{\alpha_a}\, (1-\xi_a)^{\beta_a}\, \frac{(\alpha_a+\beta_a)^{\alpha_a+\beta_a}}{\alpha_a^{\alpha_a}\beta_a^{\beta_a}}, \tag{4.69}$$

with $|N_a| \leq 1$, and

$$h(p_{\perp a}) = \sqrt{2\mathrm{e}}\, \frac{p_{\perp a}}{M'} \mathrm{e}^{-p_{\perp a}^2/M'}. \tag{4.70}$$

The latter modifies, consistently, the Gaussian $p_\perp$ width for the Sivers function; this can be seen by applying the last formula into Eq. (4.67), recasting the parameterization as

$$\Delta^N f_{a/p^\uparrow}(\xi_a, p_{\perp a}) = 2\,\mathcal{N}_a(\xi_a) \frac{\sqrt{2\mathrm{e}}}{\pi} \sqrt{\frac{1-\rho_a}{\rho_a}}\, p_{\perp a} \frac{\mathrm{e}^{-p_{\perp a}^2/(\rho_a\langle p_{\perp a}^2\rangle)}}{\pi \langle p_{\perp a}^2\rangle^{3/2}} f_{a/p}(\xi_a), \tag{4.71}$$

where

$$\rho_a = \frac{M'^2}{(\langle p_{\perp a}^2\rangle^2 + M'^2)} \tag{4.72}$$

with the natural condition $0 < \rho_a < 1$.

Notice that, since for such processes we cannot employ a formal TMD factorization, even the energy scale evolution cannot be properly taken into account. On the other hand, with the previous parameterizations we include part of it, via the DGLAP evolution of the collinear PDFs.

These parameterizations will be adopted both in the GPM and CGI frameworks, in order to better exploit the role of FSIs and ISIs in the SSAs. In principle, the most interesting phenomenological analysis would be a fit of all free parameters, in particular those related to gluon TMDs. On the other hand, available data are

not enough at the moment, so this study would not be statistically founded. For this reason, in the following we will provide *maximized* (or *saturated*) estimates, following Ref. [137, 138, 154, 155]. A direct comparison with PHENIX data [42] will allow us to exploit the potential role of the GSF in these observables.

These maximized estimates are obtained by imposing $|\mathcal{N}_a(\xi_a)| = 1$ and $\rho_a = 2/3$, both for the quark and the gluon Sivers functions. Notice that this value of ρ is chosen to maximize the first moment of the Sivers function and, consequently, its effect [156].

For the sake of clarity, only the positive value of the normalization, namely $\mathcal{N}_a(\xi_a) = +1$, will be explicitly shown in the following. This means that predictions symmetric to those presented should be possible.

4.3.3 Numerical results and comparison with data

In this section, numerical estimates within CGI-GPM framework are compared both with the corresponding GPM estimates and the (few) data points provided by the PHENIX Collaboration [42]. We adopt the parameterizations presented above, using the CTEQ6L1 set [103] for the collinear unpolarized PDFs, evaluated at a scale around the J/ψ transverse mass and including DGLAP evolution.

Regarding the J/ψ formation mechanism, both the CSM and the NRQCD approaches are considered. In the first case, the production is possible only via the color-singlet channel, while in the latter also color-octet channels have to be included.

Since the SSA is defined as a ratio of cross sections, in the CSM the dependence on the nonperturbative part of the hadronization, given by the amplitude squared of the radial wave function $|R_0(0)|^2$ or equivalently by the matrix element $\langle \mathcal{O}_1^{J/\psi}[^3S_1] \rangle$, simplifies out. The same does not happen in the NRQCD approach, where a proper set of (nonperturbative) Long-Distance Matrix Element is needed.

In particular, since we are also interested in the low-P_T region, among the sets presented in Appendix A.3, we adopt here the BK11 and the SYY13 ones, since both of them are extracted including lower-P_T data. The first set is a more traditional LDME extraction, pushed down to $P_T \sim 3$ GeV and with a more comprehensive set of data, including both pp and photoproduction; the second one, somehow more peculiar, combines, in the very low-P_T region, the LDME extraction with the Collins-Soper-Sterman (CSS) procedure [126]. Thus, while the former is more solid and expected to provide predictions reliable in the whole region explored, the application of the latter may raise some tension. Indeed, in Ref. [130], they show that the cross section is dominated by CO contributions in the very small-P_T region; this implies that for this set the CS LDME is automatically set to zero. This could represent a too strong assumption in a phenomenological analysis.

Both in the numerator and the denominator, we will consider the $2 \to 1$ and $2 \to 2$ partonic subprocesses. The first ones are given by $g\,g \to J/\psi$ and $q\,\bar{q} \to J/\psi$, while the second ones gather a wider variety of subprocesses, represented by $g\,g \to J/\psi\,g$, $g\,q(\bar{q}) \to J/\psi\,q(\bar{q})$ and $q\,\bar{q} \to J/\psi\,g$.

The unpolarized cross section, entering the SSA denominator, is given (see also Eq. (4.16)) as

$$\begin{aligned} \mathrm{d}\sigma^{\mathrm{GPM}}_{2\to1} &= \sum_{a,b} \frac{\pi}{\xi_a \xi_b s^2} \int \mathrm{d}^2\boldsymbol{p}_{\perp a}\mathrm{d}^2\boldsymbol{p}_{\perp b}\, \delta^{(2)}(\boldsymbol{p}_{\perp a} + \boldsymbol{p}_{\perp b} - \boldsymbol{P}_T) \\ &\quad \times f_{a/p}(\xi_a, p_{\perp a}) f_{b/p}(\xi_b, p_{\perp b})\, \mathcal{H}^U_{a\,b\to J/\psi}, \end{aligned} \tag{4.73}$$

$$\begin{aligned} \mathrm{d}\sigma^{\mathrm{GPM}}_{2\to2} &= \frac{1}{2(2\pi)^2}\frac{1}{2s}\sum_{a,b,c} \int \frac{\mathrm{d}\xi_a}{\xi_a}\frac{\mathrm{d}\xi_b}{\xi_b}\mathrm{d}^2\boldsymbol{p}_{\perp a}\mathrm{d}^2\boldsymbol{p}_{\perp b}\, \delta(\hat{s} + \hat{t} + \hat{u} - M^2) \\ &\quad \times f_{a/p}(\xi_a, p_{\perp a}) f_{b/p}(\xi_b, p_{\perp b})\, \mathcal{H}^U_{a\,b\to J/\psi\, c}, \end{aligned} \tag{4.74}$$

where s is the total cm energy of the process, while $\boldsymbol{P}_T$ is the J/ψ transverse momentum in the cm frame. The hard parts for the subprocesses are given in Appendix B; in addition, in the formulae above a superscript U has been added to remark that these amplitudes squared refer to the unpolarized case. In Eq. (4.73) it has been possible to integrate analytically over the momentum fractions ξ_a and ξ_b, using the complete Dirac-delta function to fix them (neglecting corrections of the order $p_\perp^2/s$) as

$$\xi_a = \frac{M_T}{\sqrt{s}}\,\mathrm{e}^{y}, \quad \xi_b = \frac{M_T}{\sqrt{s}}\,\mathrm{e}^{-y}, \tag{4.75}$$

with $M_T = \sqrt{M^2 + \boldsymbol{P}_T^2}$ being the J/ψ transverse mass and y its rapidity. This is valid independently of the parton type and flavor. A further simplification can be encountered once the parameterization given in Sec. 4.3.2 is inserted in Eq. (4.73). In this way, the integrals over the parton transverse momenta can be analytically carried out, finding

$$\begin{aligned} 2\,\mathrm{d}\sigma^{\mathrm{GPM}}_{2\to1} &= \frac{2}{s^2}\sum_{a,b}\frac{1}{\xi_a\xi_b}\frac{1}{\langle p^2_{\perp a}\rangle + \langle p^2_{\perp b}\rangle}\exp\left(-\frac{P_T^2}{(\langle p^2_{\perp a}\rangle + \langle p^2_{\perp b}\rangle)}\right) \\ &\quad \times f_{a/p}(\xi_a, p_{\perp a}) f_{b/p}(\xi_b, p_{\perp b})\, \mathcal{H}^U_{a\,b\to J/\psi}\,. \end{aligned} \tag{4.76}$$

On the other hand, in the $2\to2$ case the integrals over the momentum fractions and the transverse momenta can be performed only numerically. For completeness, we recall that in Eq. (4.74) we have integrated over the unobserved final parton phase space, getting

$$\begin{aligned} \int \frac{\mathrm{d}^3\boldsymbol{p}_c}{2E_c(2\pi)^3}(2\pi)^4\delta^{(4)}(p_a + p_b - P_\psi - p_c) &= (2\pi)\int \mathrm{d}^4 p_c\, \delta(p_c)^2\delta^{(4)}(p_a + p_b - P_\psi - p_c) \\ &= (2\pi)\,\delta\left((p_a + p_b - P_\psi)^2\right) \\ &= (2\pi)\,\delta(\hat{s} + \hat{t} + \hat{u} - M^2)\,. \end{aligned} \tag{4.77}$$

Numerical results for the unpolarized cross section are shown in Fig. 4.7. The two theoretical curves are obtained adopting the NRQCD approach, BK11 (left panel) and SYY13 (right panel) sets, as a function of the J/ψ transverse momentum, P_T, and at fixed rapidity ($y = 0$). The calculation is taken from Ref. [155], while the corresponding study within the CSM was done in Ref. [137]. The bands are obtained considering the factorization scale variation $M_T/2 \le \mu_F \le 2\,M_T$, with the central value given by $\mu_F = M_T$. The comparison with PHENIX data [41] shows a good agreement between the predictions and the experimental values.

By studying the parton and color-state decomposition, Fig. 4.8, it is clear that the

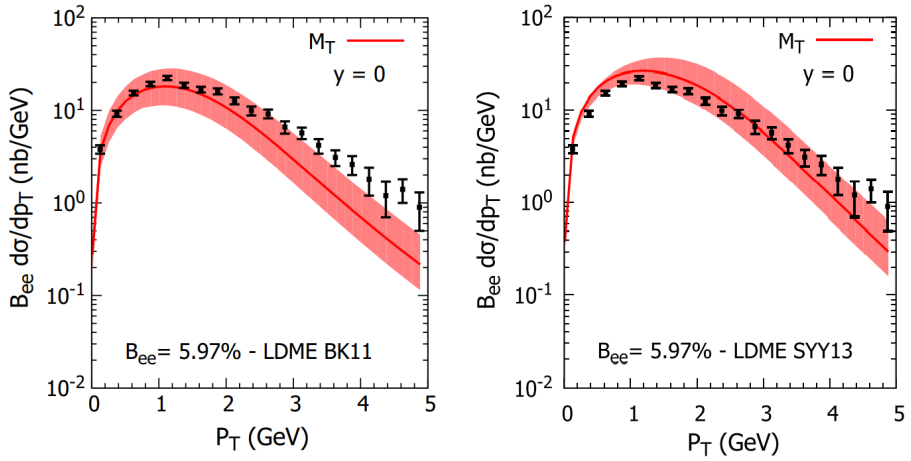

FIGURE 4.7: Estimates of the cross section for J/ψ production in unpolarized pp collisions as a function of P_T at mid-rapidity, within the NRQCD approach and adopting the BK11 (left panel) and SYY13 (right panel) sets. Central values are evaluated at the factorization scale $\mu_F = M_T$, while the uncertainty bands take into account its variation from $M_T/2$ to $2\,M_T$. Data points are from Ref. [41]; figures are taken from Ref. [155].

differential cross section is dominated by the gluon-gluon contributions, both via the CO state (blue dashed line) and, at least in the low-P_T region, via the CS one (green dot-dashed line). On this basis, it is reasonable to expect a high sensibility to the gluon Sivers function in this region. Notice that while the CS wave (left panel) undershoots the data, a proper analysis within the CSM and still adopting the GPM approach, as discussed in Ref. [137], shows a fairly good agreement between data and theoretical estimates in the small-P_T region. It is also important to observe that, within a collinear framework, by including higher-order corrections within the CSM the data description improves significantly [10].

Moving to the numerator of the asymmetry, we can evaluate it adopting either the GPM or the CGI-GPM approach. In both cases, in the $2 \to 1$ channel the light-cone momentum fractions are fixed as in Eq. (4.75)

$$\begin{aligned} \mathrm{d}\Delta\sigma^{\mathrm{GPM}}_{2\to1} &= \frac{\pi}{\xi_a\xi_b s^2}\sum_{a,b}\int \mathrm{d}^2\boldsymbol{p}_{\perp a}\mathrm{d}^2\boldsymbol{p}_{\perp b}\,\delta^{(2)}(\boldsymbol{p}_{\perp a}+\boldsymbol{p}_{\perp b}-\boldsymbol{P}_T)\,\cos\phi_a \\ &\quad\times \Delta^N f_{a/p^\uparrow}(\xi_a,p_{\perp a}) f_{b/p}(\xi_b,p_{\perp b})\,\mathcal{H}^U_{a\,b\to J/\psi}, \qquad (4.78) \\ \mathrm{d}\Delta\sigma^{\mathrm{CGI}}_{2\to1} &= \frac{\pi}{\xi_a\xi_b s^2}\int \mathrm{d}^2\boldsymbol{p}_{\perp a}\mathrm{d}^2\boldsymbol{p}_{\perp b}\,\delta^{(2)}\boldsymbol{p}_{\perp a}+\boldsymbol{p}_{\perp b}-\boldsymbol{P}_T)\,\cos\phi_a \\ &\quad\times\Big[\Delta^N f_{g/p^\uparrow}(\xi_a,p_{\perp a}) f_{g/p}(\xi_b,p_{\perp b})\,\Big(\mathcal{H}^{\mathrm{Inc}\ (f)}_{g\,g\to J/\psi}+\mathcal{H}^{\mathrm{Inc}\ (d)}_{g\,g\to J/\psi}\Big) \\ &\quad+\Delta^N f_{q/p^\uparrow}(\xi_a,p_{\perp a}) f_{\bar q/p}(\xi_b,p_{\perp b})\,\mathcal{H}^{\mathrm{Inc}}_{q\,\bar q\to J/\psi} \\ &\quad+\Delta^N f_{\bar q/p^\uparrow}(\xi_a,p_{\perp a}) f_{q/p}(\xi_b,p_{\perp b})\,\mathcal{H}^{\mathrm{Inc}}_{\bar q\,q\to J/\psi}\Big], \qquad (4.79) \end{aligned}$$

and adopting the TMD parameterizations

$$\begin{aligned} \mathrm{d}\Delta\sigma^{\mathrm{GPM}}_{2\to1} &= \frac{2\sqrt{2\mathrm{e}}}{s^2}\sum_{a,b}\frac{1}{\xi_a\xi_b}\frac{\sqrt{\rho_a(1-\rho_a)\,\langle p^2_{\perp a}\rangle}}{(\rho_a\,\langle p^2_{\perp a}\rangle+\langle p^2_{\perp b}\rangle)^2}\rho_a P_T\exp\left(-\frac{P_T^2}{(\rho_a\,\langle p^2_{\perp a}\rangle+\langle p^2_{\perp b}\rangle)}\right) \\ &\quad\times\mathcal{N}_a(\xi_a) f_{a/p}(\xi_a,p_{\perp a}) f_{b/p}(\xi_b,p_{\perp b})\,\mathcal{H}^U_{a\,b\to J/\psi}\,, \qquad (4.80) \end{aligned}$$

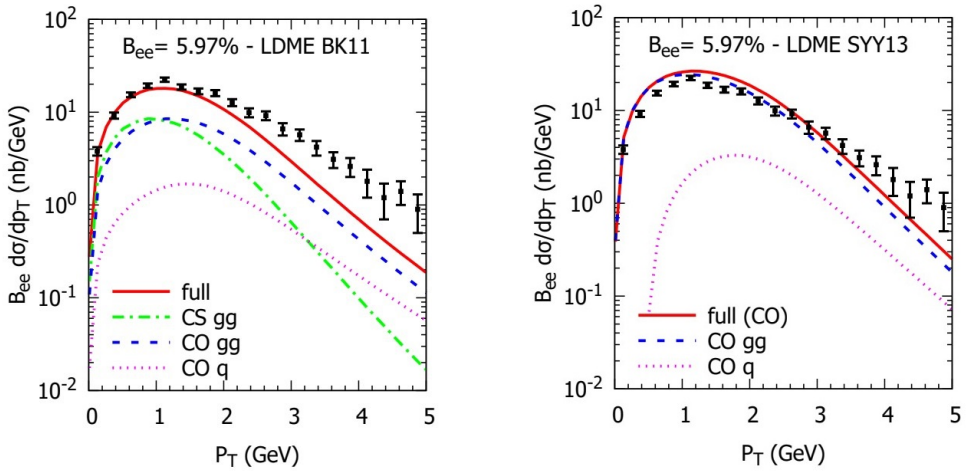

FIGURE 4.8: Partonic decomposition of the results in Fig. 4.7. Figures are taken in Ref. [155].

$$\mathrm{d}\Delta\sigma^{\mathrm{CGI}}_{2\to1} = \frac{2\sqrt{2\mathrm{e}}}{s^2}\sum_{a,b}\frac{1}{\xi_a\xi_b}\frac{\sqrt{\rho_a(1-\rho_a)\,\langle p^2_{\perp a}\rangle}}{(\rho_a\,\langle p^2_{\perp a}\rangle + \langle p^2_{\perp b}\rangle)^2}\rho_a P_T \exp\left(-\frac{P_T^2}{(\rho_a\,\langle p^2_{\perp a}\rangle + \langle p^2_{\perp b}\rangle)}\right) \times \mathcal{N}_a(\xi_a) f_{a/p}(\xi_a, p_{\perp a}) f_{b/p}(\xi_b, p_{\perp b})\,\mathcal{H}^{Inc}_{a\,b\to J/\psi}. \tag{4.81}$$

Notice that, since the process-dependent gluon hard part is *null* ($\mathcal{H}^{\mathrm{Inc}\ (f/d)}_{gg\to J/\psi} = 0$) as shown in Sec. 4.3.1, in Eq. (4.81) the hard part $\mathcal{H}^{Inc}_{a\,b\to J/\psi}$ can only assume the forms $\mathcal{H}^{Inc}_{q\,\bar{q}\to J/\psi}$ or $\mathcal{H}^{Inc}_{\bar{q}\,q\to J/\psi}$.[6] On the contrary, all channels are active in the GPM case, Eq. (4.80).

Like in the denominator, the $2\to2$ contribution to the numerator is computable only numerically, and in the two frameworks is given by

$$\mathrm{d}\Delta\sigma^{\mathrm{GPM}}_{2\to2} = \frac{1}{2(2\pi)^2}\frac{1}{2s}\int\frac{\mathrm{d}\xi_a}{\xi_a}\frac{\mathrm{d}\xi_b}{\xi_b}\mathrm{d}^2\boldsymbol{p}_{\perp a}\mathrm{d}^2\boldsymbol{p}_{\perp b}\,\delta(\hat{s}+\hat{t}+\hat{u}-M^2)\,\cos\phi_a \times \Delta^N f_{a/p^\uparrow}(\xi_a, p_{\perp a})\, f_{b/p}(\xi_b, p_{\perp b})\,\mathcal{H}^{U}_{a\,b\to J/\psi\,c}, \tag{4.82}$$

[6] Notice that the first parton in the subscript is the one coming from the polarized proton.

$$
\begin{aligned}
\mathrm{d}\Delta\sigma^{\mathrm{CGI}}_{2\to 2} = \frac{1}{2(2\pi)^2}\frac{1}{2s}\int \frac{\mathrm{d}\xi_a}{\xi_a}\frac{\mathrm{d}\xi_b}{\xi_b}\mathrm{d}^2\boldsymbol{p}_{\perp a}\mathrm{d}^2\boldsymbol{p}_{\perp b}\,\delta(\hat{s}+\hat{t}+\hat{u}-M^2)\,\cos\phi_a \\
\times\Bigg\{\Delta^N f_{g/p^\uparrow}(\xi_a,p_{\perp a})\Big[f_{g/p}(\xi_b,p_{\perp b})\,\Big(\mathcal{H}^{\mathrm{Inc}\ (f)}_{g\,g\to J/\psi\,g}+\mathcal{H}^{\mathrm{Inc}\ (d)}_{g\,g\to J/\psi\,g}\Big) \\
+ f_{q/p}(\xi_b,p_{\perp b})\,\Big(\mathcal{H}^{\mathrm{Inc}\ (f)}_{g\,q\to J/\psi\,q}+\mathcal{H}^{\mathrm{Inc}\ (d)}_{g\,q\to J/\psi\,q}\Big) \\
+ f_{\bar{q}/p}(\xi_b,p_{\perp b})\,\Big(\mathcal{H}^{\mathrm{Inc}\ (f)}_{g\,\bar{q}\to J/\psi\,\bar{q}}+\mathcal{H}^{\mathrm{Inc}\ (d)}_{g\,\bar{q}\to J/\psi\,\bar{q}}\Big)\Big] \\
+\Delta^N f_{q/p^\uparrow}(\xi_a,p_{\perp a})\Big(f_{g/p}(\xi_b,p_{\perp b})\,\mathcal{H}^{\mathrm{Inc}}_{q\,g\to J/\psi\,q}+f_{\bar{q}/p}(\xi_b,p_{\perp b})\,\mathcal{H}^{\mathrm{Inc}}_{q\,\bar{q}\to J/\psi\,g}\Big) \\
+\Delta^N f_{\bar{q}/p^\uparrow}(\xi_a,p_{\perp a})\Big(f_{g/p}(\xi_b,p_{\perp b})\,\mathcal{H}^{\mathrm{Inc}}_{\bar{q}\,g\to J/\psi\,\bar{q}}+f_{q/p}(\xi_b,p_{\perp b})\,\mathcal{H}^{\mathrm{Inc}}_{\bar{q}\,q\to J/\psi\,g}\Big)\Bigg\}.
\end{aligned}
\tag{4.83}
$$

In all previous formulae, whenever a quark or antiquark label is present, a sum over flavors up to the strange quark/antiquark is understood.

All results are in principle affected by theoretical uncertainties coming from the TMD frameworks and the quarkonium formation models used, as well as from errors in the transverse-momentum dependence of the observable. On the other hand, at the moment a reliable way to evaluate this combination of uncertainties is not possible. Despite this, it is reasonable to expect that their impact, even if potentially sizeable, is reduced by the fractional nature of the SSA. Furthermore, the predictions are not based on specific extractions of TMDs, but rather are intended to provide an estimate of the potentially maximized asymmetry, highlighting the effect of the inclusion of ISIs and FSIs. Therefore, at this level, a detailed study of the uncertainty sources is not relevant.

In Fig. 4.9 we show estimates of SSAs for quarkonium production at the cm energy of $\sqrt{s} = 200$ GeV, as a function of P_T in the forward region ($x_F > 0$), while in Fig. 4.10 the same results are presented for the backward region ($x_F < 0$). We recall that the Feynman-x is defined as

$$
x_F = \frac{P_L}{P_{L\mathrm{max}}},
\tag{4.84}
$$

where P_L is the longitudinal component of the J/ψ momentum, while $P_{L\mathrm{max}}$ is the maximal absolute value that this component can reach. In both figures, the upper panels refer to the BK11 set choice, while the lower ones to the SYY13. All predictions are compared with data points collected by the PHENIX Collaboration [42].

These figures give a very complete picture, with predictions for NRQCD and CSM in either the GPM or the CGI frameworks. While within the CSM only the GSF can be active, in particular the f-type one in the CGI approach, in principle more channels could play a role within the NRQCD approach. In the following, all cases are shown for the CGI+NRQCD framework, while within the GPM+NRQCD one, only the dominant gg contribution is given. A complete description for the latter case, including subdominant contributions, can be found in Ref. [155]. Moreover, in the lower panels, curves are evaluated only within the NRQCD approach, since the SYY13 set excludes the CS wave contribution.

Let us now discuss some phenomenological aspects, starting from the CSM. The differences between the predictions in the GPM (green dashed line) and in the CGI-GPM (light-blue dotted line) approaches can be directly understood by looking at

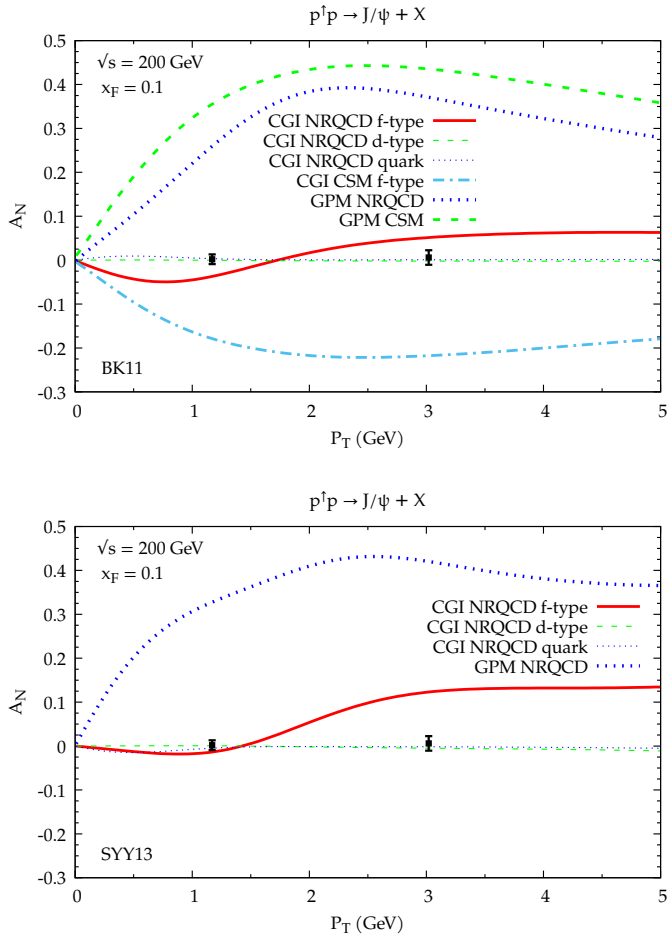

FIGURE 4.9: Maximized SSA estimates for the process $p^{\uparrow}p \to J/\psi + X$ as a function of P_T at $\sqrt{s} = 200$ GeV and for $x_F = +0.1$. We consider both the CGI-GPM and the GPM, combined with the CSM and the NRQCD approaches, adopting two LDME sets: the BK11 (upper panel) and SYY13 (lower panel). Data points are taken from Ref. [42]. Figures are taken from Ref. [154].

Eq. (4.49). Estimates of maximized asymmetries are sizeable both in the forward and the backward regions, and in both approaches. Hence, a comparison with PHENIX data suggests the potential strong suppression of the GSF, at least in this framework.

Moving to the NRQCD approach, there is a clear difference when the CGI approach is adopted compared to the GPM case. The inclusion of CO channels in the GPM approach (upper panels) leads to large SSAs (dark-blue dotted line). In this case, the asymmetry is not drastically reduced compared to the corresponding CSM case; indeed, it is even larger at very low P_T in the backward region. It is fair to expect that future data could help in putting stronger constraints on the gluon Sivers parameterization within the GPM.

Finally, the impact of the inclusion of ISIs and FSIs can be observed by looking at the different curves within the CGI+NRQCD scenario: solid red line for the f-type GSF, while dotted green and thinner dotted blue lines for, respectively, the d-type GSF and the quark Sivers function. The latter, as found in the GPM, is compatible with *zero*, while the gluon d-type, even if not exactly *null* as in the CSM case, is still negligible. The only potentially sizeable contribution is then given by the gluon

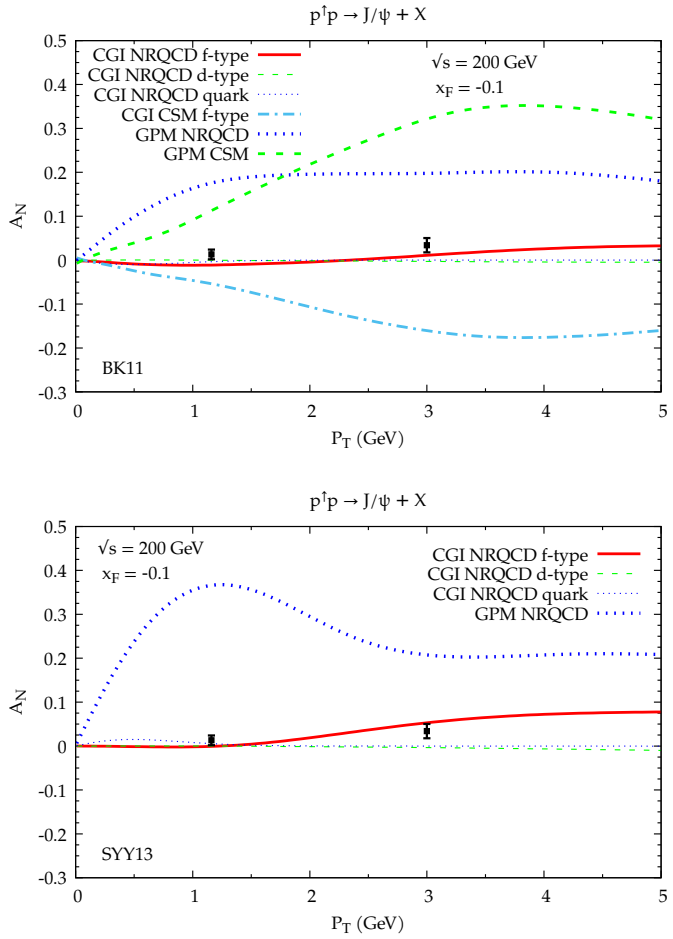

FIGURE 4.10: Same scenarios as in Fig. 4.9 but for the backward region ($x_F = -0.1$). Figures are taken from Ref. [154].

f-type Sivers function, which is found to be highly suppressed compared to other cases. Indeed, at variance with what found in the CGI+CSM framework, the backward region loses the potential role in constraining the gluon Sivers function, since maximized estimates are already compatible with data within the CGI+NRQCD framework, and in general are very small. Similarly, in the forward region, even if the estimates are a bit larger, the possibility to constrain the f-type GSF is still limited.

A complementary picture can be achieved by studying the SSA at fixed P_T as a function of x_F. In Fig. 4.11 we present the corresponding estimates at $P_T = 1.65$ GeV, adopting the kinematic set-up of the PHENIX experiment [42]. As one can see, this turns out to not be an optimal choice to constrain the f-type GSF in the NRQCD+CGI framework. Comparing with the previous figures, and as also pointed out in Ref. [154], a slightly higher P_T value (around 3 GeV) could provide a x_F distribution sizeable enough to perform more effective phenomenological studies on the f-type GSF.

Finally, it is worth addressing, through a wave decomposition analysis, the sources of cancellation that leads to such smaller estimates when the CGI+NRQCD framework is applied. In all cases discussed below, we adopt the BK11 set. Similar conclusions can be drawn also for the other LDME set. In the following figures, the

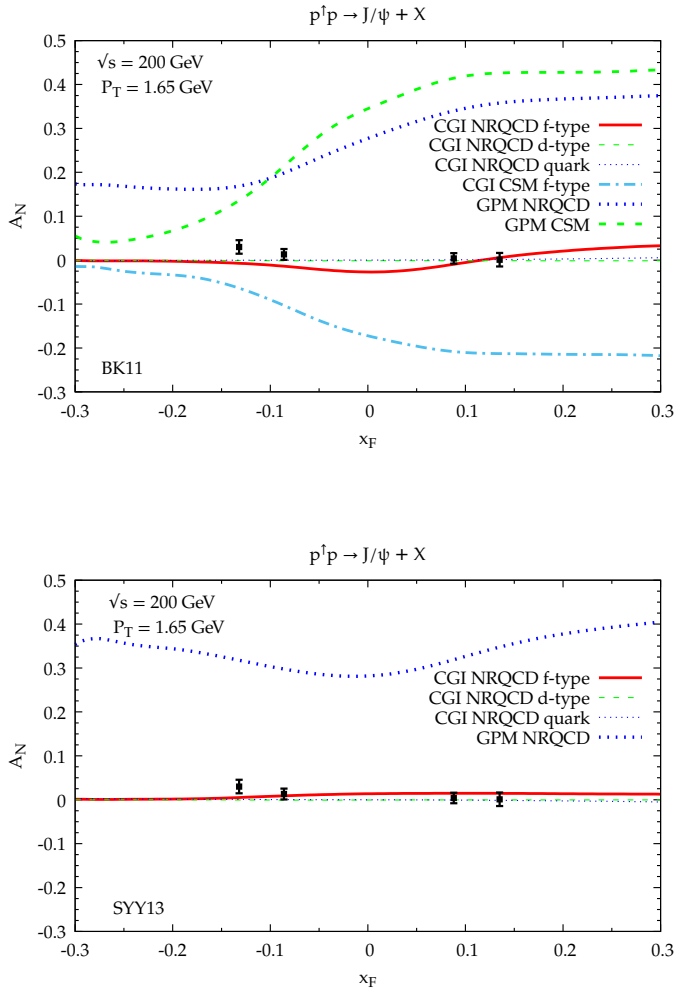

FIGURE 4.11: Same scenarios as in Fig. 4.9 but as a function of x_F at fixed $P_T = 1.65$ GeV. Figures are taken from Ref. [154].

red solid lines refer to the dominant gg contribution to A_N (including both $2 \to 1$ and $2 \to 2$ channels). For the CGI, this corresponds to the red solid lines in Figs. 4.9-4.11, while for the GPM it corresponds to the dark-blue dotted lines.

Starting from Fig. 4.12, a strong cancellation between the (CO) ${}^1S_0^{(8)}$ state and the P-wave sum ${}^3P_{[J]}^{(8)}$ occurs both in the CGI (upper panel) and the GPM (lower panel) approaches, even if with different magnitudes; this is a consequence of the relative sign of the corresponding LDMEs in the BK11 set. Notice that, since this is a wave decomposition, the single wave can potentially exceed the $|A_N| \leq 1$ limit, as happens in the GPM (lower panel) for the ${}^1S_0^{(8)}$ and ${}^3P_J^{(8)}$-waves. Moreover, there is a clear difference in the behavior of the main contributions (${}^1S_0^{(8)}$ and ${}^3P_J^{(8)}$) within the two frameworks, when one focuses on the small-P_T region. While the (relative) sign of the two curves is fixed in the whole spectrum within the GPM approach, in the CGI case a change of sign is present for both waves at $P_T \sim 1$ GeV. This is a specific characteristic of the $2 \to 2$ channel and indeed it plays a role also in the GPM case, suggesting that this effect comes from the parton dynamics and the modulation of the Sivers azimuthal phase. In the end, within the GPM, the $2 \to 1$ channel, which is significant only in the small-P_T region, is able to compensate this effect, leading

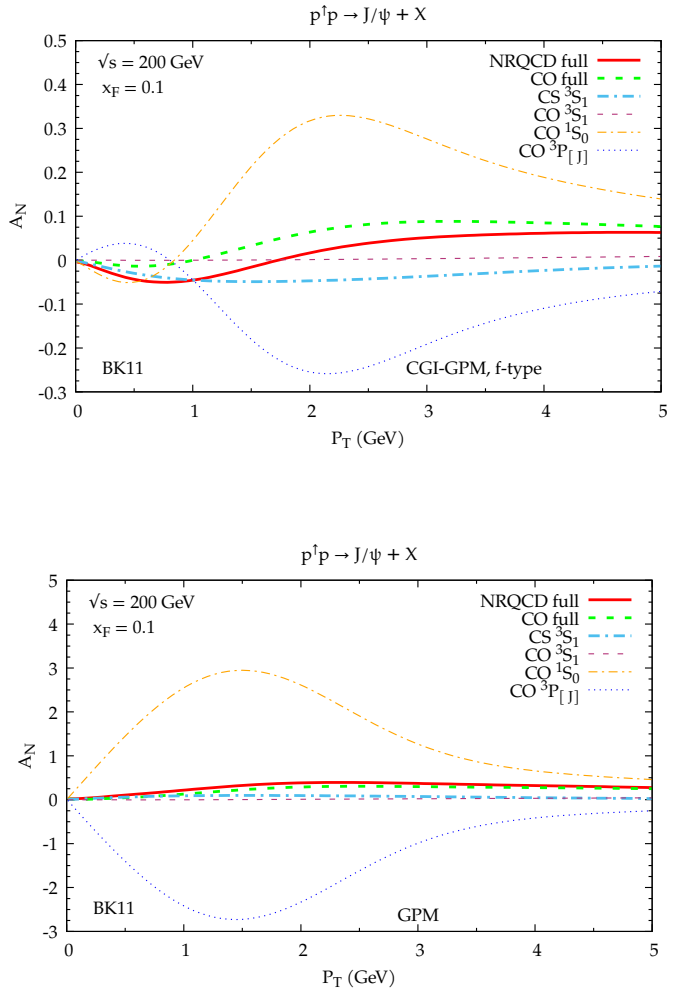

FIGURE 4.12: Wave decomposition of the maximized gluon Sivers asymmetry estimate in the forward region ($x_F = +0.1$) within the NRQCD approach, using the BK11 set. Upper panel: CGI-GPM f-type GSF; lower panel: GPM GSF. The red solid line corresponds to the full result. Figures taken from Ref. [154].

to CO curves with a define sign. We recall once again that the $2 \to 1$ channel turns out to be *null* when ISIs and FSIs are included (see Sec. 4.3.1), so this compensation effect is missing in the CGI framework.

Another source of suppression of the CGI results is due to the cancellation between the CO waves sum and the CS wave (possible only with the BK11 set). Indeed, while in the GPM approach both CS and CO estimates have the same sign, in the CGI approach the CS sign is reversed.

In the backward region, Fig. 4.13 (upper panel), while the same sources of suppression are present, there is another similar effect coming from the $\cos\phi_a$ modulation, that upon integration is even more effective in reducing the asymmetry. The reason is that, in this region, the hard parts depend only marginally (through the Mandelstam variables) on this phase.

Furthermore, from the lower panel of Fig. 4.13, showing the decomposition at fixed $P_T = 1.65$ GeV, it is clear that the above-mentioned suppression sources work actively in all x_F regions. This leads, both in the forward and backward regions, to the observed relative small maximized A_N from the f-type GSF within NRQCD.

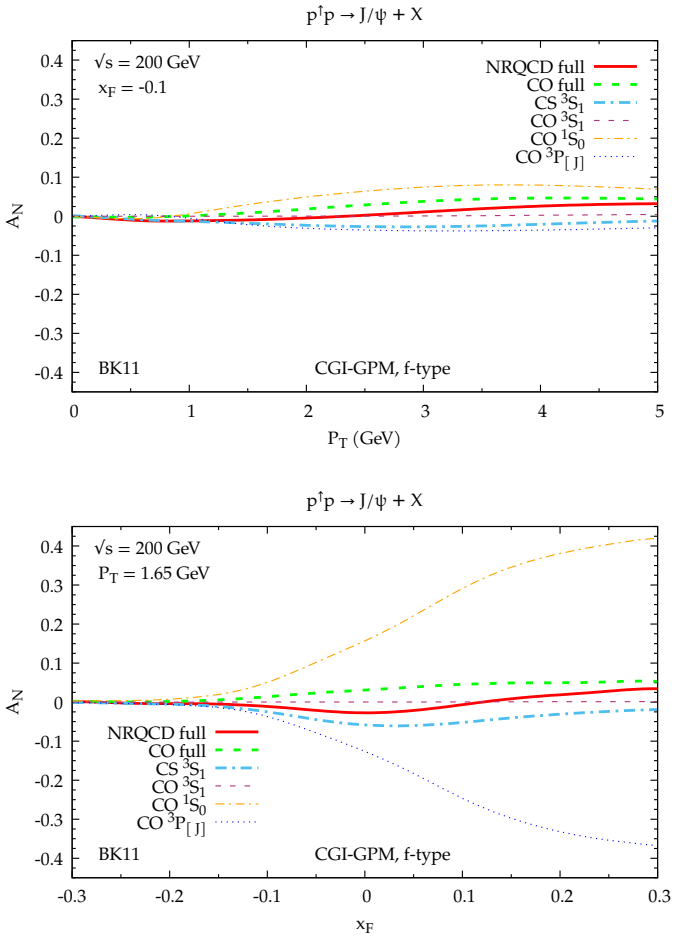

FIGURE 4.13: As in Fig. 4.12 but limited to the GSF in the CGI+NRQCD framework, as a function of P_T at fixed $x_F = -0.1$ (upper panel) and as a function of x_F at $P_T = 1.65$ GeV (lower panel). The red solid lines correspond to the full result. Figures taken from Ref. [154].

With this deep insight on the CGI+NRQCD framework, via the wave decomposition, we can also better understand the differences between this phenomenological approach and the GPM one, and consequently the impact of including ISIs and FSIs in the picture. Even if less promising compared to other frameworks, by adopting different kinematic choices one can still expect to carry out useful phenomenological analyses from which the role of the gluon distributions can be better disentangled.

As a final remark, we recall that all previous results are obtained considering the J/ψ yield in the direct channel. Nevertheless, we know that a significant amount of J/ψ data (almost 40%) comes from the χ_c feed-down contribution, see Refs. [10, 158]. Its inclusion may then lead to different SSA estimates compared to those discussed here. On the other hand, this effect requires further investigation beyond the scope of this thesis.

4.3.4 Predictions for future experiments

In conclusion of this chapter, we present some estimates for a selection of upcoming experiments. The focus will be given to the CGI+NRQCD approach. Nevertheless, predictions for the GPM and the CGI+CSM frameworks will also be given, at least

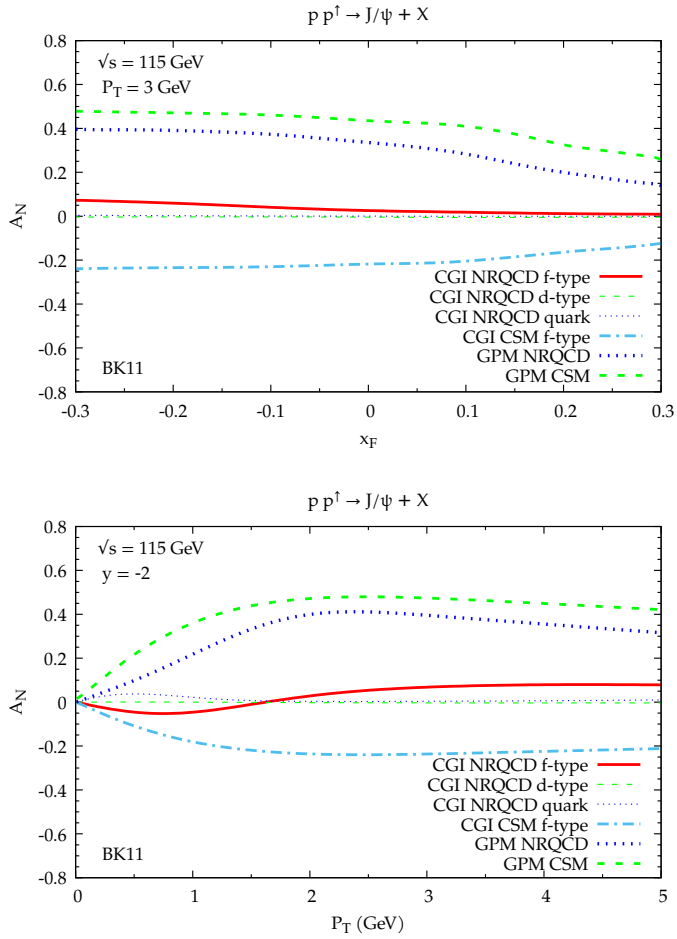

FIGURE 4.14: SSA estimates for $p^{\uparrow}p \to J/\psi + X$ at LHC-fixed target, evaluated at $\sqrt{s} = 115$ GeV. The upper panel shows the estimate at fixed $P_T = 3$ GeV as a function of x_F, while the lower panel is for fixed rapidity $y = -2$ as a function of P_T. In both cases, NRQCD curves are obtained adopting the BK11 set. Figures are taken from Ref. [154].

for the dominant contributions. We will consider only one LDME set, namely the BK11 one. In particular, we discuss:

1. LHC in fixed-target mode proposed by the LHCspin Collaboration, Refs. [159–162];

2. NICA SPD, Ref. [163];

3. SpinQuest at Fermilab, Ref. [164–166].

We recall that we keep adopting $\mathcal{N}_a(\xi_a) = 1$ and that, therefore, the sign of the maximized SSA could be reversed.

LHC fixed-target is a side-experiment proposed by the LHCb Collaboration. This installation could provide useful data in the intermediate-Q^2 and high-x region, improving the kinematic range and accuracy level reached by other experiments. It is expected to operate at cm energies around $\sqrt{s} = 115$ GeV, as adopted in our analysis. In Fig. 4.14, the upper panel, we show SSA estimates as a function of x_F at fixed

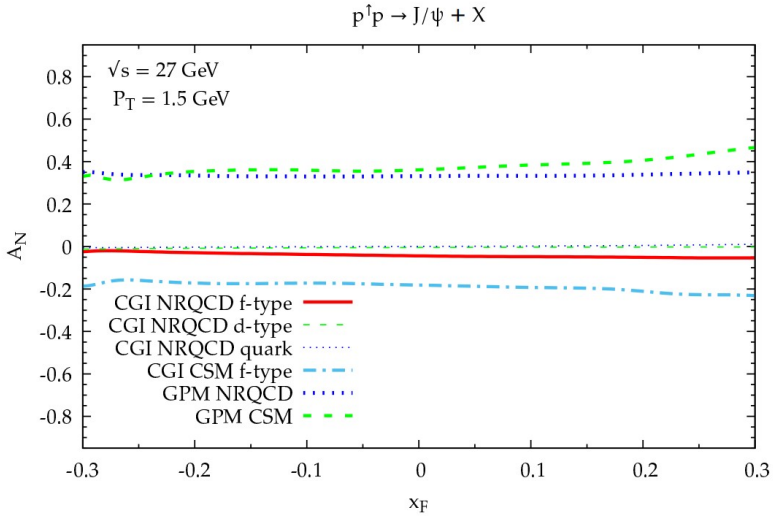

FIGURE 4.15: SSA estimates for $p^{\uparrow}p \to J/\psi + X$ at NICA, at $\sqrt{s} = 27$ GeV and fixed $P_T = 1.5$ GeV as a function of x_F. NRQCD curves are obtained adopting the BK11 set.

$P_T = 3$ GeV, while in the lower panel are at fixed rapidity $y = -2$ as a function of P_T. Notice that, due to the experimental configuration, the backward rapidity region refers to the forward one for the polarized proton target.

Experimental measurements will be extremely important to set a constraint on the Sivers functions. From the upper panel, we can see that the maximized asymmetry related to the f-type GSF could reach $A_N \sim 5\%$ in the backward rapidity; this value is potentially accessible experimentally. This is in general true for very small (less than 1 GeV) or large (greater than 3 GeV) P_T values, as can be seen from the estimates at $y = -2$ (lower panel). All other scenarios taken into account provide in general much higher A_N maximized estimates, which turn out to be in principle easier to constrain.

NICA is a planned experiment to be set in Russia. The kinematic coverage in the (x, Q^2) plane is partially overlapping with the one proposed by AFTER@LHC [160], but at lower energy (up to $\sqrt{s} = 27$ GeV) and with the possibility to polarize both (proton/deuterium) beams.

This would allow to explore not only SSAs in $pp^{\uparrow}$ collisions, but other physical quantities. In Fig. 4.15 we show maximized estimates for A_N at fixed $P_T = 1.5$ GeV for several scenarios. Also in this case, the f-type GSF provides maximized asymmetries around $A_N \sim 5\%$ in the forward region ($x_F > 0$). Other scenarios are even more promising, with $A_N \sim 40\%$ for the GPM+NRQCD and GPM+CSM frameworks and $A_N \sim 20\%$ for the CGI+CSM one. Moreover, we notice that the asymmetry value is almost stable when moving from the forward to the backward region.

We can conclude that this experimental option can represent a good tool to test and improve potential constraints obtained from other experiments, like the LHC in the fixed-target mode.

SpinQuest is a proposed experiment at FermiLab. Its main goal is somehow different from the previous ones, since it aims to explore the spin structure of the proton by looking at the contributions from the *sea* quarks. For this reason, they will operate at a cm energy even lower compared to NICA, $\sqrt{s} = 15$ GeV.

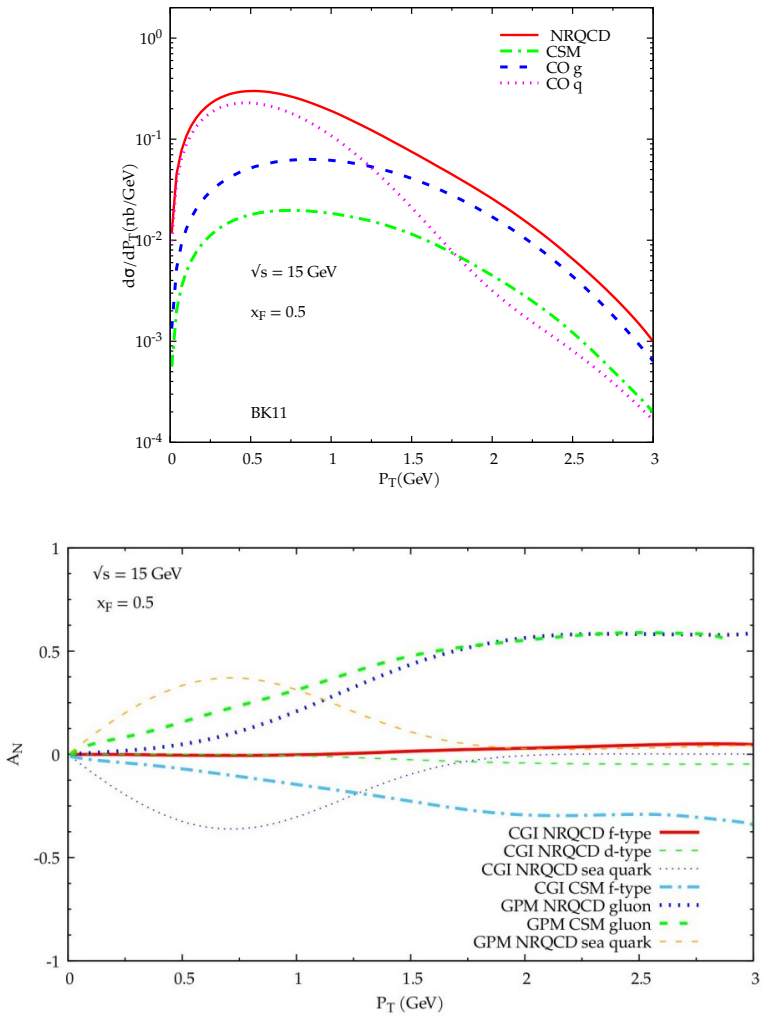

FIGURE 4.16: Upper panel: estimates for the unpolarized cross section for SpinQuest kinematics, at $\sqrt{s} = 15$ GeV and $x_F = 0.5$ as a function of P_T, within the NRQCD approach. Lower panel: maximized A_N estimates in different frameworks. Parton/color configuration decomposition is also shown. In both panels, curves are obtained adopting the BK11 set.

As one can see from Fig. 4.16 (upper panel), at low P_T ($P_T \lesssim 1$ GeV) the unpolarized cross section is dominated by the CO quark contribution, which is the sum of different channels where quark and/or antiquark are involved.

Moreover, SSA estimates, Fig. 4.16 (lower panel), clearly show that, both in the GPM+NRQCD and the CGI+NRQCD frameworks at $P_T \lesssim 1$ GeV, the result is dominated by the quark/antiquark channels. A more detailed analysis would show that, in the $P_T \lesssim 1$ GeV region, the $2 \to 1$ channel with an antiquark in the polarized proton is actually the dominant one.

At higher-P_T values, A_N is once again dominated by gluon channels, which can be used as an additional tool to learn on the GSFs. Note that in this case, within the CGI+NRQCD framework, at high-P_T the d- and f-type GSFs are both not negligible (thinner dashed green line and red solid line in the lower panel). On the other hand, their small contribution ($A_N \lesssim 5\%$ in size) makes their extraction very difficult.

The study of the GSF in the other scenarios seems more promising. As one can see, the maximized f-type GSF in the CGI+CSM framework gives A_N up to 35% at $P_T \sim 3$ GeV, while the GSF within the GPM+NRQCD and GPM+CSM approaches

leads to $A_N \gtrsim 50\%$ at $P_T > 2$ GeV. This means that any experimental information in this region could help in putting strong constraints on the GSFs.

Chapter 5

Summary and conclusions

Quarkonia, such as J/ψ mesons, are important tools to deepen our understanding of QCD. In this thesis, we adopted the NRQCD approach to study J/ψ production in both SIDIS and pp collisions.

In Chapter 2, we considered the J/ψ polarization as a potential observable to discern among different hadronization models. Thus, we presented the formalism to evaluate the structure functions $\mathcal{W}_T$, $\mathcal{W}_L$, $\mathcal{W}_\Delta$, $\mathcal{W}_{\Delta\Delta}$, and consequently the polarization parameters λ, μ, ν, for polarized J/ψ production in SIDIS. We firstly studied the kinematic region where the transverse momentum of the exchanged virtual photon is large, namely $q_T \gg \Lambda_{\rm QCD}$, and for which collinear factorization applies. We then evaluated the aforementioned helicity structure functions within the NRQCD approach, up to the order $\alpha^2\alpha_s^2$, considering CO contributions up to the order v^4 w.r.t. the CS one. The explicit form of these quantities depends on the reference frame choice: we presented our results in the *Gottfried-Jackson* frame and derived the transformations to obtain the same quantities in the *Target*, *Helicity* and *Collins-Soper* frames.

Using these results, we presented our predictions of the polarization parameters λ, ν and μ at the EIC kinematics. We proposed to study these parameters w.r.t. both z and especially $P_\perp$, *i.e.* the J/ψ energy fraction and its transverse momentum measured in a frame where the photon and proton momenta have no transverse components. Indeed, it turned out that differences between the CSM and the NRQCD estimates are more sizeable in the latter case, at least for the considered LDMEs. Moreover, such measurements at different energies, or equivalently proper binning in Q, provide precious information as well. Finally, by properly combining λ, μ and ν, one can construct rotational invariant quantities. At present, the experimental information on these quantities is not sufficient and, in any case, the available data are not accurate enough to draw definite phenomenological conclusions. Despite these difficulties, their study should be pursued, since they are both a test of the absence of systematic errors in the measurement and a tool to test theoretical models to a deeper extent.

We then discussed the formalism when the photon transverse momentum is small, $q_T \ll \mu$, with μ being a hard scale typical of the process. In this case, even if not formally proven, there are strong arguments in favor of the validity of TMD factorization. Thus, we evaluated the helicity structure functions up to order $\alpha^2\alpha_s$, including the same CO contributions as done in the collinear scheme. We found that the helicity structure functions do not depend on the reference frame choice at such small-q_T values. Moreover, only three of them survive: $\widetilde{\mathcal{W}}_T$, $\widetilde{\mathcal{W}}_L$ and $\widetilde{\mathcal{W}}_{\Delta\Delta}$. Quite remarkably, we found that the latter ($\widetilde{\mathcal{W}}_{\Delta\Delta}$) depends on $h_1^{\perp\, g}$, the linearly polarized gluon distribution inside an unpolarized proton. We therefore suggest novel experiments to extract this TMD distribution by looking, in the aforementioned transverse momentum domain, at the ν parameter, which is related to the $\cos 2\phi$ azimuthal

decay asymmetry of the J/ψ meson. Furthermore, we showed how both λ and ν (where for the latter we considered the saturation of the $h_1^{\perp g}$ positivity bound) are extremely sensitive to the LDME parameters. Measurements in this region are thus helpful in testing NRQCD and improving our knowledge on the CO LDMEs.

In Chapter 3, we studied the intermediate transverse momentum region (namely $\Lambda_{\rm QCD} \ll q_T \ll \mu$) to propose a correct TMD factorized form of the structure functions, which involves a TMD-PDF and a TMD shape function. We studied both the unpolarized and polarized J/ψ production cases, whose results are consistent with one another. In the former, we kept the dependence on the azimuthal angle of the J/ψ (ϕ_ψ), whilst in the latter, the considered angular dependence derives entirely from the solid angle (Ω) of the J/ψ decay products. Starting from the high transverse momentum region, we obtained the small-q_T behavior of the structure functions calculated within the collinear factorization approach. For the unpolarized case, we have that $F_{UU,\perp}$ and $F_{UU,\parallel}$ receive large logarithmic corrections at small q_T, which are instead absent in $F_{UU}^{\cos 2\phi_\psi}$. Moreover, $F_{UU}^{\cos\phi_\psi}$ is suppressed by a factor q_T/μ compared to the other structure functions. Similarly, in the polarized case it turns out that $\mathcal{W}_T$ and $\mathcal{W}_L$ receive the same type of large logarithmic corrections, absent for $\mathcal{W}_{\Delta\Delta}$, whilst $\mathcal{W}_\Delta$ is suppressed by a factor q_T/μ.

The large logarithms mentioned above can be resummed within the TMD framework. By requiring that the TMD expressions for the structure functions correctly match with the collinear factorization results in the intermediate transverse momentum region, we determined the perturbative tails of the shape functions. We found that these quantities do not depend on the J/ψ polarization, at least up to the considered α_s accuracy. Moreover, the transverse momentum dependence of these objects is independent of the quantum number of the intermediate Fock-state, except for the overall magnitude given by the corresponding LDME values. We emphasize that the results shown in this chapter are the updated version of Refs. [111, 112]. We also note that this result holds for any quarkonia with the same quantum numbers of the J/ψ, *e.g.* $\psi(2S)$ or $\Upsilon(nS)$.

On the other hand, $F_{UU}^{\cos 2\phi_\psi}$ and $\mathcal{W}_{\Delta\Delta}$ match with the TMD counterparts without the necessity to include a TMD shape function. Thus, a complete evaluation of the J/ψ production at the next α_s order and within the NRQCD framework is necessary to study the impact of TMDShFs on these structure functions. This calculation is still missing but would be very valuable.

Even if we were able to deduce the perturbative tail of these objects by adopting this matching procedure, we cannot predict their nonperturbative parts. However, their effects can be observed in J/ψ production and potentially in the polarization parameters measured at small transverse momentum. We point out that very recently an analysis of TMDShFs in SIDIS has been performed [167]. The authors evaluated the proper TMD evolution for the $\cos 2\phi_\psi$ azimuthal asymmetry accessible at the Electron-Ion Collider. On the other hand, the corresponding shape function was approximated at leading order (α_s^0), reducing the impact of smearing effects. Other studies are expected in the near future.

Finally, in Chapter 4, we considered different frameworks, within phenomenological TMD schemes, to evaluate SSAs for inclusive J/ψ production in pp collisions. More specifically, we adopted the GPM approach and its CGI extension, which includes the effects of initial- and final-state interactions. Their presence introduced new color factors, which are required to compute the *modified* hard scattering amplitudes. In this way, the process dependence coming from ISIs and FSIs is included in these hard parts. Moreover, when studying the gluon content of the SSA within the

CGI approach and at the one-gluon approximation, two independent gluon Sivers functions are needed, namely the d-type and f-type GSFs. Within the CSM, the SSA driven by the d-type GSF is exactly zero; at variance, the d-type may contribute to the SSA numerator within the NRQCD approach. Nevertheless, our predictions relative to PHENIX kinematics showed that (even if maximized) the d-type contribution is negligible compared to the f-type one. In addition, the quark content of the asymmetry is negligible compared to the gluon one, meaning that in both frameworks (CGI+CSM and CGI+NRQCD), the most sizeable contribution comes from the f-type GSF.

The inclusion of ISIs and FSIs, however, causes a significant reduction of the maximized asymmetry. This effect is more powerful when considering the NRQCD+CGI framework. In this case, the maximized asymmetry driven by the f-type GSF is (relatively) sizeable only at forward rapidities and P_T around $2-3$ GeV. This implies that, within this framework, the f-type GSF can hardly be constrained. Instead, other scenarios provide maximized asymmetries sizeable enough to be used to constrain (more) easily the corresponding GSFs.

We also computed maximized SSA estimates for upcoming experiments: LHC in a fixed target mode, NICA and SpinQuest. The first two cases have similar features discussed for the PHENIX setup, while in the latter we found that, if adopting the CGI+NRQCD framework, one may potentially have access to both the quark Sivers (at low P_T) and the d-type and f-type GSFs (at high P_T). Thus, these experiments could certainly help in shedding light on the role of the gluon Sivers function, as well as its process dependence.

We have to remark that the correct factorized description would require the presence of a TMDShF also for this process. The non-inclusion of this term may potentially invalidate future GSF extractions. Hence, it is essential to test the TMDShF universality (or some kind of modified universality) which may improve phenomenological analyses. Differently from SIDIS, pp collisions provide both unpolarized and polarized J/ψ production data to potentially test the impact of the TMDShF. Its inclusion in this process is still ongoing, however. In this context, we mention that the authors of Ref. [133] studied the small-P_T limit of the differential cross section for $pp \to J/\psi + X$ calculated within the collinear factorization approach and valid in the high transverse momentum region, with the inclusion of CO contributions. Their results suggest the need for a TMDShF, but its exact expression and its connection with the SIDIS one are still in progress. New exciting studies and outcomes in this field of research, from both the theoretical and experimental sides, are expected in the near future.

Appendix A

NRQCD in a nutshell

Within the NRQCD approach [6], we make explicit use of the non relativistic nature of the relative velocity v of the heavy quark-antiquark pair ($Q\bar{Q}$). For quarkonia like charmonium or bottomonium, for which $v^2 \approx 0.3$ or $v^2 \approx 0.1$,[1] we can identify three well-separated scales, namely $M^2 \gg (Mv)^2 \gg (Mv^2)^2$. The first is the typical scale of the quarkonium; Mv is its typical momentum scale, whose inverse is related to the size of the quarkonium itself; and the last one is its typical kinetic energy [6].

For quarkonium, we can assume $\alpha_s(M) \ll 1$,[2] hence effects at scale M, as the creation of the $Q\bar{Q}$, can be evaluated at perturbative level. Instead, effects at lower momentum scales (around Mv, Mv^2 and also $\Lambda_{\rm QCD}$) are factorized into long-distance matrix elements, which can potentially be evaluated via Lattice-QCD simulations or extracted from data. At the moment, they are obtained exclusively in the second way and, even if they are supposed to be universal, their values strongly depend on the performed fit.

These matrix elements follow a hierarchy, depending on their v^2 power dependence, which is predicted by the use of scaling rules [168]. Indeed, within the NRQCD approach, quarkonium production (or decay) is possible via a Fock-state n with different quantum numbers compared to the observed particle. The transition between the general state n and the quarkonium one is obtained via soft gluon emission.

This motivates a double expansion, w.r.t. both α_s and v. The (process-dependent) short-distance coefficients are evaluated with the usual perturbative expansion in α_s. Instead, by truncating the expansion w.r.t. v at the kth-order, we select which matrix elements to include in the long-distance part of the process. Explicitly, at leading order in v and for S-wave quarkonia, we have the color-singlet state with the same quantum numbers of the quarkonium, while higher order contributions are given by color-octet states.

We use the standard notation $n = {}^{2S+1}L_J^{(c)}$ to describe these states, where c indicates their color configuration, S their spin, L their orbital angular momentum and J their total angular momentum. In particular, for the J/ψ (${}^3S_1$ state) the main contributions, up to v^4 order compared to the leading one, are given by ${}^3S_1^{(1)}$, ${}^1S_0^{(8)}$, ${}^3S_1^{(8)}$ and ${}^3P_J^{(8)}$.

[1] We are considering natural units, for which $c = 1$.

[2] Note that $\alpha_s(M) \approx 0.24$ for charmonium and $\alpha_s(M) \approx 0.18$ for bottomonium.

For each state we have a different LDME value, which is connected to the modulus squared of the quarkonium radial wave function (R_0 or R_1). Explicitly, we have

$$\begin{aligned}\langle 0|\mathcal{O}_1(^{2s+1}S_J)|0\rangle &= \frac{N_c}{2\pi}(2J+1)|R_0^{(1)}(0)|^2,\\ \langle 0|\mathcal{O}_8(^{2s+1}S_J)|0\rangle &= \frac{2}{\pi}(2J+1)|R_0^{(8)}(0)|^2,\\ \langle 0|\mathcal{O}_8(^3P_J)|0\rangle &= \frac{2N_c}{\pi}(2J+1)|R_1'^{(8)}(0)|^2,\end{aligned} \tag{A.1}$$

with, assuming the standard spin symmetry,

$$\langle 0|\mathcal{O}_8(^3P_J)|0\rangle = (2J+1)\,\langle 0|\mathcal{O}_8(^3P_0)|0\rangle\,. \tag{A.2}$$

Moreover, even if the LDMEs are defined for a specific particle, one can find relations among different particles via rotational symmetries. For example, let us consider the η_c meson ($^1S_0$ state), that can be produced via $^1S_0^{(1)}$, $^1S_0^{(8)}$, $^3S_1^{(8)}$ and $^1P_1^{(8)}$ states, up to order v^4. In this case, η_c LDMEs can be related to the J/ψ ones, as follows

$$\begin{aligned}\langle 0|\mathcal{O}_1^{\eta_c}(^1S_0)|0\rangle &= \frac{1}{3}\,\langle 0|\mathcal{O}_1^{J/\psi}(^3S_1)|0\rangle\,,\\ \langle 0|\mathcal{O}_8^{\eta_c}(^1S_0)|0\rangle &= \langle 0|\mathcal{O}_8^{J/\psi}(^3S_1)|0\rangle\,,\\ \langle 0|\mathcal{O}_8^{\eta_c}(^3S_1)|0\rangle &= \langle 0|\mathcal{O}_8^{J/\psi}(^1S_0)|0\rangle\,,\\ \langle 0|\mathcal{O}_8^{\eta_c}(^1P_1)|0\rangle &= 3\,\langle 0|\mathcal{O}_8^{J/\psi}(^3P_0)|0\rangle\,,\end{aligned} \tag{A.3}$$

as shown in Eq. (3) of Ref. [169].

A.1 Amplitudes in NRQCD

The amplitudes within the NRQCD approach are evaluated as follows. At the perturbative level, we have the production of a heavy quark-antiquark pair, a $c\bar{c}$-pair for J/ψ and η_c. Then, we have to project the general $c\bar{c}$-state into a configuration with specific quantum numbers; the evaluation of the spin/angular projector for S-waves will be discussed in the next section A.2.

The nonperturbative part of the amplitude is given by the radial wave function. Depending on the specific state, the radial wave function can vanish and it is replaced by its derivative: for example, R_0 contributes to S-wave production, while R_1' to P-wave production. After the evaluation of the amplitude squared, these quantities are related to LDME parameters according to Eq. (A.1).

In particular, for the two aforementioned quarkonia (J/ψ and η_c), S- and P-waves amplitudes have to be considered. The former is given by

$$\mathcal{M} = -\frac{R_0}{\sqrt{16\pi M}}\,\mathrm{Tr}\left[O(P_h,\,0)(\not{P}_h - M)\Pi_{SS_z}\right]\,\langle 3i;\overline{3j}|1,8d\rangle\,, \tag{A.4}$$

while the latter is

$$\mathcal{M} = -i\sqrt{\frac{3}{16\pi M}}\, R_1'\ \mathrm{Tr}\left[\left.\frac{\partial O(P_h,\, k)}{\partial k_\alpha}\right|_{k=0} (\not{P}_h - M)\Pi^\alpha_{JJ_z} \right.$$
$$\left. - \frac{O(P_h,\, 0)}{M}\Big(\gamma_\alpha \Pi^\alpha_{JJ_z}(\not{P}_h + M) - (\not{P}_h - M)\Pi^\alpha_{JJ_z}\gamma_\alpha\Big)\right] \langle 3i;\overline{3j}|1,8d\rangle\,. \tag{A.5}$$

In the above expressions, P_h is the quarkonium momentum, with $P_h^2 = M^2$, while k is directly related to the relative velocity of the heavy quark and antiquark, being $k = v/2$.

In both cases, the projection into the color configuration is

$$\langle 3i;\overline{3j}|1\rangle = \frac{\delta_{ij}}{\sqrt{N_c}}, \quad \langle 3i;\overline{3j}|8d\rangle = \sqrt{2}t^d_{ij}, \tag{A.6}$$

for a CS- or a CO-state, respectively.

The operator $O(P_h, k)$ is obtained from the perturbative amplitude by excluding the spinors of the heavy quark and antiquark.

Finally, we have two different spin/angular projectors depending on the state produced. In particular, for an S-wave we have

$$\Pi_{SS_z} = \begin{cases} -\gamma^5 & \text{for } {}^1S_0 \\ \not{\epsilon}^*_{S_z} & \text{for } {}^3S_1 \end{cases} \tag{A.7}$$

and for a P-wave

$$\Pi^\alpha_{JJ_z} = \begin{cases} -\sum_{L_z} \epsilon^{*\alpha}_{L_z}\gamma^5 & \text{for } {}^1P_1 \\ \Sigma^{\alpha\beta}_{J_z}\gamma_\beta & \text{for } {}^3P_J \end{cases}, \tag{A.8}$$

where

$$\Sigma^{\alpha\beta}_{J_z} = \sum_{L_z,S_z} \langle 1L_z;1S_z|JJ_z\rangle\, \epsilon^{*\alpha}_{L_z}\epsilon^{*\beta}_{S_z}, \tag{A.9}$$

and explicitly

$$\begin{aligned}
\sum_{L_z,S_z} \langle 1L_z;1S_z|00\rangle\, \epsilon^{*\alpha}_{L_z}\epsilon^{*\beta}_{S_z} &= \frac{1}{\sqrt{3}}\left(g^{\alpha\beta} - \frac{P_h^\alpha P_h^\beta}{M^2}\right), \\
\sum_{L_z,S_z} \langle 1L_z;1S_z|1J_z\rangle\, \epsilon^{*\alpha}_{L_z}\epsilon^{*\beta}_{S_z} &= -\frac{1}{\sqrt{2}}\frac{i}{M}\epsilon^{\alpha\beta\gamma\delta}P_{h\gamma}\epsilon^*_{J_z\delta}, \\
\sum_{L_z,S_z} \langle 1L_z;1S_z|2J_z\rangle\, \epsilon^{*\alpha}_{L_z}\epsilon^{*\beta}_{S_z} &= \epsilon^{*\alpha\beta}_{J_z}.
\end{aligned} \tag{A.10}$$

Moreover, we have useful completeness relations for the quarkonium polarization vector, given by

$$\begin{aligned}\sum_{\text{pol}} \epsilon_\lambda^{*\mu}(p)\epsilon_\lambda^{\nu}(p) &= -g^{\mu\nu} + \frac{p^\mu P_h^\nu + p^\nu P_h^\mu}{p\cdot P_h} - M^2\frac{p^\mu p^\nu}{(p\cdot P_h)^2},\\ \sum_{\text{pol}} \epsilon_\lambda^{*\mu}(P_h)\epsilon_\lambda^{\nu}(P_h) &= -g^{\mu\nu} + \frac{P_h^\mu P_h^\nu}{M^2} = Q^{\mu\nu},\\ \sum_{\text{pol}} \epsilon_\lambda^{*\alpha\beta}(P_h)\epsilon_\lambda{}^{\alpha'\beta'}(P_h) &= \frac{1}{2}\left(Q^{\alpha\alpha'}Q^{\beta\beta'} + Q^{\alpha\beta'}Q^{\beta\alpha'}\right) - \frac{1}{3}Q^{\alpha\beta}Q^{\alpha'\beta'}.\end{aligned} \tag{A.11}$$

A.2 Angular/spin projector

In this section we show how to derive the projector into a state with angular quantum number $L = 0$. The explicit general form of the projector is given by

$$\mathcal{P}_{SS_z}(P_h,\, k) = \frac{1}{\sqrt{8m_Q^3}}\left[-\left(\frac{\not{P}_h}{2} - \not{k}\right) + m_Q\right]\Pi_{SS_z}\left[\left(\frac{\not{P}_h}{2} + \not{k}\right) + m_Q\right], \tag{A.12}$$

where m_Q is the heavy quark mass, P_h is the quarkonium momentum and k is half of the relative velocity of the heavy $Q\bar{Q}$-pair. The projector is valid both for scalar ($S = 0$) and vector ($S = 1$) states, with the matrix Π_{SS_z} taking a different form in the two cases (see Eq. (A.7)).

From the antisymmetric relation of the Dirac matrices and the mass relation $2m_Q = M$, it is straightforward to prove that the projector in Eq. (A.12) is equivalent to the last two terms of the trace in Eq. (A.4).

To derive Eq. (A.12), we first introduce the projector of a bound $Q\bar{Q}$-state into a specific spin configuration. This is achieved by introducing the Clebsch-Gordan coefficients, via

$$\mathcal{P}_{SS_z} = \frac{1}{\sqrt{m_Q}}\sum_{s,\bar{s}} \langle \tfrac{1}{2}s;\, \tfrac{1}{2}\bar{s}|SS_z\rangle\, v(p_v,\bar{s})\overline{u}(p_u,s), \tag{A.13}$$

where p_u and p_v are the momenta of the quark and antiquark, respectively. Note that the spinors of particles and antiparticles with momentum p can be related to the corresponding ones evaluated at rest

$$u^{(s)}(p) = (\not{p} + m)u^{(s)}(0), \quad v^{(\bar{s})}(p) = (-\not{p} + m)v^{(\bar{s})}(0). \tag{A.14}$$

Moreover, considering the non-relativistic nature of the quarkonium, we can use the following approximations

$$u_+(0) \simeq \frac{1}{\sqrt{2m_Q}}\begin{pmatrix}1\\0\\0\\0\end{pmatrix}, \quad u_-(0) \simeq \frac{1}{\sqrt{2m_Q}}\begin{pmatrix}0\\1\\0\\0\end{pmatrix},$$
$$v_+(0) \simeq \frac{1}{\sqrt{2m_Q}}\begin{pmatrix}0\\0\\0\\1\end{pmatrix}, \quad v_-(0) \simeq \frac{1}{\sqrt{2m_Q}}\begin{pmatrix}0\\0\\-1\\0\end{pmatrix}. \tag{A.15}$$

We start our derivation from the **scalar case**, where the projection is unique and described by $\mathcal{P}_{00}$. This state is the superposition of fermions in a singlet state, with opposite s_z components, namely

$$\begin{aligned}\mathcal{P}_{00}(P_h,\, k) &= \frac{1}{\sqrt{m_Q}}\sum_{s,\bar{s}}\langle\tfrac{1}{2}s;\tfrac{1}{2}\bar{s}|00\rangle\, v(\tfrac{1}{2}P_h-k,\bar{s})\overline{u}(\tfrac{1}{2}P_h+k,s)\\
&= \frac{1}{\sqrt{2m_Q}}\left[v_-(\tfrac{1}{2}P_h-k)\overline{u}_+(\tfrac{1}{2}P_h+k)-v_+(\tfrac{1}{2}P_h-k)\overline{u}_-(\tfrac{1}{2}P_h+k)\right]\\
&= \frac{1}{\sqrt{2m_Q}}\left(-\frac{1}{2}\not{P}_h+\not{k}+m_Q\right)\left[v_-(0)\overline{u}_+(0)-v_+(0)\overline{u}_-(0)\right]\left(\frac{1}{2}\not{P}_h+\not{k}+m_Q\right)\\
&= \frac{1}{\sqrt{8m_Q^3}}\left(-\frac{1}{2}\not{P}_h+\not{k}+m_Q\right)\begin{pmatrix}0&0\\-1&0\end{pmatrix}\left(\frac{1}{2}\not{P}_h+\not{k}+m_Q\right),\end{aligned} \tag{A.16}$$

where in the last line we have used the block form to simplify the notation. Notice that the matrix related to the spinors combination can be recast into the following combination of Dirac matrices

$$\begin{aligned}\gamma^5\frac{\mathbb{1}+\gamma_0}{2} &= \frac{1}{2}\begin{pmatrix}0&1\\1&0\end{pmatrix}\left[\begin{pmatrix}1&0\\0&1\end{pmatrix}+\begin{pmatrix}1&0\\0&-1\end{pmatrix}\right]\\
&= \begin{pmatrix}0&1\\1&0\end{pmatrix}\begin{pmatrix}1&0\\0&0\end{pmatrix}\\
&= \begin{pmatrix}0&0\\1&0\end{pmatrix},\end{aligned} \tag{A.17}$$

from which the projector takes a more compact form

$$\mathcal{P}_{00}(P_h,\, k) = -\frac{1}{\sqrt{8m_Q^3}}\left(-\frac{1}{2}\not{P}_h+\not{k}+m_Q\right)\left[\gamma^5\frac{\mathbb{1}+\gamma_0}{2}\right]\left(\frac{1}{2}\not{P}_h+\not{k}+m_Q\right). \tag{A.18}$$

Considering now the non-relativistic limit, which implies that k is small compared to other quantities, we have

$$\begin{aligned}
-\sqrt{8m_Q^3}\mathcal{P}_{00}(P_h,\,k) &= \left(-\frac{1}{2}\not{P}_h + \not{k} + m_Q\right)\left[\gamma^5\frac{\mathbb{1}+\gamma_0}{2}\right]\left(\frac{1}{2}\not{P}_h + \not{k} + m_Q\right) \\
&= \begin{pmatrix} 0 & -k_i\sigma^i \\ k_i\sigma^i & 2m_Q \end{pmatrix}\begin{pmatrix} 0 & 0 \\ 1 & 0 \end{pmatrix}\begin{pmatrix} 2m_Q & k_i\sigma^i \\ -k_i\sigma^i & 0 \end{pmatrix} \\
&= \begin{pmatrix} -2m_Q k_i\sigma^i & -k_i\sigma^i q_j\sigma^j \\ 4m_Q^2 & 2m_Q k_i\sigma^i \end{pmatrix} \\
&\simeq 4m_Q^2\begin{pmatrix} 0 & 0 \\ 1 & 0 \end{pmatrix} + 2m_Q k_i\sigma^i\begin{pmatrix} -1 & 0 \\ 0 & 1 \end{pmatrix} + O(k^2),
\end{aligned} \tag{A.19}$$

which can be approximated by

$$\begin{aligned}
-\sqrt{8m_Q^3}\mathcal{P}_{00}(P_h,\,k) &\sim \left(-\frac{1}{2}\not{P}_h + \not{k} + m_Q\right)\gamma^5\left(\frac{1}{2}\not{P}_h + \not{k} + m_Q\right) \\
&= \begin{pmatrix} 0 & -k_i\sigma^i \\ k_i\sigma^i & 2m_Q \end{pmatrix}\begin{pmatrix} 0 & 1 \\ 1 & 0 \end{pmatrix}\begin{pmatrix} 2m_Q & k_i\sigma^i \\ -k_i\sigma^i & 0 \end{pmatrix} \\
&= \begin{pmatrix} -2m_Q k_i\sigma^i & -k_i\sigma^i q_j\sigma^j \\ 4m_Q^2 - k_i\sigma^i q_j\sigma^j & 2m_Q k_i\sigma^i \end{pmatrix} \\
&\simeq 4m^2\begin{pmatrix} 0 & 0 \\ 1 & 0 \end{pmatrix} + 2m_Q k_i\sigma^i\begin{pmatrix} -1 & 0 \\ 0 & 1 \end{pmatrix} + O(k^2).
\end{aligned} \tag{A.20}$$

Finally, we conclude that the projector for a scalar particle has the following exact and non-relativistic approximated forms

$$\begin{aligned}
\mathcal{P}_{00} &= -\frac{1}{\sqrt{8m_Q^3}}\left(-\frac{1}{2}\not{P}_h + \not{k} + m_Q\right)\left[\gamma^5\frac{\mathbb{1}+\gamma_0}{2}\right]\left(\frac{1}{2}\not{P}_h + \not{k} + m_Q\right) \\
&\sim -\frac{1}{\sqrt{8m_Q^3}}\left(-\frac{\not{P}_h}{2} + \not{k} + m_Q\right)\gamma^5\left(\frac{\not{P}_h}{2} + \not{k} + m_Q\right).
\end{aligned} \tag{A.21}$$

Moving to the **vector case**, we have to evaluate the projector $\mathcal{P}_{1S_z}$ for all values of the spin z-component, namely $S_z = 0, \pm 1$. Since the derivation is analogous for all S_z values, it is sufficient to discuss one of the cases, *e.g.* $\mathcal{P}_{11}$. The state with $S_z = 1$

can be achieved only through the combination of v_+ and $\overline{u}_+$ spinors

$$\begin{aligned}\mathcal{P}_{11}(P_h,\,k) &= \frac{1}{\sqrt{m_Q}}\sum_{s,\bar{s}}\langle\frac{1}{2}s;\frac{1}{2}\bar{s}|11\rangle\, v(\frac{1}{2}P_h-k,\bar{s})\overline{u}(\frac{1}{2}P_h+k,s)\\ &= \frac{1}{\sqrt{m_Q}}\left[v_+(\frac{1}{2}P_h-k)\overline{u}_+(\frac{1}{2}P_h+k)\right]\\ &= \frac{1}{\sqrt{m_Q}}\left(-\frac{1}{2}\not{P}_h+\not{k}+m_Q\right)\left[v_+(0)\overline{u}_+(0)\right]\left(\frac{1}{2}\not{P}_h+\not{k}+m_Q\right)\\ &= \frac{1}{\sqrt{4m_Q^3}}\left(-\frac{1}{2}\not{P}_h+\not{k}+m_Q\right)\begin{pmatrix}0&0&0&0\\0&0&0&0\\0&0&0&0\\1&0&0&0\end{pmatrix}\left(\frac{1}{2}\not{P}_h+\not{k}+m_Q\right).\end{aligned} \tag{A.22}$$

Again, it is possible to write the projector in a more compact form, which involves the polarization vector of the quarkonium. In the case considered, the relevant polarization vector is ϵ_1^* (with helicity $+1$), defined as

$$\epsilon_1^* = \frac{1}{\sqrt{2}}\begin{pmatrix}0\\-1\\i\\0\end{pmatrix}, \tag{A.23}$$

thus

$$\not{\epsilon}_1^* = \frac{1}{\sqrt{2}}\left(-\gamma^1+i\gamma^2\right) = \sqrt{2}\begin{pmatrix}0&0&0&0\\0&0&-1&0\\0&0&0&0\\1&0&0&0\end{pmatrix} \tag{A.24}$$

and

$$\frac{\not{\epsilon}_1^*}{\sqrt{2}}\frac{\mathbb{1}+\gamma_0}{2} = \frac{\not{\epsilon}_1^*}{\sqrt{2}}\begin{pmatrix}1&0&0&0\\0&1&0&0\\0&0&0&0\\0&0&0&0\end{pmatrix} = \begin{pmatrix}0&0&0&0\\0&0&0&0\\0&0&0&0\\1&0&0&0\end{pmatrix}. \tag{A.25}$$

From this, we have that the projector is given by

$$\mathcal{P}_{11}(P_h,\,k) = \frac{1}{\sqrt{8m_Q^3}}\left(-\frac{1}{2}\not{P}_h+\not{k}+m_Q\right)\left[\not{\epsilon}_1^*\frac{\mathbb{1}+\gamma_0}{2}\right]\left(\frac{1}{2}\not{P}_h+\not{k}+m_Q\right). \tag{A.26}$$

As in the scalar case, in the non-relativistic limit the matrix $\mathbb{1}+\gamma_0$ is approximated by the identity. Indeed, the full projector is approximated by

$$\begin{aligned}
\sqrt{4m_Q^3}\mathcal{P}_{11}(P_h,\,k) &= \left(-\frac{1}{2}\not{P}_h+\not{k}+m_Q\right)\left[\frac{\not{\epsilon}_1^*}{\sqrt{2}}\frac{\mathbb{1}+\gamma_0}{2}\right]\left(\frac{1}{2}\not{P}_h+\not{k}+m_Q\right)\\
&= \begin{pmatrix} 0 & -k_i\sigma^i \\ k_i\sigma^i & 2m_Q \end{pmatrix}\begin{pmatrix} 0&0&0&0\\0&0&0&0\\0&0&0&0\\1&0&0&0\end{pmatrix}\begin{pmatrix} 2m_Q & k_i\sigma^i \\ -k_i\sigma^i & 0 \end{pmatrix}\\
&= \begin{pmatrix} 0&0&0&0\\ -2m_Qk_i\sigma^i&0&-(k_i\sigma^i)^2&0\\0&0&0&0\\4m_Q^2&0&2m_Qk_i\sigma^i&0\end{pmatrix}\\
&\simeq \begin{pmatrix} 0&0&0&0\\ -2m_Qk_i\sigma^i&0&0&0\\0&0&0&0\\4m_Q^2&0&2m_Qk_i\sigma^i&0\end{pmatrix}+O(k^2),
\end{aligned}\tag{A.27}$$

which coincides with

$$\begin{aligned}
\sqrt{4m_Q^3}\mathcal{P}_{11}(P_h,\,k) &\sim \left(-\frac{1}{2}\not{P}_h+\not{k}+m_Q\right)\frac{\not{\epsilon}_1^*}{\sqrt{2}}\left(\frac{1}{2}\not{P}_h+\not{k}+m_Q\right)\\
&= \begin{pmatrix} 0 & -k_i\sigma^i \\ k_i\sigma^i & 2m_Q \end{pmatrix}\begin{pmatrix} 0&0&0&0\\0&0&-1&0\\0&0&0&0\\1&0&0&0\end{pmatrix}\begin{pmatrix} 2m_Q & k_i\sigma^i \\ -k_i\sigma^i & 0 \end{pmatrix}\\
&= \begin{pmatrix} 0&0&0&0\\ -2m_Qk_i\sigma^i&0&-(k_i\sigma^i)^2&0\\0&0&0&0\\4m_Q^2+(k_i\sigma^i)^2&0&2m_Qk_i\sigma^i&0\end{pmatrix}\\
&\simeq \begin{pmatrix} 0&0&0&0\\ -2m_Qk_i\sigma^i&0&0&0\\0&0&0&0\\4m_Q^2&0&2m_Qk_i\sigma^i&0\end{pmatrix}+O(k^2).
\end{aligned}\tag{A.28}$$

Since the very same approximation holds for other helicity components of the J/ψ polarization vector, the projector takes the exact and approximated forms

$$\begin{aligned}
\mathcal{P}_{1S_z} &= \frac{1}{\sqrt{8m_Q^3}}\left(-\frac{1}{2}\not{P}_h+\not{k}+m_Q\right)\left[\epsilon_{S_z}^*\frac{\mathbb{1}+\gamma_0}{2}\right]\left(\frac{1}{2}\not{P}_h+\not{k}+m_Q\right)\\
&\sim -\frac{1}{\sqrt{8m_Q^3}}\left(-\frac{\not{P}_h}{2}+\not{k}+m_Q\right)\epsilon_{S_z}^*\left(\frac{\not{P}_h}{2}+\not{k}+m_Q\right)
\end{aligned}\tag{A.29}$$

for all S_z values.

By combining the two results into Π_{SS_z} in Eq. (A.7), we proved that the projector in Eq. (A.12) is correct.

A.3 Long-distance matrix elements sets

In this section we list the LDME sets used in this thesis. They are all referred to the J/ψ particle.

In particular, we consider four LDME sets, with different characteristics.
The C12 set [15] has been obtained by fitting simultaneously polarized and unpolarized direct J/ψ production data in pp collision, measured by the CDF (Run II) Collaboration in Ref. [170]; in the fit they imposed a cut on the J/ψ transverse momentum, considering only the $P_T > 7$ GeV region.
The G13 set [105] includes only unpolarized data at $P_T > 7$ GeV, from both CDF [171] and LHCb [172] Collaborations, but including also the feed-down contribution. Moreover, they test their set predicting the J/ψ polarization in pp collisions, finding a general agreement with the C12 set only when the feed-down contribution is negligible.
The BK11 set [104], differently from the previous two, includes both hadron production and photoproduction unpolarized data, with a lower cut on the J/ψ transverse momentum at around $P_T = 3$ GeV.
Finally the SYY13 set [133] is based on a different approach, combining the LDME extraction with the CSS matching procedure [126] in pp collision in the very low-P_T region. They found, however, that the J/ψ production is dominated by CO waves in this region, so the CS contribution is totally missing in their set. This implies that this contribution should be excluded *a priori*, but it could be added *a posteriori*.

The first two sets are useful when studying the quarkonium polarization states, as we did in Chapter 2. The third one is instead very versatile, and it can be used in studies at low-P_T, as done in Chapter 4 to provide our SSA estimates, or when dealing with processes involving a proton and a photon (real or virtual) in the initial state, as in Chapter 2. Finally, in the application of the fourth some tension can arise since the total absence of the CS contribution can be a too strong assumption. For this reason, we used this set only in Chapter 4.

LDME Set	$\langle \mathcal{O}_1^{J/\psi}[^3S_1] \rangle$ [GeV^3]
C12	1.16
G13	1.16
BK11	1.32
SYY13	0

TABLE A.1: LDME set (central) values for the J/ψ production via a CS state.

LDME Set	$\langle \mathcal{O}_8^{J/\psi}[^1S_0] \rangle$ [GeV^3]	$\langle \mathcal{O}_8^{J/\psi}[^3S_1] \rangle$ [GeV^3]	$\langle \mathcal{O}_8^{J/\psi}[^3P_0] \rangle$ [GeV^5]
C12	0.089	0.003	0.0126
G13	0.097	-0.0046	-0.0214
BK11	0.0304	0.00168	-0.00908
SYY13	0.1423	-0.0093	-0.0394

TABLE A.2: LDME set (central) values for the J/ψ production via a CO state; notice that for the other ^3P_J states (with $J \neq 0$) we use Eq. (A.2)).

In Tab. A.1 we present the LDME relative to the CS wave, while in Tab. A.2 we present the three dominant CO waves in J/ψ production.

We highlight the differences in the CS table. First we remark that the SYY13 set does not formally present any CS contribution, so its value is automatically set to 0. Moreover, the BK11 set presents a CS LDME value slightly different from that used in the C12 and G13 sets. Notice that, in the BK11 case, this LDME value is based on a potential model derived from the Cornell potential (combination of Coulomb and a linear dependence) and applied to the $J/\psi \to e^+e^-$ decay width, see Ref. [173]; the other two are based on the QCD-motivated potential model given by Buchmüller and Tye and evaluated in Ref. [174].

A.4 Trace relations

A.4.1 Gell-Mann matrix trace relations

Traces involving up to 3 Gell-Mann matrices t^a can be found in every QCD book, *e.g.* [175]

$$\begin{aligned} \mathrm{Tr}\left[t^a\right] &= 0, \\ \mathrm{Tr}\left[t^a t^b\right] &= \frac{1}{2}\delta_{ab}, \\ \mathrm{Tr}\left[t^a t^b t^c\right] &= \frac{1}{4}\left(d_{abc} + i f_{abc}\right). \end{aligned} \tag{A.30}$$

Moreover, for the diagrams encountered in this work and gathered in Appendix B, we need the traces involving four Gell-Mann matrices. In particular we have the difference

$$\mathrm{Tr}\left[t^a t^b t^c t^d\right] - \mathrm{Tr}\left[t^c t^b t^a t^d\right] = \frac{i}{4}\left(f_{abe}d_{cde} + d_{abe}f_{cde}\right), \tag{A.31}$$

and the sum

$$\mathrm{Tr}\left[t^a t^b t^c t^d\right] + \mathrm{Tr}\left[t^c t^b t^a t^d\right] = \frac{1}{4}\left(\frac{2}{N}\delta_{ab}\delta_{cd} + d_{abe}d_{cde} - f_{abe}f_{cde}\right). \tag{A.32}$$

To obtain these last relations the commutator

$$\left[t^a, t^b\right] = i f_{abc} t^c \tag{A.33}$$

and the anticommutator

$$\left\{t^a, t^b\right\} = \frac{1}{N}\delta_{ab}\mathbb{1}_{(N)} + d_{abc}t^c \tag{A.34}$$

have been repeatedly used.

A.4.2 Dirac matrices traces relevant in quarkonium production

When the quarkonium is produced via an S-wave following the NRQCD approach, the amplitude is evaluated as in Eq. (A.4). Summing the contribution from different diagrams, usually the inversion of the heavy quark lines relates two diagrams together. In particular for a scalar state we have the antisymmetric relations

$$\mathrm{Tr}\left[\gamma^\mu(\not{q} + M)\gamma^\nu(\not{p} - M)\gamma^5\right] = -\,\mathrm{Tr}\left[\gamma^\nu(\not{q} - M)\gamma^\mu(\not{p} - M)\gamma^5\right], \tag{A.35}$$

and

$$\mathrm{Tr}\left[\gamma^\mu(\not{a}+M)\gamma^\nu(\not{b}-M)\gamma^\rho(\not{P}-M)\gamma^5\right] = -\,\mathrm{Tr}\left[\gamma^\rho(\not{b}+M)\gamma^\nu(\not{a}-M)\gamma^\mu(\not{P}-M)\gamma^5\right], \tag{A.36}$$

while for the vector state, we found the symmetric relations

$$\mathrm{Tr}\left[\gamma^\mu(\not{a}+M)\gamma^\nu(\not{b}-M)\gamma^\rho(\not{P}-M)\not{\epsilon}^*_{S_z}\right] = \mathrm{Tr}\left[\gamma^\rho(\not{b}+M)\gamma^\nu(\not{a}-M)\gamma^\mu(\not{P}-M)\not{\epsilon}^*_{S_z}\right], \tag{A.37}$$

and

$$\mathrm{Tr}\left[\gamma^\mu(\not{a}+M)\gamma^\nu(\not{P}-M)\not{\epsilon}^*_{S_z}\right] = \mathrm{Tr}\left[\gamma^\nu(\not{a}-M)\gamma^\mu(\not{P}-M)\not{\epsilon}^*_{S_z}\right]. \tag{A.38}$$

Production of a P-wave is instead described in Eq. (A.5). In addition to the previous waves, one needs to consider traces involving the combination of Dirac matrices

$$\Gamma^\alpha = \gamma^\alpha\gamma^5(\not{P}+M) - (\not{P}-M)\gamma^5\gamma^\alpha, \quad \Gamma^{\alpha\beta} = \gamma^\alpha\gamma^\beta(\not{P}+M) - (\not{P}-M)\gamma^\beta\gamma^\alpha, \tag{A.39}$$

where the former is valid for the production of a state with $S = 0$, while the latter for $S = 1$. In this case we found the antisymmetric relations

$$\mathrm{Tr}\left[\gamma^\mu(\not{a}+M)\gamma^\nu\Gamma^{\alpha\beta}\right] = -\,\mathrm{Tr}\left[\gamma^\nu(\not{a}-M)\gamma^\mu\Gamma^{\alpha\beta}\right], \tag{A.40}$$

$$\mathrm{Tr}\left[\gamma^\mu(\not{a}+M)\gamma^\nu(\not{b}-M)\gamma^\rho\Gamma^{\alpha\beta}\right] = -\,\mathrm{Tr}\left[\gamma^\rho(\not{b}+M)\gamma^\nu(\not{a}-M)\gamma^\mu\Gamma^{\alpha\beta}\right], \tag{A.41}$$

and the symmetric ones

$$\mathrm{Tr}\left[\gamma^\mu(\not{a}+M)\gamma^\nu\Gamma^{\alpha}\right] = \mathrm{Tr}\left[\gamma^\nu(\not{a}-M)\gamma^\mu\Gamma^{\alpha}\right], \tag{A.42}$$

$$\mathrm{Tr}\left[\gamma^\mu(\not{a}+M)\gamma^\nu(\not{b}-M)\gamma^\rho\Gamma^{\alpha}\right] = \mathrm{Tr}\left[\gamma^\rho(\not{b}+M)\gamma^\nu(\not{a}-M)\gamma^\mu\Gamma^{\alpha}\right]. \tag{A.43}$$

Appendix B

Hard parts

In this appendix we gather the perturbative quantities used for the different processes studied in this thesis.

We first present the diagrams relevant in pp collisions (Sec. B.1). We will consider two quarkonia, J/ψ and η_c, produced in both CS and CO states. Moreover, we gather the color factors (CFs) relative to each diagram product in Sec. B.1.3. We remark that the following results can also be found in Refs. [150, 176].

We then move to the production of polarized and unpolarized J/ψ in SIDIS (Sec. B.2), where the cross section is parameterized via structure functions. We will present them for both cases. They can also be found in literature, *e.g.* Refs. [97, 112] for the polarized case, while Refs. [87, 125] for the unpolarized one.

In the following results the LDME will be omitted to simplify the notation.

B.1 pp collisions

In this section we provide the hard terms relative to the $pp \to \mathcal{Q} + X$ process. To highlight the differences arising from the quantum number combinations, we will take into account two quarkonia. The former, vastly investigated during this thesis, is the J/ψ, corresponding to the ${}^3S_1$ lowest energy state. The second is the η_c meson, which is a ${}^1S_0$ state.

B.1.1 LO diagrams

The production of a quarkonium $\mathcal{Q}$ in $pp \to \mathcal{Q} + X$ at first order in α_s is achieved via

$$a(p_a)\, b(p_b) \to \mathcal{Q}(P_h), \tag{B.1}$$

where the initial partons can be either gg, Fig. B.1, or $q\bar{q}$, Fig. B.2. In the following we define $P_h^2 = M^2$.

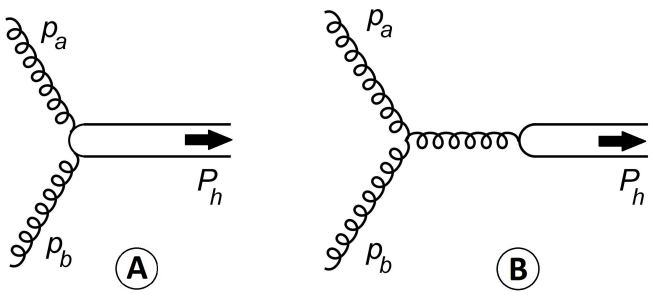

FIGURE B.1: Diagrams relative to the production of a $c\bar{c}$ pair at α_s^2 order via gg fusion.

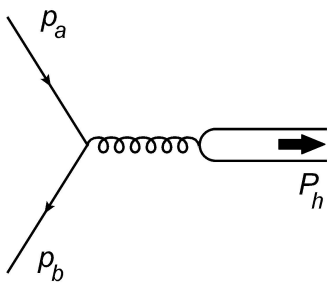

FIGURE B.2: Diagram relative to the production of a $c\bar{c}$ pair at α_s^2 order via $q\bar{q}$ annihilation.

The gg interaction diagrams translate into

$$\begin{aligned} O^A_{gg}(P,k) &= -2(4\pi\alpha_s) \\ &\quad \times \left[t^a_{ik} t^b_{kj} \not{\epsilon}_a \frac{\not{p}_b - \not{p}_a + \not{k} + M}{(p_b - p_a + k)^2 - M^2} \not{\epsilon}_b - t^b_{ik} t^a_{kj} \not{\epsilon}_b \frac{\not{p}_b - \not{p}_a - \not{k} - M}{(p_b - p_a - k)^2 - M^2} \not{\epsilon}_a \right], \\ O^B_{gg}(P,k) &= (4\pi\alpha_s)\, (i f_{abe} t^e_{ij}) \epsilon^\mu_a \epsilon^\nu_b \frac{\eta_{\mu\nu}(\not{p}_b - \not{p}_a) + 2(\gamma_\mu p_{a\nu} - \gamma_\nu p_{b\mu})}{M^2}, \end{aligned} \tag{B.2}$$

while the diagram for $q\bar{q}$ annihilation is given by

$$O_{q\bar{q}}(P,k) = (4\pi\alpha_s)\, t^e_{ij} t^e_{mn}\, \overline{v}(p_b) \gamma_\rho u(p_a) \frac{\gamma^\rho}{M^2}. \tag{B.3}$$

Color-singlet production

The results relative to the CS state depend on the quarkonium produced. In any case, a CS state can only be produced via diagram Ⓐ of Fig. B.1.

To evaluate the η_c production ($^1S_0$ state) we take into account the trace relation in Eq. (A.35) of Appendix A.4.2, which leads to

$$\left| \mathcal{M}^{gg \to {}^1S_0^{(1)}} \right|^2 = \frac{(4\pi\alpha_s)^2}{72M}. \tag{B.4}$$

The J/ψ ($^3S_1$ state), instead, cannot be produced in a CS configuration. Indeed, in this case we have to consider the trace relation in Eq. (A.38), from which

$$\left| \mathcal{M}^{gg \to {}^3S_1^{(1)}} \right|^2 = 0. \tag{B.5}$$

Color-octet production

In the CO production both gg and $q\bar{q}$ channels contribute. In the velocity expansion for the two quarkonia, both S- and P-waves are present; in particular $^1P_1^{(8)}$ contributes to η_c while $^3P_J^{(8)}$ (with $J = 0, 1, 2$) to J/ψ.

Considering first the S-waves, the gg channel leads to

$$\left| \mathcal{M}^{gg \to {}^1S_0^{(8)}} \right|^2 = \frac{5(4\pi\alpha_s)^2}{192M} = \frac{15}{8} \left| \mathcal{M}^{gg \to {}^1S_0^{(1)}} \right|^2, \tag{B.6}$$

$$\left| \mathcal{M}^{gg \to {}^3S_1^{(8)}} \right|^2 = 0, \tag{B.7}$$

while the $q\bar{q}$ one provides

$$\left|\mathcal{M}^{q\bar{q}\to{}^1S_0^{(8)}}\right|^2 = 0, \tag{B.8}$$

$$\left|\mathcal{M}^{q\bar{q}\to{}^3S_1^{(8)}}\right|^2 = \frac{(4\pi\alpha_s)^2}{27M}. \tag{B.9}$$

Notice how the $gg \to {}^1S_0^{(8)}$ is directly related to the corresponding CS case, with a proportional factor deriving from the different CFs involved (see Tab. B.1).
Moving to η_c and J/ψ production through a CO P-wave, for gg we have

$$\left|\mathcal{M}^{gg\to{}^1P_1^{(8)}}\right|^2 = \frac{9(4\pi\alpha_s)^2}{16M^3}, \tag{B.10}$$

$$\left|\mathcal{M}^{gg\to{}^3P_J^{(8)}}\right|^2 = \frac{35(4\pi\alpha_s)^2}{48M^3}, \tag{B.11}$$

and for $q\bar{q}$ annihilation

$$\left|\mathcal{M}^{q\bar{q}\to{}^1P_1^{(8)}}\right|^2 = 0, \tag{B.12}$$

$$\left|\mathcal{M}^{q\bar{q}\to{}^3P_J^{(8)}}\right|^2 = 0. \tag{B.13}$$

In the previous equations, the ${}^3P_J^{(8)}$ state is a short notation which implies a sum over states with different total angular momentum J, via Eq. (A.2).

B.1.2 NLO diagrams

The quarkonium production at α_s^3 order is described by the partonic subprocess

$$a(p_a)\, b(p_b) \to \mathcal{Q}(P_h) + x, \tag{B.14}$$

with $P_h^2 = M^2$. In particular, initial partons, a and b, can be either gg (Fig. B.3), $gq(\bar{q})$ (Fig. B.4) or $q\bar{q}$ (Fig. B.5).

The (perturbative) operators relative to the diagrams in Fig. B.3 are given by

$$\begin{aligned}
O_{gg}^{A_1}(P,k) &= 4\,(4\pi\alpha_s)^{3/2}\left\{ t^a_{ik}t^b_{kl}t^c_{lj}\frac{\not\epsilon_a\left(\not P - 2\not p_a + 2\not k + M\right)\not\epsilon_b\left(\not P + 2\not p_c - 2\not k - M\right)\not\epsilon_c^*}{[(P-2p_a+2k)^2-M^2]\,[(P+2p_c-2k)^2-M^2]}\right.\\
&\left. + t^c_{ik}t^b_{kl}t^a_{lj}\frac{\not\epsilon_c^*\left(\not P + 2\not p_c + 2\not k + M\right)\not\epsilon_b\left(\not P - 2\not p_a - 2\not k - M\right)\not\epsilon_a}{[(P+2p_c+2k)^2-M^2]\,[(P-2p_a-2k)^2-M^2]}\right\},\\
O_{gg}^{A_2}(P,k) &= O_{gg}^{A_1}(P,k)\,(c\leftrightarrow b, p_c\leftrightarrow -p_b)\,,\\
O_{gg}^{A_3}(P,k) &= O_{gg}^{A_1}(P,k)\,(a\leftrightarrow b, p_a\leftrightarrow p_b)\,,\\
O_{gg}^{B_1}(P,k) &= -2\,(4\pi\alpha_s)^{3/2}\,\epsilon_a^\mu\epsilon_b^\nu\frac{\eta_{\mu\nu}(p_a-p_b)_\rho + \eta_{\nu\rho}(p_a+2p_b)_\mu - \eta_{\rho\mu}(2p_a+p_b)_\nu}{\hat{s}}\\
&\times (if_{abe})\left[t^c_{ik}t^e_{kj}\frac{\not\epsilon_c^*(\not P + 2\not p_c + 2\not k + M)\gamma^\rho}{(P+2p_c+2k)^2-M^2} - t^e_{ik}t^c_{kj}\frac{\gamma^\rho(\not P + 2\not p_c - 2\not k - M)\not\epsilon_c^*}{(P+2p_c-2k)^2-M^2}\right],\\
O_{gg}^{B_2}(P,k) &= O_{gg}^{B_1}(P,k)(c\leftrightarrow a, -p_a\leftrightarrow p_c),\\
O_{gg}^{B_3}(P,k) &= O_{gg}^{B_1}(P,k)(c\leftrightarrow b, -p_b\leftrightarrow p_c),
\end{aligned} \tag{B.15}$$

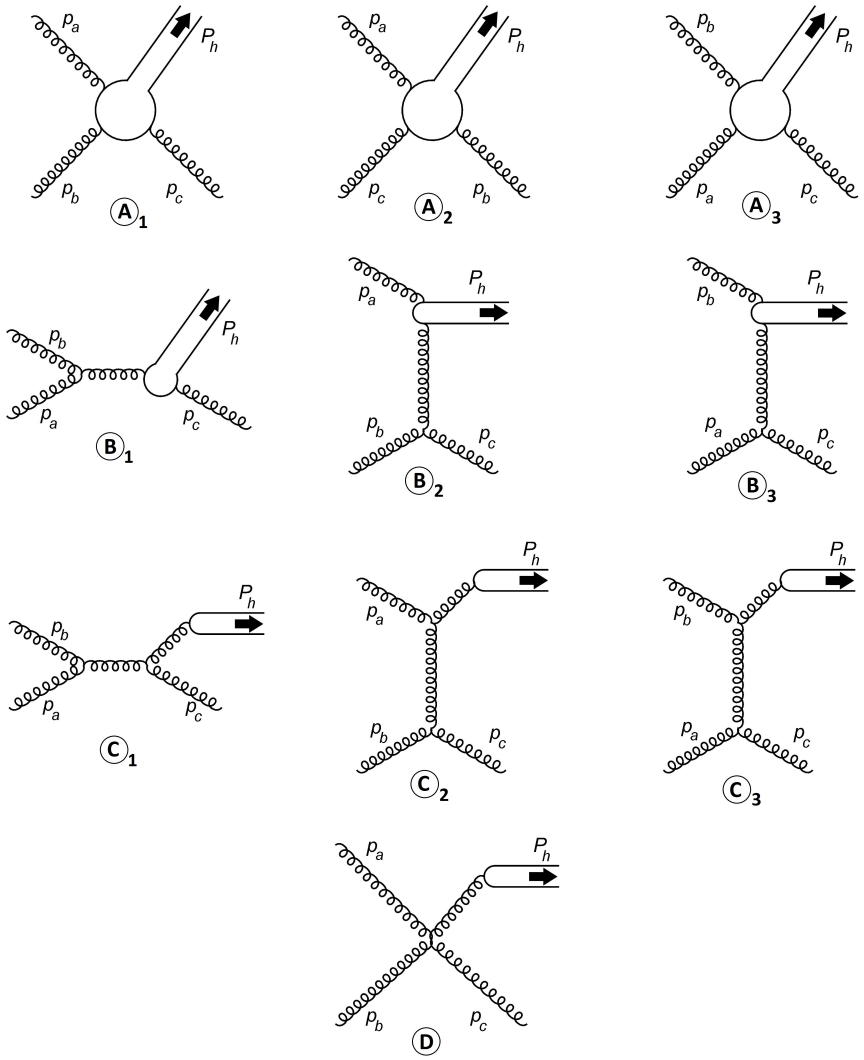

FIGURE B.3: Diagrams relative to the production of a $c\bar{c}$ pair at α_s^3 order via gg fusion.

$$
\begin{aligned}
O_{gg}^{C_1}(P,k) &= (4\pi\alpha_s)^{3/2}\,\epsilon_a^{\mu}\epsilon_b^{\nu}\epsilon_c^{*\sigma}\,f_{abe}f_{ech}t_{ij}^{h}\frac{\gamma^{\tau}}{\hat{s}M^2} \\
&\quad\times\left[\eta_{\mu\nu}(p_a-p_b)_{\rho}+\eta_{\nu\rho}(p_a+2p_b)_{\mu}-\eta_{\rho\mu}(2p_a+p_b)_{\nu}\right] \\
&\quad\times\left[\eta_{\sigma}^{\rho}(p_a+p_b+p_c)_{\tau}+\eta_{\sigma\tau}(p_a+p_b-2p_c)^{\rho}-\eta_{\tau}^{\rho}(2p_a+2p_b-p_c)_{\sigma}\right], \\
O_{gg}^{C_2}(P,k) &= O_{gg}^{C_1}(P,k)(c\leftrightarrow a,-p_a\leftrightarrow p_c), \\
O_{gg}^{C_3}(P,k) &= O_{gg}^{C_1}(P,k)(c\leftrightarrow b,-p_b\leftrightarrow p_c), \\
O_{gg}^{D}(P,k) &= O_{gg}^{D_1}(P,k)+O_{gg}^{D_2}(P,k)+O_{gg}^{D_3}(P,k),
\end{aligned}
\tag{B.16}
$$

where the last amplitude has been decomposed in three terms with different color structures

$$
\begin{aligned}
O_{gg}^{D_1}(P,k) &= (4\pi\alpha_s)^{3/2}\,t_{ij}^{h}f_{abe}f_{che}\left[(\epsilon_a\cdot\epsilon_c)\,\epsilon_b^{\tau}-(\epsilon_b\cdot\epsilon_c)\,\epsilon_a^{\tau}\right]\frac{\gamma_{\tau}}{M^2}, \\
O_{gg}^{D_2}(P,k) &= O_{gg}^{D_1}(P,q)\,(c\leftrightarrow a,-p_a\leftrightarrow p_c)\,, \\
O_{gg}^{D_3}(P,k) &= O_{gg}^{D_1}(P,q)\,(c\leftrightarrow b,-p_b\leftrightarrow p_c)\,.
\end{aligned}
\tag{B.17}
$$

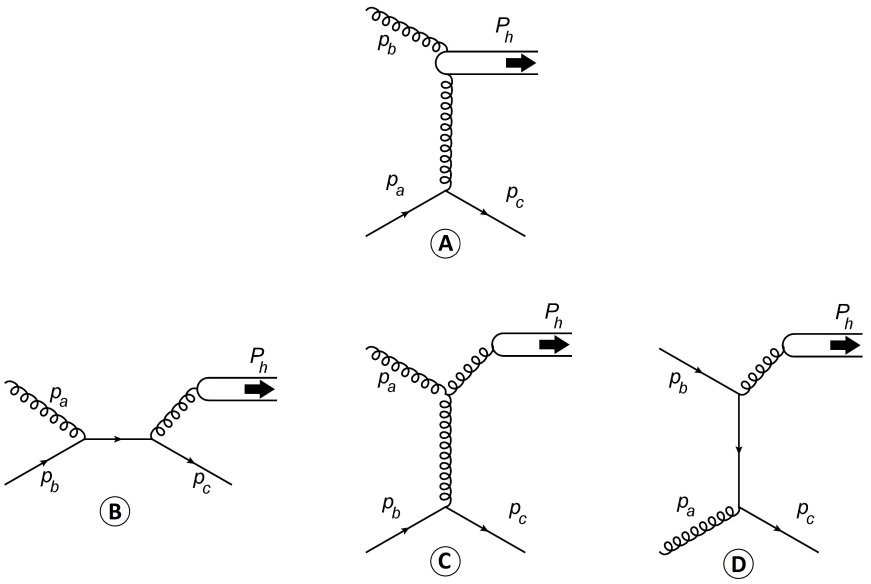

FIGURE B.4: Diagrams relative to the production of a $c\bar{c}$ pair at α_s^3 order via $gq(\bar{q})$ fusion.

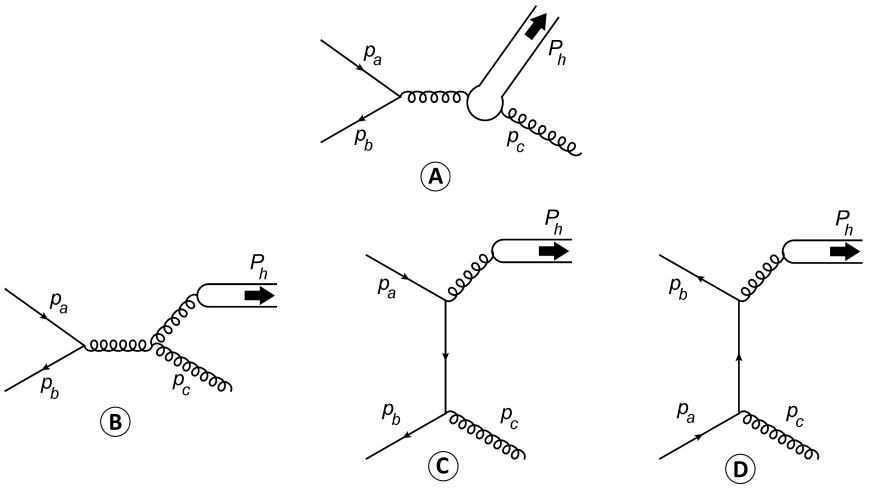

FIGURE B.5: Diagrams relative to the production of a $c\bar{c}$ pair at α_s^3 order via $q\bar{q}$ fusion.

Moreover, operators relative to $g\,q(\bar{q})$ interaction in Fig. B.4 are

$$
\begin{aligned}
O^A_{gq}(P,q) &= 2\,(4\pi\alpha_s)^{3/2}\,\frac{\overline{u}(p_c)\gamma_\rho u(p_b)}{\hat{t}}(t^e_{mn}) \\
&\quad\times\left[t^a_{ik}t^e_{kj}\frac{\not\epsilon_a(\not P-2\not p_a+2\not q+M)\gamma^\rho}{(P-2p_a+2q)^2-M^2}-t^e_{ik}t^a_{kj}\frac{\gamma^\rho(\not P-2\not p_a-2\not q-M)\not\epsilon_a}{(P-2p_a-2q)^2-M^2}\right], \\
O^B_{gq}(P,q) &= (4\pi\alpha_s)^{3/2}\,(t^e_{ij})(t^e_{ml}t^a_{ln})\frac{\overline{u}(p_c)\gamma_\tau(\not p_a+\not p_b)\not\epsilon_a u(p_b)}{\hat{s}}\frac{\gamma^\tau}{M^2}, \\
O^C_{gq}(P,q) &= (4\pi\alpha_s)^{3/2}\,(if_{ahe}t^e_{mn}t^h_{ij})\frac{\overline{u}(p_c)\gamma_\rho u(p_b)}{\hat{t}}\,\frac{\gamma_\tau}{M^2} \\
&\quad\times\epsilon^\mu_a\left[\eta^\tau_\mu(2p_a+p_b-p_c)^\rho+\eta^{\tau\rho}(2p_c-2p_b-p_a)_\mu+\eta^\rho_\mu(p_b-p_c-p_a)^\tau\right], \\
O^D_{gq}(P,q) &= (4\pi\alpha_s)^{3/2}\,(t^e_{ij})(t^a_{ml}t^e_{ln})\frac{\overline{u}(p_c)\not\epsilon_a(\not p_c-\not p_a)\gamma_\tau u(p_b)}{\hat{u}}\frac{\gamma^\tau}{M^2}.
\end{aligned}
\tag{B.18}
$$

Finally, for the $q\bar{q}$ annihilation, Fig. B.5, we have

$$
\begin{aligned}
O^A_{q\bar{q}}(P,q) &= 2\,(4\pi\alpha_s)^{3/2}\,\frac{\overline{u}(p_b)\gamma_\rho u(p_a)}{\hat{s}}(t^e_{mn}) \\
&\quad\times\left[t^c_{ik}t^e_{kj}\frac{\not\epsilon^*_c(\not P+2\not p_c+2\not q+M)\gamma^\rho}{(P+2p_c+2q)^2-M^2}-t^e_{ik}t^c_{kj}\frac{\gamma^\rho(\not P+2\not p_c-2\not q-M)\not\epsilon^*_c}{(P+2p_c-2q)^2-M^2}\right], \\
O^B_{q\bar{q}}(P,q) &= (4\pi\alpha_s)^{3/2}\,(if_{che}t^e_{mn}t^h_{ij})\frac{\overline{u}(p_b)\gamma_\rho u(p_a)}{\hat{s}}\,\frac{\gamma_\tau}{M^2} \\
&\quad\times\epsilon^{*\sigma}_c\left[\eta^\rho_\sigma(p_a+p_b+p_c)^\tau+\eta^{\rho\tau}(p_c-2p_a-2p_b)_\sigma+\eta^\tau_\sigma(p_a+p_b-2p_c)^\rho\right], \\
O^C_{q\bar{q}}(P,q) &= (4\pi\alpha_s)^{3/2}\,(t^e_{ij})(t^c_{ml}t^e_{ln})\frac{\overline{u}(p_b)\not\epsilon^*_c(\not p_c-\not p_b)\gamma_\tau u(p_a)}{\hat{t}}\,\frac{\gamma^\tau}{M^2}, \\
O^D_{q\bar{q}}(P,q) &= (4\pi\alpha_s)^{3/2}\,(t^e_{ij})(t^e_{ml}t^c_{ln})\frac{\overline{u}(p_b)\gamma_\tau(\not p_a-\not p_c)\not\epsilon^*_c u(p_a)}{\hat{u}}\,\frac{\gamma^\tau}{M^2}.
\end{aligned}
\tag{B.19}
$$

Color-singlet production

Starting once again from the CS state, the results are very different depending on the quarkonium involved. In any case, the CS state cannot be produce by a single gluon fragmentation, which restricts the contributing diagrams to: Ⓐ and Ⓑ of Fig. B.3 and diagrams Ⓐ of Figs. B.4 and B.5. For the remaining ones, we can use the trace relations in Eqs. (A.35)-(A.36) for η_c and Eqs. (A.35)-(A.36) for J/ψ. For all Ⓐ diagrams, only the anti-symmetric (symmetric) components contribute to η_c (J/ψ) production, while the opposite is true for diagrams Ⓑ in gg interaction.

The amplitudes squared for gg are then given by

$$
\begin{aligned}
\left|\mathcal{M}^{gg\to{}^1S_0^{(1)}g}\right|^2 &= (4\pi\alpha_s)^3\left[\hat{s}(\hat{t}+\hat{u})+\hat{t}\hat{u}\right]^2 \\
&\quad\times\frac{\left[\hat{s}^4+2\,\hat{s}^3(\hat{t}+\hat{u})+3\hat{s}^2(\hat{t}+\hat{u})^2+2\hat{s}(\hat{t}+\hat{u})^3+(\hat{t}^2+\hat{t}\,\hat{u}+\hat{u}^2)^2\right]}{6\,\hat{s}\,\hat{t}\,\hat{u}\,(\hat{s}+\hat{t})^2(\hat{s}+\hat{u})^2(\hat{t}+\hat{u})^2M}, \\
\left|\mathcal{M}_{gg\to{}^3S_1^{(1)}g}\right|^2 &= (4\pi\alpha_s)^3\frac{5}{108}M\frac{\hat{s}^2\left(\hat{t}^2+\hat{t}\,\hat{u}+\hat{u}^2\right)+\hat{s}\,\hat{t}\,\hat{u}\,(\hat{t}+\hat{u})+\hat{t}^2\hat{u}^2}{(\hat{s}-M^2)^2(\hat{t}-M^2)^2(\hat{u}-M^2)^2},
\end{aligned}
\tag{B.20}
$$

moreover for $gq(\bar{q})$ we have

$$
\begin{aligned}
\left|\mathcal{M}_{gq(\bar{q})\to{}^1S_0^{(1)}q(\bar{q})}\right|^2 &= -(4\pi\alpha_s)^3\frac{\hat{s}^2+\hat{u}^2}{27\,\hat{t}\,(\hat{s}+\hat{u})^2M}, \\
\left|\mathcal{M}_{gq(\bar{q})\to{}^3S_1^{(1)}q(\bar{q})}\right|^2 &= 0,
\end{aligned}
\tag{B.21}
$$

and finally for $q\bar{q}$

$$
\begin{aligned}
\left|\mathcal{M}_{q\bar{q}\to{}^1S_0^{(1)}g}\right|^2 &= (4\pi\alpha_s)^3\frac{8(\hat{t}^2+\hat{u}^2)}{81\,\hat{s}\,(\hat{t}+\hat{u})^2\,M}, \\
\left|\mathcal{M}_{q\bar{q}\to{}^3S_1^{(1)}g}\right|^2 &= 0.
\end{aligned}
\tag{B.22}
$$

Color-octet production

Moving to the production of a CO state, we have to consider once again the S- and P-waves contributions.

For both quarkonia, the expansion over velocity involves two CO S-waves, namely ${}^1S_0^{(8)}$ and ${}^3S_1^{(8)}$. The first is related to the production of a η_c in a CS state, with different CFs (listed in Tabs. B.3-B.5)

$$\begin{aligned}\left|\mathcal{M}_{gg\to{}^1S_0^{(8)}g}\right|^2 &= \frac{5(4\pi\alpha_s)^3}{16}\left[\hat{s}^2(\hat{t}^2+\hat{t}\hat{u}+\hat{u}^2)+\hat{s}\hat{t}\hat{u}(\hat{t}+\hat{u})+\hat{t}^2\hat{u}^2\right]\\ &\quad\times\frac{\left[\hat{s}^4+2\hat{s}^3(\hat{t}+\hat{u})+3\hat{s}^2(\hat{t}+\hat{u})^2+2\hat{s}(\hat{t}+\hat{u})^3+(\hat{t}^2+\hat{t}\hat{u}+\hat{u}^2)^2\right]}{\hat{s}\hat{t}\hat{u}(\hat{s}+\hat{t})^2(\hat{s}+\hat{u})^2(\hat{t}+\hat{u})^2M}\\ &= \frac{15}{8}\frac{\hat{s}^2(\hat{t}^2+\hat{t}\,\hat{u}+\hat{u}^2)+\hat{s}\hat{t}\hat{u}(\hat{t}+\hat{u})+\hat{t}^2\hat{u}^2}{\left[\hat{s}(\hat{t}+\hat{u})+\hat{t}\hat{u}\right]^2}\left|\mathcal{M}_{gg\to{}^1S_0^{(1)}g}\right|^2, \qquad \text{(B.23)}\end{aligned}$$

$$\left|\mathcal{M}_{gq(\bar{q})\to{}^1S_0^{(8)}q(\bar{q})}\right|^2 = \frac{15}{8}\left|\mathcal{M}_{gq(\bar{q})\to{}^1S_0^{(1)}q(\bar{q})}\right|^2, \qquad \text{(B.24)}$$

$$\left|\mathcal{M}_{q\bar{q}\to{}^1S_0^{(8)}g}\right|^2 = \frac{15}{8}\left|\mathcal{M}_{q\bar{q}\to{}^1S_0^{(1)}g}\right|^2. \qquad \text{(B.25)}$$

On the other hand, the ${}^3S_1^{(8)}$ state is only partially related to J/ψ production via CS state, since all diagrams contribute in this case, giving

$$\begin{aligned}\left|\mathcal{M}_{gg\to{}^3S_1^{(8)}g}\right|^2 &= \frac{(4\pi\alpha_s)^3}{72}\left[19M^4-27(\hat{s}\hat{t}+\hat{s}\hat{u}+\hat{t}\hat{u})\right]\\ &\quad\times\frac{\hat{s}^2\left(\hat{t}^2+\hat{t}\hat{u}+\hat{u}^2\right)+\hat{s}\hat{t}\hat{u}(\hat{t}+\hat{u})+\hat{t}^2\hat{u}^2}{M^3(\hat{s}-M^2)^2(\hat{t}-M^2)^2(\hat{u}-M^2)^2}\\ &= \frac{3}{10}\frac{19M^4-27(\hat{s}\,\hat{t}+\hat{s}\,\hat{u}+\hat{t}\,\hat{u})}{M^4}\left|\mathcal{M}_{gg\to{}^3S_1^{(1)}g}\right|^2, \qquad \text{(B.26)}\end{aligned}$$

$$\left|\mathcal{M}_{gq(\bar{q})\to{}^3S_1^{(8)}q(\bar{q})}\right|^2 = -\frac{(4\pi\alpha_s)^3}{108M^3}\frac{(\hat{s}^2+2M^2\hat{t}+\hat{u}^2)(4\hat{s}^2-\hat{s}\hat{u}+4\hat{u}^2)}{\hat{s}\hat{u}(\hat{t}-M^2)^2}, \qquad \text{(B.27)}$$

$$\left|\mathcal{M}_{q\bar{q}\to{}^3S_1^{(8)}g}\right|^2 = 2\frac{(4\pi\alpha_s)^3}{81M^3}\frac{(\hat{t}^2+2M^2\hat{s}+\hat{u}^2)(4\hat{t}^2-\hat{t}\hat{u}+4\hat{u}^2)}{\hat{t}\hat{u}(\hat{s}-M^2)^2}. \qquad \text{(B.28)}$$

Moving to P-waves, we consider both ${}^1P_1^{(8)}$ and ${}^3P_J^{(8)}$ (summed over the different J values) states. Due to the symmetry relations derived in Eqs. (A.40)-(A.43), the relevant CFs are related to the previous cases (see Tabs. B.3-B.5 of next section B.1.3).

From this, the production of ${}^1P_1^{(8)}$ state in the different partonic channels is given by

$$\begin{aligned}\left|\mathcal{M}_{gg\to{}^1P_1^{(8)}g}\right|^2 = &\frac{(4\pi\alpha_s)^3}{4M^2\hat{s}\hat{t}\hat{u}(\hat{u}-M^2)^3(\hat{t}-M^2)^3(\hat{s}-M^2)^3}\\
&\Big[\hat{s}^8(27\hat{t}^3+38\hat{t}^2\hat{u}+38\hat{t}\hat{u}^2+27\hat{u}^3)\\
&+\hat{s}^7(81\hat{t}^4+271\hat{t}^3\hat{u}+120\hat{t}^2\hat{u}^2+271\hat{t}\hat{u}^3+81\hat{u}^4)\\
&+\hat{s}^6(135\hat{t}^5+715\hat{t}^4\hat{u}+668\hat{t}^3\hat{u}^2+668\hat{t}^2\hat{u}^3+715\hat{t}\hat{u}^4+135\hat{u}^5)\\
&+\hat{s}^5(135\hat{t}^6+964\hat{t}^5\hat{u}+1432\hat{t}^4\hat{u}^2+1390\hat{t}^3\hat{u}^3+1432\hat{t}^2\hat{u}^4\\
&+964\hat{t}\hat{u}^5+135\hat{u}^6)\\
&+\hat{s}^4(81\hat{t}^7+715\hat{t}^6\hat{u}+1432\hat{t}^5\hat{u}^2+1640\hat{t}^4\hat{u}^3+1640\hat{t}^3\hat{u}^4+1432\hat{t}^2\hat{u}^5\\
&+715\hat{t}\hat{u}^6+81\hat{u}^7)\\
&+\hat{s}^3(27\hat{t}^8+271\hat{t}^7\hat{u}+668\hat{t}^6\hat{u}^2+1390\hat{t}^5\hat{u}^3+1640\hat{t}^4\hat{u}^4\\
&+1390\hat{t}^3\hat{u}^5+668\hat{t}^2\hat{u}^6+271\hat{t}\hat{u}^7+27\hat{u}^8)\\
&+2\hat{s}^2\hat{t}\hat{u}(19\hat{t}^7+60\hat{t}^6\hat{u}+334\hat{t}^5\hat{u}^2+716\hat{t}^4\hat{u}^3+716\hat{t}^3\hat{u}^4\\
&+334\hat{t}^2\hat{u}^5+60\hat{t}\hat{u}^6+19\hat{u}^7)\\
&+\hat{s}\hat{t}^2\hat{u}^2(\hat{t}+\hat{u})^2(38\hat{t}^4+195\hat{t}^3\hat{u}+287\hat{t}^2\hat{u}^2+195\hat{t}\hat{u}^3+38\hat{u}^4)\\
&+27\hat{t}^3\hat{u}^3(\hat{t}+\hat{u})(\hat{t}^2+\hat{t}\hat{u}+\hat{u}^2)^2\Big],\end{aligned} \tag{B.29}$$

$$\left|\mathcal{M}_{gq(\bar{q})\to{}^1P_1^{(8)}q(\bar{q})}\right|^2 = -(4\pi\alpha_s)^3\frac{3(\hat{s}^2+\hat{u}^2)}{2\hat{t}(\hat{t}-M^2)^2M^3}, \tag{B.30}$$

$$\left|\mathcal{M}_{q\bar{q}\to{}^1P_1^{(8)}g}\right|^2 = (4\pi\alpha_s)^3\frac{4(\hat{t}^2+\hat{u}^2)}{2\hat{s}(\hat{s}-M^2)^2M^3}; \tag{B.31}$$

while for ${}^3P_J^{(8)}$ state we have

$$\begin{aligned}\left|\mathcal{M}_{gg\to{}^3P_J^{(8)}g}\right|^2 = &\frac{5(4\pi\alpha_s)^3}{4M^3\hat{s}\hat{t}\hat{u}\left(M^2-\hat{s}\right)^3\left(M^2\hat{s}+\hat{t}\hat{u}\right)^3}\\
&\times\Big[7M^{16}\hat{s}^3-7M^{14}\left(5\hat{s}^4-2\hat{s}^2\hat{t}\hat{u}\right)\\
&+M^{12}\left(-85\hat{s}^3\hat{t}\hat{u}+14\hat{s}\hat{t}^2\hat{u}^2+84\hat{s}^5\right)\\
&+M^{10}\left(211\hat{s}^4\hat{t}\hat{u}-78\hat{s}^2\hat{t}^2\hat{u}^2-126\hat{s}^6+7\hat{t}^3\hat{u}^3\right)\\
&+M^8\left(-302\hat{s}^5\hat{t}\hat{u}+195\hat{s}^3\hat{t}^2\hat{u}^2-50\hat{s}\hat{t}^3\hat{u}^3+126\hat{s}^7\right)\\
&+M^6\left(275\hat{s}^6\hat{t}\hat{u}-233\hat{s}^4\hat{t}^2\hat{u}^2+95\hat{s}^2\hat{t}^3\hat{u}^3-84\hat{s}^8-14\hat{t}^4\hat{u}^4\right)\\
&+M^4\left(-157\hat{s}^7\hat{t}\hat{u}+165\hat{s}^5\hat{t}^2\hat{u}^2-98\hat{s}^3\hat{t}^3\hat{u}^3+34\hat{s}\hat{t}^4\hat{u}^4+35\hat{s}^9\right)\\
&-M^2\left(\hat{s}^2-\hat{t}\hat{u}\right)^2\left(-33\hat{s}^4\hat{t}\hat{u}-6\hat{s}^2\hat{t}^2\hat{u}^2+7\hat{s}^6-7\hat{t}^3\hat{u}^3\right)\\
&-3\hat{s}\hat{t}\hat{u}\left(\hat{s}^2-\hat{t}\hat{u}\right)^4\Big],\end{aligned} \tag{B.32}$$

$$\left|\mathcal{M}_{gq(\bar{q})\to{}^3P_J^{(8)}q(\bar{q})}\right|^2 = \frac{(4\pi\alpha_s)^3}{54M^3\hat{t}\left(\hat{t}-M^2\right)^4} \times\Big[162M^{11}\hat{t}-648M^9\hat{t}^2-105M^8+972M^7\hat{t}^3+30M^6\left(8\hat{t}+7\hat{u}\right) -648M^5\hat{t}^4-10M^4\left(43\hat{t}\hat{u}+19\hat{t}^2+21\hat{u}^2\right)+162M^3\hat{t}^5 +10M^2\hat{t}\left(27\hat{t}\hat{u}+8\hat{t}^2+22\hat{u}^2\right)-25\hat{t}^2\left(2\hat{t}\hat{u}+\hat{t}^2+2\hat{u}^2\right)\Big], \quad \text{(B.33)}$$

$$\left|\mathcal{M}_{q\bar{q}\to{}^3P_J^{(8)}g}\right|^2 = \frac{20(4\pi\alpha_s)^3}{27}\frac{\left(7M^4+3\hat{s}^2\right)\left(\hat{t}^2+\hat{u}^2\right)-2M^2\hat{s}\left(-8\hat{t}\hat{u}+\hat{t}^2+\hat{u}^2\right)}{M^3\hat{s}\left(\hat{t}+\hat{u}\right)^4}. \quad \text{(B.34)}$$

B.1.3 Color factors

In this section, the relevant, non-zero CFs appearing for different partonic subprocesses will be gathered. We present them in terms of the number of colors N.

B.1.4 Color factors at LO

At leading order, the CS state can be produced only via the diagram Ⓐ in Fig. B.1. Moreover, as also shown in the previous section, only η_c is produced in a CS configuration. Then, in this discussion only one CF is needed at LO, corresponding to

$$CU^{\text{CSM}}_{gg\to\eta_c} = \frac{1}{N(N^2-1)}. \quad \text{(B.35)}$$

Moving to the production of a CO state, the CFs are given in Tab. B.1. We see that via $gg \to \mathcal{Q}$ is possible to produce either a P-wave (${}^3P_J^{(8)}$ or ${}^1P_1^{(8)}$) or a ${}^1S_0^{(8)}$ state, while the ${}^3S_1^{(8)}$ state is produced only via $q\bar{q} \to \mathcal{Q}$.

State	Partonic process ($2 \to 1$)	Color Factor
${}^1S_0^{(8)}$ & ${}^3P_J^{(8)}$	$gg \to \mathcal{Q}$	$\frac{N^2-4}{2N(N^2-1)}$
${}^3S_1^{(8)}$	$q\bar{q} \to \mathcal{Q}$	$\frac{N^2-1}{4N^2}$
${}^1P_1^{(8)}$	$gg \to \mathcal{Q}$	$\frac{N}{2(N^2-1)}$

TABLE B.1: Color factors relative to the production of a CO state in pp collisions at LO in α_s. In the first two columns we indicate which state we are considering and via which process can be produced, while in the last column the corresponding (unpolarized) color factors are given.

Moreover, notice that the difference between the CO and CS ${}^1S_0$ states is just a factor $(N^2-4)/2$, as expected by the different projectors in Eq. (A.6).

B.1.5 Color factor at NLO

At α_s^3 order, we have three subprocesses to consider, namely $g\,g \to \mathcal{Q}\,g$, $g\,q(\bar{q}) \to \mathcal{Q}\,q(\bar{q})$ and $q\,\bar{q} \to \mathcal{Q}\,g$. The CFs for the production of η_c and J/ψ via a CS state are listed in Tab. B.2.

Quarkonium	Partonic process	Color Factor
$\eta_c[^1S_0^{(1)}]$	$gg \to \eta_c\, g$	
	$\text{Ⓐ}_1 \times \text{Ⓐ}_1$ & $\text{Ⓐ}_2 \times (\text{Ⓐ}_2, \text{Ⓐ}_3)$ & $\text{Ⓐ}_3 \times \text{Ⓐ}_3$	$\frac{1}{4(N^2-1)}$
	$\text{Ⓐ}_1 \times (\text{Ⓐ}_2, \text{Ⓐ}_3)$	$-\frac{1}{4(N^2-1)}$
	$\text{Ⓐ}_1 \times \text{Ⓑ}_1$ & $(\text{Ⓐ}_2, \text{Ⓐ}_3) \times (\text{Ⓑ}_2, \text{Ⓑ}_3)$	$\frac{1}{2(N^2-1)}$
	$\text{Ⓐ}_1 \times (\text{Ⓑ}_2, \text{Ⓑ}_3)$ & $(\text{Ⓐ}_2, \text{Ⓐ}_3) \times \text{Ⓑ}_1$	$-\frac{1}{2(N^2-1)}$
	$\text{Ⓑ}_1 \times \text{Ⓑ}_1$ & $\text{Ⓑ}_2 \times (\text{Ⓑ}_2, \text{Ⓑ}_3)$ & $\text{Ⓑ}_3 \times \text{Ⓑ}_3$	$\frac{1}{N^2-1}$
	$\text{Ⓑ}_1 \times (\text{Ⓑ}_2, \text{Ⓑ}_3)$	$-\frac{1}{N^2-1}$
	$q\bar{q} \to \eta_c\, g$	$\frac{N^2-1}{2N^3}$
	$gq(\bar{q}) \to \eta_c\, q(\bar{q})$	$\frac{1}{2N^2}$
$J/\psi[^3S_1^{(1)}]$	$gg \to J/\psi\, g$	$\frac{N^2-4}{4N^2(N^2-1)}$
	$q\bar{q} \to J/\psi\, g$	0
	$gq(\bar{q}) \to J/\psi\, q(\bar{q})$	0

TABLE B.2: Color factors relative to the production of a CS state in pp collisions at α_s^3 order. In the first column we indicate which quarkonium we are producing. In the second column we indicate the process involved and in the third column the corresponding (unpolarized) color factor to each diagram products are given; if not otherwise stated, the color factor is relative to the product $\text{Ⓐ} \times \text{Ⓐ}$.

Partonic process and state	Diagram products	Color Factor
$g\,g \to \mathcal{Q}[^1S_0^{(8)}$ & $^3P_J^{(8)}]\,g$	$\text{Ⓐ}_1 \times \text{Ⓐ}_1$ & $\text{Ⓐ}_1 \times \text{Ⓑ}_1$ & $-\text{Ⓐ}_1 \times \text{Ⓑ}_2$	$\frac{N^2-4}{4(N^2-1)}$
	$\text{Ⓐ}_2 \times \text{Ⓐ}_2$ & $\text{Ⓐ}_2 \times \text{Ⓑ}_2$ & $\text{Ⓐ}_2 \times \text{Ⓑ}_3$	$\frac{N^2-4}{4(N^2-1)}$
	$\text{Ⓐ}_3 \times \text{Ⓐ}_3$ & $-\text{Ⓐ}_3 \times \text{Ⓑ}_1$ & $\text{Ⓐ}_3 \times \text{Ⓑ}_3$	$\frac{N^2-4}{4(N^2-1)}$
	$\text{Ⓑ}_1 \times \text{Ⓑ}_1$ & $\text{Ⓑ}_2 \times \text{Ⓑ}_2$ & $\text{Ⓑ}_3 \times \text{Ⓑ}_3$	$\frac{N^2-4}{2(N^2-1)}$
	$\text{Ⓑ}_1 \times \text{Ⓑ}_2$ & $\text{Ⓑ}_1 \times \text{Ⓑ}_3$ & $-\text{Ⓑ}_2 \times \text{Ⓑ}_3$	$-\frac{N^2-4}{4(N^2-1)}$
$g\,g \to \mathcal{Q}[^3S_1^{(8)}$ & $^1P_1^{(8)}]\,g$	$\text{Ⓐ}_1 \times \text{Ⓐ}_1$ & $\text{Ⓐ}_2 \times \text{Ⓐ}_2$ & $\text{Ⓐ}_3 \times \text{Ⓐ}_3$	$\frac{N^4-2N^2+6}{4N^2(N^2-1)}$
	$\text{Ⓐ}_1 \times (\text{Ⓐ}_2, \text{Ⓐ}_3)$ & $-\text{Ⓐ}_2 \times \text{Ⓐ}_3$	$-\frac{N^2-3}{2N^2(N^2-1)}$
	$\text{Ⓐ}_1 \times (\text{Ⓑ}_1, \text{Ⓑ}_2)$	$-\frac{N^2}{4(N^2-1)}$
	$\text{Ⓐ}_2 \times \text{Ⓑ}_2$ & $-\text{Ⓐ}_2 \times \text{Ⓑ}_3$	$\frac{N^2}{4(N^2-1)}$
	$\text{Ⓐ}_3 \times (\text{Ⓑ}_1, \text{Ⓑ}_3)$	$\frac{N^2}{4(N^2-1)}$
	$\text{Ⓑ}_1 \times \text{Ⓑ}_1$ & $\text{Ⓑ}_2 \times \text{Ⓑ}_2$ & $\text{Ⓑ}_3 \times \text{Ⓑ}_3$	$\frac{N^2}{2(N^2-1)}$
	$\text{Ⓑ}_1 \times \text{Ⓑ}_2$ & $\text{Ⓑ}_1 \times \text{Ⓑ}_3$ & $-\text{Ⓑ}_2 \times \text{Ⓑ}_3$	$\frac{N^2}{4(N^2-1)}$

TABLE B.3: Non-zero, independent color factors relative to the process $g\,g \to \mathcal{Q}\,g$. Due to symmetry relations, $^1S_0^{(8)}$ and $^3P_J^{(8)}$ states have same color factors (first rows). The same is also found for $^3S_1^{(8)}$ and $^1P_1^{(8)}$ (last rows).

Partonic process and state	Diagram products	Color Factor
$g\,q(\bar{q}) \to \mathcal{Q}[^1S_0^{(8)}\ \&\ ^3P_J^{(8)}]\,q(\bar{q})$	Ⓐ × Ⓐ	$\frac{N^2-1}{4N^2}$
$g\,q(\bar{q}) \to \mathcal{Q}[^3S_1^{(8)}\ \&\ ^1P_1^{(8)}]\,q(\bar{q})$	Ⓐ × Ⓐ	$\frac{1}{4}$
	Ⓑ × Ⓑ & Ⓓ × Ⓓ	$\frac{N^2-1}{8N^2}$
$g\,q(\bar{q}) \to \mathcal{Q}[^3S_1^{(8)}]\,q(\bar{q})$	Ⓐ × Ⓑ	$\pm\frac{1}{8}$
	Ⓐ × Ⓓ	$\mp\frac{1}{8}$
	Ⓑ × Ⓓ	$-\frac{1}{8N^2}$

TABLE B.4: Non-zero, independent color factors relative to the process $g\,q(\bar{q}) \to \mathcal{Q}\,q(\bar{q})$. Due to symmetry relations, the squared product of diagram Ⓐ provides same color factors when producing $^1S_0^{(8)}$ and $^3P_J^{(8)}$ states (first row), or $^3S_1^{(8)}$ and $^1P_1^{(8)}$ states (second row). All the other products are relevant only when producing a $^3S_1^{(8)}$ state (last four rows). Moreover, if present, upper and lower signs are relative to the quark and antiquark cases, respectively.

Partonic process and state	Diagram products	Color Factor
$q\bar{q} \to \mathcal{Q}[^1S_0^{(8)}\ \&\ ^3P_J^{(8)}]\,g$	Ⓐ × Ⓐ	$\frac{(N^2-4)(N^2-1)}{4N^3}$
$q\bar{q} \to \mathcal{Q}[^3S_1^{(8)}\ \&\ ^1P_1^{(8)}]\,g$	Ⓐ × Ⓐ	$\frac{N^2-1}{4N}$
	Ⓒ × Ⓒ & Ⓓ × Ⓓ	$\frac{(N^2-1)^2}{8N^3}$
$q\bar{q} \to \mathcal{Q}[^3S_1^{(8)}]\,g$	Ⓐ × Ⓒ	$\frac{N^2-1}{8N}$
	Ⓐ × Ⓓ	$-\frac{N^2-1}{8N}$
	Ⓒ × Ⓓ	$-\frac{N^2-1}{8N^3}$

TABLE B.5: Non-zero, independent, color factors relative to the process $q\,\bar{q} \to \mathcal{Q}\,g$. Due to symmetry relations, the squared product of diagram Ⓐ provides same color factors when producing $^1S_0^{(8)}$ and $^3P_J^{(8)}$ states (first row), or $^3S_1^{(8)}$ and $^1P_1^{(8)}$ states (second row). All the other products are relevant only when producing a $^3S_1^{(8)}$ state (last four rows).

Moving to the CO production, we find that some of the CFs are equal. More specifically, we have the same CFs for $^1S_0^{(8)}$ and $^3P_J^{(8)}$ states. Furthermore, the diagrams that contribute to both $^3S_1^{(8)}$ and $^1P_1^{(8)}$ give the same CFs.

For each partonic process we find at least two diagrams whose products provide the same CFs. In particular: for $g\,g \to \mathcal{Q}\,g$ we have the correspondence $(Ⓒ_i, Ⓓ_i) \Leftrightarrow Ⓑ_i$ (with $i = 1, 2, 3$), for $g\,q(\bar{q}) \to \mathcal{Q}\,q(\bar{q})$ we have that Ⓒ ⇔ Ⓐ, and finally for $q\,\bar{q} \to \mathcal{Q}\,g$ Ⓑ ⇔ Ⓐ. Then, we will explicitly show only the independent CFs.

Moreover, if more than one product provides the same CF (including also a different sign), they will be listed together, using the notation Ⓘ × Ⓙ & Ⓚ × Ⓗ; furthermore, if the products of one diagram with two other diagrams have the same output, they will be gathered using the notation Ⓘ × (Ⓙ, Ⓚ).

Finally, the (unpolarized) CFs for $g\,g \to \mathcal{Q}\,g$ are presented in Tab. B.3, for $g\,q(\bar{q}) \to \mathcal{Q}\,q(\bar{q})$ in Tab. B.4, and for $q\,\bar{q} \to \mathcal{Q}\,g$ in Tab. B.5. Note that these CFs can have a different sign depending on whether we are considering a quark or an antiquark in $g\,q(\bar{q})$ interaction; in this case, we show the double signs, the upper sign is related to the quark, while the lower sign refers to the antiquark.

B.2 SIDIS

In this section we provide the structure functions relative to the SIDIS process $e\,p \to e'\,J/\psi + X$; differently from pp, here we will limit the discussion to the J/ψ meson.

B.2.1 LO diagrams

The partonic process for SIDIS at order $\alpha\alpha_s$ is given by

$$\gamma^*(q)\; a(p_a) \to J/\psi(P_\psi), \tag{B.36}$$

where $P_\psi^2 = M_\psi^2$ and initial parton can only correspond to a gluon, Fig. B.6.

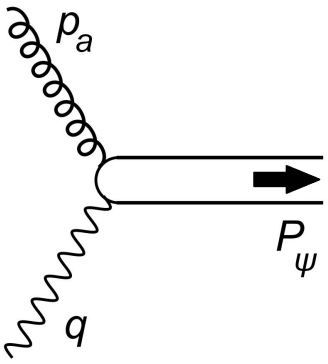

FIGURE B.6: Production of $c\bar{c}$ at 1$^{\text{st}}$ order from $\gamma\, g$ interaction.

The operator related to this diagram is given by

$$O^{A}_{\gamma^* g}{}^{\mu}(P,k) = 2\sqrt{(4\pi)^2\alpha\alpha_s}\, t^a_{ij}\left[\gamma^\mu \frac{\not p - \not q + \not k + M_\psi}{(p-q+k)^2 - M_\psi^2}\not\epsilon_a - \not\epsilon_a \frac{\not p - \not q - \not k - M_\psi}{(p-q-k)^2 - M_\psi^2}\gamma^\mu\right]. \tag{B.37}$$

Due to the Dirac matrix structure, it is clear that this diagram is related to a quarkonium production via a CO state. Unpolarized results obtained from previous operators are shown in Sec. 3.1.3 (Eq. (3.39)), while the polarized case is reported in Sec. 2.4 (Eq. (2.107)).

B.2.2 NLO diagrams

At the $\alpha\alpha_s^2$ order, the partonic process describing the J/ψ production in SIDIS is given by

$$\gamma^*(q)\; a(p_a) \to J/\psi(P_\psi) + a, \tag{B.38}$$

where the initial parton a can be either a gluon, Fig. B.7, or a quark/antiquark, Fig. B.8.

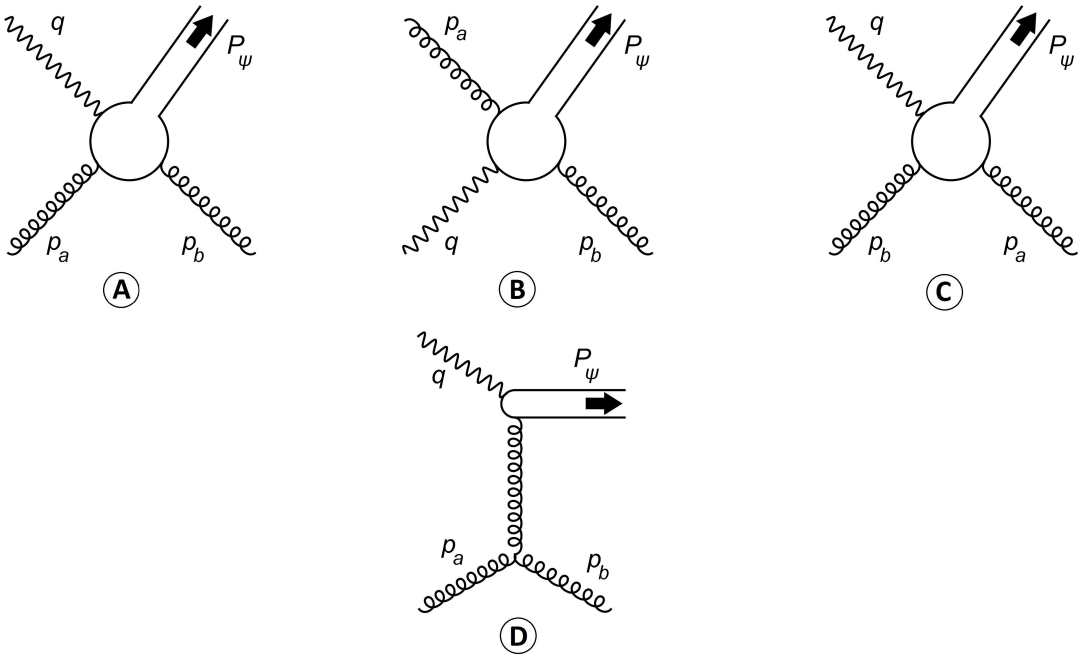

FIGURE B.7: Production of $c\bar{c}$ at 2nd order from $\gamma^* g$ interaction.

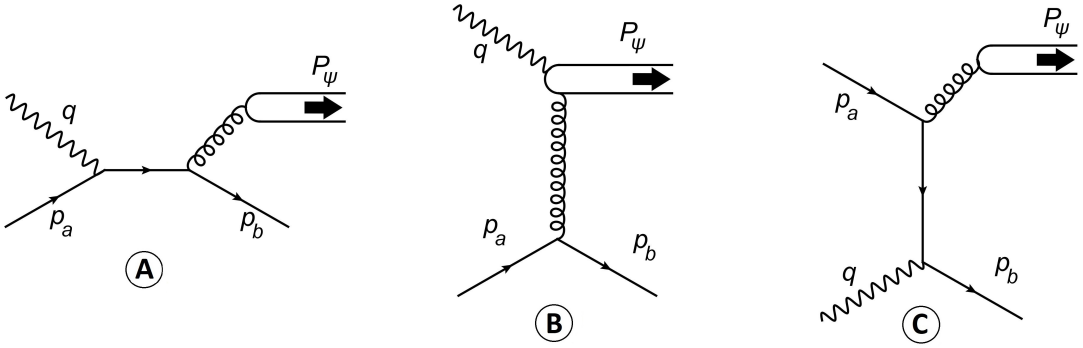

FIGURE B.8: Production of $c\bar{c}$ at 2nd order from $\gamma^* q$ interaction.

The diagrams relative to the first case are translated into the operators

$$O^A_{\gamma^* g}(P,k) = 4\sqrt{(4\pi)^3\alpha\alpha_s^2}\left\{ t^a_{ik}t^b_{kj}\frac{\gamma^\mu\left(\not{P}-2\not{q}+2\not{k}+M_\psi\right)\not{\epsilon}_a\left(\not{P}+2\not{p}_b-2\not{k}-M_\psi\right)\not{\epsilon}^*_b}{\left[(P-2q+2k)^2-M_\psi^2\right]\left[(P+2p_b-2k)^2-M_\psi^2\right]}\right.$$
$$\left. +t^b_{ik}t^a_{kj}\frac{\not{\epsilon}^*_b\left(\not{P}+2\not{p}_b+2\not{k}+M_\psi\right)\not{\epsilon}_a\left(\not{P}-2\not{q}-2\not{k}-M_\psi\right)\gamma^\mu}{\left[(P+2p_b+2k)^2-M_\psi^2\right]\left[(P-2q-2k)^2-M_\psi^2\right]}\right\},$$
$$O^B_{\gamma^* g}(P,k) = O^A_{\gamma^* g}(P,k)(q\leftrightarrow p_a),$$
$$O^C_{\gamma^* g}(P,k) = O^A_{\gamma^* g}(P,k)(b\leftrightarrow a, p_b\leftrightarrow -p_a),$$
$$O^D_{\gamma^* g}(P,k) = -2\sqrt{(4\pi)^3\alpha\alpha_s^2}\,\epsilon^\mu_a\epsilon^{*\nu}_b\frac{\eta_{\mu\nu}(p_a+p_b)_\rho-\eta_{\mu\rho}(2p_a-p_b)_\nu+\eta_{\rho\nu}(p_a-2p_b)_\nu}{\hat{t}}$$
$$\times(if_{abe})t^e_{ij}\left[\frac{\gamma^\mu(\not{P}-2\not{q}+2\not{k}+M_\psi)\gamma^\rho}{(P-2q+2k)^2-M_\psi^2}-\frac{\gamma^\rho(\not{P}-2\not{p}_b-2\not{k}-M_\psi)\gamma^\mu}{(P-2p_b-2k)^2-M_\psi^2}\right], \tag{B.39}$$

while the operators relative to the second case are

$$
\begin{aligned}
O^{A}_{\gamma^* q}(P,k) &= 2\sqrt{(4\pi)^3\alpha\alpha_s^2}\,(t^e_{mn}t^e_{ij})\frac{\overline{u}(p_b)\gamma_\rho u(p_a)}{\hat{t}} \\
&\times\left[\frac{\gamma^\mu(\not{P}-2\not{q}+2\not{k}+M_\psi)\gamma^\rho}{(P-2q+2k)^2-M_\psi^2}-\frac{\gamma^\rho(\not{P}-2\not{q}-2\not{k}-M_\psi)\gamma^\mu}{(P-2q-2k)^2-M_\psi^2}\right], \\
O^{B}_{\gamma^* q}(P,k) &= \sqrt{(4\pi)^3\alpha\alpha_s^2}\,(t^e_{ij}t^e_{mn})\frac{\overline{u}(p_b)\gamma_\tau(\not{q}+\not{p}_a)\gamma^\mu u(p_a)}{\hat{s}}\frac{\gamma^\tau}{M_\psi^2}, \\
O^{C}_{\gamma^* q}(P,k) &= \sqrt{(4\pi)^3\alpha\alpha_s^2}\,(t^e_{ij}t^e_{mn})\frac{\overline{u}(p_c)\gamma_\tau(\not{q}-\not{p}_b)\gamma^\mu u(p_a)}{\hat{u}}\frac{\gamma^\tau}{M_\psi^2}.
\end{aligned}
\tag{B.40}
$$

B.2.3 Partonic helicity structure functions

In this section, we show the analytic expressions for the partonic helicity structure functions relative to the $2 \to 2$ channel; we remark that this is the leading-order contribution to the high transverse momentum region, where collinear factorization applies.

We have selected the Gottfried-Jackson frame to present them, while the explicit forms in other frames are obtained by applying the rotational matrix in Eq. (2.82). Moreover, we decompose the $w_\Lambda^{\mathcal{P}\,(a)}$ as

$$
w_\Lambda^{\mathcal{P}\,(a)}[n] = F^{(a)}[n]\,\widehat{w}_\Lambda^{\mathcal{P}\,(a)}[n]. \tag{B.41}
$$

The prefactor $F^{(a)}[n]$ is independent of both the photon and J/ψ polarizations, given by $\mathcal{P} = \perp,\ \parallel$ and $\Lambda = T,\ L,\ \Delta,\ \Delta\Delta$, respectively. Furthermore, the modified Mandelstam variables defined in Eq. (2.69) are used once again to provide more compact expressions, while the superscript (a) and the dependence on the Fock-state n will be dropped, if not otherwise stated. Finally, we remark that, while the analytic expressions for the $w_T^{\mathcal{P}\,(a)}$ and $w_L^{\mathcal{P}\,(a)}$ were already known in Ref. [97], the complete expressions for $w_\Delta^{\mathcal{P}\,(a)}$ and $w_{\Delta\Delta}^{\mathcal{P}\,(a)}$ were first shown in Ref. [112]. We mention that, in Ref. [97] they claim to reproduce the photoproduction limit (Ref. [88]), while they found inconsistencies with Ref. [87] when comparing the unpolarized structure functions. On the contrary, the partonic helicity structure functions reported in the following correctly reproduce both photoproduction and unpolarized cases.

- $\gamma^* + q(\bar{q}) \to c\bar{c}[\,^1S_0^{(8)}] + q(\bar{q})$:

$$
\begin{aligned}
F &= -\frac{64\,e_c^2\alpha\alpha_s^2}{9M_\psi s^2 t(s+u)^2}, \\
\widehat{w}_L^{\parallel} &= 8Q^2t\left(Q^2t+su\right), \\
\widehat{w}_L^{\perp} &= 2Q^2t\left[Q^2t+s(s+u)\right]+s^2(s^2+u^2), \\
\widehat{w}_T^{\parallel} &= \widehat{w}_L^{\parallel}, \\
\widehat{w}_T^{\perp} &= \widehat{w}_L^{\perp}, \\
\widehat{w}_\Delta^{\parallel} &= \widehat{w}_\Delta^{\perp} = \widehat{w}_{\Delta\Delta}^{\parallel} = \widehat{w}_{\Delta\Delta}^{\perp} = 0.
\end{aligned}
\tag{B.42}
$$

- $\gamma^* + q(\bar{q}) \to c\bar{c}[\,^3S_1^{(8)}] + q(\bar{q})$:

$$
\begin{aligned}
F &= -\frac{16\, e_q^2 \alpha \alpha_s^2}{9 M_\psi^3 s^2 (Q^2-s)^2 (Q^2-u)^2 \left(4Q^2 t + (s+u)^2\right)}, \\
\widehat{w}_L^{\parallel} &= 32 Q^2 M_\psi^2 t^2 (Q^2-s)^2 (Q^2 t + su), \\
\widehat{w}_L^{\perp} &= 4 M_\psi^2 t \Big[2Q^8 t^2 + 2Q^6 st(s-2t+u) + Q^4 s^2 (s^2 - 2st + 2t^2 - 6tu + u^2) \\
&\quad - 2Q^2 s^3 u (s-2t+u) + 2s^4 u^2 \Big], \\
\widehat{w}_T^{\parallel} &= 8 Q^2 t (Q^2-s)^2 \Big\{ 2Q^4 t^2 + 2Q^2 t \Big[2s^2 + s(3t+u) + t(t-u) \Big] \\
&\quad + s^2 (s+t+u)^2 + t^2 u^2 \Big\}, \\
\widehat{w}_T^{\perp} &= 4Q^{10} t^3 + 4Q^8 t^2 \Big[s^2 + s(t+u) + t(t-u) \Big] \\
&\quad + 2Q^6 t \Big[s^4 - 2s^3 (t-2u) + s^2 (-7t^2 + 2tu + u^2) - 4st^2 (t-u) + t^2 u^2 \Big] \\
&\quad - 2Q^4 s \Big[s^4 (t-u) + s^3 u (5t-2u) - s^2 (2t^3 - 10t^2 u - 3tu^2 + u^3). \\
&\quad - st(2t^3 - 4t^2 u + u^3) + 2t^3 u^2 \Big] + Q^2 s^2 \Big[s^4 (t-2u) + 2s^3 (t^2 + tu - 3u^2) \\
&\quad + 2s^2 (t^3 + 3t^2 u - 2tu^2 - 3u^3) - 2su(-2t^3 - t^2 u + tu^2 + u^3) \\
&\quad + tu^2 (2t^2 - 2tu - u^2) \Big] + s^3 u (s^2 + u^2) \Big[s^2 + 2s(t+u) + 2t^2 + 2tu + u^2 \Big], \\
\widehat{w}_\Delta^{\parallel} &= 16 Q^2 M_\psi t \sqrt{(Q^2 t + su) t} (Q^2 - s)^2 \Big[2Q^2 t + s^2 + s(t+u) - ut \Big], \\
\widehat{w}_\Delta^{\perp} &= 2 M_\psi \sqrt{(Q^2 t + su) t} \Big\{ 4Q^8 t^2 + 2Q^6 t \Big[s^2 + s(u-3t) - tu \Big] \\
&\quad - Q^4 s \Big[s^3 + 2s^2 t + su(6t-u) - 4t^2 u \Big] + 2Q^2 s^2 t \Big[s(t+u) + u(u-t) \Big] \\
&\quad + s^3 u (s-u)(s+2t+u) \Big\}, \\
\widehat{w}_{\Delta\Delta}^{\parallel} &= 16 Q^2 M_\psi^2 t^2 (Q^2 t + su)(Q^2 - s)^2, \\
\widehat{w}_{\Delta\Delta}^{\perp} &= 2(Q^2 t + su) t \Big\{ -2Q^8 t + 2Q^6 \Big[s^2 + 3st + t(t+u) \Big] \\
&\quad - 4Q^4 st(s+t+u) - Q^2 s^2 (s^2 + 4su - 2t^2 + u^2) + 2s^3 u (s+t+u) \Big\}.
\end{aligned}
\tag{B.43}
$$

- $\gamma^* + q(\bar{q}) \to c\bar{c}[\,^3P_J^{(8)}] + q(\bar{q})$:

$$F = -\frac{256\, e_c^2 \alpha \alpha_s^2}{3M_\psi^3 s^2 t(s+u)^4\Big(4Q^2 t + (s+u)^2\Big)},$$

$$\begin{aligned}
\widehat{w}_L^{\parallel} = 8Q^2\Big\{ & 16Q^8 t^3 - 8Q^6 t^2\Big[- s^2 + 2s(t-u) + 4t^2 + 6tu + u^2\Big] \\
& - 4Q^4 t\Big[s^4 + 2s^3 t + s^2(5t^2 + 10tu + u^2) + 2s(-2t^3 + 3t^2 u + 7tu^2 + u^3) \\
& - t(4t^3 + 12t^2 u + 11tu^2 + 2u^3)\Big] + Q^2\Big[- 2s^6 + 4s^5(t-u) \\
& + s^4(5t^2 + 4tu - 4u^2) + 4s^3(4t^3 + t^2 u - 3tu^2 - u^3) \\
& + 2s^2(8t^4 + 32t^3 u + 21t^2 u^2 - 2tu^3 - u^4) \\
& + 4stu(8t^3 + 20t^2 u + 15tu^2 + 2u^3) + t^2 u^4\Big] \\
& + s(s+u)\Big[2s^5 + 2s^4(t+2u) + s^3 u(3t+4u) \\
& + s^2 u(16t^2 + 17tu + 4u^2) + su(16t^3 + 32t^2 u + 17tu^2 + 2u^3) + tu^4\Big]\Big\},
\end{aligned}$$

$$
\begin{aligned}
\widehat{w}_L^{\perp} &= 32Q^{10}t^3 - 16Q^8t^2\Big[s^2 + 2s(t-u) + 4t^2 + 6tu + u^2\Big] \\
&\quad + 8Q^6t\Big[2s^3(3t-u) + s^2t(7t-2u) - 2s(-2t^3 + 3t^2u + 7tu^2 + u^3) \\
&\quad + t(4t^3 + 12t^2u + 11tu^2 + 2u^3)\Big] + 2Q^4t\Big[s^4(-7t+24u) \\
&\quad - 4s^3(4t^2 + tu - 2u^2) + 2s^2u(16t^2 + 15tu - 4u^2) \\
&\quad + 4su(8t^3 + 20t^2u + 15tu^2 + 2u^3) + tu^4\Big] \\
&\quad + 2Q^2st\Big[5s^5 + 4s^4(8t-11u) + 2s^3(4t^2 + 4tu - 9u^2) \\
&\quad + 2s^2u(8t^2 + 20tu + 9u^2) + su^2(24t^2 + 40tu + 21u^2) + u^5\Big] \\
&\quad + s^2(s+u)^2\Big[s^4 + 2s^3u + 2s^2u(8t+u) + 2su(8t^2 + 8tu + u^2) + u^4\Big], \\
\widehat{w}_T^{\parallel} &= 8Q^2t\Big\{ - 8Q^8t^2 + 4Q^6t\Big[s^2 - 2su + u(4t+u)\Big] - 2Q^4\Big[s^3(3t-2u) \\
&\quad + s^2t(2t+u) - s(8t^3 + 4t^2u + 7tu^2 + 2u^3) + t(-4t^3 + 6tu^2 + 3u^3)\Big] \\
&\quad - Q^2\Big[s^4(t+6u) - 2s^3(7t^2 + 4tu - u^2) - 2s^2(6t^3 + 13t^2u + 3tu^2 - u^3) \\
&\quad + 2su(-4t^3 - t^2u + 4tu^2 + 3u^3) - tu^2(4t^2 + 6tu + 3u^2)\Big] \\
&\quad + s(s+u)\Big[s^3(4t+3u) + s^2(4t^2 + 6tu + u^2) + su^3 + u^2(4t^2 + 6tu + 3u^2)\Big]\Big\}, \\
\widehat{w}_T^{\perp} &= -16Q^{10}t^3 + 8Q^8t^2\Big[- 3s^2 - 2su + u(4t+u)\Big] + 4Q^6t\Big[2s^4 \\
&\quad + s^3(5t-2u) + s^2(10t^2 + 7tu + 2u^2) + s(8t^3 + 4t^2u + 7tu^2 + 2u^3) \\
&\quad + t(4t^3 - 6tu^2 - 3u^3)\Big] + 2Q^4\Big[2s^6 + s^5(4u-6t) - s^4(t^2 + 8tu - 4u^2) \\
&\quad + 2s^3(3t^3 + 8t^2u - 2tu^2 + 2u^3) + 2s^2(2t^4 + 9t^3u + 3t^2u^2 - 4tu^3 + u^4) \\
&\quad + 2stu(4t^3 + t^2u - 4tu^2 - 3u^3) + t^2u^2(4t^2 + 6tu + 3u^2)\Big] \\
&\quad + 2Q^2s\Big[- 3s^6 + s^5(t-9u) + s^4(6t^2 + 11tu - 12u^2) \\
&\quad + 2s^3(2t^3 + 12t^2u + 9tu^2 - 6u^3) + s^2u(12t^3 + 20t^2u + 10tu^2 - 9u^3) \\
&\quad + su^2(4t^3 + 8t^2u + 5tu^2 - 3u^3) + tu^3(4t^2 + 6tu + 3u^2)\Big] \\
&\quad + s^2(s+u)^2(s^2 + u^2)\Big[3s^2 + 6s(t+u) + 4t^2 + 6tu + 3u^2\Big], \\
\widehat{w}_{\Delta}^{\parallel} &= -8Q^2M_{\psi}\sqrt{(Q^2t + su)t}\Big\{16Q^6t^2 - 8Q^4t\Big[2t^2 + 4tu - u(s-u)\Big] \\
&\quad - 2Q^2\Big[2s^4 - s^3(3t-2u) + s^2(4t^2 + 3tu + 2u^2) \\
&\quad + s(4t^3 + 12t^2u + 11tu^2 + 2u^3) - tu(4t^2 + 8tu + 3u^2)\Big] \\
&\quad + s(s+u)\Big[3s^3 + s^2(-4t+u) + s(-8t^2 - 8tu + u^2) \\
&\quad + u(8t^2 + 12tu + 3u^2)\Big]\Big\},
\end{aligned}
$$

$$
\begin{aligned}
\widehat{w}^{\perp}_{\Delta} &= 2M_{\psi}\sqrt{(Q^2t+su)t}\Big\{ -16Q^8t^2 + 8Q^6t\Big[2t^2+4tu-u(s-u)\Big] \\
&\quad + 2Q^4\Big[2s^4+s^3(-3t+2u)+s^2(4t^2+3tu+2u^2) \\
&\quad + s(4t^3+12t^2u+11tu^2+2u^3) - tu(4t^2+8tu+3u^2)\Big] \\
&\quad - Q^2s\Big[7s^4+4s^3(t+2u)-2s^2u(6t+u)-4stu(2t+u) \\
&\quad + u^2(8t^2+12tu+3u^2)\Big] + s^2(s-u)(s+u)^2(3s+4t+3u)\Big\}, \\
\widehat{w}^{\parallel}_{\Delta\Delta} &= -16Q^2M_{\psi}^2t^2(Q^2t+su)\Big\{4Q^4t - 2Q^2(s^2-2st+2t^2+2tu+u^2) \\
&\quad + (s+u)\Big[s^2+u^2-2s(2t+u)\Big]\Big\}, \\
\widehat{w}^{\perp}_{\Delta\Delta} &= 4M_{\psi}^2(Q^2t+su)t\Big\{ -4t^2Q^6 + Q^4\Big[2s^2t-4st^2+2t(2t^2+2tu+u^2)\Big] \\
&\quad + Q^2\Big[-s^3t+s^2tu-tu^3+stu(4t+u)\Big] + s^2\Big[s^3+s^2(2t+3u) \\
&\quad + su(4t+3u)+u^2(2t+u)\Big]\Big\}. \qquad \text{(B.44)}
\end{aligned}
$$

- $\gamma^* + g \to c\bar{c}[\,^1S_0^{(8)}] + g$:

$$
\begin{aligned}
F &= \frac{32\,e_c^2\alpha\alpha_s^2}{s^2t(s+t)^2(s+u)^2(t+u)^2M_{\psi}}, \\
\widehat{w}^{\parallel}_{L} &= 4Q^2t\Big\{2Q^4t^2u^2 + 2Q^2stu(t^2+tu+2u^2) \\
&\quad + s^2\Big[s^2(t+u)^2+2s(t^3+2t^2u+2tu^2+u^3) \\
&\quad + t^2u(2Q^2+3u)+2tu^2(Q^2+u)+t^4+2t^3u+2u^4\Big]\Big\}, \\
\widehat{w}^{\perp}_{L} &= 2Q^6t^3u^2 + 2Q^4st^2u\Big[s(t+u)+t^2+tu+2u^2\Big] \\
&\quad + Q^2s^2t\Big[s^4+2s^3(t+u)+3s^2(t+u)^2+2s(t^3+3t^2u+4tu^2+2u^3) \\
&\quad + t^4+2t^3u+5t^2u^2+4tu^3+3u^4\Big] + s^3u\Big[s^4+2s^3(t+u) \\
&\quad + 3s^2(t+u)^2+2s(t+u)^3+(t^2+tu+u^2)^2\Big], \\
\widehat{w}^{\parallel}_{T} &= \widehat{w}^{\parallel}_{L}, \\
\widehat{w}^{\perp}_{T} &= \widehat{w}^{\perp}_{L}, \\
\widehat{w}^{\parallel}_{\Delta} &= \widehat{w}^{\perp}_{\Delta} = \widehat{w}^{\parallel}_{\Delta\Delta} = \widehat{w}^{\perp}_{\Delta\Delta} = 0. \qquad \text{(B.45)}
\end{aligned}
$$

- $\gamma^* + g \to c\bar{c}[^3S_1^{(1)}] + g$:

$$F = \frac{256\, e_c^2 \alpha \alpha_s^2}{27 s^2 (s+t)^2 (s+u)^2 (t+u)^2 \Big(4Q^2 t + (s+u)^2\Big) M_\psi},$$

$$\begin{aligned}
\widehat{w}_L^{\parallel} &= 4Q^2 t \Big\{ 8Q^8 t^4 + 8Q^6 t^3 \Big[s^2 - s(t-2u) - 2t(t+u) \Big] \\
&\quad + 2Q^4 t^2 \Big[s^4 + 4t^2 (t+u)^2 + s^3(-4t+6u) + 2st(2t^2 - 5tu - 7u^2) \\
&\quad + s^2(-4t^2 - 10tu + 7u^2) \Big] + 2Q^2 st \Big[s^4(-t+u) + s^3(t^2 - 3tu + 4u^2) \\
&\quad + s^2(4t^3 - 7tu^2 + 3u^3)) + st(2t^3 + 8t^2 u - 3tu^2 - 9u^3) + 6t^2 u (t+u)^2 \Big] \\
&\quad + s^2 \Big[s^4 (t^2 + u^2) + 2s^3 (t^3 + 2t^2 u + u^3) + s^2 (t^4 + 6t^3 u + 2t^2 u^2 - 4tu^3 + u^4) \\
&\quad + 2stu(t^3 + 3t^2 u - 2u^3) + 5t^2 u^2 (t+u)^2 \Big] \Big\}, \\
\widehat{w}_L^{\perp} &= 2t \Big\{ 4Q^{10} t^3 - 4Q^8 t^2 \Big[s(t-2u) + 2t(t+u) \Big] + 2Q^6 t \Big[s^3 t + 2t^2 (t+u)^2 \\
&\quad + st(2t^2 - 5tu - 7u^2) + s^2 (3t^2 - 2tu + 3u^2) \Big] + 2Q^4 s \Big[3t^2 u (t+u)^2 \\
&\quad + s^3 t(t+2u) + s^2 (5t^2 u + u^3) - st(t^3 - 2t^2 u + tu^2 + 4u^3) \Big] \\
&\quad + Q^2 s^2 \Big[s^4 t - 2s(t-u)^2 u(t+u) + 2s^3 (t+u)^2 + 3tu^2 (t+u)^2 \\
&\quad + s^2 t(t^2 + 2tu + 6u^2) \Big] + s^3 u (s+t+u)^2 (s^2 + u^2) \Big\}, \\
\widehat{w}_T^{\parallel} &= 8Q^2 M_\psi^2 (Q^2 t + su) t \Big\{ t^2 \Big[s^2 + 2Q^2 (Q^2 + t) \Big] + tu \Big[s(s+t) + 2Q^2 (s-t) \Big] \\
&\quad + u^2 \Big(s^2 - st + t^2 \Big) \Big\}, \\
\widehat{w}_T^{\perp} &= M_\psi^2 \Big\{ 4Q^8 t^4 + 4Q^6 t^3 \Big[2s(s+u) + t(t-u) \Big] + 2Q^4 t^2 \Big[s^4 - s^3 (t-6u) \\
&\quad + 2s^2 (t^2 + 2u^2) + 3st(t-u)u + t^2 u^2 \Big] + Q^2 st \Big[-s^4 (t-2u) \\
&\quad + s^3 (3t^2 + tu + 8u^2) + s^2 u (8t^2 + 3tu + 4u^2) + st(5t - 3u) u^2 + 2t^2 u^3 \Big] \\
&\quad + s^2 \Big[s^4 (t^2 + u^2) + 2s^3 u (t^2 + tu + u^2) + s^2 u^2 (4t^2 + 2tu + u^2) \\
&\quad + 2st^2 u^3 + t^2 u^4 \Big] \Big\}, \\
\widehat{w}_\Delta^{\parallel} &= -4Q^2 M_\psi \sqrt{(Q^2 t + su) t} \Big\{ 8Q^6 t^3 + 4Q^4 t^2 \Big[s(s - t + 3u) - t(2t + 3u) \Big] \\
&\quad - 2Q^2 t \Big[s^3 (t-2u) + 2s^2 u (t-2u) + stu(4t + 7u) - 2t^2 u (t+u) \Big] \\
&\quad + s \Big[s^3 (t^2 + tu + 2u^2) + s^2 (t^3 + 3t^2 u + 2u^3) - stu^2 (3t + 5u) + 3t^2 u^2 (t+u) \Big] \Big\},
\end{aligned}$$

$$
\begin{aligned}
\widehat{w}^{\perp}_{\Delta} &= M_\psi \sqrt{(Q^2 t + su)t}\Big\{ -8Q^8 t^3 - 4Q^6 t^2 (s^2 - st - 2t^2 + 3su - 3tu) \\
&\quad + 2Q^4 t \Big[s^3(t-2u) + 2s^2(t-2u)u + stu(4t+7u) - 2t^2 u(t+u) \Big] \\
&\quad - Q^2 s \Big[s^4 t + 2s^3(t^2+tu+u^2) + s^2(3t^3 + 3t^2 u - tu^2 + 2u^3) \\
&\quad - 2stu(t^2 + 2tu + 3u^2) + 3t^2 u^2 (t+u) \Big] \\
&\quad + s^2(s-u)\Big[s^3(t-u) - su^3 + tu^2(t+u) + s^2(t^2 - 2u^2) \Big] \Big\}, \\
\widehat{w}^{\parallel}_{\Delta\Delta} &= -8Q^2 M_\psi^2 (Q^2 t + su) t \Big[2Q^4 t^2 - 2Q^2 t(t^2 - su + tu) + s(s-t)u(t+u) \Big], \\
\widehat{w}^{\perp}_{\Delta\Delta} &= M_\psi^2 (Q^2 t + su) t \Big\{ -4Q^6 t^2 + Q^4 \Big[-4stu + 4t^2(t+u) \Big] \\
&\quad + Q^2 \Big[2s^3 t - 2s^2(t^2+u^2) + 2stu(t+u) \Big] + s^2(s+t+u)(s^2+u^2) \Big\}.
\end{aligned}
\tag{B.46}
$$

- $\gamma^* + g \to c\bar{c}[{}^3S_1^{(8)}] + g$:

$$
\widehat{w}^{\mathcal{P}}_{\Lambda}[{}^3S_1^{(8)}] = \frac{15}{8} \widehat{w}^{\mathcal{P}}_{\Lambda}[{}^3S_1^{(1)}]\,. \tag{B.47}
$$

- $\gamma^* + g \to c\bar{c}[{}^3P_J^{(8)}] + g$:

  The formulae for the P-wave components of $\widehat{w}_L^{\mathcal{P}}$ and $\widehat{w}_T^{\mathcal{P}}$ are not reported here, but they are available upon request as a Wolfram Mathematica notebook file. Only $\widehat{w}_\Delta^{\mathcal{P}}$ and $\widehat{w}_{\Delta\Delta}^{\mathcal{P}}$ are given below in an analytical form.

$$F = -\frac{192\sqrt{(Q^2t+su)t}\,e_c^2\alpha\alpha_s^2}{s^2t^2(s+t)^3(s+u)^4(t+u)^3\left[4Q^2t+(s+u)^2\right]M_\psi^2},$$

$$\begin{aligned}
\widehat{w}_\Delta^{\parallel} = 8Q^2t\Big\{ & 32Q^8t^3(s^3t - st^2u - s^2u^2 + tu^3) - 8Q^6t^2\Big[2s^5u + s^4(6t^2 - 2tu + 6u^2) \\
& + s^3(5t^3 + 11t^2u + 10u^3) - s^2(t^4 + 7t^3u + 6tu^3 - 4u^4) \\
& + su(-6t^4 - 11t^3u + 5t^2u^2 - 2tu^3 + 2u^4) + tu^2(-t^3 + 5t^2u + 10tu^2 + 2u^3)\Big] \\
& - 4Q^4t\Big[2s^7(t+u) + 2s^6(2t^2 + 2tu + 5u^2) + s^5(-5t^3 + 10t^2u - 4tu^2 + 20u^3) \\
& + s^4(-8t^4 - 8t^3u + 18t^2u^2 - 7tu^3 + 24u^4) \\
& - s^3(t^5 + 9t^4u + 14t^3u^2 - 15t^2u^3 + 11tu^4 - 14u^5) \\
& + s^2(2t^6 + 15t^5u + 23t^4u^2 + 16t^3u^3 + 41t^2u^4 + 5tu^5 + 6u^6) \\
& + stu(4t^5 + 23t^4u + 29t^3u^2 + 23t^2u^3 + 27tu^4 + 3u^5) \\
& + t^2u^2(2t^4 + 3t^3u - 7t^2u^2 - 12tu^3 - 3u^4)\Big] + 2Q^2\Big[2s^8(t^2 - tu - 2u^2) \\
& + s^7(7t^3 + 9t^2u + 6tu^2 - 12u^3) + s^6(3t^4 + 27t^3u + 20t^2u^2 + 28tu^3 - 20u^4) \\
& + s^5u(16t^4 + 42t^3u + 21t^2u^2 + 43tu^3 - 20u^4) \\
& + s^4(4t^6 + 8t^5u + 33t^4u^2 + 54t^3u^3 + 18t^2u^4 + 37tu^5 - 12u^6) \\
& + s^3(2t^7 + 6t^6u - t^5u^2 + 8t^4u^3 + 27t^3u^4 - 11t^2u^5 + 11tu^6 - 4u^7) \\
& + s^2tu(6t^6 + 20t^5u + 19t^4u^2 + 25t^3u^3 + 39t^2u^4 + 4tu^5 + 5u^6) \\
& + st^2u^2(6t^5 + 22t^4u + 37t^3u^2 + 52t^2u^3 + 44tu^4 + 9u^5) \\
& + t^4u^3(2t^3 + 4t^2u + tu^2 - u^3)\Big] + s(s+u)\left[s^7(3t^2 + 10tu + 7u^2)\right. \\
& + s^6(8t^3 + 26t^2u + 30tu^2 + 20u^3) + s^5(7t^4 + 20t^3u + 43t^2u^2 + 42tu^3 + 32u^4) \\
& + 2s^4(t^5 + 9t^4u + 27t^3u^2 + 35t^2u^3 + 23tu^4 + 15u^5) \\
& + s^3u(20t^5 + 48t^4u + 56t^3u^2 + 45t^2u^3 + 26tu^4 + 17u^5) \\
& + 2s^2u(3t^6 + 7t^5u + 7t^4u^2 + 14t^3u^3 + 24t^2u^4 + 12tu^5 + 3u^6) \\
& \left. + stu^2(8t^5 + 32t^4u + 57t^3u^2 + 60t^2u^3 + 37tu^4 + 6u^5) + 2t^3u^3(t^3 + 2t^2u - u^3)\right]\Big\},
\end{aligned}$$

$$
\begin{aligned}
\widehat{w}_{\Delta}^{\perp} = t\Big\{ & 64Q^{10}t^3(s^3t - st^2u - s^2u^2 + tu^3) - 16Q^8t^2\Big[2s^5u + s^4(6t^2 - 2tu + 6u^2) \\
& + s^3(5t^3 + 11t^2u + 10u^3) - s^2(t^4 + 7t^3u + 6tu^3 - 4u^4) \\
& + tu^2(-t^3 + 5t^2u + 10tu^2 + 2u^3) + su(-6t^4 - 11t^3u + 5t^2u^2 - 2tu^3 + 2u^4)\Big] \\
& - 8Q^6t\Big[2s^7(t+u) + 2s^6(t^2 + tu + 5u^2) + s^5(-5t^3 + 6t^2u - 6tu^2 + 20u^3) \\
& + s^4(-8t^4 - 8t^3u + 18t^2u^2 - 5tu^3 + 24u^4) \\
& - s^3(t^5 + 9t^4u + 14t^3u^2 - 19t^2u^3 + 9tu^4 - 14u^5) \\
& + s^2(2t^6 + 15t^5u + 23t^4u^2 + 16t^3u^3 + 43t^2u^4 + 5tu^5 + 6u^6) \\
& + stu(4t^5 + 23t^4u + 29t^3u^2 + 23t^2u^3 + 27tu^4 + 3u^5) \\
& + t^2u^2(2t^4 + 3t^3u - 7t^2u^2 - 12tu^3 - 3u^4)\Big] + 4Q^4\Big[s^8(6t^2 - 4u^2) \\
& + s^7(15t^3 + 23t^2u + 12tu^2 - 12u^3) + s^6(17t^4 + 37t^3u + 32t^2u^2 + 32tu^3 - 20u^4) \\
& + s^5(6t^5 + 28t^4u + 40t^3u^2 + 21t^2u^3 + 39tu^4 - 20u^5) \\
& + s^4(4t^6 + 10t^5u + 33t^4u^2 + 56t^3u^3 + 6t^2u^4 + 31tu^5 - 12u^6) \\
& + s^3(2t^7 + 6t^6u - 3t^5u^2 - 4t^4u^3 + 17t^3u^4 - 25t^2u^5 + 9tu^6 - 4u^7) \\
& + s^2tu(6t^6 + 20t^5u + 13t^4u^2 + 11t^3u^3 + 31t^2u^4 + 5u^6) \\
& + st^2u^2(6t^5 + 22t^4u + 37t^3u^2 + 52t^2u^3 + 44tu^4 + 9u^5) \\
& + t^4u^3(2t^3 + 4t^2u + tu^2 - u^3)\Big] + 2Q^2s\Big[s^8(-5t^2 + 12tu + 9u^2) \\
& + s^7(-13t^3 + 9t^2u + 43tu^2 + 29u^3) + s^6(-19t^4 + 2t^3u + 35t^2u^2 + 64tu^3 + 52u^4) \\
& + s^5(-9t^5 + t^4u + 53t^3u^2 + 83t^2u^3 + 88tu^4 + 62u^5) \\
& + s^4u(16t^5 + 60t^4u + 110t^3u^2 + 145t^2u^3 + 80tu^4 + 45u^5) \\
& + s^3u(6t^6 + 34t^5u + 68t^4u^2 + 105t^3u^3 + 127t^2u^4 + 47tu^5 + 21u^6) \\
& + s^2u^2(14t^6 + 52t^5u + 95t^4u^2 + 114t^3u^3 + 105t^2u^4 + 28tu^5 + 6u^6) \\
& + stu^3(10t^5 + 47t^4u + 83t^3u^2 + 79t^2u^3 + 45tu^4 + 6u^5) + 2t^3u^4(t^3 + 2t^2u - u^3)\Big] \\
& - s^2(s^2 - u^2)\Big[s^6(-t^2 + 10tu + 3u^2) + s^5(t^3 + 28t^2u + 33tu^2 + 6u^3) \\
& + s^4(3t^4 + 45t^3u + 49t^2u^2 + 41tu^3 + 6u^4) + t^2u^3(t^3 + 3t^2u + tu^2 - u^3) \\
& + s^3(t^5 + 30t^4u + 46t^3u^2 + 40t^2u^3 + 41tu^4 + 6u^5) \\
& + s^2u(7t^5 + 22t^4u + 46t^3u^2 + 49t^2u^3 + 33tu^4 + 3u^5) \\
& + stu^2(7t^4 + 30t^3u + 45t^2u^2 + 28tu^3 + 10u^4)\Big]\Big\},
\end{aligned}
$$

$$
\begin{aligned}
\widehat{w}^{\parallel}_{\Delta\Delta} = 16Q^2 M_\psi t\sqrt{(Q^2t+su)t}\Big\{ & 8Q^6t^2(s^3t-s^2u^2-st^2u+tu^3) \\
& - 2Q^4t\Big[2s^5(t+u)+4s^4(t^2+u^2)+s^3(5t^3+9t^2u+2tu^2+8u^3) \\
& - s^2(t^4+3t^3u+4tu^3-4u^4)+su(-6t^4-7t^3u+t^2u^2-2tu^3+2u^4) \\
& + tu^2(-t^3+5t^2u+6tu^2+2u^3)\Big] - 2Q^2\Big[2s^6u(t+u)+s^5u(t^2+tu+4u^2) \\
& + s^4(-t^4+t^3u+4t^2u^2+tu^3+6u^4)+s^3u(-t^4+t^3u+4t^2u^2-2tu^3+4u^4) \\
& + s^2(t^6+8t^5u+9t^4u^2+10t^3u^3+9t^2u^4+tu^5+2u^6) \\
& + stu(2t^5+10t^4u+11t^3u^2+13t^2u^3+7tu^4+u^5) \\
& + t^2u^2(t^4+2t^3u-tu^3-u^4)\Big] + s(s+u)\Big[3s^5(t+u)^2 \\
& + s^4(4t^3+9t^2u+10tu^2+5u^3)+s^3u(6t^3+15t^2u+14tu^2+7u^3) \\
& + s^2(-t^5+2t^4u+12t^3u^2+13t^2u^3+5tu^4+3u^5) \\
& - su(t^5+6t^4u+6t^3u^2+4t^2u^3-tu^4-2u^5)+2tu^4(2t^2+2tu+u^2)\Big]\Big\}.
\end{aligned}
$$

$$
\begin{aligned}
\widehat{w}^{\perp}_{\Delta\Delta} = 2M_\psi\sqrt{(Q^2t+su)t}\Big\{ & 16Q^8t^3(s^3t-s^2u^2-st^2u+tu^3) \\
& - 4Q^6t^2\Big[2s^5(t+u)+4s^4(t^2+u^2)+s^3(5t^3+9t^2u+2tu^2+8u^3) \\
& - s^2(t^4+3t^3u+4tu^3-4u^4)+tu^2(-t^3+5t^2u+6tu^2+2u^3) \\
& + su(-6t^4-7t^3u+t^2u^2-2tu^3+2u^4)\Big] - 4Q^4t\Big[s^6(t^2+tu+2u^2) \\
& + s^5(-2t^3+3t^2u-2tu^2+4u^3)+s^4(-t^4+t^3u+8t^2u^2-2tu^3+6u^4) \\
& + s^3u(t^4+t^3u+6t^2u^2-3tu^3+4u^4)+t^2u^2(t^4+2t^3u-tu^3-u^4) \\
& + s^2(t^6+8t^5u+9t^4u^2+8t^3u^3+10t^2u^4+tu^5+2u^6) \\
& + stu(2t^5+10t^4u+11t^3u^2+13t^2u^3+7tu^4+u^5)\Big] \\
& - 2Q^2st\Big[2s^7t+s^6(3t^2+3tu-5u^2)+2s^5(2t^3-t^2u-tu^2-7u^3) \\
& + s^4(5t^4+5t^3u-12t^2u^2-6tu^3-18u^4)+s^3(5t^4u-16t^2u^3-5tu^4-12u^5) \\
& + s^2u^2(11t^4+9t^3u+t^2u^2+3tu^3-5u^4)-2tu^5(2t^2+2tu+u^2) \\
& + su^3(11t^4+10t^3u+6t^2u^2-tu^3-2u^4)\Big] - s^2(s+u)\Big[s^6t(-t+u) \\
& - 2s^5(t-u)^2(t+u)+s^4(t^4+9t^3u-3t^2u^2-3tu^3-4u^4) \\
& + s^3u(12t^4+3t^3u-12t^2u^2-3tu^3-2u^4)+t^2u^4(t^2-2tu-u^2) \\
& + s^2tu(2t^4+6t^3u+3t^2u^2-3tu^3+2u^4) \\
& + stu^2(2t^4+12t^3u+9t^2u^2+2tu^3+u^4)\Big]\Big\},
\end{aligned}
\tag{B.48}
$$

B.2.4 Partonic unpolarized structure functions

For completeness, we present the partonic amplitudes squared appearing in the unpolarized J/ψ production, where all azimuthal dependencies are integrated over (see Eq. (2.24)). These quantities are obtained by combining the amplitudes squared $\mathcal{M}^{(a)}_{\mu\nu}[n]$ (for the process $\gamma^* a \to c\bar{c}[n]\, a$) with the projectors $\epsilon^{\mu\nu}_{\mathcal{P}}$ (with $\mathcal{P} = \perp, \parallel$),

where $\epsilon_\perp^{\mu\nu} = -\eta_\perp^{\mu\nu}$ and $\epsilon_\parallel^{\mu\nu} = 4\,\epsilon_\parallel^\mu \epsilon_\parallel^\nu$, namely

$$\left|\mathcal{M}_{\mathcal{P}}^{(a)}[n]\right|^2 = \frac{1}{2}\epsilon_{\mathcal{P}}^{\mu\nu}\,\mathcal{M}_{\mu\nu}^{(a)}[n], \tag{B.49}$$

as also done in Eq. (3.24).
In particular, we decompose them as

$$\left|\mathcal{M}_{\mathcal{P}}^{(a)}[n]\right|^2 = F^{(a)}[n]\,M_{\mathcal{P}}^{(a)}[n], \tag{B.50}$$

where $F^{(a)}[n]$ is a prefactor independent of the photon polarization.

In the following, we adopt the modified Mandelstam variables defined in Eq. (2.69), and we will drop the superscript (a) and the n state dependence, if not otherwise stated.

- $\gamma^* + q(\bar{q}) \to c\bar{c}[\,^1S_0^{(8)}] + q(\bar{q})$:

$$\begin{aligned} F &= -\frac{64\,e_c^2\,\alpha\alpha_s^2}{3\,M_\psi\,s^2\,t\,(s+u)^2}, \\ M_\perp &= 2\,Q^4t^2 + 2\,Q^2\,s\,t\,(s+u) + s^2\left(s^2+u^2\right), \\ M_\parallel &= 8\,Q^2\,t\left(Q^2t+su\right). \end{aligned} \tag{B.51}$$

- $\gamma^* + q(\bar{q}) \to c\bar{c}[\,^3S_1^{(8)}] + q(\bar{q})$:

$$\begin{aligned} F &= -\frac{32\,e_q^2\,\alpha\alpha_s^2}{9\,M_\psi^3\,s^2\,(Q^2-s)^2\,(Q^2-u)^2}, \\ M_\perp &= 2Q^6t^2\,(2s+t) + 2Q^4s\left[s^2u - st\,(3t-2u) - 2t^3\right] \\ &\quad + Q^2s^2\Big[s^2\,(t-2u) + 2s\left(t^2-4tu-u^2\right) + t\left(2t^2-2tu-u^2\right)\Big] \\ &\quad + s^3u\left(s^2+2st+2t^2+2tu+u^2\right), \\ M_\parallel &= 8\,Q^2\left(Q^2-s\right)^2\,t\,(s+t)^2. \end{aligned} \tag{B.52}$$

- $\gamma^* + q(\bar{q}) \to c\bar{c}[\,^3P_J^{(8)}] + q(\bar{q})$:

$$\begin{aligned} F &= \frac{256\,e_c^2\,\alpha\alpha_s^2}{3\,M_\psi^3\,s^2\,t\,(s+u)^4}, \\ M_\perp &= 8Q^6t\Big[2s^2+st+t\,(2t+u)\Big] - 2Q^4\Big[4s^4+12s^3t \\ &\quad + s^2\left(19t^2+8tu+4u^2\right) + 2st\left(6t^2+tu-2u^2\right) + t^2\left(8t^2+12tu+7u^2\right)\Big] \\ &\quad + 2Q^2s\Big[6s^4+s^3\,(7t+6u) + s^2\left(4t^2+3tu+6u^2\right) - su\left(8t^2+3tu-6u^2\right) \\ &\quad - tu\left(8t^2+12tu+7u^2\right)\Big] - s^2\,(s+u)\Big[7s^3+s^2\,(12t+7u) \\ &\quad + s\left(8t^2+16tu+7u^2\right) + s\left(8t^2+16tu+7u^2\right) + u\left(8t^2+12tu+7u^2\right)\Big], \end{aligned}$$

$$
\begin{aligned}
M_{\parallel} = & -32Q^6 t\left[s^2 - st - t\left(2t+u\right)\right] + 8Q^4\Big[2s^4 + 4s^3 t \\
& + s^2\left(5t^2 + 8tu + 2u^2\right) - 2st\left(6t^2 + tu - 2u^2\right) - t^2\left(8t^2 + 12tu + 7u^2\right)\Big] \\
& - 8Q^2 s\left(s+u\right)\Big[2s^3 + 2s^2 t + s\left(8t^2 + 5tu + 2u^2\right) + t\left(8t^2 + 12tu + 7u^2\right)\Big].
\end{aligned}
\tag{B.53}
$$

- $\gamma^* + g \to c\bar{c}[\,^1S_0^{(8)}] + g$:

$$
\begin{aligned}
F = & \frac{96\, e_c^2\, \alpha\alpha_s^2}{M_\psi\, s^2\, t\left(s+t\right)^2\left(s+u\right)^2\left(t+u\right)^2}, \\
M_{\perp} = & \, 2Q^6 t^3 u^2 + 2Q^4 s t^2 u\Big[s\left(t+u\right) + t^2 + tu + 2u^2\Big] \\
& + Q^2 s^2 t\Big[s^4 + 2s^3\left(t+u\right) + 3s^2\left(t+u\right)^2 + 2s\left(t^3 + 3t^2 u + 4tu^2 + 2u^3\right) \\
& + t^4 + 2t^3 u + 5t^2 u^2 + 4tu^3 + 3u^4\Big] + s^3 u\Big[s^4 + 2s^3\left(t+u\right) \\
& + 3s^2\left(t+u\right)^2 + 2s\left(t+u\right)^3 + \left(t^2 + tu + u^2\right)^2\Big], \\
M_{\parallel} = & \, 8Q^6 t^3 u^2 + 8Q^4 s t^2 u\Big[s\left(t+u\right) + t^2 + tu + 2u^2\Big] + 4Q^2 s^2 t\Big[s^2\left(t+u\right)^2 \\
& + 2s\left(t^3 + 2t^2 u + 2tu^2 + u^3\right) + t^4 + 2t^3 u + 3t^2 u^2 + 2tu^3 + 2u^4\Big].
\end{aligned}
\tag{B.54}
$$

- $\gamma^* + g \to c\bar{c}[\,^3S_1^{(1)}] + g$:

$$
\begin{aligned}
F = & \frac{256\, e_c^2\, \alpha\alpha_s^2}{27 M_\psi s^2\left(s+t\right)^2\left(s+u\right)^2\left(t+u\right)^2}, \\
M_{\perp} = & -4Q^6 t^2\left(s^2 + t^2\right) \\
& + 2Q^4 t\Big[s^3\left(3t - 2u\right) + 3s^2 t\left(t+u\right) + 2st^2\left(t-u\right) + 2t^3\left(t+u\right)\Big] \\
& - 2Q^2 s\Big[s^3\left(t-u\right)^2 - 2s^2 tu\left(t+u\right) - st^2 u\left(2t-u\right) - 2t^3 u\left(t+u\right)\Big] \\
& + 2s^2\Big[s^3\left(t^2 + tu + u^2\right) + s^2\left(t+u\right)^3 + stu\left(t^2 + 3tu + u^2\right) + t^2 u^2\left(t+u\right)\Big], \\
M_{\parallel} = & \, 8Q^6 t^2\left(s^2 - 2t^2\right) - 8Q^4 t\left(s^2 - 2t^2\right)\Big[s\left(t-u\right) + t\left(t+u\right)\Big] \\
& + 4Q^2 s\Big[s^3\left(t^2 + u^2\right) + 2s^2 t^2\left(t+u\right) + st^2\left(t^2 + 6tu + u^2\right) + 4t^3 u\left(t+u\right)\Big].
\end{aligned}
\tag{B.55}
$$

- $\gamma^* + g \to c\bar{c}[\,^3S_1^{(8)}] + g$:

$$
\begin{aligned}
F[\,^3S_1^{(8)}] &= \frac{15}{8} F[\,^3S_1^{(1)}], \\
M_{\perp}[\,^3S_1^{(8)}] &= M_{\perp}[\,^3S_1^{(1)}], \\
M_{\parallel}[\,^3S_1^{(8)}] &= M_{\parallel}[\,^3S_1^{(1)}].
\end{aligned}
\tag{B.56}
$$

- $\gamma^* + g \to c\bar{c}[{}^3P_J^{(8)}] + g$:

$$F = \frac{384\, e_c^2\, \alpha \alpha_s^2}{M_\psi^3 s^2 t\,(s+t)^3\,(s+u)^4\,(t+u)^3},$$

$$\begin{aligned}
M_\perp = {} & -8Q^8 t^2 \Big[2s^5 t - 2s^4 u^2 + s^3 t^2 (2t - 3u) - s^2 tu(t^2 + 3tu - 3u^2) \\
& - stu(2t^3 + t^2 u - tu^2 - u^3) + t^2 u^3 (2t + u)\Big] + 2Q^6 t \Big[4s^7 (t + u) \\
& + 4s^6 (5t^2 + 2u^2) + 4s^5 (5t^3 + 6t^2 u - 2tu^2 + 4u^3) + 2s^4 (9t^4 - 9t^3 u \\
& + 4t^2 u^2 - 6tu^3 + 4u^4) + s^3 (12t^5 - 2t^4 u - 29t^3 u^2 + 33t^2 u^3 - 12tu^4 + 4u^5) \\
& - s^2 t(2t^5 + 20t^4 u + 25t^3 u^2 - t^2 u^3 - 16tu^4 + 4u^5) - st^2 u(12t^4 + 26t^3 u \\
& + 2t^2 u^2 + tu^3 + u^4) - t^3 u^2 (2t^3 - 6t^2 u - 15tu^2 - 7u^3)\Big] \\
& - 2Q^4 \Big[2s^8 (3t^2 + tu - 2u^2) + s^7 (21t^3 + 3t^2 u + 10tu^2 - 8u^3) \\
& + s^6 (28t^4 + 15t^3 u - 15t^2 u^2 + 22tu^3 - 12u^4) + s^5 (27t^5 + 11t^4 u + 8t^3 u^2 \\
& - 20t^2 u^3 + 26tu^4 - 8u^5) + s^4 (16t^6 + 17t^5 u - 20t^4 u^2 + 2t^3 u^3 - 33t^2 u^4 \\
& + 18tu^5 - 4u^6) + s^3 t(2t^6 + 8t^5 u - 3t^4 u^2 - 19t^3 u^3 - 19t^2 u^4 - 17tu^5 + 6u^6) \\
& - s^2 t^2 (2t^6 + 14t^5 u + 30t^4 u^2 + 33t^3 u^3 + 46t^2 u^4 + 21tu^5 + 4u^6) \\
& - 2st^3 u(2t^5 + 10t^4 u + 16t^3 u^2 + 20t^2 u^3 + 19tu^4 + 7u^5) - 2t^6 u^2 (t + u)^2\Big] \\
& + Q^2 s \Big[s^8 (7t^2 - 5tu - 12u^2) + s^7 (25t^3 + 3t^2 u - 18tu^2 - 36u^3) \\
& + s^6 (37t^4 + 25t^3 u - 12t^2 u^2 - 20tu^3 - 60u^4) + s^5 (39t^5 + 39t^4 u + 16t^3 u^2 \\
& - 18t^2 u^3 - 6tu^4 - 60u^5) + s^4 (29t^6 + 83t^5 u + 72t^4 u^2 + 88t^3 u^3 + 40t^2 u^4 \\
& + 22tu^5 - 36u^6) + s^3 (9t^7 + 75t^6 u + 148t^5 u^2 + 176t^4 u^3 + 178t^3 u^4 + 102t^2 u^5 \\
& + 22tu^6 - 12u^7) + s^2 tu(22t^6 + 107t^5 u + 199t^4 u^2 + 211t^3 u^3 + 177t^2 u^4 \\
& + 73tu^5 + 9u^6) + st^2 u^2 (17t^5 + 69t^4 u + 107t^3 u^2 + 105t^2 u^3 + 71tu^4 + 21u^5) \\
& + 4t^5 u^3 (t + u)^2\Big] + s^2 (s + u)\Big[7s^7 u(t + u) + s^6 u(25t^2 + 38tu + 21u^2) \\
& + s^5 (2t^4 + 47t^3 u + 88t^2 u^2 + 78tu^3 + 35u^4) + s^4 (4t^5 + 63t^4 u + 132t^3 u^2 \\
& + 156t^2 u^3 + 98tu^4 + 35u^5) + s^3 (2t^6 + 47t^5 u + 136t^4 u^2 + 190t^3 u^3 + 156t^2 u^4 \\
& + 78tu^5 + 21u^6) + s^2 u(13t^6 + 70t^5 u + 136t^4 u^2 + 132t^3 u^3 + 88t^2 u^4 \\
& + 38tu^5 + 7u^6) + stu^2 (13t^5 + 47t^4 u + 63t^3 u^2 + 47t^2 u^3 + 25tu^4 + 7u^5) \\
& + 2t^4 u^3 (t + u)^2\Big],
\end{aligned}$$

$$
\begin{aligned}
M_{\parallel} = {} & +32Q^8t^2\Big[s^5t - s^4u^2 - 2s^3t^3 + s^2t^2u(t+3u) + stu(2t^3 + t^2u - tu^2 - u^3) \\
& - t^2u^3(2t+u)\Big] - 8Q^6t\Big[2s^7(t+u) + 4s^6(2t^2+u^2) - s^5(t^3 - t^2u + 2tu^2 - 8u^3) \\
& - s^4(21t^4 + 13t^3u + 18t^2u^2 - 2tu^3 - 4u^4) - 2s^3(6t^5 + 10t^4u + t^3u^2 + 4t^2u^3 \\
& - 6tu^4 - u^5) + 2s^2t(t^5 + 10t^4u + 11t^3u^2 + 9t^2u^3 + 6tu^4 + 5u^5) \\
& + st^2u(12t^4 + 26t^3u + 2t^2u^2 + tu^3 + u^4) + t^3u^2(2t^3 - 6t^2u - 15tu^2 - 7u^3)\Big] \\
& + 16Q^4\Big[s^8(t^2 - u^2) + s^7(3t^3 + tu^2 - 2u^3) - s^6(2t^4 + 2t^3u + 2t^2u^2 - tu^3 + 3u^4) \\
& - s^5(12t^5 + 16t^4u + 16t^3u^2 - t^2u^3 + tu^4 + 2u^5) - s^4(10t^6 + 28t^5u + 28t^4u^2 \\
& + 13t^3u^3 - 7t^2u^4 + 3tu^5 + u^6) - s^3t(t^6 + 9t^5u + 18t^4u^2 + t^3u^3 - 15t^2u^4 \\
& - 10tu^5 + 2u^6) + s^2t^2(t^6 + 7t^5u + 13t^4u^2 + 18t^3u^3 + 35t^2u^4 + 24tu^5 + 6u^6) \\
& + st^3u(2t^5 + 10t^4u + 16t^3u^2 + 20t^2u^3 + 19tu^4 + 7u^5) + t^6u^2(t+u)^2\Big] \\
& + 8Q^2s(s+u)\Big[2s^7u(t+u) + 2s^6u(3t^2 + 3tu + 2u^2) \\
& + s^5(5t^4 + 15t^3u + 18t^2u^2 + 14tu^3 + 6u^4) + s^4(15t^5 + 38t^4u + 53t^3u^2 \\
& + 40t^2u^3 + 22tu^4 + 4u^5) + s^3(15t^6 + 52t^5u + 88t^4u^2 + 81t^3u^3 \\
& + 47t^2u^4 + 19tu^5 + 2u^6) + s^2t(5t^6 + 32t^5u + 78t^4u^2 + 90t^3u^3 + 68t^2u^4 \\
& + 34tu^5 + 9u^6) + st^2u(7t^5 + 31t^4u + 47t^3u^2 + 39t^2u^3 + 23tu^4 + 7u^5) \\
& + 2t^5u^2(t+u)^2\Big]. \qquad \text{(B.57)}
\end{aligned}
$$

Appendix C

Kinematic constraints

In Chapter 2 we derived the differential cross section for J/ψ-meson production including its subsequent decay into a $\ell^+\ell^-$-pair. In particular, we showed how to evaluate the different helicity structure functions when adopting the NRQCD approach combined with the collinear factorization, providing numerical results for the EIC kinematics. In this appendix, we want to gather some useful constraints specific for the SIDIS process.

The first class of constraints, denoted here as theoretical, derive from the physical region available for each Mandelstam variable. The second one, related to the numerical computation, is due to the fact that all SIDIS variables are somehow connected to each other; thus, a constraint on one variable automatically limits all the others.

Theoretical constraints

Starting from the first class, in Sec. 2.1 we introduced the Mandelstam variables in Eq. (2.55), while their explicit formulae are given in Eq. (2.57). In the same section, the reasonable threshold condition for $\hat{s}$, related to the quarkonium mass M_ψ, was also introduced (Eq. (2.58)). Here, we present similar constraints for the remaining Mandelstam variables, related to the partonic process

$$\gamma^*(q) + a(p_a) \to J/\psi(P_\psi) + a(p'_a). \tag{C.1}$$

It is easier to consider a specific frame, and then write the results in terms of invariant quantities.
In the $\gamma^* p$ cm frame, the initial particles are back-to-back, so the photon and parton three-momenta cancel each other out,[1] leading to

$$\hat{s} = (q + p_a)^2 = (E_q + E_{p_a})^2 + (\boldsymbol{q} + \boldsymbol{p}_a)^2 = (E_q + E_{p_a})^2. \tag{C.2}$$

Moreover, the three-momenta equivalence implies a relation between the two energies

$$\boldsymbol{q} = -\boldsymbol{p}_a \quad \Rightarrow \quad E_q^2 + Q^2 = E_{p_a}^2. \tag{C.3}$$

From the previous equations, it is straightforward to derive the relation between the energy component of the initial particles with $\hat{s}$ and Q; therefore,

$$\begin{aligned} q^\mu &= \left(\frac{\hat{s} - Q^2}{2\sqrt{\hat{s}}},\ 0,\ 0,\ \frac{\hat{s} + Q^2}{2\sqrt{\hat{s}}} \right), \\ p_a^\mu &= \frac{\hat{s} + Q^2}{2\sqrt{\hat{s}}} \left(1,\ 0,\ 0,\ -1\right). \end{aligned} \tag{C.4}$$

[1] We are considering the collinear factorization framework, for which Eq. (2.53) holds.

Similar relations to Eqs. (C.2) and (C.3) hold for the final state $J/\psi + a$, from which one easily obtains the J/ψ energy explicit form. Moreover, introducing the scattering angle θ_ψ, evaluated respect to the photon direction, and imposing that the J/ψ does not have a component along the Y-axis, the J/ψ four-momentum is given by

$$P_\psi^\mu = \left(\frac{\hat{s} + M_\psi^2}{2\sqrt{\hat{s}}},\ \frac{\hat{s} - M_\psi^2}{2\sqrt{\hat{s}}} \sin\theta_\psi,\ 0,\ \frac{\hat{s} - M_\psi^2}{2\sqrt{\hat{s}}} \cos\theta_\psi \right). \tag{C.5}$$

Using these momenta explicit forms, it is possible to write the Mandelstam variables $\hat{t}$ and $\hat{u}$ in terms of $\hat{s}$ and the scattering angle θ_ψ, namely

$$\begin{aligned} \hat{t} = (q - P_\psi)^2 &= M_\psi^2 - Q^2 - 2q \cdot P_\psi \\ &= M_\psi^2 - Q^2 - \frac{1}{2\hat{s}} \left[(\hat{s} - Q^2)(\hat{s} + M_\psi^2) - (\hat{s} + Q^2)(\hat{s} - M_\psi^2) \cos\theta_\psi \right] \\ &= M_\psi^2 - Q^2 - \frac{1}{2\hat{s}} \left[\hat{s}\,(M_\psi^2 - Q^2)(1 + \cos\theta_\psi) + (\hat{s}^2 - M_\psi^2 Q^2)(1 - \cos\theta_\psi) \right] \end{aligned} \tag{C.6}$$

and

$$\begin{aligned} \hat{u} = (p_a - P_\psi)^2 &= M_\psi^2 - 2p_a \cdot P_\psi \\ &= M_\psi^2 - \frac{\hat{s} + Q^2}{2\hat{s}} \left[(\hat{s} + M_\psi^2) + (\hat{s} - M_\psi^2) \cos\theta_\psi \right] \\ &= M_\psi^2 - \frac{\hat{s} + Q^2}{2\hat{s}} \left[\hat{s}(1 + \cos\theta_\psi) + M_\psi^2 (1 - \cos\theta_\psi) \right]. \end{aligned} \tag{C.7}$$

The two extreme values of the Mandelstam variables are obtained by imposing $\theta_\psi = 0$ and $\theta_\psi = \pi$. The former gives

$$\hat{t}_{\max} = 0, \quad \hat{u}_{\min} = -(\hat{s} - M_\psi^2) - Q^2; \tag{C.8}$$

while for $\theta = \pi$ we have

$$\hat{t}_{\min} = -\frac{(\hat{s} - M_\psi^2)(\hat{s} + Q^2)}{\hat{s}}, \quad \hat{u}_{\max} = -\frac{M_\psi^2\, Q^2}{\hat{s}}. \tag{C.9}$$

All together, the Mandelstam variables are constrained according to

$$\hat{s} \geq M_\psi^2, \quad 0 \geq \hat{t} \geq -\frac{(\hat{s} - M_\psi^2)(\hat{s} + Q^2)}{\hat{s}}, \quad -\frac{M_\psi^2\, Q^2}{\hat{s}} \geq \hat{u} \geq -(\hat{s} - M_\psi^2) - Q^2. \tag{C.10}$$

Notice that the condition

$$\hat{s} + \hat{t} + \hat{u} = M_\psi^2 - Q^2 \tag{C.11}$$

is always fulfilled.

Numerical computation constraints

Moving to the numerical computation point of view, by evaluating one of the variable in a defined range, we indirectly impose limitations for all the others.

Before that, we introduce another useful quantity. Complementary to the photon virtual mass $Q^2 = -q^2$, and the Lorentz-invariant quantities x_B, y and z defined in

Eq. (2.4), we have the invariant mass W of the photon-proton system,

$$W^2 = (q + P)^2 = m_p^2 - Q^2 + 2\, P \cdot q. \tag{C.12}$$

Notice that the scalar product $P \cdot q$ is involved in the x_B, y and z definitions, see Eq. (2.4). Moreover, it is related to the cm energy of the process S via

$$P \cdot q = y\, P \cdot l = y \frac{S - m_e^2 - m_P^2}{2}, \tag{C.13}$$

where S is the total cm energy. In the previous equations we kept all the masses, although the the total cm energy of the process is usually much bigger compared to them, $S \gg m_e,\, m_p$.

Thus, it is possible to identify relations among Q^2, W and the typical SIDIS variables

$$\begin{aligned} Q^2 &= x_B\, y \left(S - m_p^2 - m_e^2\right), \\ Q^2 &= x_B \left(W^2 + Q^2 - m_p^2\right), \\ W^2 + Q^2 - m_p^2 &= y \left(S - m_p^2 - m_e^2\right), \\ W^2 - m_p^2 &= (1 - x_B)\, y \left(S - m_p^2 - m_e^2\right). \end{aligned} \tag{C.14}$$

Explicit relations can be found also for z, but they require a specific choice of the reference frame.

In the proton rest frame, where its momentum is given by

$$P = (m_p, \mathbf{0}), \tag{C.15}$$

z is obtained from the ratio between the quarkonium and photon energies, respectively E_ψ and ν,

$$z = \frac{m_p\, E_\psi}{P \cdot q} = \frac{E_\psi}{\nu}. \tag{C.16}$$

Moreover, the photon energy is related to the electron beam energy E by

$$\nu = y\, E. \tag{C.17}$$

At the same time, the hadron energy can be written in terms of more convenient quantities, corresponding to the quarkonium mass and momentum components

$$E_\psi^2 = M_\psi^2 + P_L^2 + P_T^2, \tag{C.18}$$

with the longitudinal momentum P_L that is related to the Feynman-x variable

$$x_F = 2 \frac{P_L}{\sqrt{S}}. \tag{C.19}$$

Alternatively, one can consider the cm frame, where the proton and the electron in the initial state are back-to-back, namely[2]

$$P^* = (E_p, \mathbf{0}, p), \quad l^* = (E^*, \mathbf{0}, -p); \tag{C.20}$$

in the previous definition we are imposing that the beams are along the $\hat{Z}$-axis, with the proton moving in the positive direction. Notice that the energies of the two beams are correlated, since

$$\sqrt{S} = E_p + E^*, \tag{C.21}$$

and the modulus p of the three-momentum can be derived from one of the energies, *e.g.*

$$p = \sqrt{E_p - m_p^2}. \tag{C.22}$$

In this frame, z is given by

$$z = \frac{E_p\, E_\psi^* - p\, P_L^*}{P \cdot q}, \tag{C.23}$$

where P_L^* can always be recast into x_F according to Eq. (C.19).

It is now clear that, via Eq. (C.14) and including Eq. (C.16) or (C.23) (or analogous equations), all variables are connected.

Moreover, each variable presents an upper and lower limit given by experimental conditions,

$$\begin{gathered} x_{B\,\text{min}}^{\text{exp}} \leq x_B \leq x_{B\,\text{max}}^{\text{exp}}, \quad y_{\text{min}}^{\text{exp}} \leq y \leq y_{\text{max}}^{\text{exp}}, \quad z_{\text{min}}^{\text{exp}} \leq z \leq z_{\text{max}}^{\text{exp}}, \\ Q_{\text{min}}^{\text{exp}} \leq Q \leq Q_{\text{max}}^{\text{exp}}, \quad W_{\text{min}}^{\text{exp}} \leq W \leq W_{\text{max}}^{\text{exp}}, \quad x_{F\,\text{min}}^{\text{exp}} \leq x_F \leq x_{F\,\text{max}}^{\text{exp}}. \end{gathered} \tag{C.24}$$

If these experimental boundaries are absent, the above conditions coincide with their (theoretical) physical limits. Once we have identified the available region for each variable, it is finally possible to understand how the boundaries of one variable influence the others.

Suppose for example to integrate the differential cross section over z, y, x_B in the cm frame. Integration over z will be then limited by (see also Eq. (C.23))

$$\max\left(z_{\text{min}}, \frac{2E_p\left(E_\psi - P_L\right)_{\text{min}}}{\widetilde{W}_{\text{max}}^2 + Q_{\text{max}}^2}\right) \leq z \leq \min\left(z_{\text{max}}, \frac{2E_p\left(E_\psi - P_L\right)_{\text{max}}}{\widetilde{W}_{\text{min}}^2 + Q_{\text{min}}^2}\right), \tag{C.25}$$

while x_B integration will be performed in the region

$$\begin{gathered} \max\left(x_{B\text{min}}, \frac{Q_{min}^2}{\widetilde{W}_{\text{max}}^2 + Q_{\text{min}}^2}, \frac{z\, Q_{\text{min}}^2}{2E_p(E_\psi - P_L)_{\text{max}}}\right) \\ \leq x_B \leq \\ \min\left(x_{B\text{max}}, \frac{Q_{\text{max}}^2}{\widetilde{W}_{\text{min}}^2 + Q_{\text{max}}^2}, \frac{z\, Q_{\text{max}}^2}{2E_p(E_\psi - P_L)_{\text{min}}}\right), \end{gathered} \tag{C.26}$$

[2]The superscript "$*$" implies that the quantity is measured in the cm frame.

and finally y boundaries are given by

$$\max\left(y_{\min}, \frac{\widetilde{W}^2_{\min}+Q^2_{\min}}{S}, \frac{Q^2_{\min}}{x_B S}, \frac{\widetilde{W}^2_{\min}}{(1-x_B)S}, \frac{2E_p}{S}\frac{(E_\psi - P_L)_{\min}}{z_h}\right) \leq y \leq \min\left(y_{\max}, \frac{\widetilde{W}^2_{\max}+Q^2_{\max}}{S}, \frac{Q^2_{\max}}{x_B S}, \frac{\widetilde{W}^2_{\max}}{(1-x_B)S}, \frac{2E_p}{S}\frac{(E_\psi - P_L)_{\max}}{z_h}\right), \tag{C.27}$$

where $\widetilde{W}^2 = W^2 - m_p^2$.

This example can be extended to other integration and applied to different frames.

Bibliography

[1] J. J. Aubert et al. "Experimental Observation of a Heavy Particle J". In: *Phys. Rev. Lett.* 33 (1974), pp. 1404–1406. DOI: 10.1103/PhysRevLett.33.1404.

[2] J. E. Augustin et al. "Discovery of a Narrow Resonance in e^+e^- Annihilation". In: *Phys. Rev. Lett.* 33 (1974), pp. 1406–1408. DOI: 10.1103/PhysRevLett.33.1406.

[3] R. L. Workman et al. "Review of Particle Physics". In: *PTEP* 2022 (2022), p. 083C01. DOI: 10.1093/ptep/ptac097.

[4] N. Brambilla et al. "Heavy quarkonium: progress, puzzles, and opportunities". In: *Eur. Phys. J. C* 71 (2011), p. 1534. DOI: 10.1140/epjc/s10052-010-1534-9. arXiv: 1010.5827 [hep-ph].

[5] J.-P. Lansberg. "New observables in inclusive production of quarkonia". In: *Phys. Rept.* 889 (2020), pp. 1–106. DOI: 10.1016/j.physrep.2020.08.007. arXiv: 1903.09185 [hep-ph].

[6] G. T. Bodwin, E. Braaten, and G. P. Lepage. "Rigorous QCD analysis of inclusive annihilation and production of heavy quarkonium". In: *Phys. Rev. D* 51 (1995). [Erratum: Phys.Rev.D 55, 5853 (1997)], pp. 1125–1171. DOI: 10.1103/PhysRevD.51.1125. arXiv: hep-ph/9407339.

[7] G. C. Nayak, J.-W. Qiu, and G. F. Sterman. "Nonrelativistic QCD factorization and the velocity dependence of NNLO poles in heavy quarkonium production". In: *Phys. Rev. D* 74 (2006), p. 074007. DOI: 10.1103/PhysRevD.74.074007. arXiv: hep-ph/0608066.

[8] F. Abe et al. "J/ψ and $\psi(2S)$ Production in $p\bar{p}$ Collisions at $\sqrt{s} = 1.8$ TeV". In: *Phys. Rev. Lett.* 79 (1997), pp. 572–577. DOI: 10.1103/PhysRevLett.79.572.

[9] F. Abe et al. "Production of J/ψ Mesons from χ_c Meson Decays in $p\bar{p}$ Collisions at $\sqrt{s} = 1.8$ TeV". In: *Phys. Rev. Lett.* 79 (1997), pp. 578–583. DOI: 10.1103/PhysRevLett.79.578.

[10] J. P. Lansberg. "QCD corrections to J/ψ polarisation in pp collisions at RHIC". In: *Phys. Lett. B* 695 (2011), pp. 149–156. DOI: 10.1016/j.physletb.2010.10.054. arXiv: 1003.4319 [hep-ph].

[11] S. J. Brodsky and J.-P. Lansberg. "Heavy-quarkonium production in high energy proton-proton collisions at RHIC". In: *Phys. Rev. D* 81 (2010), p. 051502. DOI: 10.1103/PhysRevD.81.051502. arXiv: 0908.0754 [hep-ph].

[12] C. Flore, J.-P. Lansberg, H.-S. Shao, and Y. Yedelkina. "Large-P_T inclusive photoproduction of J/ψ in electron-proton collisions at HERA and the EIC". In: *Phys. Lett. B* 811 (2020), p. 135926. DOI: 10.1016/j.physletb.2020.135926. arXiv: 2009.08264 [hep-ph].

[13] F. D. Aaron et al. "Inelastic production of J/ψ mesons in photoproduction and deep inelastic scattering at HERA". In: *Eur. Phys. J. C* 68 (2010), pp. 401–420. DOI: 10.1140/epjc/s10052-010-1376-5. arXiv: 1002.0234 [hep-ex].

[14] M. Butenschoen and B. A. Kniehl. "Reconciling J/ψ Production at HERA, RHIC, Tevatron, and LHC with NRQCD Factorization at Next-to-Leading Order". In: *Phys. Rev. Lett.* 106 (2011), p. 022003. DOI: 10.1103/PhysRevLett.106.022003. arXiv: 1009.5662 [hep-ph].

[15] K.-T. Chao, Y.-Q. Ma, H.-S. Shao, K. Wang, and Y.-J. Zhang. "J/ψ Polarization at Hadron Colliders in Nonrelativistic QCD". In: *Phys. Rev. Lett.* 108 (2012), p. 242004. DOI: 10.1103/PhysRevLett.108.242004. arXiv: 1201.2675 [hep-ph].

[16] R. Sharma and I. Vitev. "High transverse momentum quarkonium production and dissociation in heavy ion collisions". In: *Phys. Rev. C* 87.4 (2013), p. 044905. DOI: 10.1103/PhysRevC.87.044905. arXiv: 1203.0329 [hep-ph].

[17] G. T. Bodwin, H. S. Chung, U.-R. Kim, and J. Lee. "Fragmentation Contributions to J/ψ Production at the Tevatron and the LHC". In: *Phys. Rev. Lett.* 113.2 (2014), p. 022001. DOI: 10.1103/PhysRevLett.113.022001. arXiv: 1403.3612 [hep-ph].

[18] H.-F. Zhang, Z. Sun, W.-L. Sang, and R. Li. "Impact of η_c Hadroproduction Data on Charmonium Production and Polarization within NRQCD Framework". In: *Phys. Rev. Lett.* 114.9 (2015), p. 092006. DOI: 10.1103/PhysRevLett.114.092006. arXiv: 1412.0508 [hep-ph].

[19] A. Andronic et al. "Heavy-flavour and quarkonium production in the LHC era: from proton–proton to heavy-ion collisions". In: *Eur. Phys. J. C* 76.3 (2016), p. 107. DOI: 10.1140/epjc/s10052-015-3819-5. arXiv: 1506.03981 [nucl-ex].

[20] F. Halzen. "CVC for gluons and hadroproduction of quark flavors". In: *Phys. Lett. B* 69 (1977), pp. 105–108. DOI: 10.1016/0370-2693(77)90144-7.

[21] H. Fritzsch. "Producing heavy quark flavors in hadronic collisions — A test of quantum chromodynamics". In: *Phys. Lett. B* 67 (1977), pp. 217–221. DOI: 10.1016/0370-2693(77)90108-3.

[22] V. D. Barger, W.-Y. Keung, and R. J. N. Phillips. "Hadroproduction of ψ and Y". In: *Z. Phys. C* 6 (1980), p. 169. DOI: 10.1007/BF01588844.

[23] R. Gavai, D. Kharzeev, H. Satz, G. A. Schuler, K. Sridhar, and R. Vogt. "Quarkonium production in hadronic collisions". In: *Int. J. Mod. Phys. A* 10 (1995), pp. 3043–3070. DOI: 10.1142/S0217751X95001443. arXiv: hep-ph/9502270.

[24] G. T. Bodwin, E. Braaten, and J. Lee. "Comparison of the color-evaporation model and the nonrelativistic QCD factorization approach in charmonium production". In: *Phys. Rev. D* 72 (2005), p. 014004. DOI: 10.1103/PhysRevD.72.014004. arXiv: hep-ph/0504014.

[25] Y.-Q. Ma and R. Vogt. "Quarkonium production in an improved color evaporation model". In: *Phys. Rev. D* 94.11 (2016), p. 114029. DOI: 10.1103/PhysRevD.94.114029. arXiv: 1609.06042 [hep-ph].

[26] J. Collins. *Foundations of perturbative QCD*. Vol. 32. Cambridge University Press, 2013. ISBN: 978-1-107-64525-7, 978-1-107-64525-7, 978-0-521-85533-4, 978-1-139-09782-6.

[27] A. Bacchetta, D. Boer, C. Pisano, and P. Taels. "Gluon TMDs and NRQCD matrix elements in J/ψ production at an EIC". In: *Eur. Phys. J. C* 80.1 (2020), p. 72. DOI: 10.1140/epjc/s10052-020-7620-8. arXiv: 1809.02056 [hep-ph].

[28] F. Yuan. "Heavy-quarkonium production in single-transverse-polarized high-energy scattering". In: *Phys. Rev. D* 78 (2008), p. 014024. DOI: 10.1103/PhysRevD.78.014024. arXiv: 0801.4357 [hep-ph].

[29] A. Mukherjee and S. Rajesh. "J/ψ production in polarized and unpolarized ep collision and Sivers and $\cos 2\phi$ asymmetries". In: *Eur. Phys. J. C* 77.12 (2017), p. 854. DOI: 10.1140/epjc/s10052-017-5406-4. arXiv: 1609.05596 [hep-ph].

[30] S. Rajesh, R. Kishore, and A. Mukherjee. "Sivers effect in inelastic J/ψ photoproduction in $ep^{\uparrow}$ collision in color octet model". In: *Phys. Rev. D* 98.1 (2018), p. 014007. DOI: 10.1103/PhysRevD.98.014007. arXiv: 1802.10359 [hep-ph].

[31] D. Boer and C. Pisano. "Polarized gluon studies with charmonium and bottomonium at LHCb and AFTER". In: *Phys. Rev. D* 86 (2012), p. 094007. DOI: 10.1103/PhysRevD.86.094007. arXiv: 1208.3642 [hep-ph].

[32] W. J. den Dunnen, J. P. Lansberg, C. Pisano, and M. Schlegel. "Accessing the Transverse Dynamics and Polarization of Gluons inside the Proton at the LHC". In: *Phys. Rev. Lett.* 112 (2014), p. 212001. DOI: 10.1103/PhysRevLett.112.212001. arXiv: 1401.7611 [hep-ph].

[33] J.-P. Lansberg, C. Pisano, and M. Schlegel. "Associated production of a dilepton and a $\Upsilon(J/\psi)$ at the LHC as a probe of gluon transverse momentum dependent distributions". In: *Nucl. Phys. B* 920 (2017), pp. 192–210. DOI: 10.1016/j.nuclphysb.2017.04.011. arXiv: 1702.00305 [hep-ph].

[34] J.-P. Lansberg, C. Pisano, F. Scarpa, and M. Schlegel. "Pinning down the linearly-polarised gluons inside unpolarised protons using quarkonium-pair production at the LHC". In: *Phys. Lett. B* 784 (2018). [Erratum: Phys.Lett.B 791, 420–421 (2019)], pp. 217–222. DOI: 10.1016/j.physletb.2018.08.004. arXiv: 1710.01684 [hep-ph].

[35] F. Scarpa, D. Boer, M. G. Echevarria, J.-P. Lansberg, C. Pisano, and M. Schlegel. "Studies of gluon TMDs and their evolution using quarkonium-pair production at the LHC". In: *Eur. Phys. J. C* 80.2 (2020), p. 87. DOI: 10.1140/epjc/s10052-020-7619-1. arXiv: 1909.05769 [hep-ph].

[36] M. G. Echevarria. "Proper TMD factorization for quarkonia production: $pp \to \eta_{c,b}$ as a study case". In: *JHEP* 10 (2019), p. 144. DOI: 10.1007/JHEP10(2019)144. arXiv: 1907.06494 [hep-ph].

[37] D. Gutierrez-Reyes, Y. Makris, V. Vaidya, I. Scimemi, and L. Zoppi. "Probing transverse-momentum distributions with groomed jets". In: *JHEP* 08 (2019), p. 161. DOI: 10.1007/JHEP08(2019)161. arXiv: 1907.05896 [hep-ph].

[38] D. Boer et al. "Gluons and the quark sea at high energies: distributions, polarization, tomography". In: (2011). arXiv: 1108.1713 [nucl-th].

[39] R. Abdul Khalek et al. "Science Requirements and Detector Concepts for the Electron-Ion Collider: EIC Yellow Report". In: *Nucl. Phys. A* 1026 (2022), p. 122447. DOI: 10.1016/j.nuclphysa.2022.122447. arXiv: 2103.05419 [physics.ins-det].

[40] A. Accardi et al. "Electron-Ion Collider: The next QCD frontier". In: *Eur. Phys. J. A* 52.9 (2016). Ed. by A. Deshpande, Z. E. Meziani, and J. W. Qiu, p. 268. DOI: 10.1140/epja/i2016-16268-9. arXiv: 1212.1701 [nucl-ex].

[41] A. Adare et al. "Transverse momentum dependence of J/ψ polarization at midrapidity in $p+p$ collisions at $\sqrt{s} = 200$ *GeV*". In: *Phys. Rev. D* 82 (2010), p. 012001. DOI: 10.1103/PhysRevD.82.012001. arXiv: 0912.2082 [hep-ex].

[42] C. Aidala et al. "Single-spin asymmetry of J/ψ production in $p+p$, p+Al, and p+Au collisions with transversely polarized proton beams at $\sqrt{s_{NN}} =$ 200 GeV". In: *Phys. Rev. D* 98.1 (2018), p. 012006. DOI: 10.1103/PhysRevD.98.012006. arXiv: 1805.01491 [hep-ex].

[43] G. L. Kane, J. Pumplin, and W. Repko. "Transverse Quark Polarization in Large-p_T Reactions, e^+e^- Jets, and Leptoproduction: A Test of Quantum Chromodynamics". In: *Phys. Rev. Lett.* 41 (1978), p. 1689. DOI: 10.1103/PhysRevLett.41.1689.

[44] D. L. Adams et al. "Comparison of spin asymmetries and cross-sections in π^0 production by 200 GeV polarized anti-protons and protons". In: *Phys. Lett. B* 261 (1991), pp. 201–206. DOI: 10.1016/0370-2693(91)91351-U.

[45] D. L. Adams et al. "Analyzing power in inclusive π^+ and π^- production at high x_F with a 200 GeV polarized proton beam". In: *Phys. Lett. B* 264 (1991), pp. 462–466. DOI: 10.1016/0370-2693(91)90378-4.

[46] D. L. Adams et al. "High-x_T single spin asymmetry in π^0 and eta production at $x_F = 0$ by 200 GeV polarized anti-protons and protons". In: *Phys. Lett. B* 276 (1992), pp. 531–535. DOI: 10.1016/0370-2693(92)91679-4.

[47] D. L. Adams et al. "Large-x_F spin asymmetry in π^0 production by 200-GeV polarized protons". In: *Z. Phys. C* 56 (1992), pp. 181–184. DOI: 10.1007/BF01555512.

[48] A. V. Efremov and O. V. Teryaev. "QCD asymmetry and polarized hadron structure function measurement". In: *Phys. Lett. B* 150 (1985), p. 383. DOI: 10.1016/0370-2693(85)90999-2.

[49] J.-w. Qiu and G. F. Sterman. "Single transverse spin asymmetries". In: *Phys. Rev. Lett.* 67 (1991), pp. 2264–2267. DOI: 10.1103/PhysRevLett.67.2264.

[50] C. Kouvaris, J.-W. Qiu, W. Vogelsang, and F. Yuan. "Single transverse-spin asymmetry in high transverse momentum pion production in pp collisions". In: *Phys. Rev. D* 74 (2006), p. 114013. DOI: 10.1103/PhysRevD.74.114013. arXiv: hep-ph/0609238.

[51] K. Kanazawa and Y. Koike. "New analysis of the single transverse-spin asymmetry for hadron production at RHIC". In: *Phys. Rev. D* 82 (2010), p. 034009. DOI: 10.1103/PhysRevD.82.034009. arXiv: 1005.1468 [hep-ph].

[52] J.-w. Qiu and G. F. Sterman. "Single transverse-spin asymmetries in hadronic pion production". In: *Phys. Rev. D* 59 (1999), p. 014004. DOI: 10.1103/PhysRevD.59.014004. arXiv: hep-ph/9806356.

[53] Y. Kanazawa and Y. Koike. "Chiral-odd contribution to single-transverse spin asymmetry in hadronic pion production". In: *Phys. Lett. B* 478 (2000), pp. 121–126. DOI: 10.1016/S0370-2693(00)00261-6. arXiv: hep-ph/0001021.

[54] Y. Kanazawa and Y. Koike. "Estimate of a chiral-odd contribution to single transverse-spin asymmetry in hadronic pion production". In: *Phys. Lett. B* 490 (2000), pp. 99–105. DOI: 10.1016/S0370-2693(00)00969-2. arXiv: hep-ph/0007272.

[55] K. Goeke, A. Metz, and M. Schlegel. "Parameterization of the quark-quark correlator of a spin-$\frac{1}{2}$ hadron". In: *Phys. Lett. B* 618 (2005), pp. 90–96. DOI: 10.1016/j.physletb.2005.05.037. arXiv: hep-ph/0504130.

[56] K. Kanazawa and Y. Koike. "A phenomenological study of single transverse-spin asymmetry for inclusive light-hadron productions at RHIC". In: *Phys. Rev. D* 83 (2011), p. 114024. DOI: 10.1103/PhysRevD.83.114024. arXiv: 1104.0117 [hep-ph].

[57] K. Kanazawa, A. Metz, D. Pitonyak, and M. Schlegel. "Longitudinal–transverse double-spin asymmetries in single-inclusive leptoproduction of hadrons". In: *Phys. Lett. B* 742 (2015), pp. 340–346. DOI: 10.1016/j.physletb.2015.02.005. arXiv: 1411.6459 [hep-ph].

[58] M. Schlegel. "Partonic description of the transverse target single-spin asymmetry in inclusive deep-inelastic scattering". In: *Phys. Rev. D* 87.3 (2013), p. 034006. DOI: 10.1103/PhysRevD.87.034006. arXiv: 1211.3579 [hep-ph].

[59] K. Kanazawa, Y. Koike, A. Metz, D. Pitonyak, and M. Schlegel. "Operator constraints for twist-3 functions and Lorentz invariance properties of twist-3 observables". In: *Phys. Rev. D* 93.5 (2016), p. 054024. DOI: 10.1103/PhysRevD.93.054024. arXiv: 1512.07233 [hep-ph].

[60] L. Gamberg, M. Malda, J. A. Miller, D. Pitonyak, A. Prokudin, and N. Sato. "Updated QCD global analysis of single transverse-spin asymmetries: Extracting $\tilde{H}$, and the role of the Soffer bound and lattice QCD". In: *Phys. Rev. D* 106.3 (2022), p. 034014. DOI: 10.1103/PhysRevD.106.034014. arXiv: 2205.00999 [hep-ph].

[61] M. Anselmino, M. Boglione, and F. Murgia. "Single spin asymmetry for $p^\uparrow p \to piX$ in perturbative QCD". In: *Phys. Lett. B* 362 (1995), pp. 164–172. DOI: 10.1016/0370-2693(95)01168-P. arXiv: hep-ph/9503290.

[62] M. Anselmino and F. Murgia. "Single spin asymmetries in $p^\uparrow p$ and $\bar{p}^\uparrow p$ inclusive processes". In: *Phys. Lett. B* 442 (1998), pp. 470–478. DOI: 10.1016/S0370-2693(98)01267-2. arXiv: hep-ph/9808426.

[63] U. D'Alesio and F. Murgia. "Azimuthal and single spin asymmetries in hard scattering processes". In: *Prog. Part. Nucl. Phys.* 61 (2008), pp. 394–454. DOI: 10.1016/j.ppnp.2008.01.001. arXiv: 0712.4328 [hep-ph].

[64] M. Anselmino, M. Boglione, U. D'Alesio, E. Leader, S. Melis, and F. Murgia. "General partonic structure for hadronic spin asymmetries". In: *Phys. Rev. D* 73 (2006), p. 014020. DOI: 10.1103/PhysRevD.73.014020. arXiv: hep-ph/0509035.

[65] L. Adamczyk et al. "Transverse single-spin asymmetry and cross section for π^0 and η mesons at large Feynman x in polarized $p+p$ collisions at $\sqrt{s} = 200$ GeV". In: *Phys. Rev. D* 86 (2012), p. 051101. DOI: 10.1103/PhysRevD.86.051101. arXiv: 1205.6826 [nucl-ex].

[66] J. H. Lee and F. Videbaek. "Single Spin Asymmetries of Identified Hadrons in Polarized $p+p$ at $\sqrt{s} = 62.4$ and 200 GeV". In: *AIP Conf. Proc.* 915.1 (2007). Ed. by K. Imai, T. Murakami, K. Tanida, and N. Saito, pp. 533–538. DOI: 10.1063/1.2750837.

[67] S. S. Adler et al. "Measurement of Transverse Single-Spin Asymmetries for Midrapidity Production of Neutral Pions and Charged Hadrons in Polarized $p + p$ Collisions at $\sqrt{s} = 200$ GeV". In: *Phys. Rev. Lett.* 95 (2005), p. 202001. DOI: 10.1103/PhysRevLett.95.202001. arXiv: hep-ex/0507073.

[68] G. Igo. "New STAR transverse spin results". In: *AIP Conf. Proc.* 1523.1 (2013). Ed. by M. Capua, R. Fiore, A. Papa, A. Sabio Vera, and E. Tassi, pp. 188–193. DOI: 10.1063/1.4802147.

[69] L. C. Bland et al. "Cross sections and transverse single-spin asymmetries in forward jet production from proton collisions at $\sqrt{s} = 500$ GeV". In: *Phys. Lett. B* 750 (2015), pp. 660–665. DOI: 10.1016/j.physletb.2015.10.001. arXiv: 1304.1454 [hep-ex].

[70] X.-d. Ji, J.-P. Ma, and F. Yuan. "QCD factorization for spin-dependent cross sections in DIS and Drell–Yan processes at low transverse momentum". In: *Phys. Lett. B* 597 (2004), pp. 299–308. DOI: 10.1016/j.physletb.2004.07.026. arXiv: hep-ph/0405085.

[71] X.-d. Ji, J.-p. Ma, and F. Yuan. "QCD factorization for semi-inclusive deep-inelastic scattering at low transverse momentum". In: *Phys. Rev. D* 71 (2005), p. 034005. DOI: 10.1103/PhysRevD.71.034005. arXiv: hep-ph/0404183.

[72] S. M. Aybat, J. C. Collins, J.-W. Qiu, and T. C. Rogers. "QCD evolution of the Sivers function". In: *Phys. Rev. D* 85 (2012), p. 034043. DOI: 10.1103/PhysRevD.85.034043. arXiv: 1110.6428 [hep-ph].

[73] S. M. Aybat and T. C. Rogers. "Transverse momentum dependent parton distribution and fragmentation functions with QCD evolution". In: *Phys. Rev. D* 83 (2011), p. 114042. DOI: 10.1103/PhysRevD.83.114042. arXiv: 1101.5057 [hep-ph].

[74] M. Garcia-Echevarria, A. Idilbi, and I. Scimemi. "Soft-collinear effective theory, light-cone gauge, and the T-Wilson lines". In: *Phys. Rev. D* 84 (2011), p. 011502. DOI: 10.1103/PhysRevD.84.011502. arXiv: 1104.0686 [hep-ph].

[75] M. G. Echevarría, A. Idilbi, and I. Scimemi. "Soft and collinear factorization and transverse momentum dependent parton distribution functions". In: *Phys. Lett. B* 726 (2013), pp. 795–801. DOI: 10.1016/j.physletb.2013.09.003. arXiv: 1211.1947 [hep-ph].

[76] M. Anselmino, M. Boglione, U. D'Alesio, E. Leader, S. Melis, F. Murgia, and A. Prokudin. "Role of Collins effect in the single spin asymmetry A_N in $p^\uparrow p \to hX$ processes". In: *Phys. Rev. D* 86 (2012), p. 074032. DOI: 10.1103/PhysRevD.86.074032. arXiv: 1207.6529 [hep-ph].

[77] M. Anselmino, M. Boglione, U. D'Alesio, S. Melis, F. Murgia, and A. Prokudin. "Sivers effect and the single spin asymmetry A_N in $p^\uparrow p \to hX$ processes". In: *Phys. Rev. D* 88.5 (2013), p. 054023. DOI: 10.1103/PhysRevD.88.054023. arXiv: 1304.7691 [hep-ph].

[78] U. D'Alesio, C. Flore, and A. Prokudin. "Role of the Soffer bound in determination of transversity and the tensor charge". In: *Phys. Lett. B* 803 (2020), p. 135347. DOI: 10.1016/j.physletb.2020.135347. arXiv: 2001.01573 [hep-ph].

[79] M. Bury, A. Prokudin, and A. Vladimirov. "Extraction of the Sivers function from SIDIS, Drell-Yan, and $W^\pm/Z$ boson production data with TMD evolution". In: *JHEP* 05 (2021), p. 151. DOI: 10.1007/JHEP05(2021)151. arXiv: 2103.03270 [hep-ph].

[80] M. Boglione, U. D'Alesio, C. Flore, J. O. Gonzalez-Hernandez, F. Murgia, and A. Prokudin. "Reweighting the Sivers function with jet data from STAR". In: *Phys. Lett. B* 815 (2021), p. 136135. DOI: 10.1016/j.physletb.2021.136135. arXiv: 2101.03955 [hep-ph].

[81] M. Boglione, U. D'Alesio, and F. Murgia. "Single spin asymmetries in inclusive hadron production from semiinclusive DIS to hadronic collisions: Universality and phenomenology". In: *Phys. Rev. D* 77 (2008), p. 051502. DOI: 10.1103/PhysRevD.77.051502. arXiv: 0712.4240 [hep-ph].

[82] J. Ashman et al. "A measurement of the spin asymmetry and determination of the structure function g_1 in deep inelastic muon-proton scattering". In: *Phys. Lett. B* 206 (1988). Ed. by V. W. Hughes and C. Cavata, p. 364. DOI: 10.1016/0370-2693(88)91523-7.

[83] D. W. Sivers. "Single-spin production asymmetries from the hard scattering of pointlike constituents". In: *Phys. Rev. D* 41 (1990), p. 83. DOI: 10.1103/PhysRevD.41.83.

[84] D. W. Sivers. "Hard-scattering scaling laws for single spin production asymmetries". In: *Phys. Rev. D* 43 (1991), pp. 261–263. DOI: 10.1103/PhysRevD.43.261.

[85] L. Gamberg and Z.-B. Kang. "Process dependent Sivers function and implication for single spin asymmetry in inclusive hadron production". In: *Phys. Lett. B* 696 (2011), pp. 109–118. DOI: 10.1016/j.physletb.2010.11.066. arXiv: 1009.1936 [hep-ph].

[86] D. Graudenz. "Next-to-leading order QCD corrections to jet cross sections and jet rates in deeply inelastic electron-proton scattering". In: *Phys. Rev. D* 49 (1994), pp. 3291–3319. DOI: 10.1103/PhysRevD.49.3291. arXiv: hep-ph/9307311.

[87] B. A. Kniehl and L. Zwirner. "J/ψ inclusive production in ep deep-inelastic scattering at DESY HERA". In: *Nucl. Phys. B* 621 (2002), pp. 337–358. DOI: 10.1016/S0550-3213(01)00564-8. arXiv: hep-ph/0112199.

[88] M. Beneke, M. Kramer, and M. Vanttinen. "Inelastic photoproduction of polarized J/ψ". In: *Phys. Rev. D* 57 (1998), pp. 4258–4274. DOI: 10.1103/PhysRevD.57.4258. arXiv: hep-ph/9709376.

[89] C. S. Lam and W.-K. Tung. "Systematic approach to inclusive lepton pair production in hadronic collisions". In: *Phys. Rev. D* 18 (1978), p. 2447. DOI: 10.1103/PhysRevD.18.2447.

[90] C. S. Lam and W.-K. Tung. "Parton-model relation without quantum-chromodynamic modifications in lepton pair production". In: *Phys. Rev. D* 21 (1980), p. 2712. DOI: 10.1103/PhysRevD.21.2712.

[91] M. Beneke and I. Z. Rothstein. "Hadroproduction of quarkonium in fixed-target experiments". In: *Phys. Rev. D* 54 (1996). [Erratum: Phys.Rev.D 54, 7082 (1996)], p. 2005. DOI: 10.1103/PhysRevD.54.2005. arXiv: hep-ph/9603400.

[92] M. Beneke and I. Z. Rothstein. "ψ' polarization as a test of colour octet quarkonium production". In: *Phys. Lett. B* 372 (1996). [Erratum: Phys.Lett.B 389, 769 (1996)], pp. 157–164. DOI: 10.1016/0370-2693(96)00030-5. arXiv: hep-ph/9509375.

[93] A. K. Leibovich. "ψ' polarization due to color-octet quarkonia production". In: *Phys. Rev. D* 56 (1997), pp. 4412–4415. DOI: 10.1103/PhysRevD.56.4412. arXiv: hep-ph/9610381.

[94] U. D'Alesio, L. Maxia, F. Murgia, C. Pisano, and S. Rajesh. "J/ψ polarization in large-P_T semi-inclusive deep-inelastic scattering at the EIC". In: *Submitted for publication* (2023). arXiv: 2301.11987 [hep-ph].

[95] S. Acharya et al. "Measurement of the inclusive J/ψ polarization at forward rapidity in pp collisions at $\sqrt{\mathbf{s}} = \mathbf{8}$ TeV". In: *Eur. Phys. J. C* 78.7 (2018), p. 562. DOI: 10.1140/epjc/s10052-018-6027-2. arXiv: 1805.04374 [hep-ex].

[96] S. Chekanov et al. "Measurement of J/ψ helicity distributions in inelastic photoproduction at HERA". In: *JHEP* 12 (2009), p. 007. DOI: 10.1088/1126-6708/2009/12/007. arXiv: 0906.1424 [hep-ex].

[97] F. Yuan and K.-T. Chao. "Polarized J/ψ production in deep inelastic scattering at DESY HERA". In: *Phys. Rev. D* 63 (2001). [Erratum: Phys.Rev.D 66, 079902 (2002)], p. 034017. DOI: 10.1103/PhysRevD.63.034017. arXiv: hep-ph/0008301.

[98] H.-F. Zhang and Z. Sun. "Leptonic current structure and azimuthal asymmetry in deeply inelastic scattering". In: *Phys. Rev. D* 96.3 (2017), p. 034002. DOI: 10.1103/PhysRevD.96.034002. arXiv: 1701.08728 [hep-ph].

[99] Z. Sun and H.-F. Zhang. "QCD leading order study of the J/ψ leptoproduction at HERA within the nonrelativistic QCD framework". In: *Eur. Phys. J. C* 77.11 (2017), p. 744. DOI: 10.1140/epjc/s10052-017-5323-6. arXiv: 1702.02097 [hep-ph].

[100] M. Butenschoen and B. A. Kniehl. "Probing Nonrelativistic QCD Factorization in Polarized J/ψ Photoproduction at Next-to-Leading Order". In: *Phys. Rev. Lett.* 107 (2011), p. 232001. DOI: 10.1103/PhysRevLett.107.232001. arXiv: 1109.1476 [hep-ph].

[101] H.-F. Zhang, W.-L. Sang, and Y.-P. Yan. "Statistical analysis of the azimuthal asymmetry in the J/ψ leptoproduction in unpolarized ep collisions". In: *JHEP* 10 (2019), p. 234. DOI: 10.1007/JHEP10(2019)234. arXiv: 1908.02521 [hep-ph].

[102] D. Boer, C. Pisano, and P. Taels. "Extracting color octet NRQCD matrix elements from J/ψ production at the EIC". In: *Phys. Rev. D* 103.7 (2021), p. 074012. DOI: 10.1103/PhysRevD.103.074012. arXiv: 2102.00003 [hep-ph].

[103] J. Pumplin, D. R. Stump, J. Huston, H. L. Lai, P. M. Nadolsky, and W. K. Tung. "New Generation of Parton Distributions with Uncertainties from Global QCD Analysis". In: *JHEP* 07 (2002), p. 012. DOI: 10.1088/1126-6708/2002/07/012. arXiv: hep-ph/0201195.

[104] M. Butenschoen and B. A. Kniehl. "World data of J/ψ production consolidate NRQCD factorization at NLO". In: *Phys. Rev. D* 84 (2011), p. 051501. DOI: 10.1103/PhysRevD.84.051501. arXiv: 1105.0820 [hep-ph].

[105] B. Gong, L.-P. Wan, J.-X. Wang, and H.-F. Zhang. "Polarization for Prompt J/ψ and $\psi(2s)$ Production at the Tevatron and LHC". In: *Phys. Rev. Lett.* 110.4 (2013), p. 042002. DOI: 10.1103/PhysRevLett.110.042002. arXiv: 1205.6682 [hep-ph].

[106] M. Cacciari and M. Krämer. "Color-Octet Contributions to J/ψ Photoproduction". In: *Phys. Rev. Lett.* 76 (1996), pp. 4128–4131. DOI: 10.1103/PhysRevLett.76.4128. arXiv: hep-ph/9601276.

[107] P. Ko, J. Lee, and H. S. Song. "Color-octet mechanism in $\gamma + p \to J\psi + x$". In: *Phys. Rev. D* 54 (1996). [Erratum: Phys.Rev.D 60, 119902 (1999)], pp. 4312–4325. DOI: 10.1103/PhysRevD.54.4312. arXiv: hep-ph/9602223.

[108] M. Beneke, I. Z. Rothstein, and M. B. Wise. "Kinematic enhancement of nonperturbative corrections to quarkonium production". In: *Phys. Lett. B* 408 (1997), pp. 373–380. DOI: 10.1016/S0370-2693(97)00832-0. arXiv: hep-ph/9705286.

[109] M. Beneke, G. A. Schuler, and S. Wolf. "Quarkonium momentum distributions in photoproduction and B decay". In: *Phys. Rev. D* 62 (2000), p. 034004. DOI: 10.1103/PhysRevD.62.034004. arXiv: hep-ph/0001062.

[110] S. Fleming, Y. Makris, and T. Mehen. "An effective field theory approach to quarkonium at small transverse momentum". In: *JHEP* 04 (2020), p. 122. DOI: 10.1007/JHEP04(2020)122. arXiv: 1910.03586 [hep-ph].

[111] D. Boer, U. D'Alesio, F. Murgia, C. Pisano, and P. Taels. "J/ψ meson production in SIDIS: matching high and low transverse momentum". In: *JHEP* 09 (2020), p. 040. DOI: 10.1007/JHEP09(2020)040. arXiv: 2004.06740 [hep-ph].

[112] U. D'Alesio, L. Maxia, F. Murgia, C. Pisano, and S. Rajesh. "J/ψ polarization in semi-inclusive DIS at low and high transverse momentum". In: *JHEP* 03 (2022), p. 037. DOI: 10.1007/JHEP03(2022)037. arXiv: 2110.07529 [hep-ph].

[113] P. Faccioli, C. Lourenco, and J. Seixas. "New approach to quarkonium polarization studies". In: *Phys. Rev. D* 81 (2010), p. 111502. DOI: 10.1103/PhysRevD.81.111502. arXiv: 1005.2855 [hep-ph].

[114] P. Faccioli, C. Lourenco, and J. Seixas. "Rotation-Invariant Relations in Vector Meson Decays into Fermion Pairs". In: *Phys. Rev. Lett.* 105 (2010), p. 061601. DOI: 10.1103/PhysRevLett.105.061601. arXiv: 1005.2601 [hep-ph].

[115] P. Faccioli, C. Lourenco, J. Seixas, and H. K. Wohri. "Towards the experimental clarification of quarkonium polarization". In: *Eur. Phys. J. C* 69 (2010), pp. 657–673. DOI: 10.1140/epjc/s10052-010-1420-5. arXiv: 1006.2738 [hep-ph].

[116] P. Faccioli, C. Lourenco, J. Seixas, and H. K. Wohri. "Quarkonium polarization in pp and p-nucleus collisions". In: *Nucl. Phys. A* 855 (2011). Ed. by I. Tserruya, A. Milov, D. d'Enterria, P. Jacobs, and U. Wiedemann, pp. 116–124. DOI: 10.1016/j.nuclphysa.2011.02.027.

[117] P. Faccioli, C. Lourenco, J. Seixas, and H. K. Wohri. "Quarkonium polarization measurements". In: *Nucl. Phys. B Proc. Suppl.* 214 (2011). Ed. by Z. Conesa del Valle, E. G. Ferreiro, F. Fleuret, and J.-P. Lansberg, pp. 97–102. DOI: 10.1016/j.nuclphysbps.2011.03.065.

[118] J.-C. Peng, D. Boer, W.-C. Chang, R. E. McClellan, and O. Teryaev. "On the rotational invariance and non-invariance of lepton angular distributions in Drell–Yan and quarkonium production". In: *Phys. Lett. B* 789 (2019), pp. 356–359. DOI: 10.1016/j.physletb.2018.11.061. arXiv: 1808.04398 [hep-ph].

[119] P. Faccioli, C. Lourenco, J. Seixas, and H. K. Wohri. "Model-independent constraints on the shape parameters of dilepton angular distributions". In: *Phys. Rev. D* 83 (2011), p. 056008. DOI: 10.1103/PhysRevD.83.056008. arXiv: 1102.3946 [hep-ph].

[120] S. Palestini. "Angular distribution and rotations of frame in vector meson decays into lepton pairs". In: *Phys. Rev. D* 83 (2011), p. 031503. DOI: 10.1103/PhysRevD.83.031503. arXiv: 1012.2485 [hep-ph].

[121] Y.-Q. Ma, T. Stebel, and R. Venugopalan. "J/ψ polarization in the CGC+NRQCD approach". In: *JHEP* 12 (2018), p. 057. DOI: 10.1007/JHEP12(2018)057. arXiv: 1809.03573 [hep-ph].

[122] P. J. Mulders and J. Rodrigues. "Transverse momentum dependence in gluon distribution and fragmentation functions". In: *Phys. Rev. D* 63 (2001), p. 094021. DOI: 10.1103/PhysRevD.63.094021. arXiv: hep-ph/0009343.

[123] S. Meissner, A. Metz, and K. Goeke. "Relations between generalized and transverse momentum dependent parton distributions". In: *Phys. Rev. D* 76 (2007), p. 034002. DOI: 10.1103/PhysRevD.76.034002. arXiv: hep-ph/0703176.

[124] D. Boer, S. Cotogno, T. van Daal, P. J. Mulders, A. Signori, and Y.-J. Zhou. "Gluon and Wilson loop TMDs for hadrons of spin ≤ 1". In: *JHEP* 10 (2016), p. 013. DOI: 10.1007/JHEP10(2016)013. arXiv: 1607.01654 [hep-ph].

[125] A. Bacchetta, D. Boer, M. Diehl, and P. J. Mulders. "Matches and mismatches in the descriptions of semi-inclusive processes at low and high transverse momentum". In: *JHEP* 08 (2008), p. 023. DOI: 10.1088/1126-6708/2008/08/023. arXiv: 0803.0227 [hep-ph].

[126] J. C. Collins, D. E. Soper, and G. F. Sterman. "Transverse momentum distribution in Drell-Yan pair and W and Z boson production". In: *Nucl. Phys. B* 250 (1985), pp. 199–224. DOI: 10.1016/0550-3213(85)90479-1.

[127] S. Catani, D. de Florian, and M. Grazzini. "Universality of non-leading logarithmic contributions in transverse-momentum distributions". In: *Nucl. Phys. B* 596 (2001), pp. 299–312. DOI: 10.1016/S0550-3213(00)00617-9. arXiv: hep-ph/0008184.

[128] A. Bacchetta, M. Diehl, K. Goeke, A. Metz, P. J. Mulders, and M. Schlegel. "Semi-inclusive deep inelastic scattering at small transverse momentum". In: *JHEP* 02 (2007), p. 093. DOI: 10.1088/1126-6708/2007/02/093. arXiv: hep-ph/0611265.

[129] R. Meng, F. I. Olness, and D. E. Soper. "Semi-inclusive deeply inelastic scattering at small q_T". In: *Phys. Rev. D* 54 (1996), pp. 1919–1935. DOI: 10.1103/PhysRevD.54.1919. arXiv: hep-ph/9511311.

[130] P. Sun, B.-W. Xiao, and F. Yuan. "Gluon distribution functions and Higgs boson production at moderate transverse momentum". In: *Phys. Rev. D* 84 (2011), p. 094005. DOI: 10.1103/PhysRevD.84.094005. arXiv: 1109.1354 [hep-ph].

[131] S. Catani and M. Grazzini. "QCD transverse-momentum resummation in gluon fusion processes". In: *Nucl. Phys. B* 845 (2011), pp. 297–323. DOI: 10.1016/j.nuclphysb.2010.12.007. arXiv: 1011.3918 [hep-ph].

[132] F. Maltoni, M. L. Mangano, and A. Petrelli. "Quarkonium photoproduction at next-to-leading order". In: *Nucl. Phys. B* 519 (1998), pp. 361–393. DOI: 10.1016/S0550-3213(98)00048-0. arXiv: hep-ph/9708349.

[133] P. Sun, C. .-. Yuan, and F. Yuan. "Heavy quarkonium production at low $P_\perp$ in nonrelativistic QCD with soft gluon resummation". In: *Phys. Rev. D* 88 (2013), p. 054008. DOI: 10.1103/PhysRevD.88.054008. arXiv: 1210.3432 [hep-ph].

[134] D. Boer, J. Bor, L. Maxia, and C. Pisano. "Work in progress".

[135] R. Zhu, P. Sun, and F. Yuan. "Low transverse momentum heavy quark pair production to probe gluon tomography". In: *Phys. Lett. B* 727 (2013), pp. 474–479. DOI: 10.1016/j.physletb.2013.11.002. arXiv: 1309.0780 [hep-ph].

[136] M. G. Echevarria, T. Kasemets, P. J. Mulders, and C. Pisano. "QCD evolution of (un)polarized gluon TMDPDFs and the Higgs q_T-distribution". In: *JHEP* 07 (2015). [Erratum: JHEP 05, 073 (2017)], p. 158. DOI: 10.1007/JHEP07(2015)158. arXiv: 1502.05354 [hep-ph].

[137] U. D'Alesio, F. Murgia, C. Pisano, and P. Taels. "Probing the gluon Sivers function in $p^\uparrow p \to J/\psi\, X$ and $p^\uparrow p \to D\, X$". In: *Phys. Rev. D* 96.3 (2017), p. 036011. DOI: 10.1103/PhysRevD.96.036011. arXiv: 1705.04169 [hep-ph].

[138] U. D'Alesio, C. Flore, F. Murgia, C. Pisano, and P. Taels. "Unraveling the gluon Sivers function in hadronic collisions at RHIC". In: *Phys. Rev. D* 99.3 (2019), p. 036013. DOI: 10.1103/PhysRevD.99.036013. arXiv: 1811.02970 [hep-ph].

[139] U. D'Alesio, A. Mukherjee, F. Murgia, C. Pisano, and S. Rajesh. "Gluon TMDs and inelastic J/ψ leptoproduction at the EIC". In: *24th International Symposium on Spin Physics*. 2022. arXiv: 2203.03299 [hep-ph].

[140] U. D'Alesio, L. Gamberg, Z.-B. Kang, F. Murgia, and C. Pisano. "Testing the process dependence of the Sivers function via hadron distributions inside a jet". In: *Phys. Lett. B* 704 (2011), pp. 637–640. DOI: 10.1016/j.physletb.2011.09.067. arXiv: 1108.0827 [hep-ph].

[141] E. C. Aschenauer, U. D'Alesio, and F. Murgia. "TMDs and SSAs in hadronic interactions". In: *Eur. Phys. J. A* 52.6 (2016), p. 156. DOI: 10.1140/epja/i2016-16156-4. arXiv: 1512.05379 [hep-ph].

[142] E. Leader. *Spin in particle physics*. Vol. 15. 2011. ISBN: 978-0-511-87418-5, 978-0-521-35281-9, 978-0-521-02077-0.

[143] U. D'Alesio, F. Murgia, and M. Zaccheddu. "General helicity formalism for two-hadron production in e^+e annihilation within a TMD approach". In: *JHEP* 10 (2021), p. 078. DOI: 10.1007/JHEP10(2021)078. arXiv: 2108.05632 [hep-ph].

[144] A. Bacchetta, U. D'Alesio, M. Diehl, and C. A. Miller. "Single-spin asymmetries: The Trento conventions". In: *Phys. Rev. D* 70 (2004), p. 117504. DOI: 10.1103/PhysRevD.70.117504. arXiv: hep-ph/0410050.

[145] J. C. Collins. "Fragmentation of transversely polarized quarks probed in transverse momentum distributions". In: *Nucl. Phys. B* 396 (1993), pp. 161–182. DOI: 10.1016/0550-3213(93)90262-N. arXiv: hep-ph/9208213.

[146] S. J. Brodsky, D. S. Hwang, and I. Schmidt. "Final-state interactions and single-spin asymmetries in semi-inclusive deep inelastic scattering". In: *Int. J. Mod. Phys. A* 18 (2003). Ed. by B.-Q. Ma and K.-T. Chao, pp. 1327–1334. DOI: 10.1142/S0217751X03014678.

[147] S. J. Brodsky, D. S. Hwang, and I. Schmidt. "Initial state interactions and single spin asymmetries in Drell-Yan processes". In: *Nucl. Phys. B* 642 (2002), pp. 344–356. DOI: 10.1016/S0550-3213(02)00617-X. arXiv: hep-ph/0206259.

[148] J. C. Collins. "Leading-twist single-transverse-spin asymmetries: Drell-Yan and deep-inelastic scattering". In: *Phys. Lett. B* 536 (2002), pp. 43–48. DOI: 10.1016/S0370-2693(02)01819-1. arXiv: hep-ph/0204004.

[149] A. V. Belitsky, X. Ji, and F. Yuan. "Final state interactions and gauge invariant parton distributions". In: *Nucl. Phys. B* 656 (2003), pp. 165–198. DOI: 10.1016/S0550-3213(03)00121-4. arXiv: hep-ph/0208038.

[150] R. Baier and R. Ruckl. "Hadronic collisions: A quarkonium factory". In: *Z. Phys. C* 19 (1983), p. 251. DOI: 10.1007/BF01572254.

[151] E. L. Berger and D. L. Jones. "Inelastic photoproduction of J/ψ and Y by gluons". In: *Phys. Rev. D* 23 (1981), pp. 1521–1530. DOI: 10.1103/PhysRevD.23.1521.

[152] D. Boer, P. J. Mulders, and F. Pijlman. "Universality of T-odd effects in single spin and azimuthal asymmetries". In: *Nucl. Phys. B* 667 (2003), pp. 201–241. DOI: 10.1016/S0550-3213(03)00527-3. arXiv: hep-ph/0303034.

[153] J.-W. Qiu, W. Vogelsang, and F. Yuan. "Single transverse-spin asymmetry in hadronic dijet production". In: *Phys. Rev. D* 76 (2007), p. 074029. DOI: 10.1103/PhysRevD.76.074029. arXiv: 0706.1196 [hep-ph].

[154] U. D'Alesio, L. Maxia, F. Murgia, C. Pisano, and S. Rajesh. "Process dependence of the gluon Sivers function in $p^{\uparrow}p \to J/\psi + X$ within a TMD scheme in NRQCD". In: *Phys. Rev. D* 102.9 (2020), p. 094011. DOI: 10.1103/PhysRevD.102.094011. arXiv: 2007.03353 [hep-ph].

[155] U. D'Alesio, F. Murgia, C. Pisano, and S. Rajesh. "Single-spin asymmetries in $p^{\uparrow}p \to J/\psi + X$ within a TMD approach: role of the color octet mechanism". In: *Eur. Phys. J. C* 79.12 (2019), p. 1029. DOI: 10.1140/epjc/s10052-019-7551-4. arXiv: 1910.09640 [hep-ph].

[156] U. D'Alesio, F. Murgia, and C. Pisano. "Towards a first estimate of the gluon Sivers function from A_N data in pp collisions at RHIC". In: *JHEP* 09 (2015), p. 119. DOI: 10.1007/JHEP09(2015)119. arXiv: 1506.03078 [hep-ph].

[157] M. Anselmino, M. Boglione, U. D'Alesio, A. Kotzinian, F. Murgia, and A. Prokudin. "Role of Cahn and Sivers effects in deep inelastic scattering". In: *Phys. Rev. D* 71 (2005), p. 074006. DOI: 10.1103/PhysRevD.71.074006. arXiv: hep-ph/0501196.

[158] S. X. Oda. "J/ψ production at RHIC-PHENIX". In: *J. Phys. G* 35 (2008). Ed. by J.-e. Alam, S. Chattopadhyay, T. Nayak, B. Sinha, and Y. P. Viyogi, p. 104134. DOI: 10.1088/0954-3899/35/10/104134. arXiv: 0804.4446 [nucl-ex].

[159] S. J. Brodsky, F. Fleuret, C. Hadjidakis, and J. P. Lansberg. "Physics opportunities of a fixed-target experiment using LHC beams". In: *Phys. Rept.* 522 (2013), pp. 239–255. DOI: 10.1016/j.physrep.2012.10.001. arXiv: 1202.6585 [hep-ph].

[160] C. Hadjidakis et al. "A fixed-target programme at the LHC: Physics case and projected performances for heavy-ion, hadron, spin and astroparticle studies". In: *Phys. Rept.* 911 (2021), pp. 1–83. DOI: 10.1016/j.physrep.2021.01.002. arXiv: 1807.00603 [hep-ex].

[161] P. Di Nezza, V. Carassiti, G. Ciullo, P. Lenisa, L. L. Pappalardo, E. Steffens, and A. Vasilyev. "Internal gas target experiments at the LHC". In: *PoS* SPIN2018 (2019). Ed. by P. Lenisa, G. Ciullo, M. Contalbrigo, and L. Pappalardo, p. 011. DOI: 10.22323/1.346.0011.

[162] C. A. Aidala et al. "The LHCSpin Project". In: (2019). arXiv: 1901.08002 [hep-ex].

[163] A. Arbuzov et al. "On the physics potential to study the gluon content of proton and deuteron at NICA SPD". In: *Prog. Part. Nucl. Phys.* 119 (2021), p. 103858. DOI: 10.1016/j.ppnp.2021.103858. arXiv: 2011.15005 [hep-ex].

[164] C. A. Aidala et al. "The SeaQuest spectrometer at Fermilab". In: *Nucl. Instrum. Meth. A* 930 (2019), pp. 49–63. DOI: 10.1016/j.nima.2019.03.039. arXiv: 1706.09990 [physics.ins-det].

[165] D. Keller. "The Transverse Structure of the Deuteron with Drell-Yan". In: (2022). arXiv: 2205.01249 [nucl-ex].

[166] FNAL. *SpinQuest/E1039*. URL: https://spinquest.fnal.gov/.

[167] J. Bor and D. Boer. "TMD evolution study of the $\cos 2\phi$ azimuthal asymmetry in unpolarized J/ψ production at EIC". In: *Phys. Rev. D* 106.1 (2022), p. 014030. DOI: 10.1103/PhysRevD.106.014030. arXiv: 2204.01527 [hep-ph].

[168] G. P. Lepage, L. Magnea, C. Nakhleh, U. Magnea, and K. Hornbostel. "Improved nonrelativistic QCD for heavy-quark physics". In: *Phys. Rev. D* 46 (1992), pp. 4052–4067. DOI: 10.1103/PhysRevD.46.4052. arXiv: hep-lat/9205007.

[169] M. Butenschoen, Z.-G. He, and B. A. Kniehl. "η_c Production at the LHC Challenges Nonrelativistic QCD Factorization". In: *Phys. Rev. Lett.* 114.9 (2015), p. 092004. DOI: 10.1103/PhysRevLett.114.092004. arXiv: 1411.5287 [hep-ph].

[170] T. Affolder et al. "Measurement of J/ψ and $\psi(2S)$ Polarization in $p\bar{p}$ Collisions at $\sqrt{s} = 1.8$ TeV". In: *Phys. Rev. Lett.* 85 (2000), pp. 2886–2891. DOI: 10.1103/PhysRevLett.85.2886. arXiv: hep-ex/0004027.

[171] D. Acosta et al. "Measurement of the J/ψ meson and $b-$hadron production cross sections in $p\bar{p}$ collisions at $\sqrt{s} = 1960$ GeV". In: *Phys. Rev. D* 71 (2005), p. 032001. DOI: 10.1103/PhysRevD.71.032001. arXiv: hep-ex/0412071.

[172] R. Aaij et al. "Measurement of J/ψ production in pp collisions at $\sqrt{s} = 7$ TeV". In: *Eur. Phys. J. C* 71 (2011), p. 1645. DOI: 10.1140/epjc/s10052-011-1645-y. arXiv: 1103.0423 [hep-ex].

[173] G. T. Bodwin, H. S. Chung, D. Kang, J. Lee, and C. Yu. "Improved determination of color-singlet nonrelativistic QCD matrix elements for S-wave charmonium". In: *Phys. Rev. D* 77 (2008), p. 094017. DOI: 10.1103/PhysRevD.77.094017. arXiv: 0710.0994 [hep-ph].

[174] E. J. Eichten and C. Quigg. "Quarkonium wave functions at the origin". In: *Phys. Rev. D* 52 (1995), pp. 1726–1728. DOI: 10.1103/PhysRevD.52.1726. arXiv: hep-ph/9503356.

[175] E. Leader and E. Predazzi. *An Introduction to gauge theories and modern particle physics. Vol. 2: CP violation, QCD and hard processes*. Vol. 4. Cambridge University Press, 1996. ISBN: 978-0-521-49951-4, 978-1-139-24099-4.

[176] P. L. Cho and A. K. Leibovich. "Color-octet quarkonia production. II". In: *Phys. Rev. D* 53 (1996), pp. 6203–6217. DOI: 10.1103/PhysRevD.53.6203. arXiv: hep-ph/9511315.